

Année : 2010

THÈSE

présentée à

**L'U.F.R. DES SCIENCES ET TECHNIQUES
DE L'UNIVERSITÉ DE FRANCHE-COMTÉ**

pour obtenir le

**GRADE DE DOCTEUR DE L'UNIVERSITÉ
DE FRANCHE-COMTÉ**

en AUTOMATIQUE

(Ecole Doctorale Sciences Physiques pour l'Ingénieur et Microtechniques)

**Etude du comportement mécanique des microbulles.
Application à la conception d'une table actionnée
pour la micromanipulation en milieu liquide**

par

Cyrille Lenders

Soutenue le 2 Septembre 2010

devant la Commission d'Examen :

Président:

Gérard DEGREGZ

Professeur, Université libre de Bruxelles

Rapporteurs :

Charles BAROUD

Professeur, Ecole Polytechnique

Enrico FILIPPI

Professeur, Faculté Polytechnique de Mons

Examinateur :

Pierre COLINET

Chercheur Qualifié F.R.S.- FNRS, Université libre de Bruxelles

Directeurs de thèse :

Nicolas CHAILLET

Professeur, Université de Franche-Comté

Pierre LAMBERT

Professeur, Université libre de Bruxelles

Co-directeurs de thèse :

Michaël GAUTHIER

Chargé de Recherche CNRS, FEMTO-ST/AS2M

Alain DELCHAMBRE

Professeur, Université libre de Bruxelles

Thèse réalisée en cotutelle avec l'Université libre de Bruxelles.

Résumé

Cette thèse a pour contexte la micromanipulation en milieu liquide. Cette thématique scientifique vise à comprendre les phénomènes qui interviennent lors de la manipulation dans un liquide de microcomposants, dont la taille peut varier entre 1 μm et quelques millimètres. Les travaux de cette thèse se sont focalisés sur l'étude des forces de tension de surface en milieu immergé, car elles bénéficient d'effets d'échelle favorables. L'idée poursuivie est d'utiliser des bulles de gaz comme un moyen d'actionnement dans les milieux liquides, et nécessite d'étudier les propriétés mécaniques de ces bulles. L'originalité de l'approche repose sur la combinaison de deux effets : la tension de surface et la compressibilité du gaz.

La première étape a été l'étude d'un moyen efficace pour générer une unique bulle de gaz de taille voulue. Après une analyse exhaustive, il est apparu que la génération de bulle par le contrôle en volume était une méthode prometteuse. Nous avons alors développé un modèle permettant de prédire la taille d'une bulle, et mis en évidence la possible existence d'une instabilité de la croissance de ces bulles. Une étude analytique adimensionnelle nous a permis de définir un critère pour prédire l'existence ou non de cette instabilité.

La seconde étape a porté sur la caractérisation mécanique en régime quasi statique d'une bulle de gaz en contact avec deux solides. Le but étant de prédire la force générée par une bulle de gaz sur les solides ainsi que sa raideur. Le modèle implémenté a permis de déduire des propriétés intéressantes des bulles de gaz, notamment une grande compliance dont la valeur peut être contrôlée par des paramètres fluidiques. Cette propriété de compliance étant très recherchée en micromanipulation, un démonstrateur exploitant les bulles de gaz a été conçu. Il s'agit d'une microtable compliant actionnée par trois bulles. Ces travaux ouvrent la voie vers de nouveaux modes d'actionnement ou de capteur utilisant la transduction entre une énergie fluide et mécanique opérée par un ménisque capillaire.

Mots clef: Micromanipulation, Bulles, Compliance, Tension de surface

Abstract

The scope of this thesis is micromanipulation in liquid media. This scientific field aims at understanding the relevant phenomena existing during the manipulation in a liquid of microcomponents having a size between $1\ \mu\text{m}$ and a few millimeters. This work focuses on the study of surface tension forces in immersed media, because they have favorable scaling effect. The main idea is to use gas bubbles as actuation mean in a liquid, and requires to study the mechanical properties of these bubbles. The originality of the approach is the combination of two effects: surface tension and gas compressibility.

The first step was the study of an efficient mean to generate a single bubble of predefined size. After a detailed review, it appeared that volume controlled bubble generation was a promising method. We have then developed a model to predict the size of a bubble, and emphasized the possible existence of a growing instability. An analytic dimensionless study allowed to define a criterion to predict the existence of this instability.

The second step aimed at the mechanical characterization in quasi static equilibrium of a gas bubble caught between two solids. The purpose is to predict the force generated by the bubble, together with its stiffness. The model implemented allowed to infer interesting properties, notably a high compliance whose value is controllable by fluidic parameters. This compliance property being very important during micromanipulation, a demonstrator making use of gas bubbles has been designed and manufactured. It consists in a compliant microtable actuated by three bubbles. This work opens the way to new actuation or sensing means, using the transduction between fluidic and mechanic energy operated by a capillary bridge.

Keywords: Micromanipulation, Bubbles, Compliance, Surface Tension

Remerciements

La thèse est un parcours enrichissant mais semé d'embûches, à l'issue duquel l'un des apprentissages majeur est d'entrevoir l'étendue de notre ignorance. Au terme de ces années de recherche, on ne peut que ressentir de la frustration de ne pas avoir eu le temps d'ouvrir toutes les portes qui s'offraient à nous, mais les connaissances engrangées et les compétences acquises en valaient la peine.

De nombreuses personnes ont contribué à enrichir ces années. Je tiens en premier lieu à remercier Pierre Lambert et Michaël Gauthier pour les nombreux conseils qu'ils ont pu me prodiguer pour mener à bien ce travail. Leurs avis, leur aide et leur soutien m'ont toujours été précieux.

Je tiens également à remercier Alain Delchambre et Nicolas Chaillet pour m'avoir accueilli dans leur laboratoire et m'avoir fait confiance en me donnant l'opportunité de réaliser cette thèse.

Je remercie Messieurs Baroud, Colinet, Degrez et Filippi, d'avoir accepté de siéger dans mon jury de thèse. J'ai beaucoup apprécié leurs remarques pertinentes et les confrontations de point de vue. J'espère que les idées développées dans ce travail pourront leur être utiles.

Je remercie le Bureau des Relations Internationales de l'ULB ainsi que le crédit Tournesol du WBI, pour m'avoir aidé à financer mes séjours à Besançon.

Mes pensées vont également à mes collègues, tant à Bruxelles qu'à Besançon. L'excellente ambiance qui règne au sein des équipes a donné lieu à de nombreuses discussions intéressantes, et m'a permis de conserver un certain optimisme lorsque les difficultés s'amoncelaient. Je remercie en particulier Aline, qui a eu la force de supporter mes plaintes incessantes, et Jean-Baptiste, pour sa vision toujours originale des choses.

Je remercie Julien, d'avoir accepté de relire le manuscrit et d'avoir ainsi évité certains quiproquos résultants de tournures de phrase malheureuses.

D'une manière générale, je remercie aussi tous ceux qui ont réussi à me faire oublier que je ne parviendrai pas à terminer ce travail dans les temps.

Enfin, je tiens à remercier tous mes proches pour leur soutien moral lors de ces dernières années. En particulier, je remercie Evelyne, mon épouse, pour m'avoir épaulé et surtout m'avoir supporté pendant ces derniers mois. Merci de ne pas m'avoir tenu rigueur d'avoir si souvent ramené mes frustrations et mes doutes à la maison, et d'avoir su me rassurer.

Contents

1	Introduction	1
1.1	Microworld: Stakes and Challenges	1
1.1.1	Scaling Laws	2
1.2	Introduction to Micro-Assembly	3
1.3	Introduction to Micro-Assembly in Liquid Media	5
1.4	Objectives of the Thesis	5
1.5	Manuscript Layout and Reading Suggestion	6
1.5.1	Reading Suggestion	6
1.6	Thesis Joint Supervision	7
I	Review of Forces Acting on Immersed Microsystems	9
2	Microforces Modeling	11
2.1	Study of Forces in Microsystems	11
2.1.1	Force Models	11
2.1.2	Similarity Laws	12
2.2	Review of Major Forces Acting in Liquid Media	13
2.2.1	Electro-Hydrodynamic Forces	14
2.2.2	Hydrodynamic Forces	16
2.2.3	Surface Tension Forces	16
2.3	Example of Microvalves	17
2.3.1	Devices with a Moving Part	18
2.3.2	Devices Without Moving Part	18
2.4	Conclusions	19
3	About Surface Tension	21
3.1	Origin of Surface Tension Forces	21

3.1.1	Surface Energy	21
3.1.2	Wettability	23
3.2	Modeling Surface Tension	24
3.2.1	Surface Tension Force	25
3.2.2	Pressure drop Across Interface	26
3.2.3	Capillary Force	27
3.3	Measuring Surface Tension	28
3.3.1	Capillary Rise	29
3.3.2	Detachment Methods	29
3.3.3	Use of drops or bubbles	30
3.4	Influencing Parameters	31
3.4.1	Temperature	31
3.4.2	Contamination	32
3.4.3	Electrowetting	33
3.5	Implications for Microsystems	33
3.5.1	Crossing the Free Surface of a Liquid	33
3.5.2	Statistical Self Assembly of Microcomponents	34
3.5.3	Bubbles Preventing Solid Contact	35
3.6	Conclusion	35
 II Study and Application of Surface Tension Forces in Liquid Media		37
4	Controlled Generation of a Gas Bubble	39
4.1	Bubble Generation Mean	39
4.1.1	Electrolysis	40
4.1.2	Cavitation	42
4.1.3	Thermal Growth	43
4.1.4	Pressure Controlled Gas Injection	44
4.1.5	Volume Controlled Gas Injection	47
4.1.6	Comparison of the Different Generation Means	48
4.2	Model of the Volume Controlled Generator	50
4.2.1	Gas Bubble in Liquid Media	50
4.2.2	Device Description	51
4.2.3	Model of Bubble Height	51

4.2.4	Limit of the Model	55
4.2.5	Parameters Sensitivity	56
4.2.6	Dimensionless Analysis and Stability Criterion	60
4.3	Experimental Validation of the Volume Controlled Bubble Generation Model	66
4.3.1	First Experimental Setup	66
4.3.2	Second Experimental Setup	75
4.3.3	Conclusion of Experimental Validation	77
4.4	Examples of Application	81
4.4.1	Pressure Sensor	81
4.4.2	Bubble as Compliant Actuator	82
4.5	Conclusions	83
5	Compliance of a Gas Bubble	85
5.1	Modeling the Compliance of a Gas Bubble	85
5.2	Description of the Prototype	86
5.2.1	Application Context	86
5.2.2	Design of the Prototype	88
5.2.3	Device Advantages	93
5.3	Force Generated by a Gas Bubble	95
5.3.1	Hypothesis	95
5.3.2	Equations	96
5.3.3	Determination of Bubble Profile	97
5.3.4	Application of the Model	99
5.3.5	Limitation of the Model	100
5.3.6	Analysis of the Model	101
5.3.7	Parabolic Approximation	114
5.4	Validation of the Model	119
5.4.1	First Experimental Trials	119
5.4.2	Validation Strategy	120
5.4.3	Test Bed Design	121
5.4.4	Technological Issues	122
5.4.5	Methodology for Results Analysis	128
5.4.6	Experimental Results	131
5.4.7	Conclusion on the Experimental Results	133
5.5	Improvement of the Prototype	136

5.5.1	Layout of the device	136
5.5.2	Manufacturing	136
5.5.3	Lateral Forces	137
5.6	Conclusions	138
6	Perspectives and Conclusions	139
6.1	Prospective Developments	139
6.1.1	Controlled Microtable	139
6.1.2	Dynamics of the Table	140
6.1.3	Non Axisymmetric Bubbles	142
6.2	Conclusions	142
A	Demonstration of Jurin's Law	145
B	Construction of Fifth Order Polynomial Modeling Volume Controlled Bubble Generator	147
C	Demonstration for Equality of Forces Along Bubble Profile	149
D	Demonstration for Nullity of Force for Part-Spherical Profiles	151
E	Complements About Forces Acting on Immersed Microcomponents	153
E.1	Electrophoresis	153
E.2	Dielectrophoresis	154
E.3	Hydrodynamic Forces	154
F	List of Publication	159

List of Figures

1.2.1 View of ruby balls repelling one another	4
1.3.1 View of the Pronomia micro-assemblia station	5
2.2.1 Electrophoresis: ionic layers	15
2.2.2 Pressure in a Stokes flow	17
3.1.1 Illustration of surface tension	22
3.1.2 Origin of surface tension	22
3.1.3 Illustration of Young-Dupré equilibrium equation	24
3.1.4 Illustration of static, advancing and receding angles	24
3.1.5 Illustration of fluid anchoring	25
3.2.1 Geometric definition of mean curvature	26
3.2.2 Origin of the pressure force in surface tension modeling	27
3.2.3 Illustration of capillary forces self centering property	28
3.3.1 Illustration of liquid rise in a capillary tube	29
3.3.2 Surface tension measurement by Wilhelmy method	30
3.3.3 Surface tension measurement using drops or bubbles	31
3.4.1 Evolution of water surface tension with respect to temperature	32
3.5.1 View of a piezoelectrically actuated microgripper	34
3.5.2 Statistical self assembly using surface functionalization	35
3.5.3 Microbubbles preventing the contact between two solids	36
4.1.1 Concept of a single bubble generator	40
4.1.2 Electrode used for electrolysis based bubble generator testing	42
4.1.3 Working principle of the pressure controlled bubble generator	44
4.1.4 Height of a bubble with a pressure controlled generator	45
4.1.5 View of the pressure regulator used in the pressure controlled bubble generator	46
4.1.6 Working principle of the volume controlled bubble generator	47

4.2.1 Influence of surface tension and amount of gas mole on the diameter of a free gas bubble	51
4.2.2 Schematic representation of the volume controlled bubble generator	52
4.2.3 Model of the volume controlled bubble generator	52
4.2.4 Bubble height in a volume controlled generator, first set of parameters	55
4.2.5 Bubble height in a volume controlled generator, second set of parameters	56
4.2.6 Evolution of $m_i \Delta x_i$ with ΔV for first set of parameters	58
4.2.7 Evolution of $m_i \Delta x_i$ with ΔV for second set of parameters	59
4.2.8 Numerical dimensionless threshold for bubble growth instability	62
4.2.9 Contour plot of $\partial \hat{V} / \partial \tilde{h}$ with respect to \tilde{h} and \tilde{E} , in the case $\tilde{P} = 10$	64
4.2.10 \tilde{h}^* function of \tilde{P}	65
4.2.11 Analytical σ threshold	66
4.2.12 Analytical dimensionless threshold between stable and unstable bubble generation	67
4.3.1 Schematic representation of the first experimental setup for the validation of the volume controlled bubble generation model	68
4.3.2 View of the connection to the pressure sensor	69
4.3.3 Illustration of the image analysis software	70
4.3.4 View of bubble growth instability	70
4.3.5 Experimental validation of the volume controlled bubble generator, first setup, first set of parameters	71
4.3.6 Experimental validation of the volume controlled bubble generator, first setup, second set of parameters	72
4.3.7 Comparison of pressure measurement with pressure sensor and by image analysis	74
4.3.8 Schematic view of the second experimental setup used to validate the volume controlled bubble generation model	75
4.3.9 View of a large bubble: it does not comply with the hypothesis of part-spherical shape	76
4.3.10 Calibration of the compression system of second experimental setup	77
4.3.11 Experimental results on the second test bed	79
4.3.12 Summary of experimental validations	80
4.4.1 Height of a bubble with respect to pressure and channel diameter	82
4.4.2 Schematic view of a bubble based pressure sensor	83
4.4.3 Illustration of the relation between laser beam displacement and pressure to measure	84
4.4.4 Illustration of volume controlled generation with two outlet channels having a different diameter	84

5.1.1 Modeling a bubble as a spring	86
5.2.1 Spring hold compliant table	87
5.2.2 Illustration of the efficiency of a compliant table during the "peg in hole" benchmark test	88
5.2.3 Illustration of an orthoplanar spring	89
5.2.4 Schematic view of the bubble supported compliant table	90
5.2.5 Illustration of the simple and improved anchoring methods	90
5.2.6 Dimensions of prototype tables	91
5.2.7 Actual view of two tables	91
5.2.8 View of a table with improved anchoring circle manufactured on a CNC milling machine	92
5.2.9 View of the three actuated DOF	93
5.2.10 Illustration of the working principle of the compliant table device	94
5.3.1 Geometry of bubble between two solids	95
5.3.2 Free Body Diagram of the table around one bubble	96
5.3.3 Free body diagram in the case of through holes	97
5.3.4 View of input and output parameters of the model	98
5.3.5 View of the iterative procedure to calculate bubble profile	99
5.3.6 Pressure repartition in the case of a table with blind holes or through holes .	100
5.3.7 Evolution of surface tension force and pressure force along symmetry axis (z) with the gap	103
5.3.8 Illustration of the effect of total gas volume variation	104
5.3.9 Comparison of bubble profiles obtained with blind holes and through holes .	106
5.3.10 Evolution of the force and contact angles for different gas volumes when using a table with through holes	107
5.3.11 Comparison of bubble profiles and force obtained for different table hole diameters	109
5.3.12 Comparison of the force with respect to gap distance for a scaled model . . .	112
5.3.13 Design flow chart for compliant table	113
5.3.14 Illustration of parabolic approximation of bubble profile	114
5.3.15 Illustration of the profiles obtained by ODE calculation and parabolic approximation	117
5.3.16 Evolution of the mean curvature and force at both ends of the parabolic approximation profile, compared to ODE resolution	118
5.4.1 View of the prism used to perform force measurement in water with an AFM	120
5.4.2 Methodology of bubble force measurement using an AFM	120
5.4.3 View of the actual setup for the AFM-based force measurement of a bubble .	121

5.4.4 Views of the bubble and the AFM tip used to measure the force generated by a bubble	121
5.4.5 View of an approach-recede curve to estimate qualitatively the force generated by a bubble	122
5.4.6 Procedure of the experimental validation	123
5.4.7 Schematic view of the second experimental setup used to validate the volume controlled bubble generation model	123
5.4.8 View of the actual test cell, comprising the platform and the optical system .	124
5.4.9 View of the flexible hoses connections	125
5.4.10 Illustration of the parallax effect	125
5.4.11 Example of image capture with two tables load	126
5.4.12 Schematic explaining calibration error due to the difference of plane position relative to the camera	126
5.4.13 Experiment to illustrate gas mole decrease over time in an air-water system .	127
5.4.14 Comparison of permeability model of gas permeation through flexible hoses with experiments	127
5.4.15 Illustration of a liquid inclusion in a flexible hose	128
5.4.16 View of free bubble measurement	129
5.4.17 Example of bubble profile measurement	130
5.4.18 Illustration of gap measurement	131
5.4.19 Comparison between model and experiments	132
5.4.20 Comparison between experiments and model with a linear correction of gas mole number	133
5.4.21 Proposition to enhance the contrast of bubble borders	134
5.4.22 View of the test bed placed in the AFM device of the BEAMS Department .	135
5.5.1 View of suggested improvement of the device platform layout	136
5.5.2 View of a manufacturing test of a new platform layout using excimer laser . .	137
5.5.3 Design of a device with 6 bubbles	137
6.1.1 View of different variants of the force model	140
6.1.2 Proposition of a feedback loop to control the position of the table	140
A.0.1 Schematic view of equilibrium in Jurin's law	145
A.0.2 Schematic view of pressure distribution in Jurin's law	146
C.0.1 Equilibrium of a meniscus slice	149
D.0.1 Schematic of force balance in the case of a bubble having a part spherical shape	152

E.3.1 Velocity field around a sphere	155
E.3.2 Hydrodynamic force acting on a microsphere	155
E.3.3 Comparison of drag coefficient	156
E.3.4 Working principle of a feeder based on hydrodynamic forces	157

List of Tables

3.1.1 Value of γ for typical liquids at 25°	23
4.1.1 Comparison of the different bubble generation means	49
4.2.1 Definition of model parameters	53
4.2.2 Sets of parameters for model interpretation	54
4.2.3 Parameters variation used to calculate the variation of the output Δh	58
4.3.1 Sets of parameters for experiments made on the first test bed	71
4.3.2 Sets of parameters for experiments made on the second test bed	77
5.3.1 Examples of receding angles (source: [52])	101
5.3.2 Recurrent parameters for model analysis	102
5.3.3 Parameters for the simulations to compare the effect of gas system volume	104
5.3.4 Simulation parameters to compare blind holes (B) and through holes (T)	105
5.3.5 Parameters for the simulations to evaluate the effect of anchoring diameter s_2 variation	108
5.3.6 Parameters for the simulations to evaluate scaling effects on the device	111
5.3.7 Parameters for the comparison between parabolic approximation and ODE calculation	117
5.4.1 Mass of the tables and the force they apply on each bubble	128
5.4.2 Measurement of the diameter of the anchoring circles	129
5.4.3 Input parameters for the experimental validation of model predicting the force developed by a gas bubble	132
5.4.4 Maximal variations of n corresponding to the smallest gap (experimental results) for each test and corresponding permeation time	133
5.5.1 Parameters of excimer laser used to manufacture prototypes	137
E.3.1 Comparison of sedimentation velocity	156
F.0.1 List of Symbols	162

Chapter 1

Introduction

This first chapter will present the scope and the objectives of this work whose context deals with manipulation of micro-objects whose typical size is between a microns and a millimeter. We will briefly introduce the specificities of the behavior of these micro-objects and will focus on the micromanipulation problematic and issues. In this field, our works are focused on micromanipulation in liquids, whose specificities compared to current approaches in the air will be presented.

Finally we will detail the objectives of this thesis and present the layout of the manuscript.

1.1 Microworld: Stakes and Challenges

All around us in our daily life, we see the results of technological miniaturization. Think of cellular phones which are smaller and smaller while including more and more functions, or of all the sensors present in today's car. The prefix micro, that will be intensively used in this work, refers to small dimensions. More specifically, we consider dimensions that are in the range of $1\mu\text{m}$ to a few millimeters. As a reference, a human hair is around $100\mu\text{m}$ thick, and a blood cell has a diameter around $8\mu\text{m}$. We define the concept of microworld as all the specificities inherent to the micro-objects and their interaction with their environment.

For a few decades, industries and researchers have shown a growing interest for microworld. Indeed microsystems are interesting for many reasons: they are more compact and require less material to be built. But they also require less energy to run and have a smaller inertia. The components are generally manufactured using parallel technologies, which allows to manufacture several units simultaneously, decreasing the costs.

There are several sectors interested in components and system miniaturization. A first example is the electronic industry. Currently, the smallest SMD components have a dimension of $.4\text{mm} \times .2\text{mm}$, while in the nineties, the usual size for these components was $3.2\text{mm} \times 1.6\text{mm}$. Miniaturization of electromechanical devices, such as sensors and actuators, has also been studied a lot these years, with the development of MEMS: micro electromechanical systems. Now these systems are generally at the crossing of several scientific fields. Optical MEMS for example, combines the features of MEMS with mirrors, lenses and optic fibers [39]. Another topic which is intensively studied is the Lab-On-Chip. By combining microfluidics, i.e. fluids flowing in microchannels, with analysis systems, it is possible to conduct fluid analysis using a very small amount of material. Typical application is blood analysis [37]. Microfluidics is also studied to create heat sinks with a circulating cooling fluid. Target application is to cool microelectronic processors for example [67]. Biomedical devices designers are generally also

interested by microcomponents. It allows to design devices that can penetrate the human body while creating less injuries, like for mini-invasive surgery. It also makes devices more portable, such as automatic drug delivery systems. For example, many developments have been made to design implantable micropump for insulin delivery. Such device could measure glycemia and adjust the volume of insulin to deliver [81].

The most significant point about microworld is that a microsystem is not a small macrosystem. Indeed, physical phenomena do not affect small and large objects in the same way. The observation of nature. For example, the system used by birds to fly is not the same as flying insects. Some insects are able to lift loads equivalent to several times their weight, while larger animals are not. We can also observe the difference when throwing rocks and sand in a river: rocks will sink, and the grains of sand will follow the river flow. These differences are explained by scaling laws.

The fact that microsystems behave differently from macrosystems seems puzzling, but this opens the way to new implementations of functions, or even provides opportunities not imaginable at macroscale. This requires also new way of thinking. Indeed, tasks that seems easy at macroscale can become tricky at microscale. For example, when small components with a specific gravity larger than water are dropped in water, they stay on the surface of the liquid, thanks to capillary force.

1.1.1 Scaling Laws

Scaling laws explain how the relative effect of different phenomena changes with respect to the size of objects and therefore show the difference between microsystems and macrosystems.

Let us illustrate this by a simple example. Suppose an object has a characteristic size a . It could be for example the diameter of a sphere or the width of a cube. Suppose a force F_1 is proportional to a^3 , and suppose another force F_2 is proportional to a^2 . F_1 could be for example the weight of the object, and F_2 could be the force exerted by a vacuum gripper, which is proportional to the contact surface. For high values of a , F_1 is larger than F_2 . This is why large objects are not lifted using a vacuum gripper. If an object is 10 times larger than another, its weight is 1000 times larger, and the force from the gripper is only 100 times larger. On the contrary, a vacuum gripper is very efficient for small objects.

More generally, relative effect of a force will be determined by the exponent of the characteristic length in its mathematical formulation. The smaller the exponent, the more important the force becomes when the size of the object decreases. Volume forces are therefore negligible compared to surface forces below a certain size. And surface forces become negligible compared to linear forces below a certain size.

Typically, the weight of an object and the buoyancy force acting on an immersed object are proportional to the cube of the characteristic length. The pressure, and some electrostatic forces are proportional to the square of the characteristic length. And we will demonstrate in Chap. 2 that hydrodynamic forces and surface tension forces are proportional to the length.

Naturally, this scale effect analysis is limited for the dimension range where the same physics rules micro- and macrosystems. Indeed models are built on hypotheses, and the model will be valid only as long as these hypothesis are satisfied. For example, there is a size limitation to the use of Navier-Stokes equation to study gas flows in microchannels, because Navier-Stokes equation is based on the hypothesis that the medium is continuous. If the channel size is close to the mean free path of gas molecules, this hypothesis is not correct anymore, and a statistical approach is necessary. At an air pressure of 101325Pa, the mean free path is around 70nm [4]. As long as the hypothesis of a model are satisfied,

the same physics apply and the scaling of the phenomenon according to the exponent of the characteristic length is admissible.

1.2 Introduction to Micro-Assembly

Micro-assembly refers to the assembly of components having a characteristic length between $1\mu\text{m}$ and a few millimeters. Usually, it is composed of different tasks: picking a component, moving it to the desired location, and finally releasing the component. Numerous systems are still assembled from discrete components. For example, analog watches, optical fibers in optoelectronic systems, wirebonding to create the connections between components or between component and the macroscopic system,... Assembling such components has to deal with the specificities of microworld.

The first step of the assembly consists in picking the component. For this operation, the gripper must be able to catch a single component. Repulsive forces can prevent the gripper of reaching the component, repelling it as the gripper approaches. Moreover, the gripper is supposed to pick up only one component. But due to adhesion forces (Van der Waals, capillary or electrostatic forces), different components are likely to stick to one another. To tackle these problems, strategies can be developed to hold components at specific locations, separated from one another.

When the gripper successfully caught a single component, the next step is to move it to the desired location. The movement of the gripper may be very fast to ensure high production rate. In this case, the inertia of the system must be taken into account to avoid the ejection of the component, or oscillations of the system. The positioning of the component must have a precision which is at least an order of magnitude below the size of the components. Generally the issue is not the resolution or repeatability of the positioning system: commercial positioning systems with a repeatability of a few tenth of nanometer are available. Positioning errors arise essentially because of parasitic forces moving the component.

To ensure this positioning, vision systems are sometimes used, either to allow the operator to view the scene in case of manual positioning, or to allow automatic shape recognition in case of automatic positioning. But this technology presents also challenges because of the reduced depth of view, reduced field of view and light reflections. Therefore, it is not easy to see the surrounding materials when performing an assembly task. Sometimes micro-assembly systems provide force feedback measurement. This is interesting to avoid breaking the component by applying a force too large, or to control the insertion of a component in another one.

When the component reaches finally its location, the gripper must release it. If the component is not secured when it is placed, there is a risk that it changes its position when the gripper releases it. Repulsion forces can indeed apply as soon as the component is not hold anymore in the gripper. On the contrary, adhesion forces may also occur between the gripper and the component. In that case, the gripper cannot release the object.

We give here two examples to illustrate the challenge micromanipulation.

In the case of the assembly of a watch ball bearing [53], the components are small ceramic balls having a diameter of $500\mu\text{m}$. Five of these balls must be placed in the cavities of a bearing (outer diameter of the bearing: $\approx 8\text{mm}$). In this case, the balls are delivered in bulk. The first problem is to catch one and only one ball. Two different phenomena are competing in this case. First, the electrostatic repulsion: if the balls and the gripper are electrically charged (Fig. 1.2.1), by triboelectrification for example, the balls could escape when the

gripper approaches. Second, the adhesion forces: contact forces, originated from capillary condensation for example [14], make the different balls stick together. So it is difficult to catch a ball, and if the gripper gets one, it is not certain that only one ball is picked up. Finally, if the gripper catches successfully a single ball, and places it at the right location, it must finally release the component without moving it. The solution proposed in [53] is to use a capillary gripper, which is a single finger gripper using surface tension forces of a liquid bridge to lift object, much like someone who would lick their finger to lift salt grains. The release of the object is done mechanically pushing the ball against a lateral wall of its cavity, hence shearing and finally breaking the liquid bridge.



Figure 1.2.1: View of 500 μm diameter ruby balls repelling one another because of electrostatic forces. These forces are large enough to compensate the weight of the balls

In the case of SMD components placement, the components have to be placed and oriented precisely. Up to now, the machines used in industries generally use vacuum grippers to pick up the components. These machines are able to place up to 36000 component per hour, with less than 10 defects per million, and with a precision of about 40 μm and repeatability down to 9 μm . In this case, the components are delivered in tapes, clearly separated from each others. These machines could suffer from two problems. First, the high rate of placement sometimes induces shock in the components when it hits the substrate, and may damage it [78]. Second, if the size of components continues to decrease, vacuum grippers could become inefficient, because the size of the noses would have to be very small, which could induce problem to generate the pressure variations.

Currently, except for SMD electronic components, the automation of micro-assembly task is difficult. Indeed, the effects of microworld forces are difficult to predict, and this is not compatible with the requested reliability of the process. The knowledge of a model of these forces is not always sufficient to calculate the forces, as the input parameters are not necessarily accessible. Electrostatic forces for example are modeled by Coulomb law, but it is based on the electrical charges in or on the objects, and these data are not easy to acquire.

Because automatic assembly could drastically reduce the total manufacturing costs, engineers usually develop strategies to tackle handling problem. These strategies can be classified in three categories. The first approach is to avoid as much as possible the parasitic forces. One example is to use non contact handling, using pressure waves to move objects [91]. Another approach is to make use of these forces, using for example of gripper based on surface tension effects. The last approach consists in taking measures to minimize these forces.

1.3 Introduction to Micro-Assembly in Liquid Media

Working in a liquid combines two micromanipulation strategies. The basic idea was to minimize the effect of parasitic forces [32]. Electrostatic forces are based on Coulomb law. Therefore, the force generated by the presence of electric charges can be reduced if the working medium has a high relative permittivity. Moreover, if the liquid contains ions in solution, these ions can contribute to the electric charge balancing. Surface tension forces exist only if there is an interface. When working in air, even if no liquid is poured in the system, capillary condensation can be responsible for the creation of liquid bridges from ambient humidity.

But the presence of the liquid will also provide opportunities for new manipulation concepts. One example is the design of a gripper based on the solidification of the liquid, creating a temporary solid bridge between the component and the gripper [64]. Naturally, making the manipulation in a liquid requires adapted manipulators, vision systems and sensors. Figure 1.3.1 shows a picture of a micro-assembly station developed in the French National Research Agency ANR PRONOMIA project.

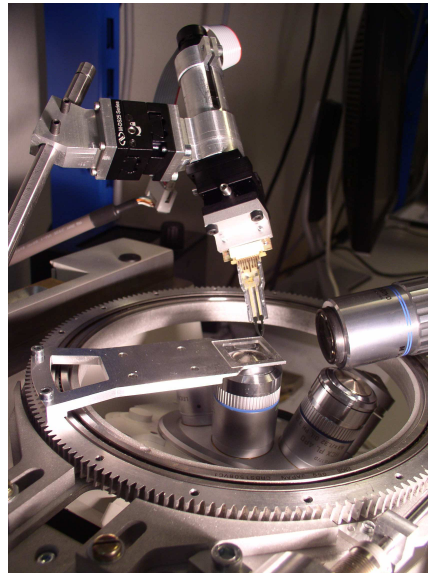
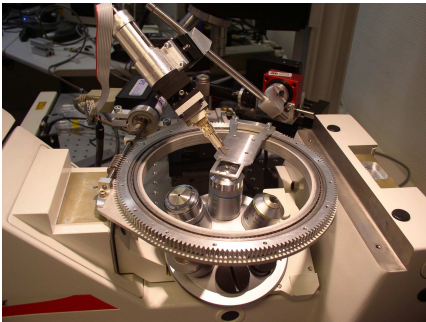


Figure 1.3.1: View of the Pronomia micro-assembly station, able to perform micro-assembly tasks in liquid medium

However, when the operations are performed in a liquid, immersed objects are subjected to other forces. To make efficient designs, it is essential to be conscious of these forces. This will be presented in Chap. 2.

1.4 Objectives of the Thesis

The main objective of this thesis is to study the forces acting on immersed micro-objects. More specifically, this work will be focused on surface tension effects, which appear when a bubble is present in the system. We will therefore study the mechanical behavior of a bubble, more specifically we will take an interest in studying the effect of the presence of a bubble between two solids.

Models to describe the mechanics of surface tension already exist [52], but they are limited

to the study of liquids, or at least they do not take the compressibility of the medium into account. The first major contribution of this work is to couple the mechanical models for surface tension with the compressibility of gases.

The study of the mechanical behavior of a bubble requires also a mean to generate these bubbles. Ideally, the generator should be able to control the size of the bubble. Usually, people developing models to predict the size of bubbles are interested in continuous bubble generator, with applications in chemistry for example. We have therefore investigated different means to generate single gas bubbles having a predefined size. One of the underlying objective was therefore to find the most promising method to generate bubbles. We have developed a model to predict the size of the bubble, and to validate this model experimentally.

The second underlying objective was to model the force generated by a bubble between two solids, to analyze the model to understand how to make use of these bubbles and to validate it experimentally.

1.5 Manuscript Layout and Reading Suggestion

This manuscript is separated in two parts.

The first part is a review of the predominant forces acting on immersed microsystems. Chapter 2 presents the main reason why modeling forces is so important for microsystems. We also briefly review in this chapter the three main force families. From this review we select the most promising force, on which we focus afterward. Chapter 3 details the origin of surface tension, and the existing models to predict the force induced by surface tension.

The second part contains the contributions of this work: the study of surface tension effects in liquid media, and an example of application of these effects. More specifically, the second part presents the study of microbubble behavior. Chapter 4 presents the developments of the bubble generator. In this chapter, we review different principles to generate bubbles, and we compare them to select the most promising method to study microbubbles properties. This chapter contains also the mathematical model describing the working principle of the selected generator, and the analysis of this model. From this analysis, we demonstrate that an instability during bubble growth may occur. We lead a numeric and then an analytic dimensionless analysis to define a criterion able to predict the existence of the instability. Finally, we present the experimental validation of the model. Chapter 5 presents the study of the force generated by a microbubble between two planes, and the application chosen to make use of these forces: an actuated table for micromanipulation. We then propose a model for the force generated by a bubble, and we analyze this model to understand the influence of the various parameters. From this analysis, we present some design guidelines to get the best of microbubbles. Finally, we present the experimental validation of the model, and deduce improvements that could be brought to the prototype. Chapter 6 presents ideas for prospective developments and the conclusions of this thesis.

1.5.1 Reading Suggestion

For the attention of readers running out of time and wanting to go straight to the point, we hereby propose a reading suggestion containing the essential elements to understand the models developed in this thesis.

- Sect. 2.2.3: Why taking surface tension into account is important in microsystems?

- Sect. 3.1: Why does surface tension exist?
- Sect. 3.2: How to model mechanical effects of surface tension?
- Sect. 4.2: How to predict the size of a bubble with the proposed generator?
- Sect. 4.3: How has been validated the model predicting the size of a bubble?
- Sect. 5.2: How to make use of microbubbles properties?
- Sect. 5.3: How to predict the force generated by a bubble?
- Sect. 5.4.4: How to efficiently perform experiments with microbubbles?
- Sect. 5.4.6: How has been validated the model predicting the force of a bubble?
- Sect. 5.5: What are the prospective developments to achieve?

1.6 Thesis Joint Supervision

This thesis has been realized under a joint supervision with the BEAMS Department of ULB (Université libre de Bruxelles, Belgium) and the AS2M Department of the Femto-ST institute, UFC (Université de Franche-Comté, France).

Most of the theoretical developments were made at ULB, while most of the technological development and experimental setups were developed at UFC. Beyond this formal barrier, this joint supervision has been an opportunity to working in two different labs, discuss with two different teams, and discuss ideas. This was also an opportunity to see the related projects and refine the context to this thesis.

Part I

Review of Forces Acting on Immersed Microsystems

Chapter 2

Microforces Modeling

In Chap. 1, we have presented the challenges of micromanipulation. The idea of performing the manipulations in a liquid environment to address some of the problems inherent to micromanipulation has also been presented.

Working in a liquid environment requires to know the forces acting on immersed micro-objects. In this chapter, we will first remind in Sect. 2.1 the stakes of force modeling in microsystems. Then we present in Sect. 2.2 a review of the most relevant forces acting on microcomponents in a liquid, and compare them on basis of their controllability and scaling effect. We finally give the example of microvalves design in Sect. 2.3 to illustrate how to make use of microworld properties.

Among the reviewed forces, surface tension force is the most promising. It will be studied extensively in Chap. 3.

2.1 Study of Forces in Microsystems

To efficiently design a system, it necessary to understand the physics of the key phenomena. In a mechanical system, this means notably to predict the forces acting on the components. One way of predicting the force is to develop a mathematical model of the phenomenon.

2.1.1 Force Models

By modeling a force, we mean finding a mathematical expression that predicts the amplitude of the force with respect to a set of parameters. The validity of a model is generally limited to a certain domain, and the hypothesis made to develop the model should always be indicated. The model will provide important information such as the relevant parameters playing a role in the phenomenon, and their relative sensitivity. Let us point out that sometimes, the knowledge of a model is not sufficient to quantitatively predict the behavior of a system, because the inputs of the model are impossible to acquire. The mathematic relations defining the model can also be complex and impossible to solve analytically.

Let us consider electrostatic forces as example. A well known model for these forces is Coulomb law. This model tells that the force is proportional to the electrostatic charge carried by the object, and to the electrostatic field. It demonstrates that the amplitude of the force is inversely proportional to the permittivity of the medium surrounding the system, from which we infer that working in a medium having a large permittivity is a way to reduce

electrostatic forces. Yet it is not necessarily possible to predict exactly the electrostatic force acting on an object, because it is difficult to know the charge acquired by an object.

If the mathematical model is too complex to be solved analytically and numerically, it is possible to perform experiments on prototypes of the device. But manufacturing the device can be expensive since the fixed costs such as mask development cannot be passed on a large production batch. To tackle this problem, engineers can make use of similarity laws, but we will demonstrate that they are of limited use in the case of microsystems.

2.1.2 Similarity Laws

Sometimes, the system is so complex that, instead of modeling it entirely, it is more efficient to test it experimentally. However, building the device can be expensive, for example if it is large (airplane) or if it is small (manufacturing technologies requiring to develop masks for example).

In the case of large system, engineers generally make use of similarity laws. These are based on Buckingham theorem and dimensionless numbers [87]. This method allows to infer the behavior of a system based on a scaled prototype of the device. The advantage is that it is easier and cheaper to build the scaled prototype than the real device.

One could think of using this method in the case of microsystems, and build large systems with conventional manufacturing means to study the microsystem. Buckingham theorem and dimensionless numbers are useful, notably because they allow to reduce the number of parameters in a mathematical relation. But we will demonstrate that using these concepts with similarity laws to study a scaled prototype is not always possible.

To apply this method, the first step is to detect all parameters playing a role in the working principle. Then, from these parameters, dimensionless numbers are built. This is generally done using the dimensional matrix, in which each line corresponds to an elementary unit (length, mass, time, ...) and each column corresponds to a parameter. The elements of the matrix represent the exponent of the unit in parameter dimension. For example if the parameter is a velocity, element in the line corresponding to length is 1 and element in the line corresponding to time is -2 , the other elements in the column are 0.

The number of parameters minus the rank of the dimensional matrix corresponds to the number m of dimensionless number π_i that cannot be composed by multiplying or dividing other dimensionless numbers together. Buckingham theorem tells that the behavior of a system is a function of all these dimensionless numbers:

$$\Psi(\pi_1, \pi_2, \dots, \pi_m) = 0 \quad (2.1.1)$$

Therefore, if each of the dimensionless number is unchanged, the behavior of the system will be alike. So if the scaled model of the device is built in such a way that each of the dimensionless number is the same as for the real device, the behavior of the real system can be inferred from the behavior of the scaled prototype. If it is not possible to keep each of the dimensionless number constant, the similarity is not exact, and some distortion is induced by the differences.

In [60], we have shown that increasing the size of the geometries of microsystem makes it impossible to keep dimensionless numbers constant, because it is not possible to find materials having adequate physical parameters, or it limits the allowed magnification. This has been illustrated on the example of a microvalves based on a moving ball.

For example, if the objective is to measure the flow through the valve with respect to the pressure difference between input and output, it is possible to find this relation from dimensionless numbers:

$$\frac{U_2}{U_1} = \frac{d_1 \rho_1 \mu_2}{d_2 \rho_2 \mu_1} \quad (2.1.2)$$

where U is the fluid flow, d is the diameter of the input channel, ρ is the fluid density and μ is the dynamic viscosity of the fluid. Index 1 refers to the real device, and 2 refers to the scaled prototype.

From there, we see that if the fluid is the same in both systems, the flow in the large system would be inversely proportional to the geometric enlargement of the system, complicating its measurement. A solution would be to have a liquid with a larger viscosity in the large system than in the small system. In microfluidic systems, Reynolds number is usually small, because diameter of the channels is small. This means that viscous effects are more significant than inertial effects. This is why the scaled model must be used with fluid having a larger viscosity.

We can see from this example that magnifying the models requires to use materials with different parameters to take effects of microscale. But it is not always possible, since it may sometimes require parameters values that do not exist. This is why it is not possible to use this method for surface tension forces. Indeed, we have also studied the case of the same ball valve, but adding the presence of a gas bubble in the system. In this case, we have to deal also with surface tension. Because surface tension does not span over a wide range of values (for common liquids at 20°C, between 20 mN/m for silicone oils and 72 mN/m for water), we suppose that surface tension remains constant. To keep predominance of surface tension effect compared to gravity effect, this involves using a fluid with a low density in the scaled model. The magnifying ratio is therefore limited by the smallest density available. If we consider a density of 700kg/m³, the magnifying ratio is only 1.2.

Buckingham theorem and dimensionless numbers can be very useful to study microsystems, as we will see in Sect. 4.2.6. But similarity laws show limitations to use a scaled prototype to study a system because it is not possible to find adequate materials to avoid distortion. In fact, it is even hazardous because using this method will give results that are not reliable. The example of microvalve illustrates this: if the designer neglects the effect of surface tension, it will be masked in the scaled prototype. Indeed, small bubbles will not much influence the behavior of the large device. This is another argument urging the need for mathematical models of these microworld major forces.

2.2 Review of Major Forces Acting in Liquid Media

In this section, we will briefly review three predominant forces of the microworld: electrohydrodynamic forces, hydrodynamic forces and surface tension forces. Some complements about these forces can be found in App. E.

Usually, the three forces that are most often described in microsystems are electrostatic force, Van der Waals force and surface tension force. Some papers also mention the magneto-hydrodynamic force. Intentionally, we will not present the Van der Waals force nor the magneto-hydrodynamic force.

Van der Waals force is often mentioned in the literature about microsystems. The origin of this force is due to the presence of electric dipoles in molecules of matter. According to Lambert [51], this force is only relevant at very small distances (around 100nm), and their

effects are reduced because of surface roughness and because of the presence of water between the objects. Therefore, we will not consider these forces.

Magneto-hydrodynamics (MHD) is the study of the interaction between a magnetic field and the movement of particles carrying an electric or magnetic charge in a fluid, such as ions dissolved in a liquid. This phenomenon will have an influence essentially on the fluid, but not directly on the immersed solids. An example of application is proposed by Affanni [1], who uses MHD to design a microstirring device. Stirring devices are needed in microfluidic systems where fluids have to be mixed, to induce a chemical reaction for example. Indeed, simply having two channels flowing into one channel is not sufficient because of large viscous to inertial effect ratio in microsystems: both fluids flow side by side in the channel.

2.2.1 Electro-Hydrodynamic Forces

Electro-hydrodynamic forces are the forces due to the interaction between an electrostatic field and the charged particles (ions) or charged objects immersed in a liquid. We will describe two different phenomena: electrophoresis and dielectrophoresis.

Electrophoresis

When a solid is immersed in a polar liquid, or at least containing ions, a thermodynamic equilibrium is established and the surface acquires electric charges. Therefore, ions carrying an opposite charge are attracted by object surface. This creates an electrical double layer (EDL) around the object. Far away from the object, the global charge seems to be zero, but close to the object, the effect of the ion cloud can be significant. For example, it can be responsible to prevent colloids¹ to flocculate (form aggregates).

Generally, the model of electrophoresis is based on the existence of three different layers around the solid. The first layer contains the electric charges carried by the solid. The second layer, called Stern layer, contains ions from the solution which are strongly bound to the solid. A third layer, called diffuse layer, contains the rest of the ionic cloud. The electric potential decreases with respect to the distance from solid surface (Fig. 2.2.1).

When an external electric field is generated, the particles are exposed to an electrostatic force due to the interaction of the electric field and the electric charges carried by the solid. It is generally admitted that a part of the ionic cloud is moving with the particle delimiting a shear plane. This part corresponds approximately to the second layer. An important parameter for electrophoresis is defined from this consideration: zeta-potential (ζ -potential). It is the electric potential at the location of the shear plane, assuming the potential is zero in the bulk liquid.

Electrophoresis is notably used as a separation method in chemistry or biotechnology [13]. Since the different elements present in the liquid have not the same ζ -potential, the application of an electric field induces forces with a different amplitude for each element.

Of course, the electric field must be continuous, not alternating, otherwise there would be no mean effect.

Let us also mention that researches are made concerning the functionalization of surfaces. This technology is based on chemical treatments of surfaces to change the polarity of surfaces. This polarity can even be controlled by changing the pH of the solution, allowing for example to change forces from attractive to repulsive [22, 23].

¹small particles suspended in a liquid

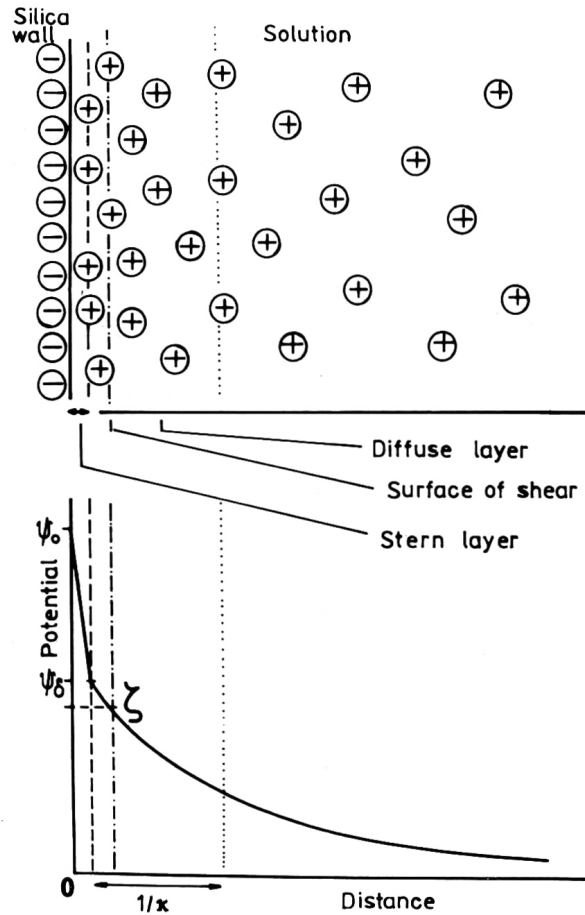


Figure 2.2.1: Schematic illustration of the different ionic layers and the corresponding electric potential (source [30])

Let us finally mention the electro-osmosis phenomenon, which is basically the same phenomenon as electrophoresis, except that the ionic cloud is generated from the wall of the flow channel. When applying an electric field to the liquid, the cloud will acquire a velocity, and will drag the fluid with it. This produces a flow with a uniform profile [27].

Dielectrophoresis

Dielectrophoresis (DEP) refers to the effect of a non uniform electric field on a polarizable element.

If a polarizable solid is placed in an electric field, the electric charges of the solid will move according to their sign and the direction of the electric field. The solid is therefore polarized, as a dipole. If the electric field is uniform, the global effect is zero because of symmetry. But if the field is non uniform, there is a force resulting from the interaction between the field and the electric charges.

One advantage of DEP compared to electrophoresis is that alternative fields are used. This is useful if the electrodes generating the field are placed in the liquid, without insulator. The use of an alternative field allows to avoid the creation of gas bubbles by electrolysis.

These bubbles could perturbate the behavior of the system.

Because the materials will determine if DEP force will induce a repulsive or an attractive behavior, and the amplitude of the effect, DEP can be used to separate different particles [63, 84, 31]. It is also used to trap particles in areas where the DEP force is minimal, which is a function of the gradient of electric field [41, 15].

The study of DEP forces is usually studied numerically to optimize the electric field layout for the considered application [47]. Some authors have for example designed 3D structures to increase the field variations, and to avoid the constraint of working in a plane [84, 90].

2.2.2 Hydrodynamic Forces

Hydrodynamic forces are due to the interaction of the fluid flow with the solid. Since Reynolds number are small in microfluidics, the effect of inertia is small compared to viscous effect. From our macroscopic common sense, it is like using fluids with a high viscosity.

As an illustration, we will study the case of a sphere in a liquid. Any relative velocity between the fluid and the solid will induce an hydrodynamic force.

A first approximation, valid for $Re < 1$, is to consider a Stokes flow. In this case, the flow is supposed to be axisymmetric around the sphere, incompressible, and the velocity of approach, U_∞ is assumed uniform and oriented according to x axis. This approximation is valid for a mobile sphere in a quiescent liquid, or for a static sphere in a flowing fluid.

This configuration leads to a linear variation of pressure distribution around sphere surface [33]:

$$P = -U_\infty \mu a \left(\frac{3x}{2(x^2 + y^2 + z^2)^{\frac{3}{2}}} \right) \quad (2.2.1)$$

where μ is the fluid viscosity and a is the radius of the sphere. Profile of pressure distribution along x -axis is shown in Fig. 2.2.2.

In this case, the drag force is given by [33]

$$F_{HD} = 6\pi a \mu U_\infty \quad (2.2.2)$$

If $Re \geq 1$, Stokes approximation is not valid anymore because the flow is not axisymmetric anymore, and turbulences appear downstream [43].

Simulations are useful for complex configurations or when $Re \geq 1$, since there is no analytical solution in these cases. But numerical simulations must take into account 3D instabilities for $Re > 200$.

It is important to notice that for $Re \leq 1$, hydrodynamic force is proportional to the radius of the sphere, which means that from a scaling law point of view, hydrodynamic forces are predominant in microfluidics.

2.2.3 Surface Tension Forces

Surface tension forces arise when an interface between two materials exists in a system. This kind of force has two advantages compared to the two other forces presented above.

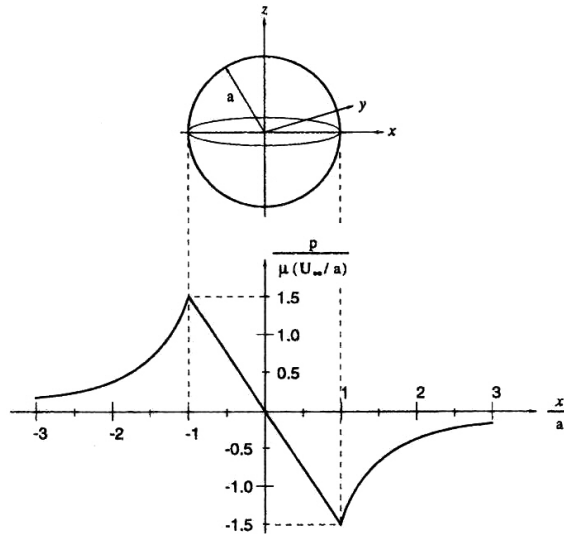


Figure 2.2.2: View of pressure distribution along flow axis in a Stokes flow. The pressure variation is linear (source [33])

First, the scaling laws are favorable, since this force is proportional to the characteristic dimension of the objects. This will be demonstrated in Sect. 3.2.3.

Second, the parameters governing this force are more easy to control with classic mechanical devices: pressure, temperature, geometry... While the other presented forces require control of chemical composition of the liquid (pH, ionic strength), to design specific electrode layout to control the electric field, or to study carefully the geometry of the device to optimize liquid flow stream.

For these reasons, we have decided to focus on surface tension forces in the next sections of this work. Chapter 3 will introduce more deeply surface tension and its effects on microsystems. The major contribution of this work will be the introduction of gas compressibility property to surface tension model.

2.3 Example of Microvalves

In this section we will study the case of microvalves, in order to illustrate the concepts presented in the previous sections. These devices are used in microfluidic systems to stop fluid flow in microchannels. Microvalves can be found in every microfluidic device, but essentially in laboratories-on-chip, micro total analysis systems, and fuel cells.

The topic of microvalves has been extensively studied during the past decade, and very innovative devices, based on the specificities of microworld, have been proposed. A review of these designs has been proposed by Oh [74]. The purpose of this section is therefore also to present designs making use of principles which are specific to microworld.

All microvalves can be classified according to different criteria. Are they passive or active? If they are active, are they normally open, normally closed or bistable? Have they a moving part or not? Are they suitable for any kind of fluid?

In [60] we have demonstrated that devices using a moving part to close the flow channel could suffer from the presence of bubbles, because bubbles could prevent the sealing of the channel. Moreover, if the parts coming to contact are rigid, any geometric flaw will induce a leakage, which could be significant compared to the nominal flow.

We will present here some of the most relevant microvalve designs.

2.3.1 Devices with a Moving Part

These devices all include a moving component having the purpose of shutting the flow channel. The different designs differentiate from each others by the actuation mean, and by the type of moving part.

Yoshida [98] proposes a valve based on the movement of a silicon membrane, lifted by electrostatic forces. The membrane is extended to a silicon solid part closing the inlet channel. The membrane is used as the first electrode of a capacitor, and when a voltage is applied on the capacitor, the electrostatic pressure lifts the membrane, and allows the fluid to flow.

The design proposed by Takao [88] is also based on the movement of a membrane. In this case, the membrane, made of PDMS, is the sealing part. It is actuated by expanding the gas contained in a sealed volume with an electrical heater. Luque [66], Ohori [75] and Suzuki [86] propose to use PDMS membrane, but with a pressure controlled actuation. In this case, the membrane is pushed on its seat by applying a pressure on its opposite side.

Selvaganapathy [82] uses a similar concept. In this case, a parylene membrane is shaped to be a portion of the flow channel. This membrane is surrounded by a closed volume containing solid paraffin. Electrical heaters are used to make a phase change in the paraffin, which induce a volume increase. This pushes the membrane, and closes the channel.

Sobocinsky [83] proposes to use a steel membrane, actuated by a piezoelectric element.

Cantilever beams are also used as moving parts. They can be actuated by the fluid flow, as in the design proposed by Koch [50]. In this case, the fluid pushes on the beam. This pressure bends the beam when flowing forward, and pushes the beam on a seat when flowing backwards. Ayhan [5] and Kim [49] propose a design with a cantilever actuated by a piezoelectric element.

Finally, we can also mention Kim [48] who designed a passive microvalve based on the use of a hydrogel part. The hydrogel part is swollen with water until it makes contact with the seat. Then its intrinsic compliance is used: when the upstream pressure is large enough, the hydrogel part moves and allows the fluid to flow.

2.3.2 Devices Without Moving Part

By making use of some properties of the microworld, researchers have been able to design valves without moving part.

For example, Well [94] proposes to use phase change and to solidify the flowing fluid by mean of a Peltier actuator. This actuator freezes the fluid, provided that the fluid solidification is not too low (the device has been designed for water based fluids). This technology is suitable for microworld because the volumes to freeze is small, allowing closing times down to around 10ms.

Another example is given by Feng [29]. In this case, the working principle is based on surface tension. It is therefore valid only where an interface exists. The idea is to create an

energy barrier, requiring an increase of pressure in the fluid to cross the valve. Two variations are proposed: a sudden section reduction in the flow channel, and an hydrophobic coating placed in a region of the channel. In both cases, interface front must change its geometry before it can move forward. And to create this change, an increase of pressure is required. Melin [70] also makes use of surface tension in a mixing device. The device has two inputs and one output, and the flow is blocked in the valve unless both inputs are supplied with liquid.

Suzuki [85] makes also use of surface tension, but in a different way. In this design, bubbles are generated electrochemically, until they fill completely a cavity in the fluidic system. The bubble is thus used as a part obstructing the microchannel, except that the part is generated from the fluid itself. Variations can be found in [96] where two bubbles are generated in chambers next to the channel. Growing these bubbles allows to control the fluid flow, by gradually reducing the channel section.

These working principles could not be used in macroscopic designs, making them innovative. Moreover, they are efficient because they are somehow adapted to the microscale. For example, both designs are very effective against leakages, or against dust contamination that could prevent the closing of a moving part on its seat.

2.4 Conclusions

In this chapter, we have shown that it was important to dispose of mathematical models to better understand the behavior of systems at the microscale. Even if the models are not always suitable to efficiently predict the dynamics of a system because it is not possible to access the input data needed, such as for electrostatic forces, models are useful to find the relevant parameters of an effect, in order to avoid it, to minimize, or to maximize it. Indeed, the forces of microscale should not always be considered as unwanted parasitic effects. Original and innovative designs can make use of these effects, such as presented in the case of microvalves.

We have shown that the similarity laws are of limited use to model effects of microscale, because there is no material with suitable properties to avoid distortion. However, dimensionless numbers and Buckingham theorem, which are based only on mathematical considerations, remain relevant and will be used in Chap. 4.

We have taken the example of microvalve to illustrate that microscopic devices should not be reduced macroscopic devices. Some designs found in the literature are clearly inspired from macroscopic designs, and could suffer from the predominance of forces specific to microworld.

We have presented three major forces of the microworld: electrohydrodynamic force, hydrodynamic force and surface tension force. From now on, we will focus on surface tension effects. The next chapter presents the origin of this phenomenon and its applications to microworld.

Chapter 3

About Surface Tension

In the previous chapters, we have introduced the micromanipulation in liquid media, and we have underlined its advantages. Then we have urged the need for models of the predominant forces acting on immersed micro-objects. We have briefly reviewed the most relevant forces, and concluded that surface tension forces are of major interest because they have favorable scaling effects and are easy to control compared to the other forces.

In this chapter, Sect. 3.1 first explains the origin of surface tension. Section 3.2 will detail how to model surface tension and present the parameters involved. Section 3.3 presents some devices typically used to measure the main parameter. Finally Sect. 3.4 introduces main factors influencing the surface tension.

These results will be used in the next chapters, where we will first develop a mean to control the generation of a gas bubble (Chap. 4), and then we will characterize the mechanical behavior of a microbubble (Chap. 5).

3.1 Origin of Surface Tension Forces

A glass may be filled slightly above its rim without overflowing. It seems that the liquid is confined on the top of the glass by a kind of membrane. This is a typical illustration of surface tension effects. There are many other examples. Why a pendant drop does not fall? How comes a liquid does not flow spontaneously through a very small hole? What makes our hair stick together when they are wet? What allows some insects to walk on water surface?

All these examples find their origin in surface tension phenomenon. If all the enumerated examples may be seen at human scale, they do not influence our daily life. On the contrary, surface tension is a predominant phenomenon at smaller scale. Surface tension effects appear when there is an interface between two materials somewhere in the system. The behavior of the interface is a function of the surface energy of fluids and, in case of contact with a solid, of the wettability of the liquid on the surface.

3.1.1 Surface Energy

Molecules of fluid located inside the fluid are equally attracted by the surrounding molecules. But a molecule located at the interface of the fluid is not surrounded by the same molecules all around (Fig.3.1.2). This induces a difference of energy for the molecules at the interface



Figure 3.1.1: Illustration of surface tension. (a) An insect, called water strider, is able to float on the surface of water because surface tension compensates its weight. (b) It is possible to fill a container slightly above its rim without creating an overflow, because surface tension confine the liquid

compared to molecules inside the fluid.

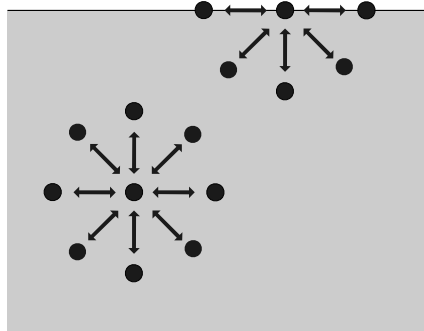


Figure 3.1.2: Illustration of the origin of surface tension. Molecules in the medium are attracted uniformly in all directions, while molecules at the interface are attracted only from one side

This difference of energy is proportional to the number of molecules at the interface, so basically it is proportional to the area of the interface. It is also proportional to the cohesion energy of the molecules. The parameter characterizing the difference of energy at the interface is called *surface tension* and noted γ , having the dimensions of an energy per surface unit.

Therefore, surface tension at the interface between a fluid and another material depends on the nature of both media. If the interface separates a liquid and a gaseous medium, like air, γ typically ranges from 20 mNm^{-1} to 72 mNm^{-1} . Values for typical liquids are found in table 3.1.1.

These nominal values are influenced by temperature, since cohesion energy depends on temperature [20]. Of course it is also sensitive to contamination, especially for liquids with large cohesion energy. For example, surface tension of pure water is $\gamma = 72 \text{ mNm}^{-1}$, but this value will decrease if the interface is contaminated by other components (see Sect. 3.4). Hence it is important to use pure water during experimentations, or to use liquids which are less sensitive to contamination.

If a liquid drop is not in contact with a solid, and if the effects of external forces applied on this drop are negligible compared to surface tension, the shape of the drop will spontaneously

tend to a sphere. In the next section, we will outline the behavior of a drop when it is in contact with a solid.

Table 3.1.1: Value of γ for typical liquids at 25° [52, 20]. Other values can be found in [55, 76]

Liquid	γ (mNm ⁻¹)
Mercury	485
Water	72
Glycerol	63
Water (100°)	58
Acetone	24
Ethanol	23
Silicone oil	~ 20

3.1.2 Wettability

Wettability is a parameter characterizing the fact that a liquid droplet spreads on a surface, or on the contrary keeps the shape of a pearl.

Young-Dupré Relation

Suppose a drop of fluid 1 is placed on a solid in a surrounding fluid 2. Wettability depends on the surface tension of the solid in contact with fluid 1 (γ_{s1}), the surface tension of the solid in contact with fluid 2 (γ_{s2}), and the surface tension at the fluid 1-fluid 2 interface γ . Young-Dupré equation:

$$\gamma \cos(\theta) = \gamma_{s1} - \gamma_{s2} \quad (3.1.1)$$

is an equilibrium relation that defines the wettability of fluid 1 by mean of a contact angle θ (Fig.3.1.3). If $\theta < \pi/2$, the solid surface is wetted by fluid 1. If $\theta > \pi/2$, the solid surface is not wetted by fluid 1 [20]. If fluid 1 is water and fluid 2 is air, the surface is said *hydrophilic* if $\theta < \pi/2$ and *hydrophobic* if $\theta > \pi/2$. Recently, surfaces called superhydrophobic were developed. For these surfaces, $\theta \sim \pi$ and a water drop does not wet the solid at all. These surfaces are interesting because they avoid water to penetrate through fibers of this material (for clothes) and because they have self cleaning properties (on windows for example, the water drops slip taking dusts with them) [12, 18, 93].

Anchoring the Fluid

The contact angle is a function of the surface energies around the triple line, which is the location where the three media are in contact. However, it is generally observed that the angle will change if the fluid moves on the surface. This leads to the definition of the advancing angle and the receding angle: the fluid will not move forward unless the contact angle reaches the advancing angle, and it will not move backward unless the contact angle is reduced down to the receding angle. This is illustrated on Fig. 3.1.4.

This acts as an energy barrier, and it can be used to confine a fluid on a surface. This is for example why water droplets will not roll down a glass plate unless the plate is tilted and

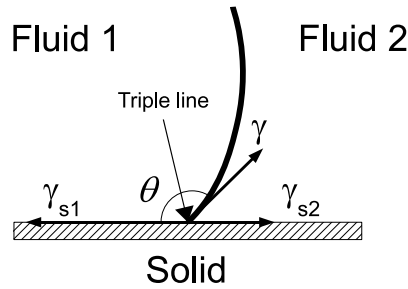


Figure 3.1.3: Illustration of Young-Dupré equilibrium equation. In the configuration shown, fluid 1 does not wet the surface. Surface energy γ_{s1} is larger than γ_{s2} , so $\theta > \pi/2$. The location of one point of the triple line, where the three media are in contact, is also shown



Figure 3.1.4: View of a water droplet (diameter: about 5mm) on a PTFE surface. Illustration of the difference between static contact angle (a), and advancing (on the left) and receding (on the right) angles (b)

the drop volume is large enough to make the contact angle reach the advancing angle value. This confinement may be improved if there is a border beyond which the contact angle has to increase. There are two main methods used to implement such confinement: a chemical method and a mechanical method (Fig.3.1.5).

The chemical method consists in modifying the surface tension of the substrate in some region with a chemical treatment, which may be the deposition of an hydrophobic layer (PTFE for example) on an hydrophilic surface (or vice versa). The mechanical method consists in creating a shoulder (sudden variation of surface angle) where the variation of the contact angle is henceforth much larger.

3.2 Modeling Surface Tension

Surface tension determines the shape of the interface between fluids but also induce significant forces on a solid in contact with the interface. Indeed, from a mechanical point of view, surface tension is an energy per surface unit (Jm^{-2}), but also a force per length unit (Nm^{-1}). It acts exactly as if the interface was a stretched membrane, hence inducing a force. In this section, we will explain how to model this force.

There are two main mechanical actions applied by surface tension: the force arising tangent to the interface and established along the triple line, and a pressure, consequence of the pressure drop across the interface.

It is important to notice that the descriptions hereafter are valid for one interface. In the case of a thin film, like a soap bubble, there are two interfaces: one on each side of the thin

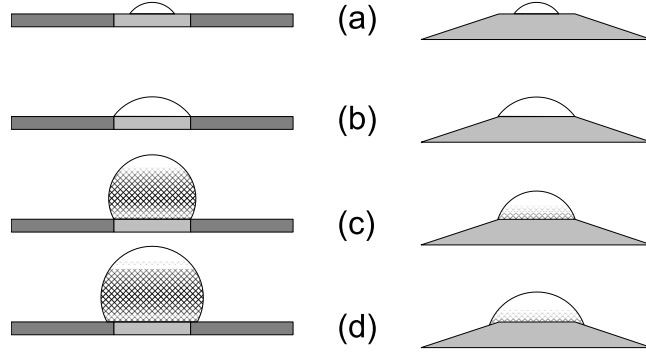


Figure 3.1.5: Illustration of fluid anchoring. Suppose a drop of liquid wetting a surface. The volume of the drop is progressively increased ($a \rightarrow b$). To anchor the drop, it is possible either to change surface energy (left) or to change the tilt angle of the surface (right). On the left, the dark grey parts are treated to have larger energy at liquid-solid interface than at gas-solid interface. The liquid does not wet the dark grey surface, so to penetrate this area (d), the contact angle must increase ($b \rightarrow c$). On the right, the contact angle remains constant, but since the slope of the surface changes, the angle must increase ($b \rightarrow c$) before the drop expands to this area (d)

film.

3.2.1 Surface Tension Force

When an interface is in contact with an object, it creates a triple line along the points where the three materials are in contact. If the interface is seen as a membrane, this membrane is pulling the object.

Suppose $\bar{\mathbf{l}}_t$ is the unitary vector which is normal to the triple line and tangent to the interface. The force due to the surface tension in the interface is the integration of the surface energy γ along this triple line (TL), directed along $\bar{\mathbf{l}}_t$:

$$\bar{\mathbf{F}}_{TS} = \int_{TL} \gamma \bar{\mathbf{l}}_t dl \quad (3.2.1)$$

In case the geometry of the system is axisymmetric, (3.2.1) can be simplified. The triple line is in this case a circle. Suppose r_1 is the radius of this circle. Suppose $\bar{\mathbf{l}}_z$ is the unitary vector along the symmetry axis. The contact angle θ of a fluid on the solid is defined as the angle between a straight line tangent to the solid and a straight line tangent to the interface, both tangents coincident on the triple line (Fig.3.1.3). In this case, the only component of $\bar{\mathbf{F}}_{TS}$ that does not void is the component along the symmetry axis. Equation (3.2.1) can be simplified:

$$\bar{\mathbf{F}}_{TS} = 2\pi r_1 \gamma \sin(\theta) \bar{\mathbf{l}}_z \quad (3.2.2)$$

It is interesting to notice that $\bar{\mathbf{F}}_{TS}$ is always positive, i.e. the interface is always pulling the solid.

3.2.2 Pressure drop Across Interface

Because of tension in the interface, its curvature induces a pressure drop. Let us imagine a box covered with a membrane. If the pressure inside the box is larger than outside, the membrane would puff out; while if the pressure inside is lower than outside, the membrane would become strained into the box. In a similar way, the curvature of the interface is a consequence of a pressure drop established in the interface. However, the surface tension is much lower than usual tension in macroscopic membrane, hence the pressure drops are lower. The shape of the interface is highly sensitive to the pressure difference and this fact can be exploited in order to build a high sensitivity pressure sensor (see Sect. 4.4.1).

Suppose two fluids, (1) and (2), separated by an interface. The pressure difference is modeled by Laplace law:

$$\Delta P = P_1 - P_2 = 2\gamma H \quad (3.2.3)$$

which links pressure drop across interface (ΔP) to the mean curvature at a point of the interface (H) and surface tension (γ). The mean curvature H is a geometric parameter of the interface (Fig. 3.2.1). Suppose $\bar{\mathbf{l}}_n$ is the normal vector to the surface at the considered point. There is an infinity of planes containing $\bar{\mathbf{l}}_n$, each cutting the surface. The intersection between a plane and the surface is a curve, for which a curvature can be calculated. Among all these planes, one contains the curve with the largest curvature, and another, which is orthogonal to the first one, contains the curve with the smallest curvature. The mean curvature of the surface H is the mean of these two curvatures. Remark that the curvatures are algebraic values that can be either positive (if the center of curvature is inside the fluid 1, or negative (if the center of curvature is outside the fluid 1)). H could vary along the two dimensions of the interface, while this would mean that the pressure drop ΔP also varies.

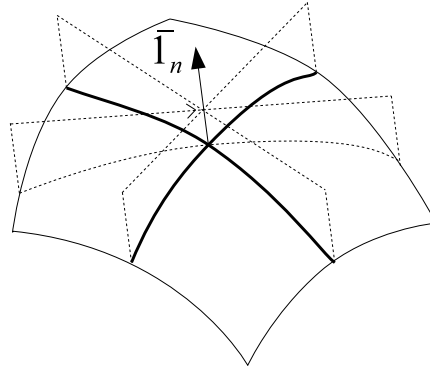


Figure 3.2.1: Geometric definition of mean curvature. At the considered point, the intersection of a plane containing the normal vector $\bar{\mathbf{l}}_n$ and the surface is a curve. Among all possible planes, two of them, orthogonal to each other, will produce the curves with the maximal and minimal curvatures. Mean curvature is the arithmetic mean of these curvatures

Suppose Σ is the area delimited by the triple line on the solid. Suppose also that the solid considered is completely immersed in fluid 1, the fluid outside the interface (Fig. 3.2.2). Suppose $\bar{\mathbf{l}}_n$ is the outwards unitary vector which is normal to surface of Σ . Pressure force \bar{F}_P is then given by:

$$\bar{F}_P = - \iint_{\Sigma} \Delta P \bar{\mathbf{l}}_n d\Sigma \quad (3.2.4)$$

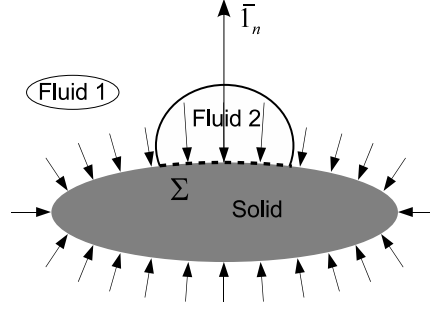


Figure 3.2.2: Origin of the pressure force. Due to pressure drop across the interface, the pressure inside the fluid is different (here larger) than the pressure outside. When summing all contributions of pressure, the only component left is the amplitude of the pressure drop integrated on the surface Σ delimited by the triple line.

Equation (3.2.3) can be simplified in the case of an axisymmetric configuration, and if ΔP may be assumed constant. In this case, suppose the triple line is a circle having a radius r_1 . Because of symmetry, \bar{F}_P will be directed along the symmetry axis. All other components of the force will be void. Suppose $\bar{1}_z$ is the unitary vector along the symmetry axis. Under these assumptions, (3.2.4) then becomes:

$$\bar{F}_P = -\pi r_1^2 \Delta P \bar{1}_z \quad (3.2.5)$$

Which, combined with (3.2.3), gives:

$$\bar{F}_P = -2\pi r_1^2 \gamma H \bar{1}_z \quad (3.2.6)$$

The intensity of \bar{F}_P is proportional to surface tension γ , to the area of projected surface of Σ , and to mean curvature of interface H . It is important to emphasize that H could be either positive or negative, leading to a force that could have any of the two directions along symmetry axis.

3.2.3 Capillary Force

The total force due to the surface tension and the curvature of the interface is called the *capillary force* and is the vectorial sum of \bar{F}_{TS} and \bar{F}_P :

$$\bar{F}_{cap} = \bar{F}_{TS} + \bar{F}_P \quad (3.2.7)$$

Bond number is a dimensionless number characterizing the ratio of gravity effect to surface tension effect. It is generally written:

$$Bo = \frac{\rho g l^2}{\gamma} \quad (3.2.8)$$

where ρ is the density of the fluid, g is the gravitational constant and l is the characteristic length of the capillary bridge. The study of surface tension will be relevant for configurations having $Bo < 1$, which means that surface tension effects are predominant on gravity effect. The characteristic length to match the condition $Bo = 1$ is called the capillary length.

For air-water couple at 25° , the capillary length is 2.7 mm. Therefore if the dimension of the capillary bridge is smaller, surface tension effect will be predominant compared to the weight.

If the dimension of fluid volume are such that $Bo < 1$, the hydrostatic pressure may be supposed uniform along the vertical dimension, hence the curvature of the interface is constant. In the case of an axisymmetric configuration, the shape of the interface is a portion of a sphere. From (3.2.2), (3.2.6) and (3.2.7), in the case of a half-sphere drop in contact with a plane, the capillary force can be formulated:

$$F_{cap} = 2\gamma\pi R + 2\pi R\gamma\sin(\theta) \quad (3.2.9)$$

Equation (3.2.9) shows that the capillary force is proportional to R . This force depends on the characteristic length of the bubble, while other forces like weight or buoyancy are proportional to the volume of the bubble, i.e. R^3 . Because of this difference in the exponent of the characteristic length, the capillary force becomes predominant when the dimensions of the system are reduced. This is why the presence of bubbles in macroscopic systems is generally not an issue, while in microsystems they could hinder its behavior.

A very interesting property of capillary force is that it is self-centering. Indeed, the capillary bridge between a component and a substrate will always tend to have a minimal energy. Any lateral deformation of the capillary bridge from its equilibrium position will increase the surface area, and the capillary forces will tend to return the position of the component to the most favorable position (Fig. 3.2.3).

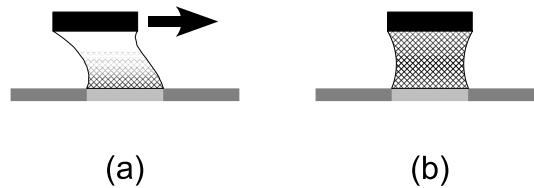


Figure 3.2.3: Capillary forces are self-centering. If the capillary bridge (hatching) is stretched laterally (a), the capillary forces will spontaneously tend to move the bridge back to its position to minimize energy (b)

Micro-assembly makes use of this principle to automatically position components on substrate. This is known as *capillary self-assembly* [68]. If the substrate is functionalized as explained in Sect. 3.1.2, it is possible to create localized anchoring points for the components. This method is statistical, but it is massively parallel (many components are placed at the same moment).

3.3 Measuring Surface Tension

The measurement of surface tension is necessary for various industrial applications. For example: to predict whether an ink will efficiently cover a surface, or for the metalization of surfaces. It is also an important parameter to predict the size of droplets of a sprayed liquid. There are several procedures to measure the surface tension of a liquid. We present hereafter some of them. The reader can find more details in [28, 56, 76, 80].

3.3.1 Capillary Rise

If a tube, opened on both ends and having a small inner radius r , is pushed into liquid (density ρ_l) through a free surface, the free surface in the tube will be at a different level than the free surface outside the tube. For example, with a glass tube in water, the water will spontaneously rise in the tube. This phenomenon is known as the capillary rise (see Fig.3.3.1) and is described by Jurin's Law:

$$\gamma = \frac{r\rho_l g h}{2 \cos \theta} \quad (3.3.1)$$

where g is the gravitational constant and h is the level of fluid in the tube compared to free surface. One can notice that the phenomenon will be more pronounced for tube having a small diameter.

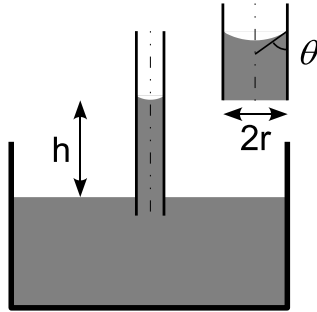


Figure 3.3.1: Illustration of liquid rise in a capillary tube. In this illustration, contact angle θ is smaller than $\pi/2$, the liquid is wetting the surface of the tube, hence the liquid rises. If the liquid does not wet the surface, the level of liquid would be below the free surface in the container

Equation (3.3.1) can be easily demonstrated considering the equilibrium of the liquid column in the tube with the surface tension force (App. A). In order to determine the surface tension of the liquid, the radius of the tube has to be measured accurately. Moreover, height h is function of contact angle θ , and θ is function of the tube material and the liquid. If the liquid wets well the surface ($\theta = 0^\circ$) or on the contrary the liquid does not wet the surface ($\theta = 180^\circ$), (3.3.1) may be accordingly simplified. Another option to use if contact angle is difficult to measure is to use two tubes of the same material, but having a different diameter.

3.3.2 Detachment Methods

Another approach consists in measuring the force needed to extract an object that has been put in contact with the liquid surface, and then deduce surface tension from (3.2.1).

If the object is a plate immersed vertically (Fig. 3.3.2), it is known as the *Wilhelmy* method. If the object is a ring, it is known as the *du Noüy* method. The advantage of these detachment method is that the contact angle can often be supposed to be zero¹. However, the geometry of the object must be precisely known, and the maximum force measured is usually reached before the detachment occurs. In a variant of Wilhelmy method, the plate may also stay in the liquid, and the force is measured directly. In this case the force is function of

¹Reference [56] specifies that detachment force is not affected by contact angles lower than 30°

surface tension but also of the contact angle, which has to be measured. Finally, a dynamic version of Wilhelmy method, using a cylinder, allows to measure surface tension as well as contact angle [80], using a continuous force measurement while the cylinder penetrates the liquid. It is often necessary to calibrate these devices with a liquid of predefined surface tension.

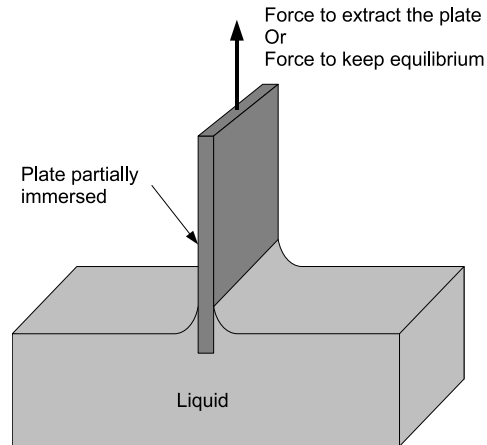


Figure 3.3.2: Illustration of the Wilhelmy method. A vertical plate is immersed in the liquid. Due to surface tension, a force is applied on the plate at the liquid-gas interface. One method consists in measuring the force at the equilibrium position. Another method consists in measuring the force required to extract the plate for the liquid

3.3.3 Use of drops or bubbles

It is also possible to determine the surface tension of a liquid using (3.2.2), (3.2.6) and the geometry of a pendant drop or a drop laying on a surface. The different methods are illustrated on Fig. 3.3.3. The first method is called *sessile drop method* and consists in laying a drop on a surface. The shape of the interface will be a function of the hydrostatic pressure inside the drop, surface tension and liquid density. A variant is to use pendant drop. The main difficulty in this case is to analyze the complete profile of the interface, in order to determine all parameters (curvature, contact angle, height, ...). Since, once again, the contact angle might be difficult to measure, a variant of the pendant drop technique consists in growing drops until they break away. In this case, several drops are released, and their weight is measured. Then it is supposed that surface tension force was equal to the weight of the released drop. However, it is necessary to make a correction, since the volume of the pendant drop is not equal to the volume of the released drop after breaking. This later is smaller, and some amount of liquid stays at the extremity of the tip where the drops are generated [56]. Another approach consists in generating bubbles of inert gas in the liquid. If the hole from which the bubbles are generated is small enough ($Bo < 1$, see (3.2.8)), the bubble can be seen as spherical caps (pressure inside the bubble is uniform if the variation of hydrostatic pressure is low). Equation (3.2.3) reveals that the pressure is maximal when the radius of the sphere is minimal, which occurs when the bubble is hemispherical. Surface tension can be deduced from measuring the pressure at which bubbles begin to be released.

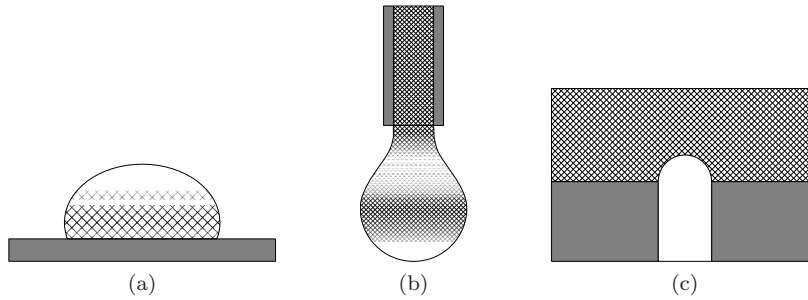


Figure 3.3.3: Illustration of surface tension measurement methods using drops or bubbles. (a) Sessile drop method: the contact angle and curvature of a drop lying on a surface is analyzed. (b) Pendant drop method: several drops are generated by growing until they fall from the tube, and surface tension is deduced from the weight of one pendant drop. (c) Bubble generation method: the maximal pressure in the bubble is reached when its shape is a half-sphere (for small diameters), surface tension is deduced from diameter of hole and maximal pressure before bubbles are released

3.4 Influencing Parameters

Surface tension can be influenced by several parameters. We review here the influence of temperature and the risk of contamination. We also present the electrowetting technique, to show the influence of electrostatic field.

If, because of a local change of one of these parameters, surface tension in an interface is not uniform, the gradient of surface tension will cause a deformation or even a movement of the interface. This phenomenon is known as the Marangoni effect.

3.4.1 Temperature

One of the most important parameters is temperature. Since surface tension is linked to cohesion energy of the molecules, and since a temperature rise gives more energy to the molecules, making their displacement easier, surface tension usually tends to decrease when the temperature increases [56]. Empiric relations exist to calculate the surface tension at different temperatures. The simplest one is a linear approximation:

$$\gamma = \gamma_a + k \cdot T \quad (3.4.1)$$

where γ_a is a constant, k is the partial derivative of surface tension with respect to the temperature, and T is the absolute temperature. This simple relation is generally acceptable for temperature variations of a few tenth of degrees around the reference temperature, which is usually ambient temperature, or fusion temperature if this latter is higher. Parameter values are to be found in reference tables (for example in [55]).

Another expression which has been introduced by Van Der Waals is valid between triple point and critical point:

$$\gamma = \gamma_0 \left(1 - \frac{T}{T_c}\right)^a \quad (3.4.2)$$

where T_c is the temperature at the critical point, and γ_0 and a are constants for the fluid. Once again, these parameters are to be found in reference tables.

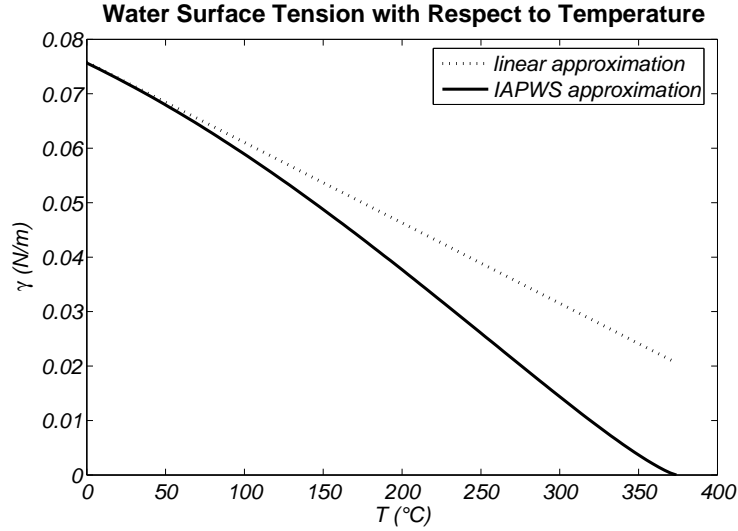


Figure 3.4.1: Evolution of water surface tension with respect to temperature

Other relations (Eötvös, Macleod) propose to take into account the molar density of the fluid. For water, (3.4.2) is not accurate. A better relation is given by [17]:

$$\gamma = B \left(\frac{T_c - T}{T_c} \right)^\mu \left(1 + b \left(\frac{T_c - T}{T_c} \right) \right) \quad (3.4.3)$$

with the following constant values: $B = 0.2358 \text{ N m}^{-1}$, $b = -0.625$, $\mu = 1.256$ and $T_c = 647.15 \text{ K}$.

A comparison of (3.4.1) and (3.4.3) is shown in Fig.3.4.1 for temperature ranging from triple point to critical temperature. The evolution of surface tension around ambient temperature remains quite low. Indeed, from (3.4.3), we see that $\gamma = 72.7 \cdot 10^{-3} \text{ N m}^{-1}$ at 20° , $\gamma = 72.0 \cdot 10^{-3} \text{ N m}^{-1}$ at 25° . The variation is lower than 1%, hence we will consider surface tension of water equal to $72 \cdot 10^{-3} \text{ N m}^{-1}$ for the rest of this document. An exhaustive list of surface tension for pure material, liquid mixes, inorganic compounds, molten salts or solutions can be found in [55].

3.4.2 Contamination

The presence of another substance than the fluid at the interface can change molecular interaction energy, hence change the value of surface tension. This is also true if the interface is the seat of chemical reactions, changing the properties of molecules. For example, oxidation of a liquid metal can change significantly the value of surface tension. A daily life example is the use of detergent in water, which reduces this surface tension by disrupting the hydrogen bonds. For the experimentations performed during this work, special care has been taken to work with pure liquids, and to clean components before experiments.

3.4.3 Electrowetting

If a liquid drop is only partially wetting a substrate, and if an electric field is applied on the liquid, the shape of the drop will change. Generally, the drop will flatten when the electric field increases. This phenomenon, known since 1875 [62], is now known under the name *electrowetting*.

The experiments were generally performed by applying a voltage on the liquid and on the substrate. The phenomenon is also true for couple of liquids, for example water and mercury. The main problem was the apparition of an electrolysis phenomenon. This issue has been resolved by placing on a conductive solid substrate a thin layer of dielectric material [7], for example PTFE which is hydrophobic. This approach is known as *ElectroWetting On Dielectric* (EWOD). The usual approach to model this phenomenon is to translate the influence of the voltage on the contact angle of the interface [71]:

$$\cos(\theta) = \cos(\theta_0) + \frac{\epsilon_0 \epsilon_r U^2}{2d\gamma} \quad (3.4.4)$$

where θ is the contact angle, θ_0 is the contact angle when no voltage is applied, U is the voltage applied between substrate and fluid, d is the thickness of the dielectric layer, $\epsilon_0 \epsilon_r$ is the dielectric constant of the dielectric (insulating) layer. γ is the surface tension at liquid–fluid interface (the fluid surrounding the liquid drop may be either a gas or a liquid). However, (3.4.4) has limitations since the contact angle does not effectively go beyond a saturation value. Moreover, it is obviously not physically possible to have the second member of the equation larger than 1.

Jones [45] gives another approach where he proposes to distinguish the effect of electrostatic potential on contact angle from its effect on the movement of the center of mass of the liquid, while usually both phenomena are thought to be linked. He bases his reasoning on the fact that some authors have observed that microscopically, the contact angle does not change when a voltage is applied: the modified angle is only apparent, some distance away from the triple line. He proposes an approach based on the electrostatic energy and presents the variation of the apparent contact angle as a consequence of the movement to a more favorable energetic configuration.

An example of application has been given by Berge [8] by proposing a fluid lens whose focal distance can be adjusted by mean of a voltage. Other applications presented frequently are the use of electrowetting as a way to move droplets on active substrate matrices.

3.5 Implications for Microsystems

We have explained in Sect. 3.2.3 that surface tension effects becomes predominant at microscale. They appear if an interface exists in the system. In immersed microsystem, bubbles are responsible for the existence of these effects. We will present here some examples of how surface tension can be disruptive.

Later on, we will focus on the study of microbubbles in microsystems.

3.5.1 Crossing the Free Surface of a Liquid

Generally given as an illustration of surface tension, it is commonly known that small objects can float on the free surface of liquids, even if their density is larger than the density of the

liquid. In Sect.3.2.3, we have shown that capillary force becomes larger than volume force like the weight of an object. This is why small objects float, while large objects sink.

This may be in some case disruptive, for example if fragile objects have to be put in, or removed from liquids. In these cases, particular care should be taken when moving these objects across the interface. When these objects cross the free surface, they are subjected to the surface tension force generated by the interface. As a consequence, the object is hold by the interface, which could lead to its break.

As example of such objects, let us mention an AFM² probe which is a kind of cantilever beam, and finger based microgrippers whose fingers are usually beam shaped.

AFM probes have a low stiffness. They are usually used close to a surface and the measurement of deflection of the probe is used to reconstruct the shape of the scanned surface. In micromechanics, it is common to use AFM probes to measure forces having a range below 1 μN [26, 35, 42, 44, 57]. These AFM probes are usually made of silicon, which is a brittle material.

The same consideration applies for microgripping devices based on fingers, as illustrated on Fig. 3.5.1. To perform micromanipulation in a liquid environment, the gripper has to be immersed, and the terminal organs, used as fingers, will have to withstand the crossing of free surface.

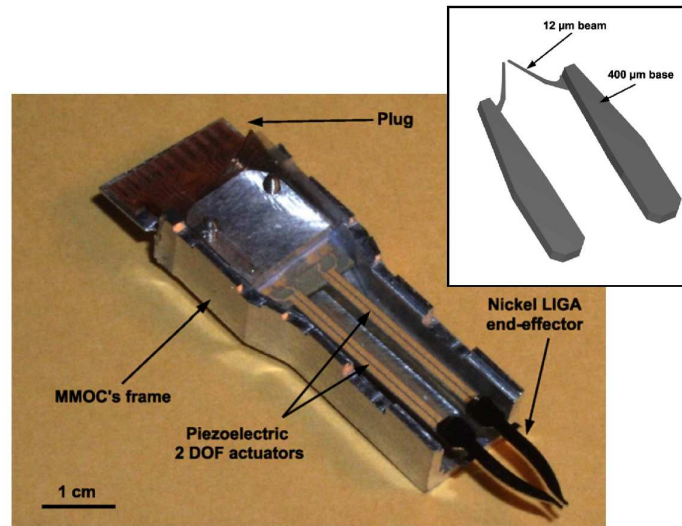


Figure 3.5.1: View of a piezoelectrically actuated microgripper (MMOC tweezer, source: [2])

3.5.2 Statistical Self Assembly of Microcomponents

Current developments in micro-assembly try to use the assembly property of capillary forces to make assembly of a large number of components. The main advantages are that this assembly method is massively parallel, and operates without contact.

One method consists in using surface functionalization, i.e. change the properties of one surface of the component in order for the component to have a more favorable energetic configuration if the functionalized surface is in contact with the substrate (which may also

²Atomic Force Microscope

be functionalized). Statistically, if a large number of components is dropped in the liquid, and because the probability of a correct assembly is increased by mean of the functionalization, the components tend to assemble as expected [69].

Unfortunately, the presence of gas bubbles inside the liquid disrupts the process by either sticking components together, hence they do not necessarily have the opportunity to mate the expected face to the substrate, or by preventing the contact of the component with the substrate. This is illustrated in Fig. 3.5.2.

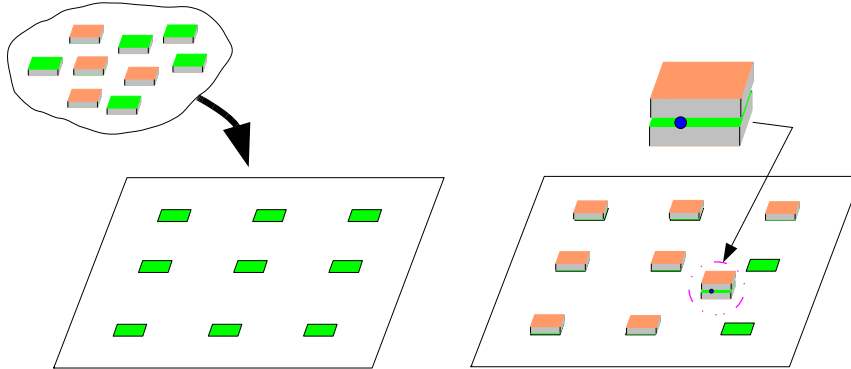


Figure 3.5.2: Statistical self assembly using surface functionalization. Energetic configuration is more favorable if green faces come in contact with green faces on the substrate. But if a bubble creates a bridge between two components, these components cannot have the right face coming in contact with the substrate

3.5.3 Bubbles Preventing Solid Contact

A bubble in a liquid is a kind of sticking balloon. This will be detailed in Sect. 5. This means that if a bubble is trapped between two solids, the bubble will exert a repulsive force if both solids come to one another, and it will exert an attractive force if the two solids are moving away from each other.

We have already presented in Chap. 2 the case of microvalves with a moving part, whose blocking part cannot reach its seat because of a bubble. We have also presented the self-assembly principle which could also be affected by the presence of a bubble preventing the contact between the component and the substrate.

Finally, the manipulation of a component, i.e. the gripping, positioning and release of a component, could be disrupted by a bubble (Fig. 3.5.3).

We see from these examples that the presence of a bubble can lead to problems in microsystems, but we will show in Chap. 5 that it may also bring benefits. It is in this case necessary to generate these bubbles, and this is the subject of the next section.

3.6 Conclusion

Surface tension appears because of the difference of energy existing on both sides of an interface between two materials, inducing an energy in the interface. This phenomenon is characterized by a physical property depending mainly on the materials, called *surface*

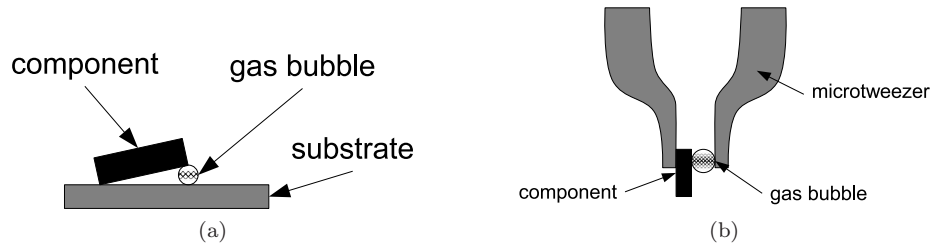


Figure 3.5.3: Microbubbles can prevent the contact between two solids. (a) A bubble can prevent the correct positioning of a component on a substrate. (b) A bubble can prevent the correct positioning of a component in a gripper device, and hinder its release

tension and noted γ . From a mechanical point of view, it induces forces on objects that are in contact with the interface.

We have seen that surface tension induces important effects on components of small dimensions, typically less than 1 mm. It is clear that this property of interfaces must not be neglected when designing a micrometric device, or when performing micro-assembly tasks. Since this work is focused on forces acting on solids in liquid medium, it is necessary to take into account the effect of interfaces in the system.

To better understand the physics of surface tension, we have also presented some typical methods for measuring surface tension. These methods make use of the properties of surface tension. We have also indicated some external factors that influence the surface tension, such as temperature, contamination or an external energetic contribution such as with electrowetting. One important results is that surface tension of water can be reasonably assumed to be constant from 20°C to 25°C, with $\gamma = 72 \cdot 10^{-3} \text{ N m}^{-1}$.

In the case of immersed microsystems, surface tension effects arise notably when small bubbles are present in the system. We have given some illustrations of the perturbations that microbubbles could induce in microsystems. However, we have seen in Sect. 2.3 that making use of the specific microworld phenomena can lead to innovative designs, and gas bubbles have promising properties. Indeed, it is possible to control the bubble and to exploit the capillary force as actuation principle. Moreover, a bubble is intrinsically compliant, which is an interesting property in the field of micromanipulation since it can tackle some problems due to relative positioning error. Finally, a bubble is cheap and can be easily regenerated if needed.

These advantages show that microbubbles could be used in microsystems. To use them, it is of course necessary to be able to create these bubbles in a controlled way. This is the aim of Chap. 4. Thereafter we will study the compliance of the bubble in Chap. 5.

Part II

Study and Application of Surface Tension Forces in Liquid Media

Chapter 4

Controlled Generation of a Gas Bubble

In Chap. 1, we have presented the interest of performing micromanipulation tasks in a liquid environment. Then, in Chap. 2, we have urged the need for models describing the forces acting on immersed micro-objects. We decided to focus on surface tension forces, and we have seen in Chap. 3 that surface tension is a predominant phenomenon at microscale. The arise of this phenomenon in immersed microsystems is linked to the existence of an interface, such as the surface of gas bubbles.

This phenomenon is a promising actuation mean. To study the mechanical behavior of gas bubbles, it is necessary to dispose of a controlled bubble generator. In this chapter, we present models and experiments to find a way to generate bubbles in a controlled way. In this case, the purpose is to generate a single bubble with a definite geometry. We will first explain in Sect. 4.2.1 the specificities of gas bubbles, which is driven by the coupling between the gas compressibility and the surface tension. Then we will compare in Sect. 4.1 different means to generate bubbles. We will select the most appropriated mean for the study of microbubble effects in a microsystem, and we will develop in Sect. 4.2 a model to predict the geometry of the generated bubble, taking surface tension and gas compressibility into account. The experimental validation of the model is then presented in Sect. 4.3. Finally, we present in Sect. 4.4 two potential applications of microbubbles.

4.1 Bubble Generation Mean

To study the influence of a gas bubble on solid components immersed in a liquid, it is necessary to have a bubble generation mean.

Many authors have studied the generation of bubbles in a liquid, but most often in the case of chemical reactors, colloids or hydrodynamic studies. Some of them [89, 73] have studied the continuous generation of gas bubbles in cross flow liquid (the liquid flows perpendicularly to the axis of the orifice from which the bubbles are grown), or more generally the case of multiphase microflows [6]. Others [95, 97] have proposed numerical methods to calculate the shape of bubbles, but once again it concerns a continuous bubble generation.

Our goal is to generate a single bubble while controlling its size, and without releasing it from the bubble generator (Fig. 4.1.1).

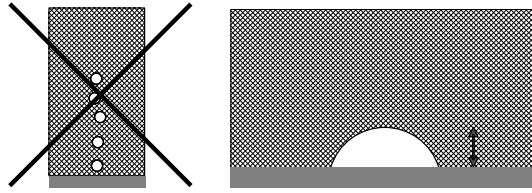


Figure 4.1.1: Usually, bubble generators are designed to generate several bubbles of a predefined size (left). Our goal is to generate a single bubble, without releasing it, and controlling its size (right)

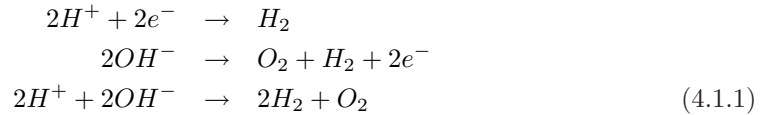
We will briefly review five methods to generate single bubbles: electrolysis, cavitation, thermal growth, pressure controlled gas injection and volume controlled gas injection.

4.1.1 Electrolysis

Electrolysis uses electrical current to transform ions in a liquid phase to atoms which are in turn going to transform to gas molecules. It is of course necessary to have a liquid containing ions. This is not an issue for aqueous solutions since water spontaneously dissociates in H^+ and OH^- ions. But this method is not relevant for other liquids like oils for example.

Basics

The general principle is based on the combination of electrical charges to ions in such a way that gas molecules can be generated. For example, for water, the reaction equations are:



To model the physics, we assume that all charges injected by a current are converted to gas molecules. Two molecules of H_2 and one molecule of O_2 are formed when 2 electrons are injected in the system. The amount of gas moles n depends on the electrical charge injected C and the Faraday constant¹ F_a :

$$\begin{aligned}
 n_{H_2} &= \frac{C}{F_a} \\
 n_{O_2} &= \frac{C}{2F_a}
 \end{aligned}
 \tag{4.1.2}$$

Parameters

Equation (4.1.2) is however not sufficient to fully describe the phenomenon. Many other parameters, such as presence of dissolved gas, ionic strength of the liquid, electrode roughness,

¹Faraday constant represents the amount of electric charge (C) of one mole of electrons: $F_a = 96485 \text{ Cmol}^{-1}$

electrode wettability, ... have also an influence [9]. The predominant, or limiting, step of the gas generation is not easy to find, as it is function of the whole setup: in some cases reaction kinetics is limiting the gas production, in other cases it might be the adsorption of ions at the electrode surface, or the mass transfer to or from the electrode [19].

Another parameter is the voltage, which must be at least equal to redox potential of water, which is 1.23 V. Practically, the minimal voltage is also function of the electrodes used to perform the electrolysis.

The location of bubble growth is called nucleation site. It is an area favorable to gas release, for example because there is a defect on the electrode or in the liquid, or because the liquid is oversaturated at that place. In our case, it is important to predict where the bubble will grow, so it is necessary to predetermine the nucleation sites. This will be clearly a limitation of this method to control the generation of gas bubbles.

Finally, it must be mentioned that some particular phenomena linked to electrolysis have been observed and are clarified by [65]. These phenomena are for example oscillating bubbles, or bubbles that keep contact with the electrode even with a contact angle of almost 180° .

Experimentations

From (4.1.2), it seems easy to control the amount of gas moles by controlling the electric charge injected into the system. To control the amount of electric charge, our first idea was to use a capacitor, loaded at a the voltage required to activate electrolysis. Thin-film insulated copper wires having a diameter of 0.25mm were used as electrodes. We made a test using a 100 nF capacitor, but even when loading it at 5 V, no bubble appeared. This means that probably not all the electric charges are converted in gas, unlike supposed in (4.1.2). We made a second test connecting the electrodes directly to a voltage source. In that case, it was possible to generate bubbles, and the bubble growth rate was larger for higher voltages.

In order to promote the generation of a bubble at a precise location, i.e. to master the position of the nucleation site, we tried to use patterned electrodes. The electrodes we used were designed to have sharp tips. Because the electric field is larger around these tips, they should be the location of bubble growth. These electrodes were manufactured by gold deposition on a glass substrate, using the same mask as for microweeder, called Sift [2]. The connection to power supply was made of the same thin-film insulated copper wires as above, connected to the electrodes with a conductive glue (silver-filled epoxy resin - Epo-Tek®H22 from Epoxy Technology, Inc.). They are illustrated on Fig. 4.1.2.

When the voltage U (continuous) is progressively increased, the first bubbles appear on the conductive glue, at $U = 2.5$ V. Obviously, the roughness of this material creates more favorable nucleation sites. The first bubbles at the tips appear for $U = 3.2$ V. If we repeat the experiments, we observe that the nucleation site is not always the same. Sometimes, the bubbles appear at the tip of the conductive pattern, sometimes they appear between the tips, on the glass substrate. Moreover, the electrodes are damaged after a few experiments: the metal does not adhere anymore on the glass substrate.

From these experiments, we concluded that it is difficult to predict the location of nucleation sites. This is furthermore confirmed by [58, 92]: these authors created special microfabricated designs as nucleation sites. Generally, electrolysis is used in devices where bubbles are confined in a volume. In this case, several small bubbles coalesce to form one larger bubble, used for example as actuator. Such devices have been used for example by [3, 10, 77].

In our setup the size of the bubble is not predictable, since we do not record the total electric charge injected. This could be done with a current integration circuit for exam-

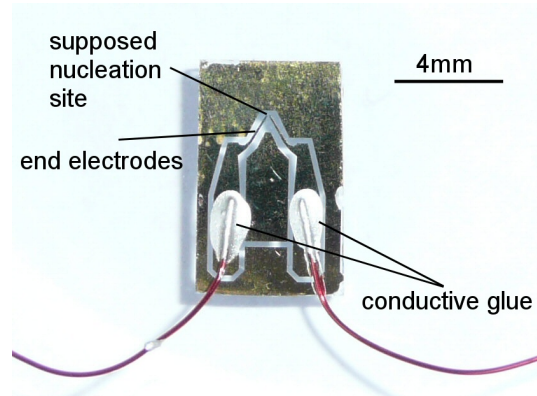


Figure 4.1.2: View of the patterned electrode used for electrolysis test. The electrode is gold patterned on a glass substrate. The wires are bounded with a silver-filled epoxy resin

ple. However one must be careful with this measure since ions could transfer some charges while not participating to the gas production. We observed that the bubble growth was relatively slow, making it possible to stop the power supply when the size of the bubble was approximately acceptable.

Limitations and Advantages

To summarize the performances, we state that:

- ⊕ There is no pneumatic connection, eliminating the risk of a leak
- ⊕ The system is easy to operate
- ⊖ The design of an efficient generator is not easy, because several parameters must be taken into account: type of electrodes (material, roughness, size), ionic properties of the liquid, . . .
- ⊖ The nucleation sites are difficult to control, and require specific micromanufacturing
- ⊖ The gases produced are linked to the ions in liquid. It is not possible to use this method with any liquid or any gas.

In this work we will not further develop an electrolytic bubble generator. However we will use this design to perform qualitative tests of force measurement 5.4.1, where a bubble will be generated, no matter its size or location, then its size and location are estimated in order to perform the experiment.

4.1.2 Cavitation

Basics

When the pressure in a liquid falls beneath the vapor pressure, the liquid spontaneously evaporates and gas bubbles are formed.

This phenomenon is not easy to control, since depression must be created locally. Generally, this happens when a fluid flow accelerates due to a smaller channel section. Bubbles

appear in the flow where the pressure is lower. But in that case, the bubble is necessarily in a flow, and may not be created in a quiescent liquid. Moreover, if the pressure rises further in the flow, the bubble will collapse.

And in this case, the exact location of the bubble growth site is not precisely known.

Limitations and Advantages

To summarize the performances, we state that:

- \oplus There is no pneumatic connection
- \oplus There is no need to bring energy: it is included in the fluid flow
- \ominus The principle of cavitation requires the creation of a depression, usually in a flow. Bubbles are not easy to control since they must remain in the low pressure area
- \ominus It is difficult to predict exactly where a bubble will grow
- \ominus The gas produced is the vapor phase of the liquid. According to the fluid, the temperature must be in accordance to the existence of a liquid-gas transition.

This method is not adequate to the study of bubble effects in microsystems. However, it was important to remind that such gas production mechanism exists, because if it occurs in a microfluidic circuits, the presence of bubbles may have an impact on the system behavior.

4.1.3 Thermal Growth

Basics

Like in Sect. 4.1.2, the idea is to create a phase change and to evaporate the liquid. But in this case, the change occurs thanks to a rise of the temperature up to the boiling point.

This method can be implemented in microcircuits by creating small resistive circuits that will use joule effect to heat the fluid [54]. It is also possible to use laser beam focused a one point.

This method is often compared to electrolysis method decribed in Sect. 4.1.1. The major drawbacks of thermal growth are the amount of energy needed to evaporate the fluid, which is larger than the energy needed to dissociate the fluid, and the fact that if the temperature goes spontaneously down, the bubble will condensate spontaneously.

The method issues the same drawback as electrolysis: it is difficult to grow one single bubble at a predefined location. Generally, several small bubbles coalesce to form one larger bubble.

Limitations and Advantages

To summarize the performances, we state that:

- \oplus There is no pneumatic connection
- \oplus The system is easy to operate

- \oplus The design of an efficient generator is relatively easy, it only requires a heater, which is usually a resistive circuit or focused laser
- \ominus The nucleation sites are difficult to control, since bubbles may appear anywhere in the heated area.
- \ominus The size of the bubble is not easy to control, since it results generally from the coalescence of several bubbles

We will not investigate further this method since the size of the bubbles is not easy to control.

4.1.4 Pressure Controlled Gas Injection

All gas generation methods presented above have the same issue: the precise location of bubble growth is difficult to predict. An easy solution is to inject gas directly in the liquid at an orifice. In that case, the location of bubble growth is exactly the injection point.

The method proposed here manages the gas injection by controlling the pressure in an infinite gas tank. It is illustrated in Fig. 4.1.3

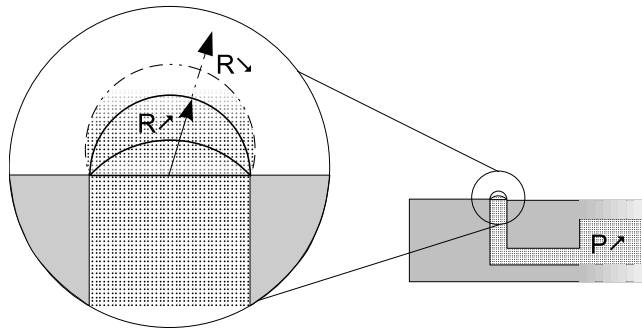


Figure 4.1.3: Working principle of the pressure controlled bubble generator. A channel leads to bubble growing location. An increase of pressure leads to a decrease of bubble radius. Since the minimum radius corresponds to a half sphere, it is not possible to grow a bubble larger than a half sphere with this generation mean

Basics

In this case, the control of the bubble size is directly linked to Laplace equation (3.2.3). We assume the pressure in the gas circuit to be uniform. If the outlet channel is circular and its diameter below the capillary length, the shape of the bubble is assumed to be a spherical cap. This is because the hydrostatic pressure is approximately uniform along the bubble. The pressure drop across the interface is henceforth also uniform. So the mean curvature of the bubble is uniform, which means the shape is a portion of a sphere. The mean curvature of the spherical cap is the inverse of its radius. So ΔP is maximal for a half sphere, and $\Delta P = 0$ when the bubble is flat. If the pressure is larger than the pressure needed to get a half sphere, the bubbles will grow infinitely, which means that they will lift off when buoyancy force is large enough and the bubbles will be generated continuously. This is moreover the basis of a surface tension measurement method (Sect. 3.3.3).

If s_1 is the diameter of the output channel, γ the surface tension at gas-liquid interface, h the height of the bubble, R the radius of the spherical cap, it is possible to find a relation between h and ΔP .

$$h = R - \sqrt{R^2 - \frac{s^2}{4}} = \frac{2\gamma}{\Delta P} - \sqrt{\frac{4\gamma^2}{\Delta P^2} - \frac{s^2}{4}} \quad (4.1.3)$$

We have plotted the height of the bubble with respect to pressure drop for two configurations in Fig. 4.1.4. On this figure, it is clear that the pressure drop is low compared to atmospheric pressure.

Hence there are two major drawbacks for this method: it is not possible to create bubbles larger than a half sphere, and the pressure regulation must be very accurate since the sensitivity of bubble height with pressure is large. This is especially true if the outlet channel is large. So the smaller the bubbles are, the easier it is to control their height with pressure control.

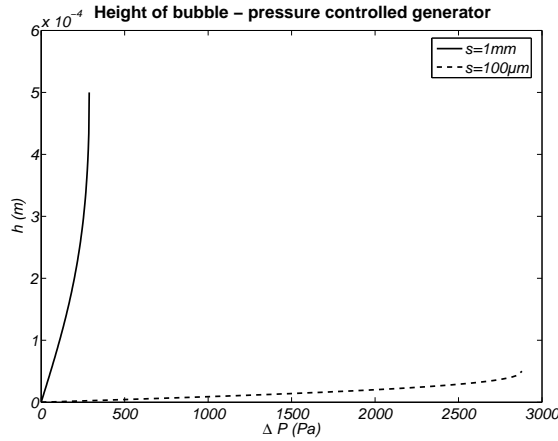


Figure 4.1.4: Height of a bubble function of ΔP , the pressure drop across the interface, in this case the increase of pressure in the gas circuit with respect to pressure outside the bubble. In this graph, $\gamma = 72 \cdot 10^{-3} \text{Nm}^{-1}$. The pressure control is easier if outlet channel has a small diameter

Experimentations

We made some tests to validate this theory. We used a voltage controlled industrial pressure regulator (type *ITV2030-31F2BS3-Q* from *SMC*), with a maximum output pressure of 500 kPa and a 0 – 10 V command voltage (Fig. 4.1.5). This pressure regulator is supplied by industrial quality compressed air (purity of the gas is not guaranteed). It is connected to in vitro fertilization micropipettes, made of borosilicate glass. Three types have been used:

- MIC-50-30 Intracytoplasmic Sperm Injection (ICSI), having an inner diameter of 5 – 6 μm , having a bevel of 8 – 9 μm at the tip
- MPH-XLG-0 Holding micropipette, having an inner diameter of 25 μm
- MDP-190-0 Denuding micropipette, having an inner diameter of 190 μm



Figure 4.1.5: View of the pressure regulator used in the pressure controlled bubble generator

With MIC-50-30 micropipettes, the maximal pressure before continuous bubbling is 69 kPa. If $\gamma = 72 \text{ Nm}^{-1}$, this would correspond to a tip diameter $s = 4.17 \mu\text{m}$ (it would require 58 kPa to exhaust bubbles from a $5 \mu\text{m}$ tip). We did not have optical resolution that allowed us to view the bubbles growing in water. Hence we cannot confirm that the real diameter was $5 \mu\text{m}$, or if a partial occlusion due to particles in water could be the reason of the difference of pressure.

With MPH-XLG-0 micropipettes, the maximal pressure before continuous bubbling is 10 kPa. If $\gamma = 72 \text{ Nm}^{-1}$, this would correspond to a tip diameter $s = 28.8 \mu\text{m}$ (it would require 12 kPa to exhaust bubbles from a $25 \mu\text{m}$ tip). In this case it was possible to see the growing of a bubble, but the resolution of the pressure controller was not sufficient to have an effective size control (10 kPa correspond to 0.2 V control voltage, i.e. 2% of the full scale). Indeed, the controller seems to have discrete output pressures, not a continuous variation.

With MDP-190-0 micropipettes, the least pressure variation induced continuous bubbling.

These tests underline the need of a high resolution pressure regulator to efficiently control the height of a bubble, which is difficult to achieve for technological reason.

Limitation and Advantages

To summarize the performances, we state that:

- \oplus The pressure is easy to control with industrial pressure regulator
- \oplus It is possible to inject any gas in any liquid
- \oplus The location of the bubble growth area is clearly defined, since it is the outlet channel
- \ominus It is not possible to grow a bubble larger than a half sphere
- \ominus The bubble growth is very sensitive to pressure changes, so the control is not easy, especially for large outlet channel ($\sim 1 \text{ mm}$)
- \ominus The pneumatic connections could be cumbersome in a microdevice

Because of the difficulty to precisely control the bubble growth and the limitation $2h \leq s$, we will not investigate any further this bubble generator.

4.1.5 Volume Controlled Gas Injection

This is another version of gas injection based bubble generator. In this case, the volume of a finite gas tank is reduced, pushing the gas in the liquid and creating the bubble. This is illustrated in Fig. 4.1.6.

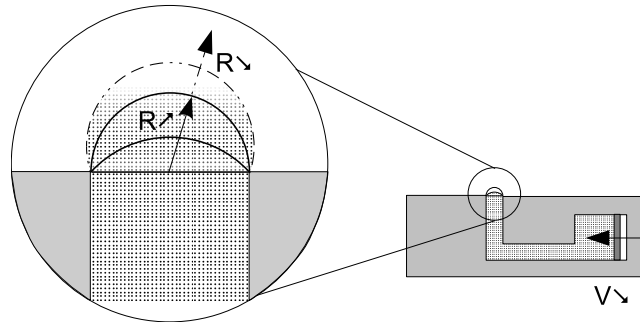


Figure 4.1.6: Working principle of the volume controlled bubble generator. A finite volume of gas is confined in a chamber. By reducing this volume, the gas is expelled through a channel to the bubble growing location. By this means, it is possible to inject any gas at a predefined location. The ability to grow any size of bubble will however be subjected to a further condition detailed in the next section

Basics

The device is like a syringe pump. However, it is not correct to assume that the volume swept by the piston in the syringe will be the volume of the bubble. Surface tension will play in this case a considerable role.

In this case, control of bubble height will be based on the control of the volume in the gas container. In the case of a syringe, it is function of the position of the piston. But a priori, there is no limitation to the height of the bubble, unlike a pressure based control. The only size limitation appears when the bubble is so large that the adhesion forces on the edge of outlet channel are no longer large enough to balance the buoyancy force.

This device will be extensively developed in Sect. 4.2.

Limitation and Advantages

- ⊕ The change of volume in the gas container is easy to control, for example with a syringe pump
- ⊕ It is possible to inject any gas in any liquid
- ⊕ The location of the bubble growth area is clearly defined, since it is the outlet channel
- ⊖ The gas container has a limited volume, which could be problematic in some cases, like the generation of several bubbles, while refilling the container requires to open it
- ⊖ The pneumatic connections could be cumbersome in a microdevice

This device has major advantages to other solutions: the size is easy to control, and any gas can be injected in any liquid (possible use of different liquids to vary surface tension). Finally, the location of the bubble is precisely defined.

We will develop extensively this method in the next sections.

4.1.6 Comparison of the Different Generation Means

Table 4.1.1 summarizes the advantages and drawbacks of the different bubble generation means presented in this section. The most promising method to study the mechanical behavior of microbubbles is the volume controlled generator. With this method, the location of the bubble is precisely known, and it should be possible to grow a bubble of any size. Its only drawback is that this method requires pneumatic connections from the gas container to the outlet channel. These connections could induce leaks, or increase the overall dimensions of the device using the generator. However, these issues can be resolved using microfluidic manufacturing technologies, as we will propose in the perspectives of this work (Sect. 5.5).

For these reasons, we will focus on this bubble generator, and we will develop in the next section a model to predict the size of the generated bubble.

Table 4.1.1: Comparison of the different bubble generation means

	Hydrolysis	Cavitation	Thermal growth	Pressure controlled injection	Volume controlled injection
Bubble size control	Complex	Complex	Complex	Easy	Easy
Bubble size restrictions	No	No	No	Limited to half sphere	No, on restrictive condition (Sect. 4.2.6)
Bulkiness	Low	Low	Low	Could be large because of pneumatic connections	Could be large because of pneumatic connections
Gas/liquid restrictions	Requires ions of gas molecules	Depends on liquid vapor pressure	Depends on liquid boiling temperature	No	No
Bubble location	Difficult to predict	Difficult to predict	Difficult to predict	Bubble grows from pneumatic exhaust channel	Bubble grows from pneumatic exhaust channel

4.2 Model of the Volume Controlled Generator

The volume controlled bubble generator seems to be the most interesting in order to study the mechanical properties of a microbubble. But its design must take into account surface tension effects, which will notably compress the gas. The main contribution compared to the model exposed in Sect. 3.2.3 is that we take into account the compressibility of the gas. We will first show an example of the relevance of the coupling between surface tension and gas compressibility.

4.2.1 Gas Bubble in Liquid Media

The distinctiveness of gas bubbles compared to a liquid droplet is that it is a compressible medium. This means that in the models it is not correct to assume the volume of gas to be constant. Since surface tension is responsible for a pressure drop across the liquid-gas interface (3.2.3), the volume of an immersed gas bubble will be smaller if γ is larger. To model this, we will make use of the classical gas law:

$$PV = n R_g T \quad (4.2.1)$$

where n is the amount of gas moles present in the system, T is the absolute temperature, $R_g = 8.314 \text{ J mol}^{-1} \text{ K}^{-1}$ is the gas constant, P is the pressure in the gas system and V is the volume of the gas system. The condition of constant volume is replaced by a constant number of molecules n .

Let us consider a single bubble in a liquid. If its diameter is small, i.e. lower than the capillary length (3.2.8), the bubble can be supposed to be spherical. Indeed, in this case the hydrostatic pressure outside the bubble is approximately constant, hence the mean curvature of the interface is constant (3.2.3). According to Laplace Law (3.2.3), the pressure inside the bubble increases with an increase of H , the mean curvature, which in the case of a sphere of radius R is equal to R^{-1} , and with an increase of surface tension γ at the gas-liquid interface. If P_0 is the pressure outside the bubble, i.e. the sum of atmospheric pressure and hydrostatic pressure, the combination of (4.2.1) and (3.2.3) leads to:

$$\left(P_0 + \frac{2\gamma}{R} \right) \frac{4\pi R^3}{3} = n R_g T \quad (4.2.2)$$

where n and T are assumed to be constant.

Figure (4.2.1) shows the influence of surface tension on a free immersed gas bubble. It is clear that the impact of surface tension on the bubble radius through gas compressibility is not negligible in the microscale. This phenomenon is thus essentially significant at microscale. For bubbles of 10^{-14} mol (bubbles of a few micrometers), the relative variation of diameter induced by a surface tension $\gamma = 72 \cdot 10^{-3} \text{ N m}^{-1}$ is about 26%.

We will demonstrate further ahead that these variations could be even more significant with other configurations, when the bubble is connected to a larger gas circuit for example (Sect. 5.3.6).

To develop the model predicting the size of a bubble generated from a volume controlled generator, we will describe the device and its parameters.

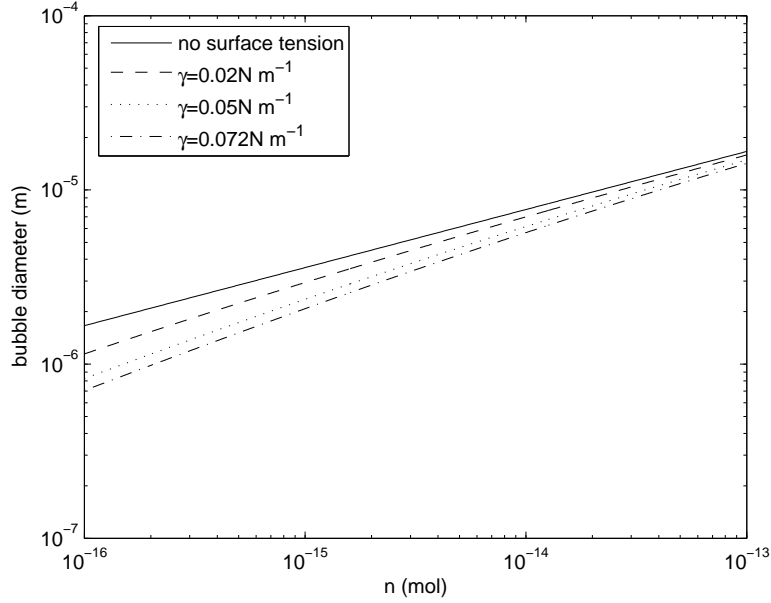


Figure 4.2.1: Influence of surface tension and amount of gas mole on the diameter of a free gas bubble in a liquid. The influence of surface tension is more significant for small bubbles, and liquid-gas couples having a high surface tension ($T = 293.15\text{K}$, $P_0 = 101325\text{Pa}$)

4.2.2 Device Description

The device is like a syringe pump and is schematically represented on Fig. 4.2.2. The parameters are summarized in table 4.2.1. The syringe is filled with the gas to inject, then the syringe tip is immersed in a liquid, near the free surface so that hydrostatic pressure can be neglected. The generation of a bubble is done by pushing the piston. The orientation of the tip (downwards or upwards) has no influence on the gas generation, since we are working with characteristic length below the capillary length. The gravity can henceforth be neglected, and the orientation has no influence. The gas circuit includes the gas in the container and the gas in the bubble. It is clear that in the configuration shown in Fig. 4.2.2, the variation of volume ΔV in the gas circuit is given by:

$$\Delta V = \delta S \quad (4.2.3)$$

The next developments will be done using ΔV as it is a more general formulation. The model we will develop is to determine the height of the bubble h as a function of volume variation ΔV . We will see that it is possible to act on other parameters to modify the height of the bubble.

4.2.3 Model of Bubble Height

The purpose of the model developed in this section is illustrated on Fig. 4.2.3. The output of the model is the geometry of the generated bubble, which under the assumption we make has the shape of a portion of a sphere. Since we assume that the bubble is anchored to the border of the outlet channel having a diameter s , the geometry of the bubble can be deduced

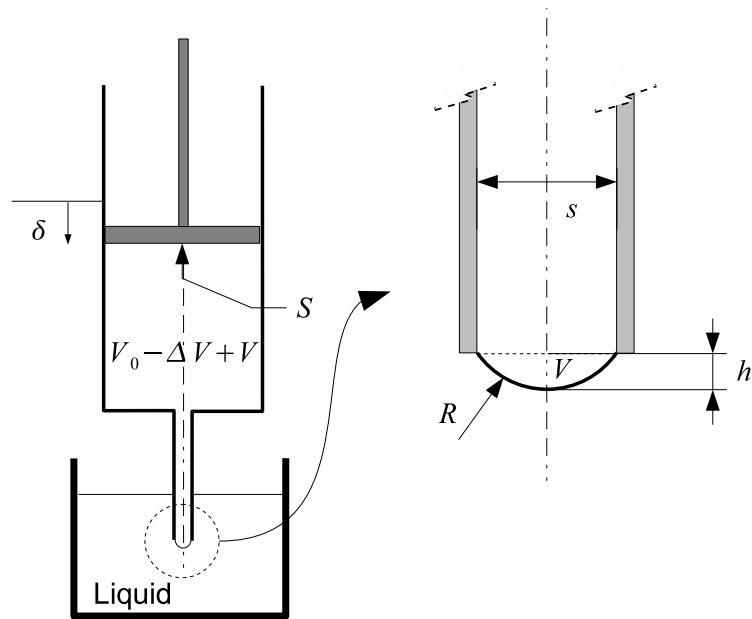


Figure 4.2.2: Schematic representation of the volume controlled bubble generator. The device is essentially a syringe pump. The various parameters used in the model are shown

from its height h .

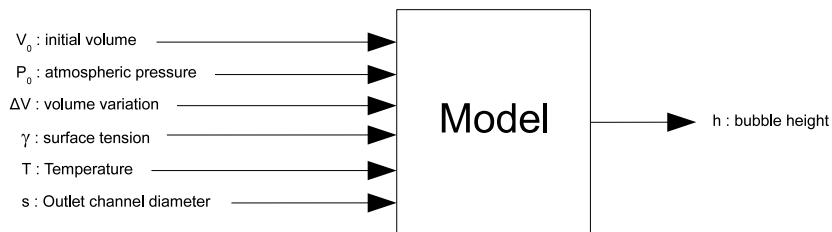


Figure 4.2.3: Model of the volume controlled bubble generator. The output of the model is the geometry of the bubble, which we assume to be a portion of a sphere.

Equations

To model the height of a bubble generated by a volume controlled generator, we base the reasoning on the next equations. We assume that the number of mole in the system is constant. Consequently, the total volume of gas is not constant due to the compressibility of the medium which is subject to surface tension force.

Laplace equation (3.2.3) links pressure drop across bubble interface, surface tension and the mean curvature of the interface. We assume the pressure inside the bubble to be constant, and since we suppose that the bubble is smaller than the capillary length, the mean curvature is constant. Finally, assuming an axisymmetric configuration, the geometry of the bubble is a spherical cap (radius R):

$$\frac{2\gamma}{R} = P - P_0 \quad (4.2.4)$$

Table 4.2.1: Definition of model parameters

Parameter	Description
V_0 (m ³)	Initial volume in the syringe
V (m ³)	Volume of gas in the spherical cap
ΔV (m ³)	Variation of container (positive if volume decreases)
δ (m)	Displacement of the piston
γ (N m ⁻¹)	Surface tension at the liquid-gas interface
P_0 (N m ⁻²)	Atmospheric pressure
P (N m ⁻²)	Pressure in the gas tank
T (K)	Temperature of the system
R_g (N m mol ⁻¹ K ⁻¹)	Universal gas constant
n (mol)	Total number of gas mole in the system
S (m ²)	Section of the piston
s (m)	Exhaust channel diameter
R (m)	Radius of the spherical cap
h (m)	Height of the spherical cap

The gas law is used to take into account the volume variation induced by pressure variation:

$$P(V + V_0 - \Delta V) = n R_g T \quad (4.2.5)$$

It is possible to write equations linking the radius of the spherical cap R , the height of the bubble h , the syringe tip diameter s and the volume of the spherical cap V :

$$R = \frac{s^2}{8h} + \frac{h}{2} \quad (4.2.6)$$

$$V = \frac{\pi h}{6} \left(\frac{3s^2}{4} + h^2 \right) \quad (4.2.7)$$

The combination of (4.2.4), (4.2.5), (4.2.6) and (4.2.7) leads to a fifth degree polynomial (see Appendix B for the complete development).

$$\begin{aligned} & \frac{\pi}{12} P_0 h^5 + \frac{\pi}{3} \gamma h^4 + \frac{\pi}{12} P_0 s^2 h^3 + \left(-\frac{1}{2} n R_g T + \frac{1}{2} P_0 (V_0 - \Delta V) + \frac{\pi}{4} \gamma s^2 \right) h^2 \\ & + \left(\frac{\pi}{64} P_0 s^4 + 2\gamma (V_0 - \Delta V) \right) h + \frac{1}{8} P_0 s^2 (V_0 - \Delta V) - \frac{1}{8} n R_g T s^2 = 0 \end{aligned} \quad (4.2.8)$$

Equation (4.2.8) is an implicit analytic function giving $h = f(V_0, P_0, \gamma, T, R_g, n, s, \Delta V)$. h is a function of 8 parameters. n could be seen as a dependent parameter if the initial filling of the container is made at atmospheric conditions ($P_0 V_0 = n R_g T$). We have chosen to leave it as an independent parameter to keep the ability to modify the value independently from the initial filling conditions, for example to consider supplementary gas injection or a gas leak. To the best of our knowledge, there is no analytical solution to explicit a fifth degree polynomial. However, it is easy to solve it numerically, with for example the `roots` function in *Matlab*.

Table 4.2.2: Sets of parameters for model interpretation

Parameters	First set	Second set	Units
V_0	2×10^{-6}	5×10^{-9}	(m ³)
n	8.175×10^{-5}	2.044×10^{-7}	(mol)
s	2×10^{-3}	150×10^{-6}	(m)
ΔV	$0 \rightarrow 2 \times 10^{-6}$	$0 \rightarrow 5 \times 10^{-9}$	(m ³)

Our main interest is to find the height of the bubble with respect to container volume variation, but (4.2.8) allows us to check the influence of other parameters. Since it is a fifth order polynomial, we know there is 1, 3 or 5 real solutions h for sets of other parameters.

Shape of the Solution

To check the shape of the solution $h = h(\Delta V)$ and make it easier to interpret the multiplicity of solutions, we propose two sets of parameters. In each case, we suppose to inject air in water, and we assume $\gamma = 72 \cdot 10^{-3} \text{ N m}^{-1}$. We also suppose to work at normal atmospheric pressure $P_0 = 101325 \text{ Pa}$, and normal temperature $T = 298.15 \text{ K}$. As a reminder, gas constant is $R_g = 8.314 \text{ J mol}^{-1} \text{ K}^{-1}$. The value for other parameters are summarized in table 4.2.2.

The first set corresponds to a larger syringe ($13.3 \times$ larger outlet tip diameter and $400 \times$ larger volume) than the second one. In this table, the values of n are calculated using the ideal gas law. This means that we suppose the syringe is filled with air under atmospheric conditions. In each case, we will compare the results with the height of a bubble of incompressible fluid. This height is the height of a spherical cap having a volume equal to ΔV , the volume swept by the piston. The evolution of bubble height h with syringe tank volume variation is shown in Fig. 4.2.4 for the first set of parameters and Fig. 4.2.5 for the second set of parameters.

The analysis of the results for the first set of parameters shows that there is only one solution for the whole range of ΔV . The combination of gas compressibility and surface tension clearly has an influence and leads to a smaller gas bubble volume than what could be expected. This phenomenon tends to disappear for large bubbles, since the effects of surface tension decrease with the size of the bubble. A large bubble has a smaller curvature, so the pressure drop is lower and the effect of gas compressibility disappears.

The results for the second set of parameters shows even more consequences of compressibility and surface tension. In this case, there is a range of ΔV values for which there are three solutions. If ΔV is increased progressively, the curve $h(\Delta V)$ reaches a point (I in Fig. 4.2.5) where its slope changes sign after being infinite. If ΔV increases beyond point I , the height of the bubble has no choice but to jump to the other solution (Arrow on Fig. 4.2.5), creating a sudden change in the bubble size. Of course, these results are for quasi-static situation, so the change of height is not instantaneous, but this shows an instability in the bubble growing.

This means also that it is not possible to grow a bubble of any size with the second set of parameters. The area between point I and its corresponding solution on the upper curve is not accessible. One should also notice that the height variation at point I is significant: in this configuration, it increases by a factor 7. In this case, the buoyancy forces are generally large enough to lift the bubble. It is interesting to notice that point I is located approximately at $h = s/2$, i.e. when the bubble is a half sphere. The interpretation of this result is that in some cases, there is an accumulation of energy in the form of a pressure rise in the gas

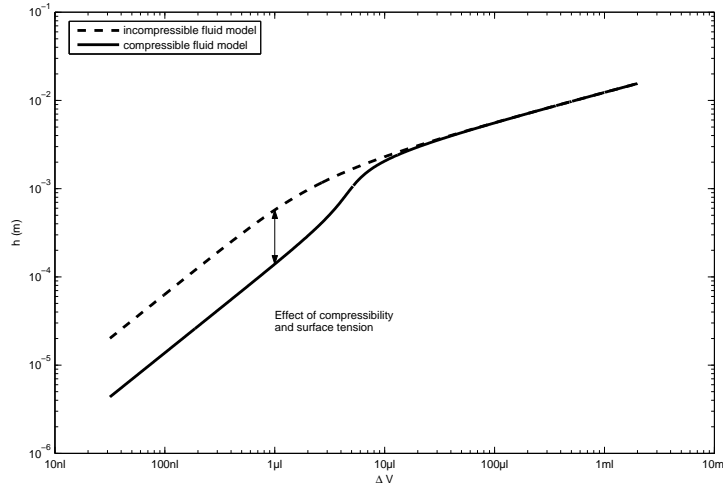


Figure 4.2.4: Evolution of bubble height with volume variation (first set of parameters), i.e. with the volume swept by the piston in the syringe. The incompressible fluid model represents the height of a bubble having the same volume as ΔV , as if the fluid has a constant volume. The influence of gas compressibility and surface tension clearly have an influence on the volume of the bubble for small bubbles. In this configuration, there is a direct relation between ΔV and h

system. When the bubble grows from $h = 0$ to $h = s/2$, the pressure in the gas circuit increases, but when $h > s/2$, the pressure decreases. The accumulated pressure induces then a rapid growth of volume.

It should be interesting to find a criterion on the setup parameters to predict whether an instability is likely to occur (as for the second set of parameters) or if the growing will be continuous (as for the first set of parameters). This is done in Sect. 4.2.6, where we will translate our model in a dimensionless form. Before, we will first lead a sensitivity analysis of the model parameters, in order to better understand the reaction of the system to a change of parameter.

4.2.4 Limit of the Model

Since the pressure inside a bubble increases for small bubbles, it is interesting to check whether the liquefaction of the gas could occur due to pressure rise.

It is important to note that it is not possible to liquefy a gas if its temperature is larger than the critical temperature. For example, critical temperature of nitrogen is $T_c = 126$ K, and for oxygen $T_c = 155$ K. Hence, liquefaction of air is not possible around ambient temperature, no matter how large the pressure is.

However, carbon dioxide has a critical temperature of 304 K, which is a bit larger than ambient temperature. Critical pressure of carbon dioxide is around $7.4 \cdot 10^6$ Pa. To reach such pressure inside the bubble, their diameter has to be around 10 to 40 nm at $T = 293$ K, which is very small. At this level, the ideal gas law model is not correct anymore, because in this model, gas molecules are supposed not to interact with each other.

Other gases have a critical temperature reasonably larger than ambient temperature, like

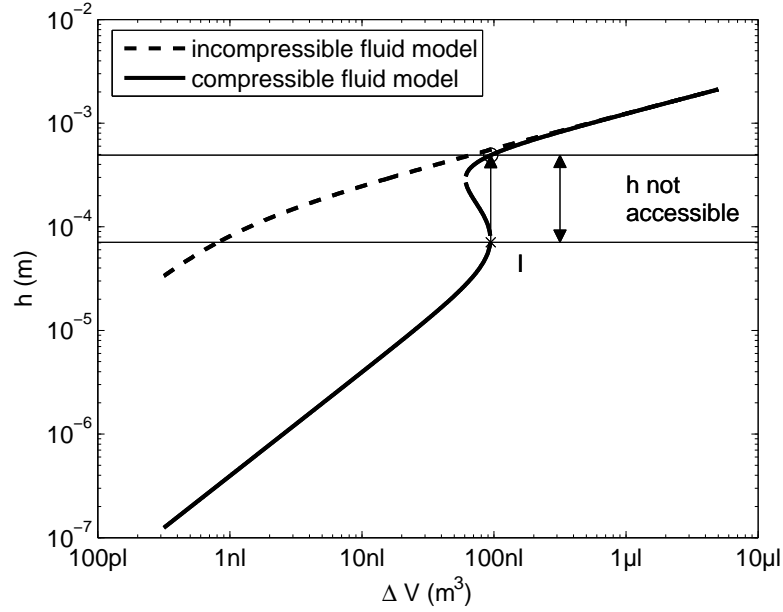


Figure 4.2.5: Evolution of bubble height with volume variation (second set of parameters), i.e. with the volume swept by the piston in the syringe. In this configuration, the model gives three solutions for a range of ΔV . Physically, the bubble will grow all the way to point I , then its height will jump suddenly to the upper curve. This growing instability means there is a whole range of height that cannot be reached

ammonia: $T_c = 405.5$ K. However, the pressure to liquefy the gas at ambient temperature is still in the range of 1 MPa, leading to bubble diameter of 90 nm to 320 nm.

To avoid model deviation due to the proximity of critical state of fluid, we shall consider only gas bubbles with characteristic dimensions in the range of $1\mu\text{m}$ to a few mm.

4.2.5 Parameters Sensitivity

In this section, we try to understand the sensitivity of the model to each of its parameters. With this study, the global understanding of the model will be easier, since the influence of a variation of one parameter will be calculated.

Gradient Method

To determine the sensitivity of the model to its parameters, we will calculate the partial derivative of the function $h = f(V_0, P_0, \gamma, T, R_g, n, s, \Delta V)$.

Since it is not possible to find the explicit form of (f), it is not possible to find the analytical expressions of its partial derivatives. We will calculate these derivatives numerically. Of course, it is necessary to set a working point, i.e. a realistic combination of the parameters, prior to proceed with this calculation.

The sensitivity factors m_i are defined as follow:

$$m_i = \frac{\partial h}{\partial x_i} \quad (4.2.9)$$

Giving:

$$\Delta h = \sum_i \frac{\partial h}{\partial x_i} \Delta x_i = \sum_i m_i \Delta x_i \quad (4.2.10)$$

These sensitivity factors will help to understand how sensitive is the output of the model to any variation of its inputs. Since the input parameters have significantly different order of magnitude, we search for the absolute variation of the output Δh , not for a relative variation. Indeed, 5% variation of pressure means about 5000Pa, which is quite high, while 5% variation of γ is about 4Nm^{-1} , which is reasonable.

The first indication is the sign of the factor. For example, if m_j is negative, an increase of parameter j will produce a decrease of the output. A second indication is the relative importance of the factors, showing to which parameter the model is the most sensitive.

The calculation of the partial derivatives is performed using a finite difference method. We calculate the value h at the working point, then we increase parameter j by 10^{-7} and calculate² the corresponding output h^+ , then we decrease parameter j by 10^{-7} and calculate the corresponding output h^- . The partial derivative for parameter j is then given by:

$$\frac{\partial h}{\partial x_j} = \frac{h^+ - h^-}{x_j \cdot 2 \cdot 10^{-7}} \quad (4.2.11)$$

The factor is calculated for each parameter. Remember that $n = \frac{P_0 V_0}{R_g T}$ is calculated for the working point, simulating the filling of the syringe up to volume V_0 under P_0 and T . However, when we calculate for example the sensitivity factor m_{P_0} , we suppose that the outer pressure changes while the amount of gas molecules in the system remains constant. The calculation of m_n reflects a variation of the amount of gas molecules while other parameters are kept constant, for example if more gas is injected in the syringe from outside.

Results

We present here the results of the sensitivity calculation in the two configurations presented in Sect. 4.2.3.

These results show the evolution of the sensitivity of the output to a variation of each parameter: $m_i \Delta x_i$, with respect to different working points represented by different ΔV , for the first set then the second set of parameters presented in table 4.2.2. The values for Δx_i are chosen as realistic variations, shown in Tab. 4.2.3.

To improve readability, we present the results in logarithmic scales. Because some coefficients m_i are negative, we present the positive results in one plot, and absolute values for negative results in a second plot.

The results for the first set of parameters is shown in Fig. 4.2.6. The results for the second set is shown in Fig. 4.2.7. From these results, we see that an increase of ΔV , n or T leads to an increase of h , while an increase of V_0 , γ or P_0 leads to a decrease of h . We also see that ΔV is an interesting actuation mean since its effect is predominant, together with an increase of n or a decrease of P_0 . We also see that the sensitivity to surface tension is maximal at

²The value of the interval has been chosen small enough to ensure convergence of the derivative value

Table 4.2.3: Parameters variation used to calculate the variation of the output Δh

input	variation
V_0	+5%
P_0	+10Pa
γ	+5 10^{-3} Nm^{-1}
T	+1 K
s	+5%
ΔV	+5% of maximal ΔV

the inflection of $h(\Delta V)$. For s , an increase of its value would increase h before the inflection point, while it would decrease h after the inflection point. These results show that using ΔV as actuation is a relevant choice. Another interesting choice is the use of temperature.

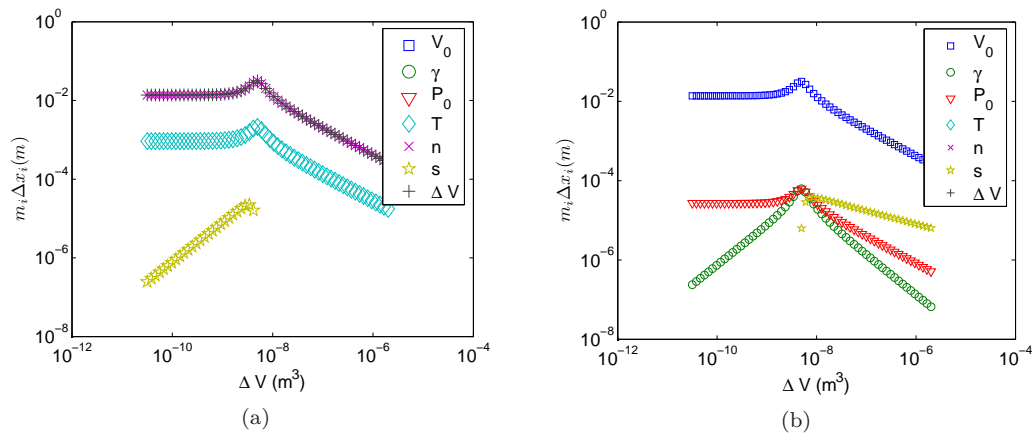


Figure 4.2.6: Evolution of $m_i \Delta x_i$ with ΔV for first set of parameters (see table 4.2.2). (a) positive values, (b) negative values

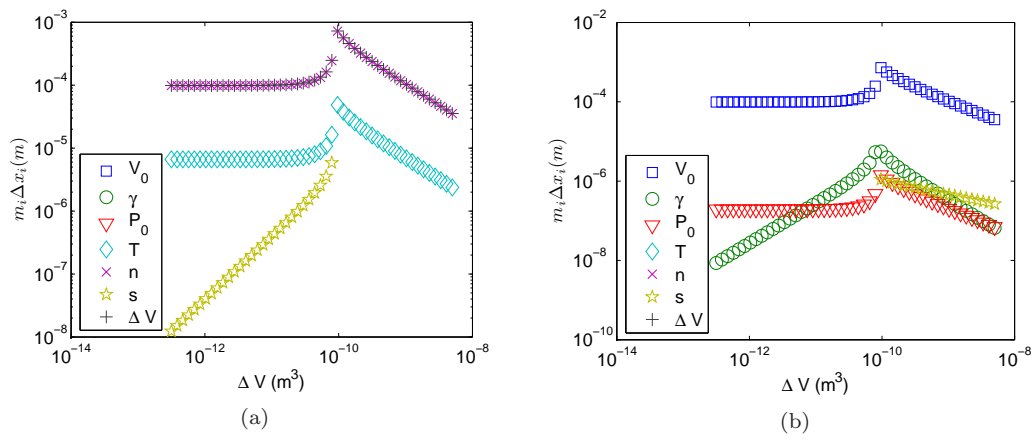


Figure 4.2.7: Evolution of $m_i \Delta x_i$ with ΔV for second set of parameters (see table 4.2.2). (a) positive values, (b) negative values

4.2.6 Dimensionless Analysis and Stability Criterion

We have seen in Sect. 2.1.2 that dimensionless numbers are useful to study a scaled model of a device, or to reduce the number of parameters in a model [87]. On the base of a dimensionless analysis of (4.2.8), we are going to show that the growth instability can be described by a dimensionless number.

Buckingham Theorem

It is possible to construct a set of dimensionless number using Buckingham theorem. In our case, the model can be expressed in the form:

$$\Psi(V_0, \Delta V, h, \gamma, P_0, T, R_g, n, s) = 0 \quad (4.2.12)$$

There are nine parameters and five different dimensions are used (length, mass, time, temperature and mole). In the dimensional matrix hereafter, element i, j indicates the exponent of the i^{th} dimension in the j^{th} parameter:

$$\overline{\overline{D}} = \begin{array}{l} \text{mass} \\ \text{length} \\ \text{time} \\ \text{temperature} \\ \text{moles} \end{array} \left| \begin{array}{ccccccccc} V_0 & \Delta V & h & \gamma & P_0 & T & n & s & R_g \\ \hline 0 & 0 & 0 & 1 & 1 & 0 & 0 & 0 & 1 \\ 3 & 3 & 1 & 0 & -1 & 0 & 0 & 1 & 2 \\ 0 & 0 & 0 & -2 & -2 & 0 & 0 & 0 & -2 \\ 0 & 0 & 0 & 0 & 0 & 1 & 0 & 0 & -1 \\ 0 & 0 & 0 & 0 & 0 & 0 & 1 & 0 & -1 \end{array} \right. \quad (4.2.13)$$

The rank of $\overline{\overline{D}}$ is 4, so according to Buckingham's theorem, it is possible to find $9 - 4 = 5$ linearly independent relations between the exponents of each parameters. This leads to 5 independent dimensionless numbers: none of these 5 numbers can be found by a combination of the 4 others. To find such parameters, we only need to calculate the kern of $\overline{\overline{D}}$.

The problem of this method is that any combination of these terms will also produce a dimensionless number. It is not possible to predict which among all these possibilities will give the most relevant number to predict whether an instability will occur or not.

Dimensionless Equation

The solution to find the adequate dimensionless numbers is to formulate (4.2.8) in a dimensionless form. The idea is to norm every parameter of this equation. We propose to norm the parameters as follows:

$$\begin{aligned} \tilde{E} &= \frac{n R_g T}{\gamma s^2} & \widetilde{\Delta V} &= \frac{\Delta V}{s^3} & \tilde{P} &= \frac{P_0}{\gamma/s} \\ \tilde{h} &= \frac{2h}{s} & \tilde{V} &= \frac{V_0}{s^3} \end{aligned} \quad (4.2.14)$$

Note that $\tilde{h} = 1$ means the bubble is a half sphere. Equation (4.2.8) then becomes:

$$\begin{aligned} & \frac{\pi}{384} \tilde{P} \tilde{h}^5 + \frac{\pi}{48} \tilde{h}^4 + \frac{\pi}{96} \tilde{P} \tilde{h}^3 + \left[-\frac{\tilde{E}}{8} + \frac{\tilde{P}}{8} (\tilde{V} - \widetilde{\Delta V}) + \frac{\pi}{16} \right] \tilde{h}^2 \\ & + \left[\frac{\pi}{128} \tilde{P} + (\tilde{V} - \widetilde{\Delta V}) \right] \tilde{h} + \frac{\tilde{P}}{8} (\tilde{V} - \widetilde{\Delta V}) - \frac{\tilde{E}}{8} = 0 \end{aligned} \quad (4.2.15)$$

As predicted by Buckingham's theorem, $\tilde{h} = \tilde{f}(\tilde{E}, \tilde{P}, \tilde{V}, \widetilde{\Delta V})$ is now a function of 4 parameters instead of 8 in the dimensional formulation. We have reduced the number of parameters by 4, which was the rank of \overline{D} .

Other simplifications can also be done in (4.2.15). The form of the equation shows that \tilde{V} and $\widetilde{\Delta V}$ are always together. It is possible in this case to reduce even more the number of parameters, posing:

$$\widehat{V} = \tilde{V} - \widetilde{\Delta V} \quad (4.2.16)$$

$$\begin{aligned} & \frac{\pi}{384} \tilde{P} \tilde{h}^5 + \frac{\pi}{48} \tilde{h}^4 + \frac{\pi}{96} \tilde{P} \tilde{h}^3 + \left(-\frac{\tilde{E}}{8} + \frac{\tilde{P}}{8} \widehat{V} + \frac{\pi}{16} \right) \tilde{h}^2 \\ & + \left(\frac{\pi}{128} \tilde{P} + \widehat{V} \right) \tilde{h} + \frac{\tilde{P}}{8} \widehat{V} - \frac{\tilde{E}}{8} = 0 \end{aligned} \quad (4.2.17)$$

\widehat{V} represents the normalized volume of gas remaining in the container after the movement of the piston. \widehat{V} cannot be relevant to predict any instability in the system. Indeed, this parameter is a function of ΔV , and the existence or absence of instability cannot depend on the position of the piston. The actual position of the piston does not have any influence on the fact that at a certain position, the bubble will grow suddenly. From a mathematical point of view, the function $h = h(\Delta V)$ does not depend on the abscissa point ΔV . As the instability is defined by the shape of this function, instability is not characterized by parameter ΔV . We can therefore state that the existence of an instability, if any, could be influenced by two dimensionless numbers: \tilde{E} and \tilde{P} .

Numerical Approximation

In order to verify the existence of a threshold value for \tilde{E} and \tilde{P} beyond which an instability would occur, we made several simulations in which we varied the input parameters value. In each case, we checked if an instability occurs. The results are shown in Fig. 4.2.8. To identify the existence of an instability, we check the number of real solutions for (4.2.8): if there is more than one solution for a value of ΔV , we conclude the configuration lead to an unstable bubble growth.

In some cases, the combinations of parameters we used led to the same dimensionless values for \tilde{P} and \tilde{E} . It is interesting to note that there is no \tilde{P}, \tilde{E} couple leading to both stable and unstable growth. This confirms that only these two parameters are relevant to predict the existence of the instability.

There is a clear border between stable and unstable growth. This border can be approximated reasonably with a line in the bilogarithmic axes:

$$\log \tilde{E} = 2 \log \tilde{P} \quad (4.2.18)$$

Therefore, a stability condition regarding the experimental setup is:

$$\tilde{P}^2 > \tilde{E} \quad (4.2.19)$$

In its dimensional form, this criterion is:

$$\left(\frac{P_0 s}{\gamma} \right)^2 > \frac{n R_g T}{\gamma s^2} \quad (4.2.20)$$

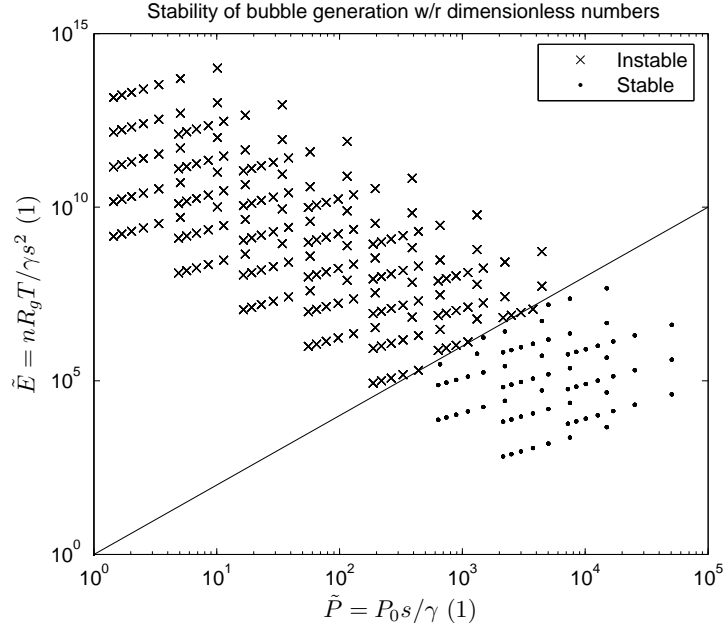


Figure 4.2.8: We have run several simulations varying the input parameters. The crosses represent the configurations that led to an instability during bubble growing. The dots represent the configurations for which the growing was continuous. There is a clear border between the two situations that can be approximated by a line

This lead to a new dimensionless number, σ :

$$\sigma = \frac{P_0^2 s^4}{\gamma n R_g T} \quad (4.2.21)$$

with the stability condition being simply:

$$\sigma > 1 \quad (4.2.22)$$

If the gas container is filled under atmospheric conditions,

$$n R_g T = P_0 V_0 \quad (4.2.23)$$

and σ can be rewritten in terms of easily measurable parameters:

$$\sigma = \frac{P_0 s^4}{\gamma V_0} \quad (4.2.24)$$

This criterion tells us that instability is more likely to occur if the gas container is large, the surface tension is high, the atmospheric pressure is low and the diameter of the injection point is small. A large surface tension and a small diameter will induce large surface tension effects, while a large gas container and a small atmospheric pressure will increase the effect of gas compressibility.

Analytical Approach

The results presented in Sect. 4.2.6 are only numeric. It is not possible to know if the criterion is correct for every single couple \tilde{P}, \tilde{E} other than those presented in Fig. 4.2.8. Moreover, the line separating both regions is only approximative. Therefore we will also search for an analytic approach.

The method is based on the study of the partial derivative $\partial\hat{V}/\partial\tilde{h}$: in the case of an instability, the curve $\tilde{h}(\Delta\hat{V})$ has a vertical tangent corresponding to the condition:

$$\text{instability} \Leftrightarrow \exists \tilde{h} \in \mathbb{R}, \frac{\partial\hat{V}}{\partial\tilde{h}} = 0 \quad (4.2.25)$$

Using the symbolic toolbox of Matlab, it is easy to find the partial derivative:

$$\frac{\partial\hat{V}}{\partial\tilde{h}} = \frac{1}{16 \left(\tilde{h}^2 \tilde{P} + 8\tilde{h} + \tilde{P} \right)^2} \left(-\pi \tilde{P}^2 \tilde{h}^6 - 16\pi \tilde{P} \tilde{h}^5 - 3\pi \tilde{P}^2 \tilde{h}^4 - 64\pi \tilde{h}^4 - 32\pi \tilde{P} \tilde{h}^3 - 3\pi \tilde{P}^2 \tilde{h}^2 - 64\tilde{h}^2 \pi - 16\tilde{h} \pi \tilde{P} + 128\tilde{h}^2 \tilde{E} - \pi \tilde{P}^2 - 128\tilde{E} \right) \quad (4.2.26)$$

It is remarkable that for $\tilde{h} = 1$, $\partial\hat{V}/\partial\tilde{h} = -\pi/8$, whatever the values of \tilde{E} and \tilde{P} . This means that an instability does not occur strictly at $h = s/2$ (the half-sphere configuration).

We consider a constant value of parameter \tilde{P} . The condition (4.2.25) can be presented in a (\tilde{h}, \tilde{E}) plane. Indeed, it is possible to plot the values of \tilde{h}, \tilde{E} for which $\partial\hat{V}/\partial\tilde{h} = 0$. An example is shown in Fig. 4.2.9 for $\tilde{P} = 10$.

The bubble growth will be stable if there is no intersection of the line $\tilde{E} = \text{constant}$ with the contour $\partial\hat{V}/\partial\tilde{h} = 0$. We see in Fig. 4.2.9 that there is a range for \tilde{E} where this condition is satisfied. The limit value \tilde{E}^* is where the contour $\partial\hat{V}/\partial\tilde{h} = 0$ is minimal. This value correspond to a value \tilde{h}^* that seems close to $\sqrt{2} \approx 1.41$. The condition (4.2.25) is equivalent to:

$$\forall \tilde{P}, \text{instability} \Leftrightarrow \tilde{E} > \tilde{E}^* \quad (4.2.27)$$

This new criteria enables to determine an analytic expression of the criteria.

To find the value of \tilde{h}^* , we consider the implicit equation $\partial\hat{V}/\partial\tilde{h} = 0$:

$$\begin{aligned} & (-\pi \tilde{P}^2 \tilde{h}^6 - 16\pi \tilde{P} \tilde{h}^5 - 3\pi \tilde{P}^2 \tilde{h}^4 - 64\pi \tilde{h}^4 - 32\pi \tilde{P} \tilde{h}^3 \\ & - 3\pi \tilde{P}^2 \tilde{h}^2 - 64\tilde{h}^2 \pi - 16\tilde{h} \pi \tilde{P} + 128\tilde{h}^2 \tilde{E} - \pi \tilde{P}^2 - 128\tilde{E}) = 0 \end{aligned} \quad (4.2.28)$$

from which we extract $\tilde{E}_0 = \tilde{E}_0(\tilde{h}, \tilde{P})$, which is the equation of contour 0 in Fig. 4.2.9. We look for \tilde{h}^* such that $\partial\tilde{E}_0/\partial\tilde{h} = 0$:

$$\frac{\partial\tilde{E}_0}{\partial\tilde{h}} = \frac{\pi \left(\tilde{h}^2 \tilde{P} + 8\tilde{h} + \tilde{P} \right) \left(\tilde{P} \tilde{h}^5 + 4\tilde{h}^4 - \tilde{P} \tilde{h}^3 - 8\tilde{h}^2 - 2\tilde{P} \tilde{h} - 4 \right)}{32 \left(\tilde{h} - 1 \right)^2 \left(\tilde{h} + 1 \right)^2} \quad (4.2.29)$$

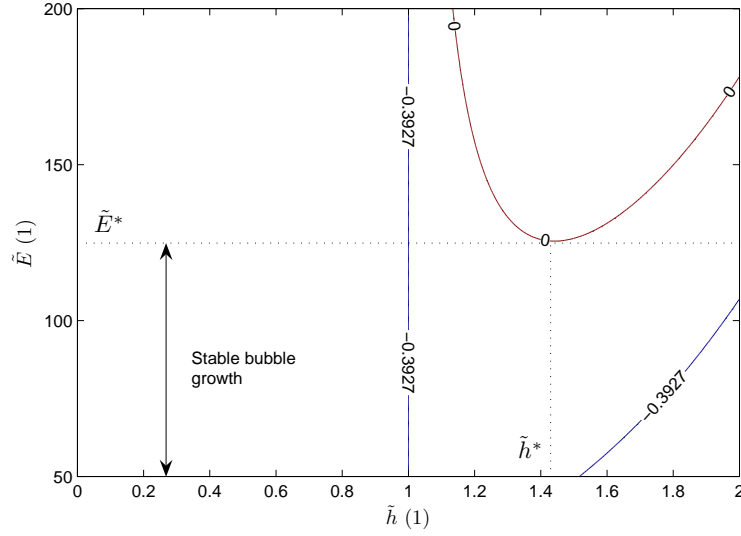


Figure 4.2.9: Contour plot of $\partial\hat{V}/\partial\tilde{h}$ with respect to \tilde{h} and \tilde{E} , in the case $\tilde{P} = 10$. There is a range of \tilde{E} values for which the line $\tilde{E} = \text{constant}$ has no intersection with the contour corresponding to $\partial\hat{V}/\partial\tilde{h} = 0$. The limit value is in this case between 100 and 150, and the corresponding \tilde{h} value is just before 1.5. The value of the partial derivative for $\tilde{h} = 1$ is always $-\pi/8 \approx -0.3927$

The first term of the numerator of (4.2.29) is equal to zero only for negative values of \tilde{h} which is not an acceptable solution. The second term will give us \tilde{h}^* with respect to \tilde{P} . For large values of \tilde{P} , the second term gives an asymptotic value of \tilde{h}^* :

$$\begin{aligned} \lim_{\tilde{P} \rightarrow \infty} \left(\tilde{P}\tilde{h}^5 + 4\tilde{h}^4 - \tilde{P}\tilde{h}^3 - 8\tilde{h}^2 - 2\tilde{P}\tilde{h} - 4 \right) &= \tilde{P}(\tilde{h}^5 - \tilde{h}^3 - 2\tilde{h}) \\ &= \tilde{P}\tilde{h}(\tilde{h}^2 - 2)(\tilde{h}^2 + 1) \end{aligned} \quad (4.2.30)$$

so the only real positive value is $\tilde{h}^* = \sqrt{2}$, as expected from Fig. 4.2.9. The evolution of \tilde{h}^* with respect to \tilde{P} is shown in Fig. 4.2.10. The asymptotic value is reached very quickly, and it is legitimate to assume $\tilde{h}^* = \sqrt{2}$ if $\tilde{P} \geq 10$.

Now if we return to (4.2.26) and replace in this partial derivative \tilde{h} by $\tilde{h}^* = \sqrt{2}$, we find a relation between \tilde{E} and \tilde{P} :

$$\frac{\partial\hat{V}}{\partial\tilde{h}} \Big|_{\tilde{h}=\tilde{h}^*} = \frac{-384\pi + 128\tilde{E} - 144\sqrt{2}\pi\tilde{P} - 27\tilde{P}^2}{16(8\sqrt{2} + 3\tilde{P})^2} = 0 \quad (4.2.31)$$

We can solve this equation with respect to \tilde{P} and find the relation that links \tilde{P} and \tilde{E} so that the instability exists. We note these values \tilde{P}^* and \tilde{E}^* . The only real positive root is:

$$\tilde{P}^* = \frac{8(-3\sqrt{2}\pi + \sqrt{6\pi\tilde{E}^*})}{9\pi} \quad (4.2.32)$$

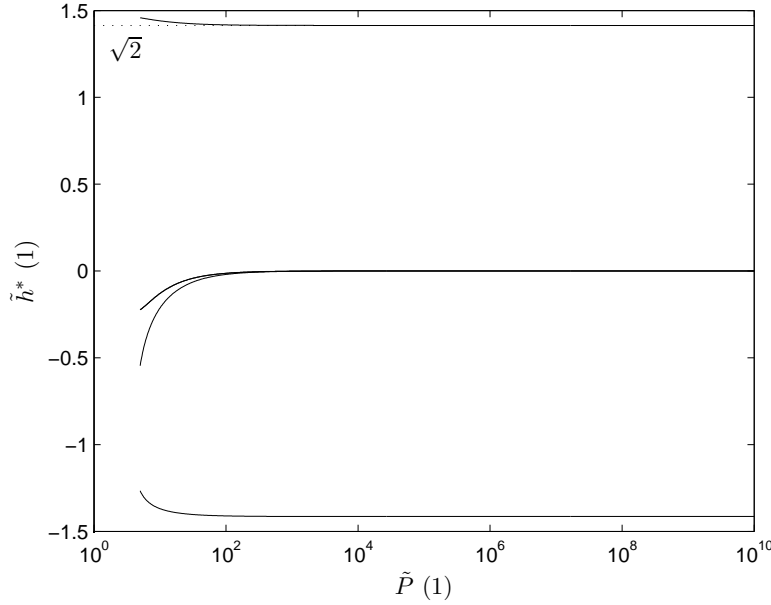


Figure 4.2.10: \tilde{h}^* is the value at which the instability occurs (i.e. $\partial\tilde{E}_0/\partial\tilde{h}|_{\tilde{h}=\tilde{h}^*} = 0$). It is clear that \tilde{h}^* reaches quickly its asymptotic value $\sqrt{2}$. It is henceforth legitimate to state $\tilde{h}^* = \sqrt{2}$ if $\tilde{P} \geq 10$

Equation (4.2.32) is an analytical expression of the stability condition between \tilde{E} and \tilde{P} . For large values of \tilde{E}^* , it is possible to find an asymptotic value for the relation (see Fig. 4.2.11):

$$\tilde{P}_{lim}^* = \frac{8\sqrt{6\pi\tilde{E}_{lim}^*}}{9\pi} \quad (4.2.33)$$

We see that the criterion is close to the asymptotic value for $\tilde{P} \geq 1000$. The stability criterion formulated from the numeric approximation is then:

$$\begin{aligned} \tilde{P}_{lim}^{*2} &= \frac{128}{27\pi} \tilde{E}_{lim}^* \\ \sigma &= \frac{128}{27\pi} \end{aligned} \quad (4.2.34)$$

It is slightly different from the value we found from the numerical approximation.

If we plot this criterion in Fig. 4.2.8, we see there are some values that cross the border. This is due to the numerical search of instability: if the configuration is almost stable, the range of h for which there are 3 solutions is short, and it is likely that the software jumps across this range, considering an unstable configuration to be stable (Fig. 4.2.12).

Stability Criterion

We have established a criterion σ allowing to predict if a volume controlled bubble generator will allow to grow bubbles continuously, or if the bubble will grow suddenly beyond a certain

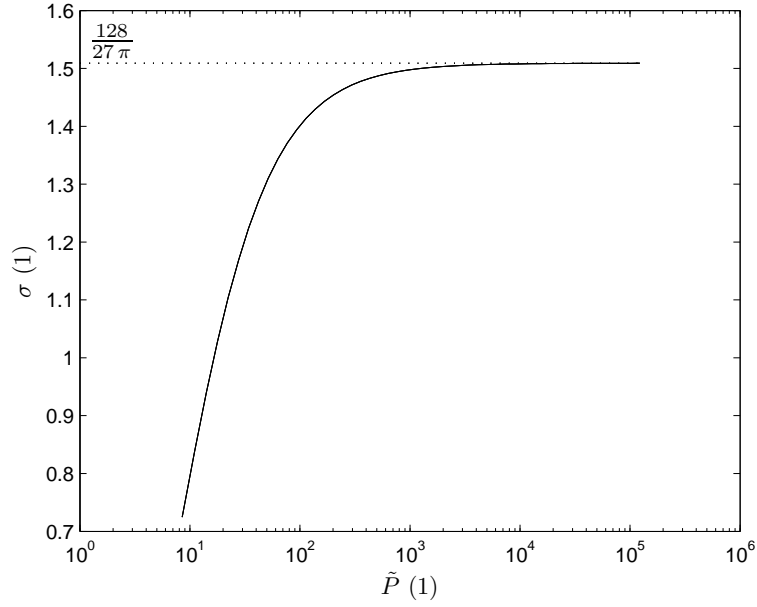


Figure 4.2.11: This analytic study shows that the threshold value for the dimensionless number $\sigma = \tilde{P}^2/\tilde{E}$ depends on the dimensionless pressure \tilde{P} . However, for values of \tilde{P} larger than 1000, σ tends to the asymptotic value $\frac{128}{27\pi}$

height.

The threshold of this criterion is constant for value of \tilde{P} larger than 1000: $\sigma = \frac{128}{27\pi}$.

4.3 Experimental Validation of the Volume Controlled Bubble Generation Model

To validate the model developed in Sect. 4.2.3 (Fig. 4.2.3), we made experiments on two different experimental setups.

4.3.1 First Experimental Setup

The first test bed is directly inspired from the syringe pump principle. It is represented schematically in Fig. 4.3.1.

The container is a syringe, and the volume variation is induced by the displacement of the piston. This displacement is operated manually using a micropositioning stage from *PI*. We used two different types of syringe:

- Syringe type "Exmire microsyringe MS-X05 ", volume 5 μL . Piston diameter is 0.35mm (measured with a caliper)
- Syringe type "Narishige ITO", volume 800 μL . Piston diameter is 5mm (measured with a caliper)

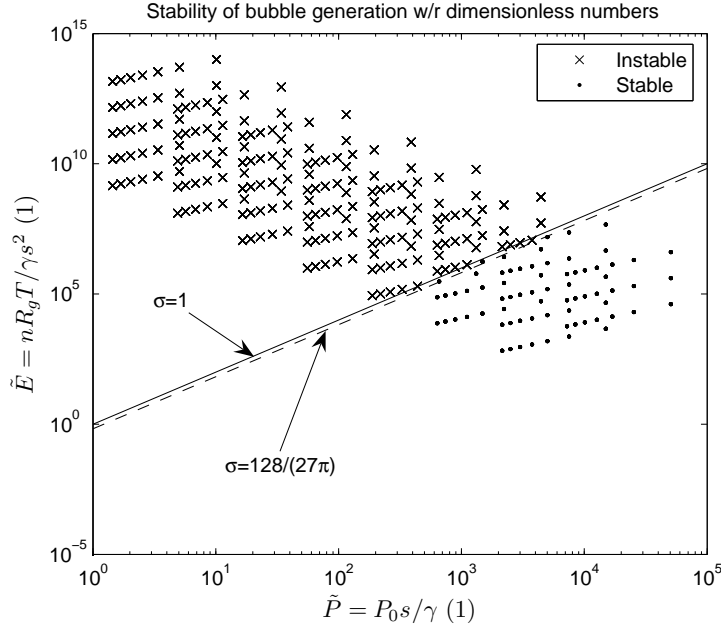


Figure 4.2.12: Illustration of the analytical threshold between stable and unstable configurations. The error from numerical approximation obviously comes from the software instability detection, which considers stable an unstable configuration close to the limit

The outlet channel is a MDP-190-0 in vitro fertilization micropipette (Denuding micropipette), made of borosilicate glass. They have a nominal inner diameter of 190 μm .

The shape of the bubble is recorded with a magnifying optic mounted on a camera. The recorded images are analyzed on a computer with an own made Matlab code. The height of the bubble can therefore be correlated to the setup parameters and the position of the piston in the syringe.

A pressure sensor (*PMP-1400* from *Druck - GE*) has also been included later on the system, to correlate the curvature of the bubble to the pressure drop across its interface. The connection of the sensor to the rest of the system is presented in Fig. 4.3.2. The signal of the pressure transducer has been digitalised using a National Instrument USB acquisition system, with a sampling rate of 1kHz. Then it has been filtered using a moving average on 25 samples.

Setup Issues

The building and use of the test bed faced several issues that deserve some explanations.

Pressure Sensor The pressure sensor measures gauge pressure and has a range of 10^5Pa . It is designed to work with any fluid non corrosive to stainless steel. Special care has to be taken because there is a quite large dead volume in the sensing area of the sensor.

To reduce this volume, we tried to fill a large volume of the gas circuit with an incompressible fluid (water). However, this method was not accurate, since there is no mean to drain gas bubble out of the pressure sensor chamber. Moreover, surface tension effect at the interfaces of bubbles inside the gas circuit could modify the behavior of the system.

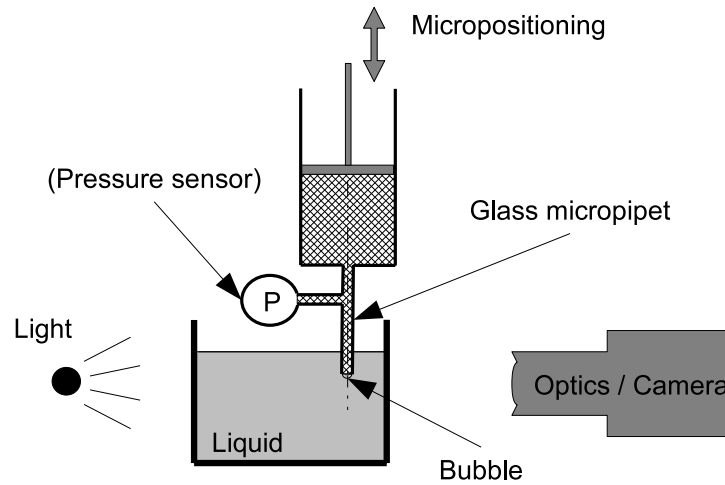


Figure 4.3.1: Schematic representation of the first experimental setup for the validation of the volume controlled bubble generation model

Vision System The vision system is used to determine the shape of the bubble. We measure the bubble height and its curvature to estimate pressure inside the bubble. The calibration of the image, i.e. the corresponding between real length and pixels, is done using *Newport* micropositioning stages. The syringe is mounted on a set of three orthogonal micropositioning stages. One is used to focus the image (axis in the direction of the vision system). The two others allow to center the image. The calibration is done using these latter axes: the image contains a mark which is moved along the two directions from one edge of the image to the other, and the displacement is measured on the micropositioning axes. Using a vision system to look at a microsystem in a liquid is not easy, because of multiple reflections that could occur in the liquid (larger refraction index than air). The best image is obtained when the pipette is close to the wall near the objective of the camera, so that the optic path between the object and the camera is as short as possible in the liquid. However, the automation of shape recognition is difficult because of these reflections (for example, the top of the bubble is in some case dark when the bubble is small, and white when it is large).

Light Source The light is essential to have a well contrasted image. The best results were obtained using a diasopic lighting, i.e. the light source is located in the back of the object, and is transmitted through the object plane to the camera. It is important to have a light source powerful enough to deal with the magnification of the optics. The smaller the object, the more light density is needed. But it is also important to have a light source that does not give off heat that could affect the bubble growth. A classical incandescent bulb gave off too much heat, and a LED backlight was not powerful enough. The best result was reached using an optical fiber with a source using a 150W quartz bulb. Since the viewing field is small, a simple 1/8" gooseneck fiber fulfills our needs. In these conditions, the water appears white in the image, and the gas is dark.

Fluidic System As outlet channel, we have used *MDP-190-0* micropipettes. These pipettes should have a nominal inner diameter of 190 μm . However, when we measured the diameter with our calibrated vision system, it appears the diameter is only about 150 μm (measurement: $s = 155 \pm 3 \mu\text{m}$). Only the measured value is used to compare the experimental results with the model. Examples of this pipette can be seen in Fig. 4.3.2 and Fig. 4.3.3.

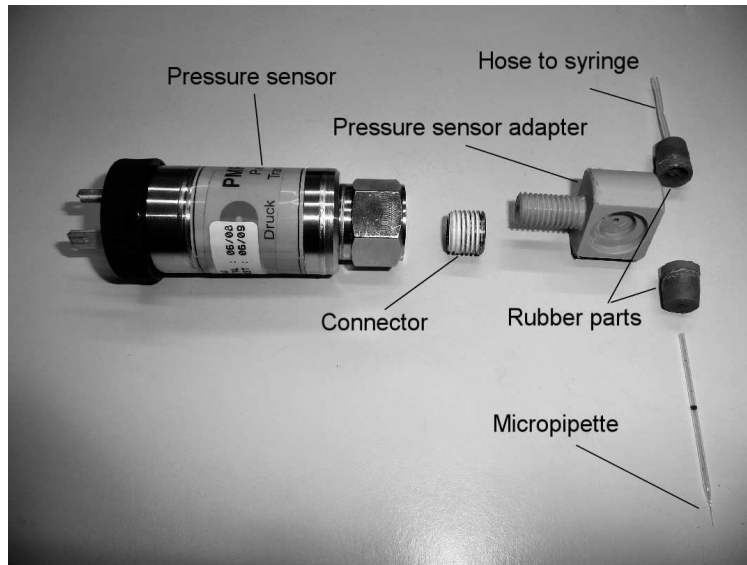


Figure 4.3.2: View of the connection to the pressure sensor. This connection actually increases considerably the dead volume, mainly because of the rubber parts ensuring leak tightness with the micropipette and the flexible hose to the syringe, and because of the dead volume in the sensor itself

The micropipettes were cleaned in absolute ethanol in an ultrasonic bath for one minute before use.

One should care that the gas system is efficiently leak tight. Indeed, the volumes of gas may be small and the system will be sensitive to a variation of the number of gas molecules.

Contamination of the liquid may induce problems of two types. First, it may alter the surface tension properties. Second, any deposition of particles could jam up the gas channel.

Special care should be taken to avoid liquid contamination. In these experiments, the liquid was changed frequently to keep it as clean as possible.

Image Analysis Software We developed a Matlab code to analyse the shape of the bubble generated. More specifically, the code outputs the height of the bubble, to be compared to the model.

The user indicates manually the both contact points of the bubble with the tip of the pipette (left and right), and a third point at the liquid-gas interface. The software finds the circle through the three points, and uses the first two points as the base of the bubble. The height is deduced from the radius of the circle and the distance between the two base points. In some cases, the contrast of the image was good enough to automatically detect the edge of the bubble, making possible the automatic detection of bubble apex. In that case, the first two points only are needed, and the bubble height is measured directly from the distance between the apex and the basis. Figure 4.3.3 illustrates a result.

Synchronizations Images are recorded on a computer. The displacement of the piston is done manually. The synchronization of the displacement with the image is done by moving the piston for a constant value ($50\mu\text{m}$) at a constant frequency which is low enough to assume a static equilibrium of the bubble (typically 1 displacement every 5s). The synchronization of

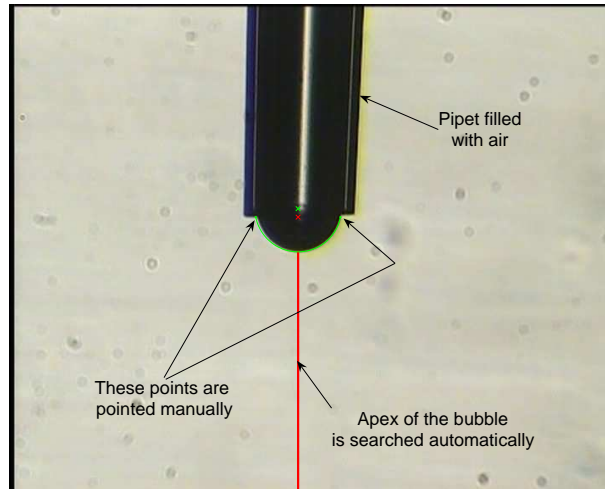


Figure 4.3.3: Illustration of the image analysis software. The bubble grows at the end of the glass pipet. The user has to click on the two ends of the bubble basis. In some case, the contrast is good enough to detect the apex of the bubble automatically. Otherwise, the user selects a third point of the bubble

pressure transducer signal with the image analysis has been done using the instability of the bubble. When the instability point is reached, the bubble explodes and lifts off, leaving the outlet channel with an interface having a different curvature (Fig. 4.3.4). Hence, the pressure across the interface changes suddenly when the bubble lifts off, allowing to synchronize the movie with the pressure measurement.

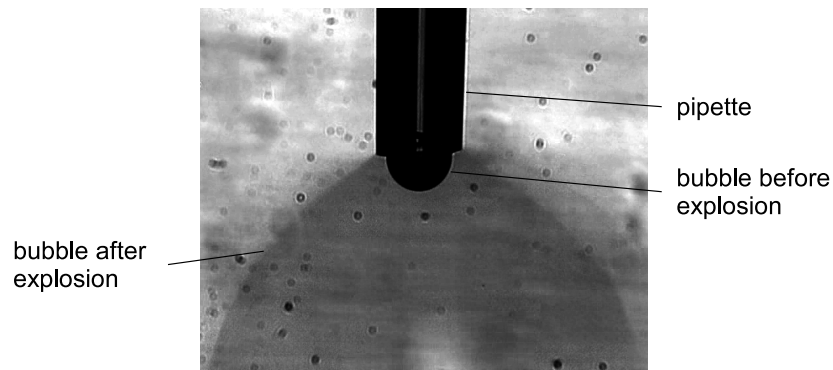


Figure 4.3.4: View of a bubble growth instability. The video frame recorded the image of bubble before and after exploding

First Setup Results

These experiments were performed with water as liquid and air as gas. We made two different sets of measurement, according to the type of syringe used. For the first set, we used the small syringe (*Exmire MS-X05*). For the second set, the large syringe (*Narishige ITO*) was

Table 4.3.1: Sets of parameters for experiments made on the first test bed

Parameters	Set 1	Set 2
V_0	$47.6 \cdot 10^{-9} \text{ m}^3$ (estimation including connections)	$809 \cdot 10^{-9} \text{ m}^3$ (estimation including connections)
S	$9.62 \cdot 10^{-8} \text{ m}^2$	$1.96 \cdot 10^{-5} \text{ m}^2$
s	$150 \cdot 10^{-6} \text{ m}$	$150 \cdot 10^{-6} \text{ m}$
σ	$1.49 \cdot 10^{-2}$	$1.28 \cdot 10^{-3}$

used together with the pressure sensor, which makes the evaluation of the volume in the syringe less accurate due to the dead volume in the pressure sensor.

The parameters for both experimental setups are summarized in table 4.3.1. The difference is essentially the initial volume V_0 and the section of the piston S , which induce a variation of the sensitivity of ΔV to the resolution of the positioning stage. The other parameters are: $P_0 = 101325 \text{ Pa}$ (not measured), $\gamma = 72 \cdot 10^{-3} \text{ Nm}^{-1}$, and the temperature which varied between 298 K and 308 K (for theoretical curve, we used 298 K). The dimensionless number σ is also indicated in the table, and shows that these experiments should lead to unstable bubble growth.

In Fig. 4.3.5 we have plotted the results of the first set of experiments, in dimensionless form. The experiment has been performed twice. The shape of the theoretical model shows good adequacy to the experimentation points, except that there seems to be an offset. This offset can be easily explained. The point at which we start the experimentation ($\Delta V = 0$) should correspond to a flat bubble ($h = 0$). But it is very difficult during the experiment to determine the exact zero height. An horizontal offset is henceforth acceptable.

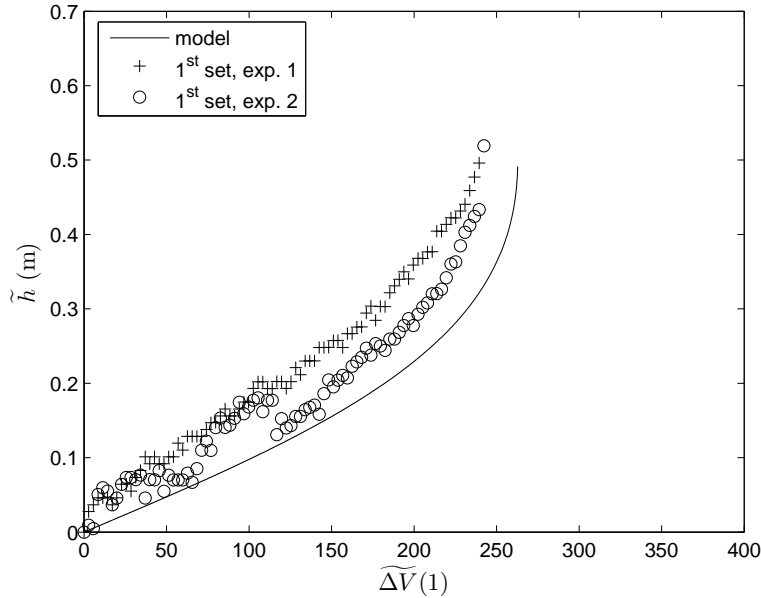


Figure 4.3.5: Experimental validation of the volume controlled bubble generator, first setup, first set of parameters. The model fits well the experimentation points, except an horizontal offset whose origin is due to the manipulation

In Fig. 4.3.6, we have plotted the results of the second set of experiments (first setup), in dimensionless form. The experiment has also been performed twice. In this setup, the pressure sensor has been included. We generated several bubbles successively. When the bubble expands due to instability, another bubble starts to grow.

To correct the offset error, we made a least squares research so that the model fits best the experimental points. We see that the model fits indeed well the experimentation points. The bubbles generated after the first one have similar behavior, but the results are not exactly the same. This is due to the variation of the parameters in the system, since some gas has been released.

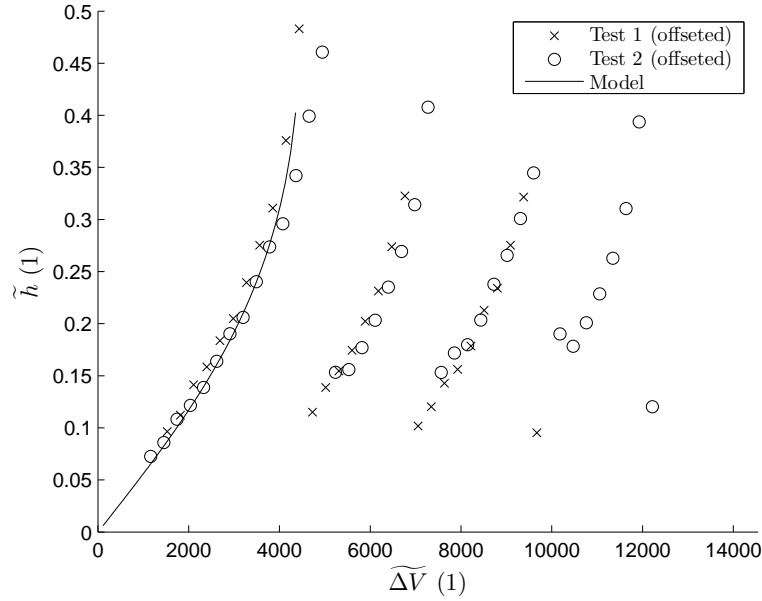


Figure 4.3.6: Experimental validation of the volume controlled bubble generator, first setup, second set of parameters. For each of the two repetitions, we regenerated other bubbles after each release due to the instability. The model fits well the experimentation points

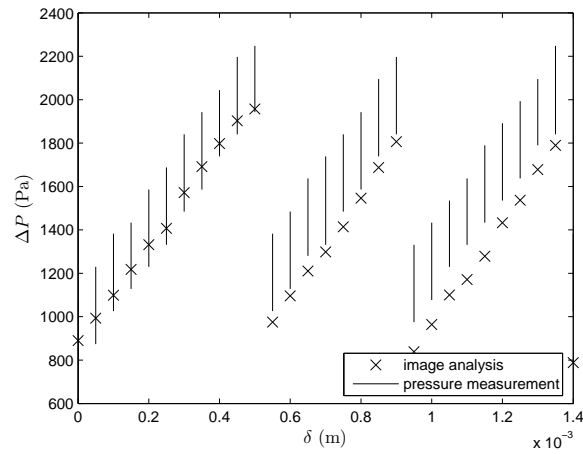
Another result of this experimental setup is the pressure measurement. The results are shown in Fig. 4.3.7 for the two experimentations. The pressure sensor was chosen to be used with smaller output channels as well. In this experimental setup, and because of technological limitations, we used only the large pipettes, and the pressure will rise only to around 2000Pa, which is 2% of the full scale range of the sensor. The signal was rather noisy. To filter it, we first made a moving average on 25 samples. Then we searched for the minimal and the maximal value on a 0.5s time interval around the moment corresponding to the captured video frame.

The vertical bars represent the range of pressure value in this time interval of 0.5s. The crosses represent the pressure deduced from image analysis, using Laplace equation (4.2.2). Pressure sensor measurements and image analysis measurements show good agreement for the first step of the experimentations.

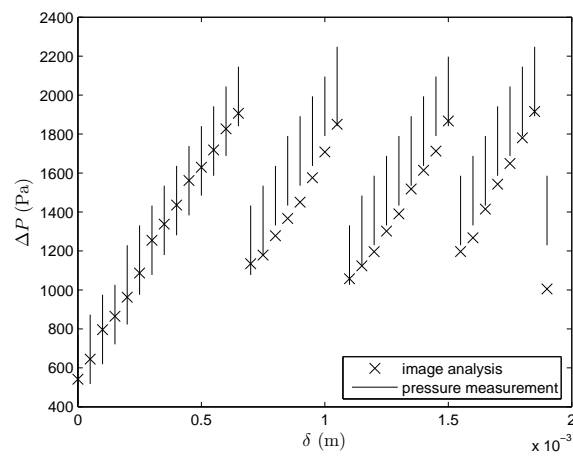
We observe however that results from the pressure sensor tend to be larger than the results from image analysis for the next steps of the experimentations. Since the correspondence between both measurements relies only on Laplace equation there could be four explanations for this deviation. A modification of surface tension is possible, but the contamination of

the liquid should lead to a lower value, which is the contrary of the measurement. Another explanation concerns an error in geometry measurement, such as image calibration error. But it should occur for every measurement, including the first one. Thirdly we have considered that the pressure measurement is not localized at the same place than the image measurement. Indeed the pressure sensor is connected to the gas system a few centimeters above the micropipette tip. Between these two locations, any free surface due to liquid or gas inclusion could modify the pressure. However in this case there is no reason why this problem should evolve during the experiment. Therefore the most likely explanation is a drift of the pressure sensor.

We can conclude that using an adequate pressure sensor, it is possible to measure the pressure, and henceforth the height of the bubble, from a distant location.



(a)



(b)

Figure 4.3.7: Comparison of pressure measurement ((a) first repetition, (b) second repetition): crosses represent the pressure deduced from image analysis together with Laplace law, and the vertical lines show the results from pressure sensor measurement. The line stands for the range of value in a time interval around the video frame used for image analysis. The trend to overestimate pressure from pressure sensor measurement is most likely explained by a drift of the sensor, which is in this case used at only 2% of its full scale

4.3.2 Second Experimental Setup

So far we have demonstrated the validity of the volume controlled bubble generator, but only in situations where an instability during the bubble growth occurs (i.e. $\sigma < 1$). In this case, we will demonstrate the continuous growing of a bubble in case of a small gas container and a larger outlet channel.

The second test bed is based on volume variation, but does not use syringe. It is schematically represented on Fig. 4.3.8. The bubble is generated from a platform made of aluminum which is immersed in the liquid. This platform contains three through holes³ having a diameter of 1.23mm, 1.26mm and 1.25mm for hole 1, 2 and 3 respectively. These holes are each connected to a different flexible hose made of silicone and having an inner diameter of 0.5mm. At the other end, the flexible hoses are connected to a large tank filled partially with liquid (water), partially with gas (air). The tank can be isolated with valves placed on the hoses.

The idea is that the gas container for the bubble generator is the flexible hose. The volume of gas is limited by pushing incompressible fluid from the large tank into the hoses until the gas remaining between the liquid from the tank and the outlet channel on the platform reaches the desired set point.

To vary the volume of the container and therefore push the gas out of the platform to generate bubbles, we only have to compress the hose where it contains liquid. To compress the hoses, we have placed them between a fixed wall and a micropositioning stage.

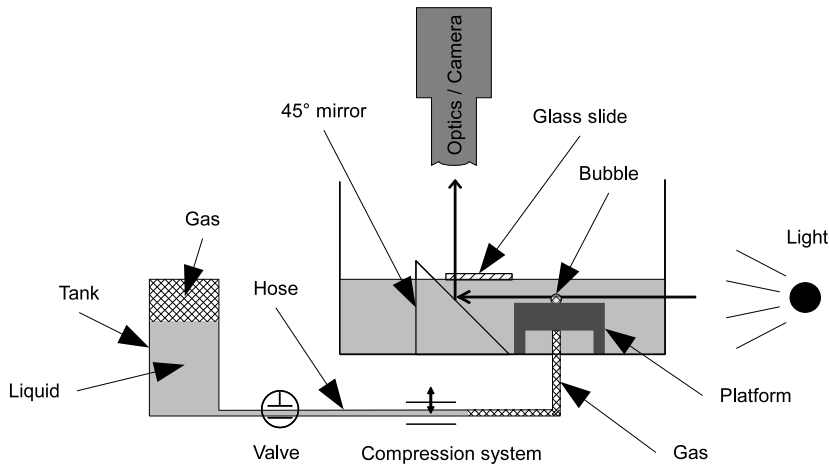


Figure 4.3.8: Schematic view of the second experimental setup used to validate the volume controlled bubble generation model

Setup Issues

The second version of the syringe pump test bed has the advantage that the leakages should be reduced because of the few connections. It has also a rather small volume compared to some syringe, because of the low diameter of the flexible hose. However, it also has some issues, in addition to those of the first test bed.

³Choosing the number of holes in the platform will be justified in Chap. 5.

Because of the actuation system, the allowed volume variations are small. It depends on the contact surface of the compression system. But of course, if we want to increase the volume that can be pushed, the sensitivity regarding the compression system displacement will increase. In our case, the hoses are compressed again the moving stage of a *Newport M-SDS40* micropositioning stage.

The calibration of the system is necessary since the ratio between the hose compression and the volume variation is non linear. Consequently we have monitored the displacement of the micropositioning stage with a *Keyence LC-2440* laser displacement sensor. We have filled the hose with an incompressible fluid (water), and we have captured image of the liquid droplet forming at the outlet channel on the platform. Hence the volume of the drop corresponds to the volume pushed by the compression system. To filter the results, we made a polynomial fitting to find a function giving ΔV with respect to the movement of the micropositioning stage. The correspondence between the table position and the volume pushed, together with the polynomial fittings, is shown in Fig. 4.3.10 for the first hole. The polynomials are degree 6 for first and second hole, and degree 9 for the third hole. Because of the polynomial fitting, there are some ripples in the curves. But these ripples appear when the flexible is completely squeezed (the volume does not increase anymore), which is beyond the range of interest for our experiments.

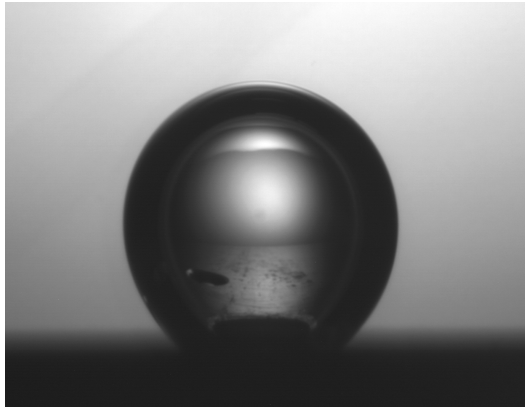


Figure 4.3.9: Stable bubble growth: when the bubble becomes larger than the capillary length, the hypothesis of spherical shape is not valid anymore. The pressure is larger at the bottom, creating the buoyancy force. The real bubble is taller than predicted by the model

A video camera is placed above the system, and a 45° mirror is used to view the bubbling area. This system is interesting if the area of interest is surrounded by other measurements devices, such as an atomic force microscope (this will be detailed in Sect. 5.4). However in that case, the optic path crosses the free surface of the liquid. We have seen experimentally that the images are more clear if we place a thin glass slide floating on the surface of the water, so that the optic path crosses no free liquid-air surface.

Second Setup Results

The experimental parameters of this setup have been summarized in table 4.3.2. The three tests have been performed on the hole 1. The liquid we used is water and the gas is air. The only parameter changing from one experiment to the other is the initial volume. Pressure has been assumed to be $P_0 = 101325\text{Pa}$, temperature to be $T = 298.15\text{K}$, and surface tension

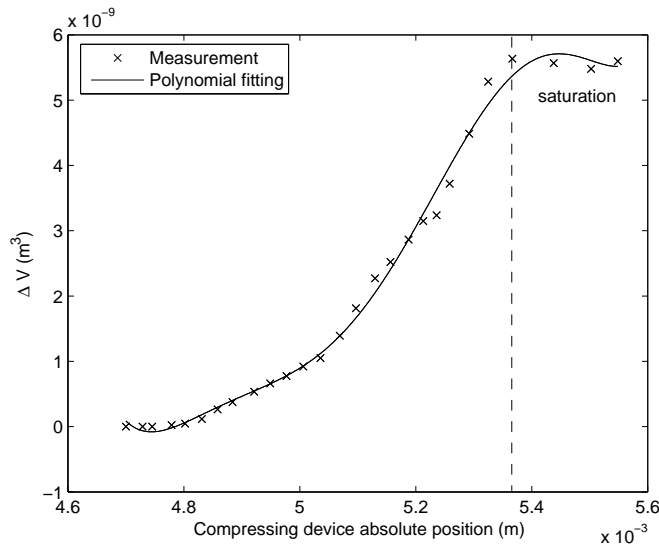


Figure 4.3.10: Calibration of the compression system for volume variation and the polynomial fitting used during experimentations. The ripples are due to the polynomial fitting when the pushed volume does not increase anymore (saturation because the hose is fully squeezed). This is beyond the range of interest for our experiments

Table 4.3.2: Sets of parameters for experiments made on the second test bed

Parameters	Set 1	Set 2	Set 3
V_0	$98.2 \cdot 10^{-9} \text{ m}^3$	$78.5 \cdot 10^{-9} \text{ m}^3$	$58.9 \cdot 10^{-9} \text{ m}^3$
s	$1.23 \cdot 10^{-3} \text{ m}$	$1.23 \cdot 10^{-3} \text{ m}$	$1.23 \cdot 10^{-3} \text{ m}$
σ	32.9	41.2	54.9

to be $\gamma = 72 \cdot 10^{-3} \text{ Nm}^{-1}$.

The results of the three experiments are shown on Fig. 4.3.11. It must be noted that when the bubble reaches a certain height larger around the capillary length, the hypothesis of part spherical shape is not correct anymore. This is why for large values of ΔV , the model underestimates the height of the bubble (Fig. 4.3.9). These reasons explain the deviation of the experimentation points and model for large ΔV values. For small values of ΔV , the bubble is pushed from the hole and is not immediately anchored on the edge of the border. This explains the deviations of the experimentation points and model for small values of ΔV .

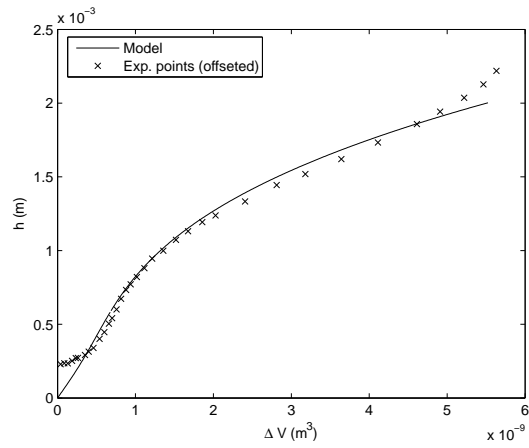
4.3.3 Conclusion of Experimental Validation

The experiments performed on both experimental setups corroborate the model of bubble generation based on volume control, established in Sect. 4.2.3. Besides, we have seen that there exists, as predicted, two cases of bubble growth: one is discontinuous, as seen on the experimentations performed on the first test bed, the second is continuous as seen on the experimentations performed on the second test bed. Figure 4.3.12 shows a summary of two test results, each made on a different experimental setup. The dimensionless number established in Sect. 4.2.6 is useful to predict the continuous or discontinuous growth, based

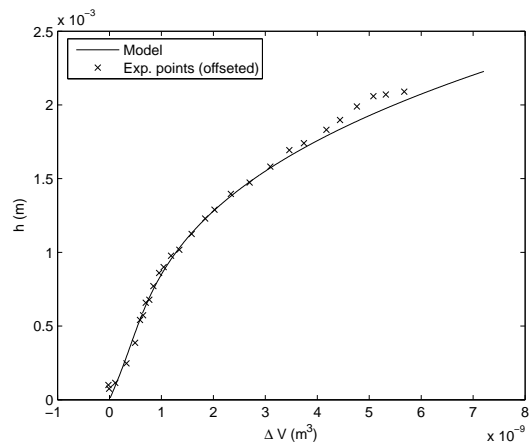
on the parameters of the setup. It shows, for example, that if a bubble of any size must be generated from a small hole, the gas volume must be lower than a value predicted by dimensionless criterion:

$$V_0 < \frac{27 \pi P_0 s^4}{128 \gamma} \quad (4.3.1)$$

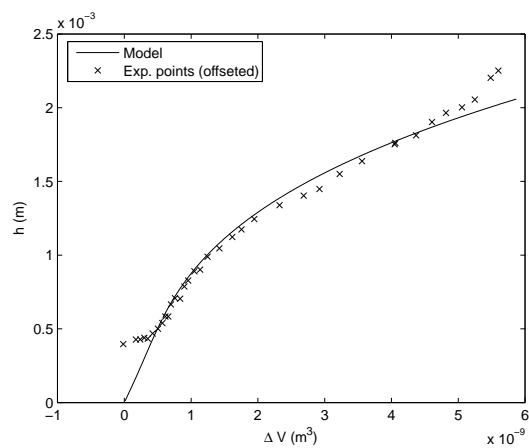
We have also demonstrated that the pressure measurement is a good indicator of the bubble shape. This could allow to avoid the use of expensive and bulky image acquisition system. Besides, the pressure measurement can be localized anywhere in the gas system. This could be an advantage if for example the space around the bubble is restricted.



(a) Experimentation set 1



(b) Experimentation set 2



(c) Experimentation set 3

Figure 4.3.11: Experimental results on the second test bed. This validates the model for the continuous bubble generation

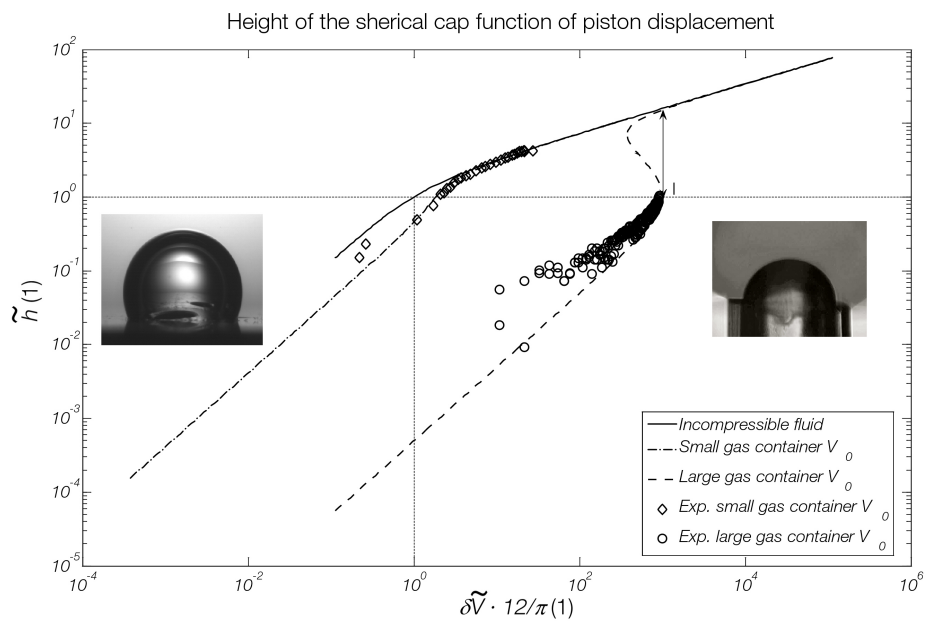


Figure 4.3.12: Summary of experimental validation on both setup, allowing to validate both stable and unstable bubble growth. This figure combines the results of parameters set 1 in table 4.3.1 and parameters set 2 in table 4.3.2. The results have been plotted in a dimensionless form

4.4 Examples of Application

In this section, we present two examples of useful application of micro-gas bubbles. First, we propose to use a bubble as a pressure sensor. Second, we propose to use a bubble as a compliant actuator.

4.4.1 Pressure Sensor

We have seen, in the description of the pressure controlled bubble generator (Fig. 4.1.4) that the height of a bubble could be very sensitive if the diameter of the outlet channel is large. But on the other hand, a large diameter means that the maximal pressure is low. The reason is based, once again, on Laplace equation (4.2.4). We propose to design a gauge pressure sensor that converts the pressure to a certain height.

In this example, we will always suppose that the gas is air and the liquid is water, so the surface tension is $\gamma = 72 \cdot 10^{-3} \text{Nm}^{-1}$. To design a gauge pressure sensor, we can start from the maximal pressure to measure. Assuming the shape of the bubble to be a portion of a sphere, and since the maximal pressure is reached when the height of the bubble is equal to the radius of the outlet channel (half sphere, $h = s/2$), the size of the outlet channel is given from (4.2.4):

$$s_{max} = \frac{4\gamma}{\Delta P_{max}} \quad (4.4.1)$$

From this relation, we see that the maximum pressure range decreases if the diameter of the hole increases. Since the diameter hole should not be too close to capillary length to avoid gravity effects to be predominant, there is a minimal value for the pressure range. If we consider the maximal diameter to be 2.5 mm, the minimal pressure range is 115 Pa. If the pressure applied on a system with $s = s_{max}$ is larger than ΔP_{max} , the bubble will grow indefinitely until it lifts off, and some gas will be lost from the system.

Equation (4.1.3) gives the height of the bubble with respect to pressure and channel diameter. Results of pressure to height conversion for 3 different values of channel diameter s are shown in Fig. 4.4.1. If for example we need a pressure sensor to read pressure up to 200 Pa, we could use any outlet channel size up to 1.44 mm. Any diameter smaller than that will support a pressure of 200 Pa, but it is clear from this figure that the height variation will be lower if the diameter is smaller.

The height of the bubble could be measured by either a vision system, either a laser beam using bubble interface as a reflection surface. We show in Fig. 4.4.2 the schematic diagram of the bubble based pressure sensor using a laser beam to measure the height. The laser beam is emitted vertically down to bubble surface, at a distance ρs of bubble axis. If an horizontal beam sensor is placed horizontally at a distance d of the bubble base, a variation of bubble height h will induce a variation of the beam impact point on the sensor. If p is the distance between bubble axis and the impact point, it is possible to find the following relation:

$$p = \tan(2\theta) (d - h + \tan(\theta/2) \rho s) \quad (4.4.2)$$

where:

$$\theta = \arcsin \left(\frac{\rho s}{\frac{s^2}{8h} + \frac{h}{2}} \right) \quad (4.4.3)$$

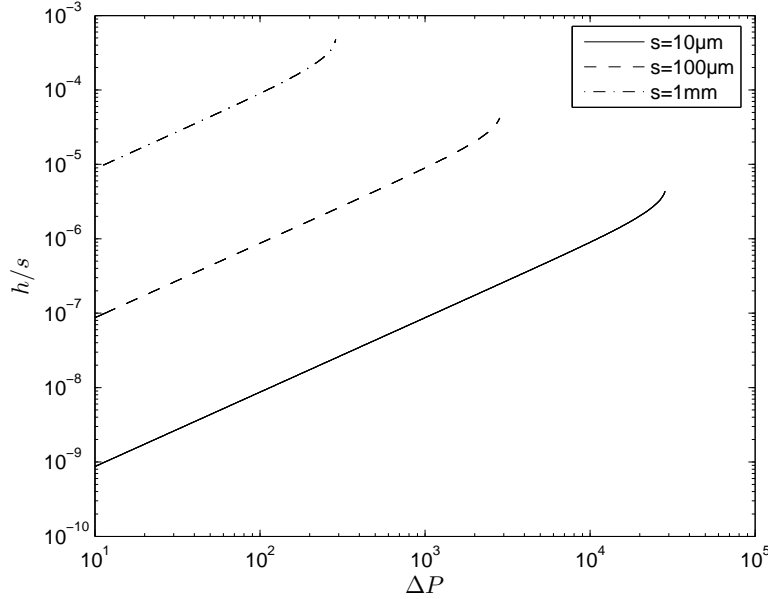


Figure 4.4.1: Evolution of the height (h) of an air bubble in water with respect to the pressure variation (ΔP) and the outlet channel diameter (s)

Figure 4.4.3 shows an example of the relation between beam displacement p and pressure to measure ΔP for an outlet diameter $s = 1\text{mm}$. The beam sensor is supposed to be at $d = 1\text{cm}$ of bubble base.

Such a sensor shows good theoretical linearity and should be easy to include in a microfluidic circuit. It could be used together with the volume controlled bubble generator to monitor the shape of the generated bubble as described in Sect. 4.3. However, there is a limitation for systems with multiple outlet channels due to surface tension. Indeed, if the system has two outlet channels with different diameters, the bubble from the largest channel will always be larger. Indeed, the pressure in the gas circuit is uniform, meaning the radius of the bubbles must be the same. If the configuration allows bubbles to grow continuously, the bubble from the small channel will shrink beyond the half sphere configuration, while the bubble from the large channel will continue to grow. Henceforth, the channel used as pressure sensor should not be larger than the main channel. This issue is illustrated in Fig. 4.4.4.

4.4.2 Bubble as Compliant Actuator

A second example is the main reason of the developments presented in this chapter: using a bubble as a compliant actuator.

We have seen that a bubble is able to generate a force that could be used to move or at least support immersed objects. Besides, a bubble is intrinsically compliant since it is made of compressible gas and since its borders are able to change their shape. This idea will lead us to the developments presented in Chap. 5, where we propose a mechanical characterization of a bubble caught between two solids in term of force and stiffness.

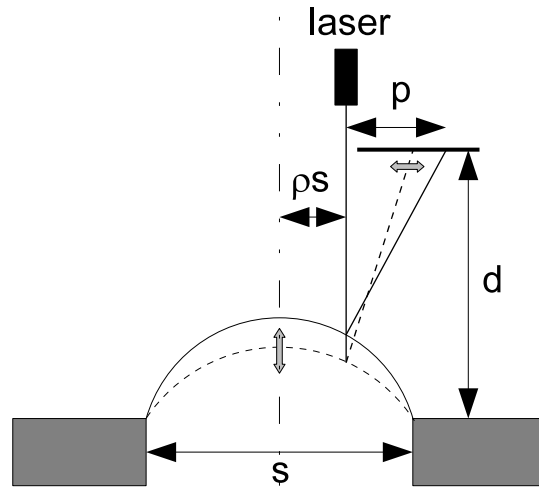


Figure 4.4.2: Schematic view of a bubble based pressure sensor using a laser beam to measure the height variation of the bubble induced by a pressure change

4.5 Conclusions

We have seen in this chapter that gas microbubbles in immersed environment induce effects that are not negligible at microscale. Therefore, we suggest that it could be interesting to make use of these bubbles. To achieve this, it is necessary to be able to generate these bubbles in a controlled way. We have reviewed some bubble generation principles and we concluded that the most adequate is a volume controlled bubble generator. We developed a mathematical model of this generator and showed that surface tension and gas compressibility could lead to an unstable bubble growth. A dimensionless study of this model allowed us to find a criterion based on setup parameters that predicts the existence of the instability. This model has been validated experimentally on two different setups. Finally, we presented some examples of bubble based applications in microsystems.

In order to be used in microrobotic application, microbubbles must be characterized mechanically. The idea of using bubbles as compliant actuator will be developed in the next chapter. Bubbles as pressure sensors will not be developed in this work, and will be part of the perspectives.

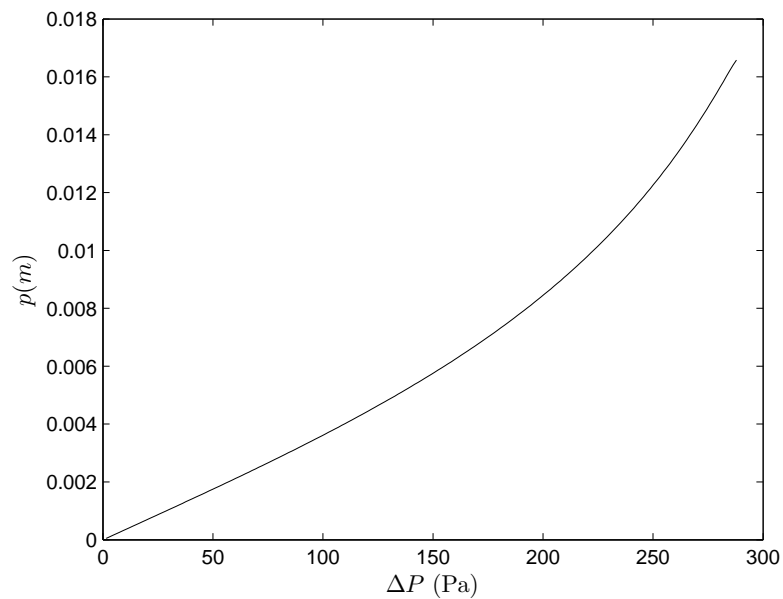


Figure 4.4.3: Illustration of the relation between laser beam displacement and pressure to measure. In this example, the outlet channel has a diameter $s = 1\text{mm}$ and the beam sensor is located at $d = 1\text{cm}$ of bubble base

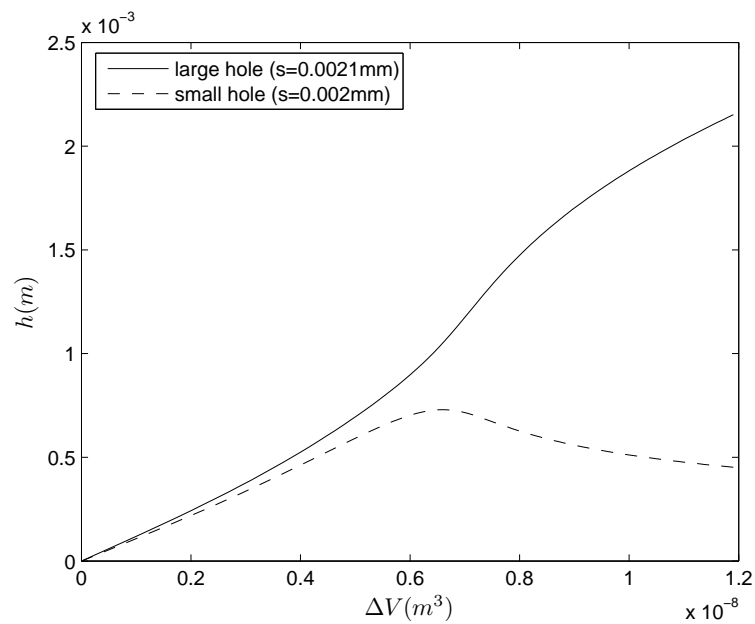


Figure 4.4.4: Illustration of volume controlled generation with two outlet channels having a different diameter. The parameters are those of the first configuration of table 4.2.2. The pressure in the gas circuit being equal, the radius of the bubbles must be the same, making the bubble from the smaller outlet channel smaller. Only the bubble from the large channel continues its growth beyond the half sphere configuration, while the height of the other bubble diminishes

Chapter 5

Compliance of a Gas Bubble

After having presented the interest of micromanipulation in liquid media in Chap. 1 and the different relevant forces acting on immersed micro-objects in Chap. 2, we have focused on surface tension forces. We have detailed surface tension in Chap. 3 and explained that microbubbles could be the root cause of this phenomenon in immersed systems. To study the effects of such bubbles, we have proposed and modeled in Chap. 4 a method to control the generation of a gas bubble in a liquid media, taking account of surface tension effects and gas compressibility, based on a volume controlled generator.

This chapter deals with the study the mechanical stiffness of a bubble. This physical property is a first step towards designing devices making use of bubble properties. In this chapter, we first introduce in Sect. 5.1 the purpose of compliance modeling, then we describe in Sect. 5.2 a prototype using microbubbles. Keeping this prototype as case study, we build in Sect. 5.3 the model of the force exerted by the bubble on the solids with respect to the gap between them. We will then discuss the results of the model, and use this model to size up the prototype of demonstrator making use of bubble properties. Finally, we use in Sect. 5.4 a manufactured prototype of the demonstrator device to validate the model. Based on all these considerations, we finally propose improvements of the prototype in Sect. 5.5, and present the conclusions in Sect. 5.6

The next chapter will present the perspectives of this work and the conclusions.

5.1 Modeling the Compliance of a Gas Bubble

In this chapter, we will consider the case of a bubble caught between two solid surfaces. We will develop a model linking the properties of the bubble (number of gas mole n , geometry of its borders) and the distance between both solids (called the gap, u) to the force generated by the bubble (Fig. 5.1.1). Compliance is defined as the inverse of mechanical stiffness. This is a first step to understand the complete dynamics of the system.

The model we have developed can be applied to any structure, but as guideline of this chapter, we will study the design of an isostatic structure lying on three bubbles which consists in a compliant table that could be used as a support to perform microrobotic tasks. The model is useful to design this kind of compliant device and also to determine an estimation of the force applied on the structure.

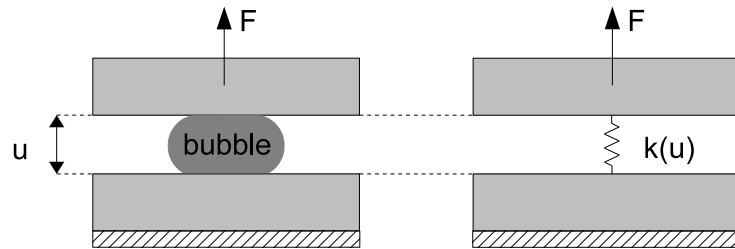


Figure 5.1.1: The purpose of this model is to calculate the force generated by a bubble caught between two solids, with respect to physical and geometrical parameters, notably the gap distance u between both solids. From a mechanical point of view, we search the stiffness of a bubble, as if the bubble was replaced by a non linear spring

5.2 Description of the Prototype

This chapter illustrates how to make use of gas bubbles in immersed microsystems, and how to take benefits from their properties. Even if the models presented are valid for any system configuration, we have chosen a specific application to illustrate the models, and to validate them.

The thread of this chapter will be the development of a 6 DOF compliant table that is intended to be used as a support for robotic micro-assembly tasks. Among these 6 DOF, 3 can be actuated. This section describes the prototype of this device.

5.2.1 Application Context

We have already explained the advantages of working in a liquid environment (Sect. 1.3). Additionally, the device we propose is compliant, which is a very important property for micromanipulation applications. Indeed, robotic micromanipulation can be used to manipulate objects in the field of optoelectronics (optical fibers), MEMS components, microelectronic systems packaging, microfluidics (Lab-On-Chip) or biologic cells manipulation. It deals with the manipulation and assembly of components having dimensions that may be within 10^{-6} m to 10^{-3} m range.

An important issue in micromanipulation is that the positioning of the components has to be very accurate, due to the small dimensions. Systems with a few nanometer precision exists [40], but they generally have a limited stroke, even if they are used with mechanical amplifier. Moreover, the manufacturing accuracy of the components may be between 10^{-7} m and $25 \cdot 10^{-6}$ m [79], which is proportionally larger than those of macroworld. Finally, some adhesion forces, that are not controllable, may also interfere with the gripping or placement of the components [16].

The components manipulated are generally made of brittle materials, like silicon or glass, or should not get stressed, like biological cells for example. Henceforth, any relative position error between the component and its assembly site should be avoided. To tackle this problem, one solution is to use compliant structures [16].

A first approach is to use a compliant gripper [21, 59]. But this approach carries some drawbacks. The gripper is generally moving during the assembly operation. If the speed of the gripper is high, it could induce vibrations that could hinder the correct positioning of the component. Moreover, the structure usually used to increase the compliance is based

on cantilever beams. These could also suffer from buckling when gripping the object, which would then lead to its loss or at least modify its position.

We suggest that the compliance should be present in the table carrying the system being assembled. This idea is also presented by Clévy [16]. He proposes a compliant table supported by three mechanical springs (Fig. 5.2.1). With this configuration, the table shows a vertical stiffness of 6.7 N m^{-1} , and the global assembly system is improved.

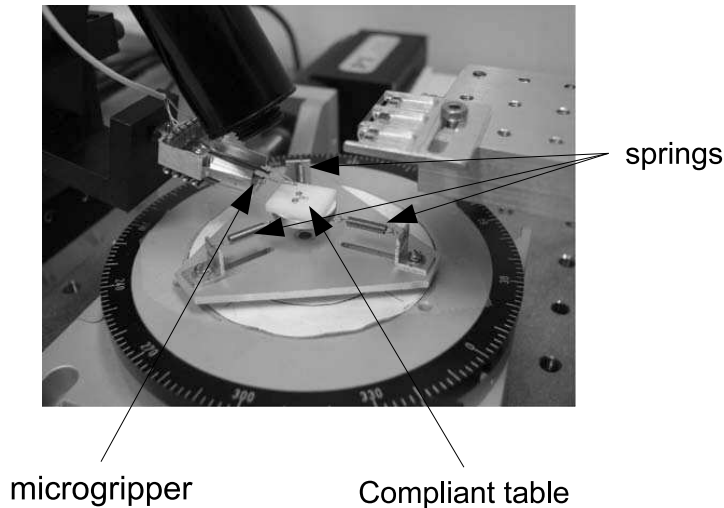


Figure 5.2.1: Illustration of the spring hold compliant table proposed by Clévy, used to perform microassembly tasks (Source [16]). The springs have a free length of 12mm and a stiffness of 54 N m^{-1} , and the table is made of aluminum and has a diameter of 15 mm

A common benchmark to test the efficiency of an assembly system is the "peg in hole" test. It consists in performing the tasks of inserting a pin in a bore. This operation requires a good alignment of the pin before insertion. Since parasitic forces may change the relative position of the object and the gripper, this alignment is difficult to achieve. But using a compliant table, the alignment errors are somehow corrected by the movement of the table itself. This is illustrated in Fig.5.2.2. This demonstrates the usefulness of compliant tables for microassembly tasks.

Hu [40] proposed another design of 6DOF compliant table. His design is based on flexible hinge structures, actuated by piezoelectric elements. Hu does not give information about the stiffness of the table, but since the compliant elements are connected to the piezoelectric actuators, it is probably relatively large.

Other structures that are often used in microsystems are orthoplanar springs, also called spiders. The stiffness of structures such as the one represented in Fig. 5.2.3 is given by [38] (for one arm):

$$k = \frac{b h^3 E}{L^3} \quad (5.2.1)$$

where b is the width of one arm, h is the thickness of one arm, L is the length of one arm and E is the Young modulus. For example, with $h = 0.25 \cdot 10^{-3} \text{ m}$, $b = 0.75 \cdot 10^{-3} \text{ m}$, $L = 15 \cdot 10^{-3} \text{ m}$ and $E = 190 \cdot 10^9 \text{ Pa}$, the stiffness of the entire spring having 3 supports with 2 arms, is given by:

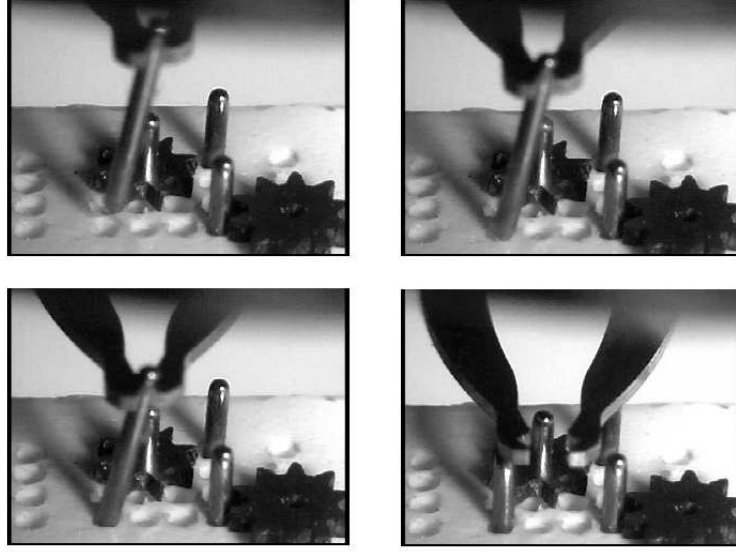


Figure 5.2.2: Illustration of the efficiency of a compliant table during the "peg in hole" benchmark test. The alignment errors between pin and bore are absorbed by the movement of the table (Images captured from a video from C. Clévy [16])

$$k = 3 \frac{b h^3 E}{2 L^3} \approx 990 \text{ N m}^{-1} \quad (5.2.2)$$

Orthoplanar springs and conventional helical springs have in common that to have a low stiffness, they have to be either large or fragile. It is moreover difficult to actuate them directly. Bubbles can assess these issues, as it will be demonstrated by our model in Sect. 5.3.

5.2.2 Design of the Prototype

The device we propose is based on a mobile solid, called the table, supported by three bubbles. These bubbles are generated from a second solid, called the platform. Three holes are therefore made on the top plane of the platform, which are connected through flexible hoses to a gas container. The volume of this gas container can be adjusted to change the height of the bubble. The device is illustrated in Fig. 5.2.4.

Bubbles are anchored to both table and platform thanks to a sharp edge which produces a geometric anchoring (Sect. 3.1.2). In the platform, the anchoring is realized by the gas circuit outlet holes. In the table, the anchoring is realized by holes too. We will consider two configurations: blind holes and through holes. Through holes are supposed to be easier to manufacture with microfabrication technologies such as DRIE, since only a circle has to be etched (like a core drilling), while with blind holes the entire disk must be etched.

The prototype has been realized in aluminum. To reduce the weight of the table, it has been shaped like a clover. Because the table should be as small as possible in order to avoid its own weight to be too large compared to bubble force, and because of the dimension of commercially available flexible hose to make the connection to the gas circuit, we have chosen the anchoring circle diameter in the platform to be $s_1 = 10^{-3}$ m, and in the table

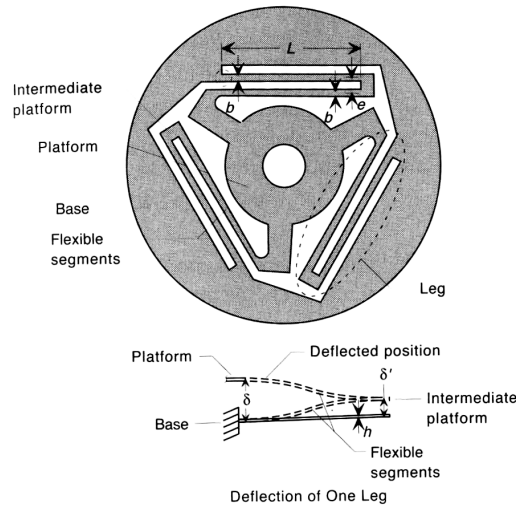


Figure 5.2.3: Illustration of an orthoplanar spring (Source [38]). The deflection of the beams supporting the table provides the compliance of the table

$s_2 = 800 \cdot 10^{-6}$ m, with centers of circles being on the vertices of an equilateral triangle, at 2.5 mm from each other.

The connections between the platform and the gas tank are made with silicone flexible hoses. The outlet holes where the bubbles are generated are directly connected to the hoses.

The realization of the prototype was made using a CNC milling machine. Four different tables were designed with either through or blind holes, and with improved anchoring circles or with simple anchoring circles. The improved anchoring circle consists in making a circular groove around the hole. The inner circle of the groove constitutes the anchoring circle. Because of the vertical side, the contact angle is theoretically 90° larger than for the configuration without groove (Fig. 5.2.5). The profile must therefore bend more before the bubble can escape.

The different versions are illustrated in Fig. 5.2.6, and an actual view of two tables is illustrated in Fig. 5.2.7. However, the milling of the groove in the case of improved anchoring circles could not be achieved with this manufacturing technology, making this version not usable (Fig. 5.2.8). This is only a technological issue, and the results with such anchoring system would provide better results than with the simple anchoring circles. Solutions to tackle this problem will be proposed in Sect. 5.5.

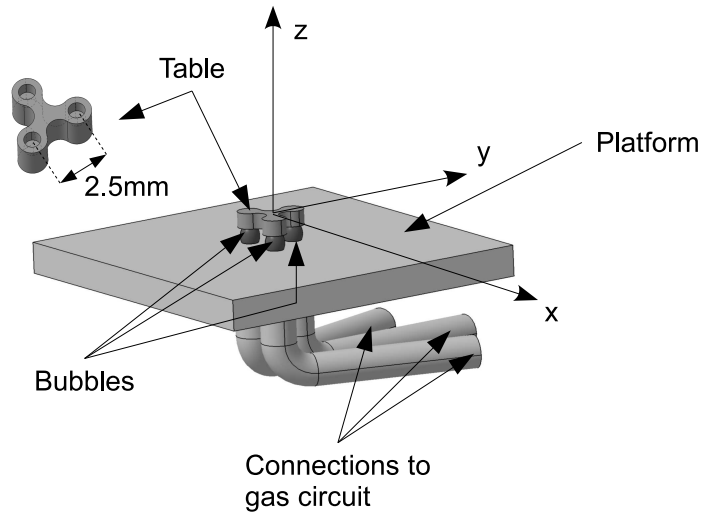


Figure 5.2.4: Schematic view of the bubble supported compliant table

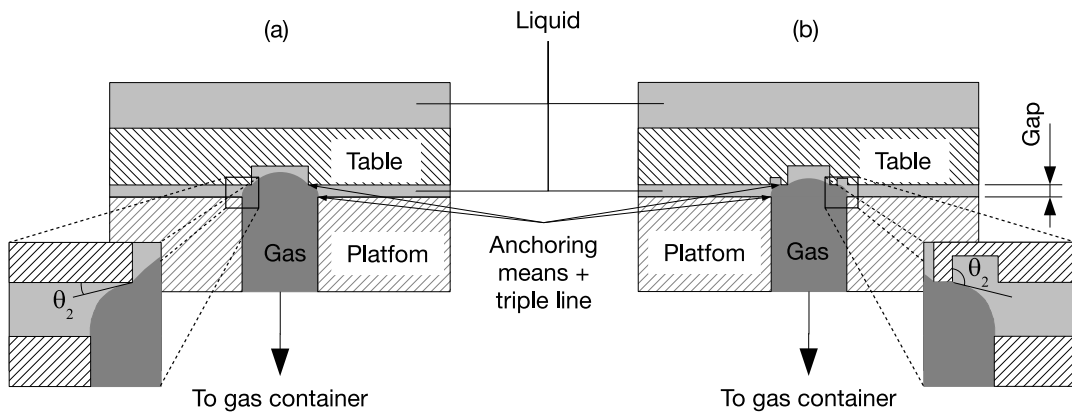


Figure 5.2.5: Illustration of the simple (left) and improved (right) anchoring methods. Both are mechanical method, but the right configuration uses a circular groove forcing the profile to travel an additional 90° compared to the simple configuration before the bubble can escape. The same method could be used on the platform

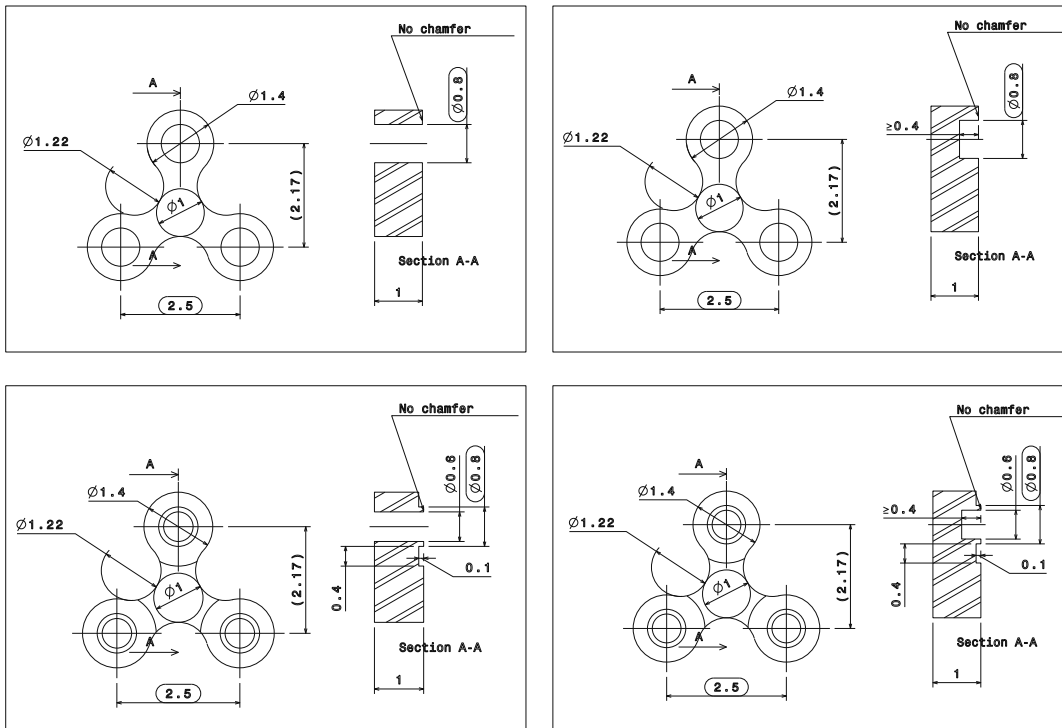


Figure 5.2.6: Dimensions of prototype tables. Four variants have been considered, but due to technological issues, the variant having a groove to improve bubble anchoring was not usable.



Figure 5.2.7: Actual view of two tables

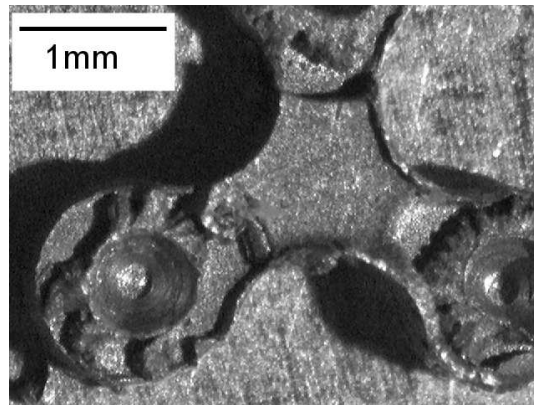


Figure 5.2.8: View of a table with improved anchoring circle manufactured on a CNC milling machine. The result is not usable

5.2.3 Device Advantages

This device has several advantages compared to traditionally used compliant systems such as springs. These advantages are listed below and will be demonstrated with the model developed in Sect. 5.3.

- **Compacity.** For an equivalent stiffness, bubbles are more compact than conventional springs.
- **Strength.** If a small stiffness is required, conventional springs are either large, or use thin wires. These are therefore easy to break, and if they are broken, they need a complete replacement. On the contrary, our system can be easily repaired. Indeed, the main risk is that the bubble escapes its location if the table is pushed too far, or that the bubble leaves the table or splits if the table is pulled too far. But even if this occurs, a new bubble can easily be regenerated if necessary, and the table can be simply laid on the bubble again.
- **Assembly.** Thanks to self-assembly properties of the capillary forces, the assembly of the table on the bubble is very simple and does not require a precision positioning device. If the centers of the anchoring circles on the table overlay with the centers of the anchoring circles on the platform, the assembly of the table will accept some alignment errors. If the bubbles touch the anchoring circles, the system will automatically tend to minimize lateral surfaces, correcting initial positioning error.
- **Actuation.** On the contrary to conventional springs, bubbles are easy to actuate from the volume controlled generator. It is possible to change their height, hence changing the height of the support points and moving the table.
- **Sensing.** It is possible to use the pressure in the bubble to infer the measurement of the force exerted by the bubble.
- **Manufacturing.** The design of the device is simple. Depending on the desired size of the bubbles, it is possible to use conventional means to manufacture the device.
- **Adjustable Stiffness.** As it will be demonstrated in Sect. 5.3, the stiffness of a bubble depends on the total volume of the gas system. It is therefore possible to change the stiffness of a bubble, without changing the geometrical design of the table nor the platform.

The 3 actuated DOF of the compliant table are shown in Fig. 5.2.9. Some of the properties, such as compliance and use as actuator, are illustrated in Fig. 5.2.10.

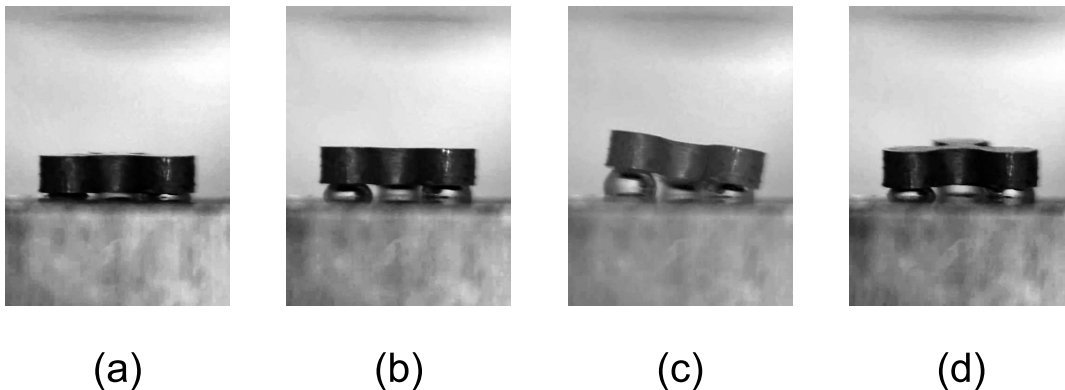


Figure 5.2.9: View of the three actuated DOF: (a) reference position, (b) vertical translation (here $\approx 250 \mu\text{m}$), (c,d) rotations (here $\approx 10^\circ$)

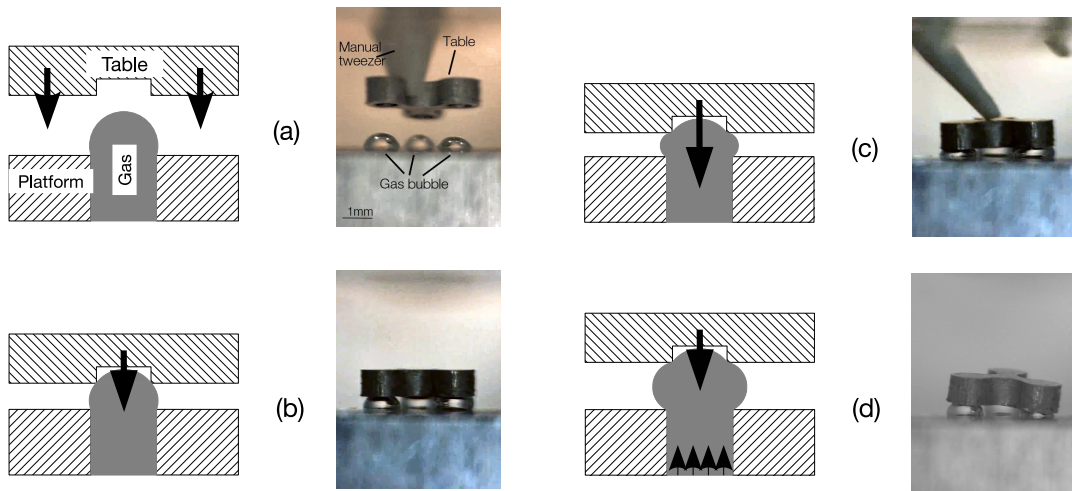


Figure 5.2.10: Illustration of the working principle of the compliant table device. First, the table is put on the bubbles (a). Thanks to self assembly property, the table is automatically centered above the platform. The table exerts a load on the bubbles, changing their shape (the gap decreases, and the mean curvature increases) (b). If a supplementary load is applied (here by pushing slightly on the table with a tweezer), the table moves because the bubbles change their geometry to compensate the new load, giving compliance to the table (c). Finally, if the bubble generator is actuated to increase the size of some bubbles, it is possible to move the table. The bubbles are in this case used as actuators (d)

5.3 Force Generated by a Gas Bubble

In this section, we will develop a model of the force generated by a bubble with respect to several parameters such as the distance between both solid parts u , the pressure outside the bubble P_0 and mole number n , and the boundary of bubble interface. We will then present the application of the model for the design of a compliant table lying on 3 bubbles. We will analyze these results, give some interpretation and infer interesting properties for bubbles.

5.3.1 Hypothesis

We assume that both solids have anchoring means to maintain the bubble.

We also assume that the bubbles have an axisymmetric profile. The anchoring means must therefore manage the triple line to be a circle, on both solids. We state s_1 is the diameter of the triple line circle on the bottom solid, and s_2 is the diameter of the triple line circle on the top solid. The symmetry axis is z , with the unitary vector $\bar{1}_z$ going from the bottom solid towards the top solid (Fig. 5.3.1).

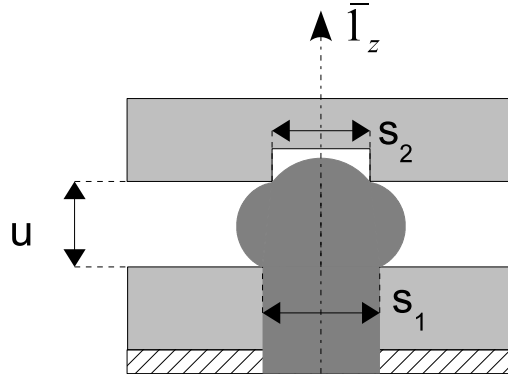


Figure 5.3.1: Geometry of bubble between two solids: view of the anchoring circles (s_1 and s_2), gap (u) and symmetry axes ($\bar{1}_z$)

We also assume that the gap (u) between both solids is smaller than the capillary length. Therefore we suppose that the pressure in the liquid is constant along bubble profile. Moreover, if we suppose there is not fluid displacement inside the bubble (quasi-static situation), the pressure in all the gas circuit may be assumed uniform. From Laplace equation (3.2.3), we assume that the mean curvature of the profile H is the same all along the gap distance.

We consider that the bottom solid is fixed, and the top solid is mobile. The bubble is assumed to be generated from a volume controlled generator, V_0 being the volume of gas in the gas tank, and V being the volume of the bubble.

Finally, let us point out that the originality of this model is that it does not suppose a constant volume, since gases are compressible. Nevertheless we will assume that the amount of gas molecules is constant, i.e. that the number of mole n is constant. This hypothesis was already stated in Chap. 4.

5.3.2 Equations

As already mentioned in Sect. 3.2, the total force exerted by a bubble on two solids, called the capillary force, is the sum of two forces: one arising from the pressure difference between the inner and the outer side of the bubble, and the other arising from the tension in the bubble interface. Figure 5.3.2 shows the free body diagram of the system. Since we suppose the top solid is mobile, we also add his weight and the buoyancy force. The buoyancy force taking the hydrostatic pressure effect in account, we do not represent the pressure field acting on the surface of the solid. We only represent the supplementary pressure on the disk limited by the triple line.

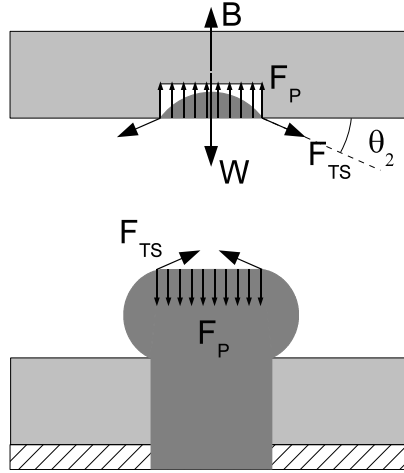


Figure 5.3.2: Free Body Diagram of the table around one bubble. To ease the interpretation, the bubble has been cut in the bottom plane of the table. We have illustrated F_{TS} which is the force component from surface tension, F_P which is the force component from pressure drop, W which is the third of table weight, and B which is the third of buoyancy force

According to the hypothesis, the pressure force is given by (Sect. 3.2.2):

$$\bar{F}_P = -\Delta P \frac{\pi s_2^2}{4} \bar{\mathbf{1}}_z = \frac{-\pi s_2^2 \gamma H}{2} \bar{\mathbf{1}}_z \quad (5.3.1)$$

and the surface tension force is given by (Sect. 3.2.1):

$$\bar{F}_{TS} = \pi s_2 \gamma \sin(\theta_2) \bar{\mathbf{1}}_z \quad (5.3.2)$$

where θ_2 is the contact angle of the profile with the top solid. It is important to notice that the contact angles for both solids can be different. Because we suppose the triple line is anchored, the contact angle is not constant and will depend on the gap u and the mean curvature H .

The capillary force generated by the bubble is the sum of both contributions:

$$\bar{F} = \bar{F}_P + \bar{F}_{TS} = \left(\frac{-\pi s_2^2 \gamma H}{2} + \pi s_2 \gamma \sin(\theta_2) \right) \bar{\mathbf{1}}_z \quad (5.3.3)$$

In the case of a table with through holes, we cannot consider that the pressure contribution is applied on the table. It is therefore possible to consider another free body diagram

(Fig. 5.3.3). We consider that the anchoring circle is submitted to two different surface tension forces: one from the lateral interface, and the other from the top interface, caught in the table hole. However, the surface tension force from the top interface is equal to the pressure force acting on the section of the table hole. This may be seen from the equilibrium of the bubble portion caught in the table hole, and from the demonstration that in the case of a bubble having the shape of a portion of a sphere, the amplitude of the pressure force is equal to the amplitude of the surface tension force (D). Therefore, the formulation of the capillary force in this configuration is exactly the same as for a table with blind holes.

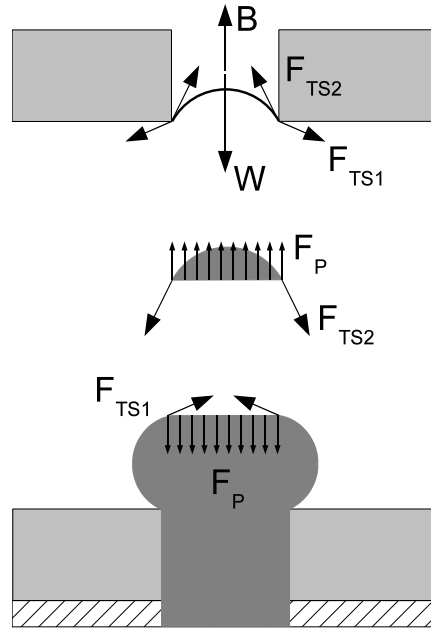


Figure 5.3.3: Free body diagram in the case of through holes. In this case, the table is subjected to two surface tension forces: F_{ST1} from the lateral interface, and F_{ST2} from the top interface. However, the amplitude of F_{ST2} is equal to the pressure force F_P , as illustrate on the free body diagram of the bubble portion caught in the table (in the center in this figure)

Another option is to consider the free body diagram of the following set: the table and the part of bubble caught in the table. In this case the pressure contribution can be considered as acting on the cut plane. The free body diagram is in this case the same as in the configuration with blind holes.

From this equation, we see that the knowledge of γ and of the geometry of bubble interface profile characterizes completely the force. Indeed, the curvature H and the contact angle θ_2 can all be determined if the equation of the profile is known.

We can conclude that to calculate the force, we need to calculate the profile.

5.3.3 Determination of Bubble Profile

In this section, we propose a method to find the profile of the bubble under the constraint to have a specific number of mole. We will first propose a general method based on an ordinary differential equation. The numeric resolution of this ODE may be time consuming, which

may be prohibitive in case the model is used in a control system. Therefore we will also propose in Sect. 5.3.7 an approximation, less accurate but faster to calculate.

In this approach, we consider the system whose inputs are the number of gas mole n and the gap distance u , and whose outputs are the force F and the mean curvature of the profile H (Fig. 5.3.4).

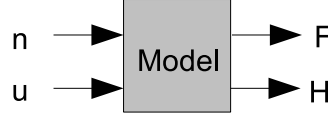


Figure 5.3.4: View of input and output parameters of the model

From the hypothesis of constant H and axisymmetric surface, it can be demonstrated that the equation of the profile in cylindrical coordinates $r(z)$ is given by [52]:

$$\frac{\Delta P}{\gamma} = 2H = -\frac{\frac{\partial^2 r}{\partial z^2}}{\left(1 + \left(\frac{\partial r}{\partial z}\right)^2\right)^{\frac{3}{2}}} + \frac{1}{r \left(1 + \left(\frac{\partial r}{\partial z}\right)^2\right)^{\frac{1}{2}}} \quad (5.3.4)$$

This ODE is a boundary value problem, because of the anchoring of the profile. Hence, if origin of z axis is on the surface of bottom solid, the boundary conditions are:

$$\begin{cases} r(0) = \frac{s_1}{2} \\ r(u) = \frac{s_2}{2} \end{cases} \quad (5.3.5)$$

The method to find bubble profile is shown in Fig. 5.3.5. We define the geometry parameters s_1 , s_2 , u , and we assume a value for H . Equation (5.3.4) is solved using the `BVP4C` function of Matlab library, constrained by boundary values (5.3.5). This function enables to determine the profile $r(z)$. The volume of the gas bubble V is calculated from this profile using a numeric trapezoidal integration method (function `trapz` of Matlab). The number of mole in the system is then calculated considering the total volume of gas, the absolute pressure inside the gas system and the temperature:

$$n = \frac{(P_0 + 2\gamma H)(V_0 + V)}{R_g T} \quad (5.3.6)$$

The calculated mole number n is compared to the set point. The value of H is calculated by a Newton method where we calculate the value of n for 2 values of H : n_a for H_a and n_b for H_b ¹. We make a linear approximation between these points to find H_c corresponding to the set point for n . Then the calculation of the actual n_c value is made with H_c . If n_c is not equal to the n set point within a predefined tolerance, a new iteration is launched between either H_a and H_c or H_b and H_c , depending on which value is closer to the target.

When the profile satisfying the constraints has been found, the force can be easily calculated from (5.3.3). The mean curvature is calculated directly in the algorithm, and the contact angle can be easily calculated from the derivative of the profile:

$$\frac{1}{\tan(\theta_2)} = -\left. \frac{dr}{dz} \right|_{z=u} \quad (5.3.7)$$

¹ H_a and H_b are initially chosen to be $1.0002\times$ and $0.9998\times$ the value of H

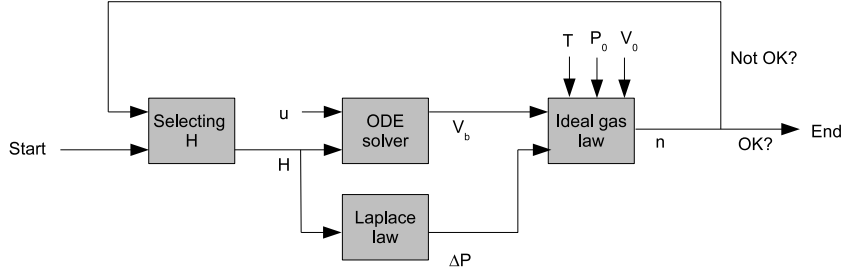


Figure 5.3.5: View of the iterative procedure to calculate bubble profile. First, a value of H is assumed. It is chosen with respect to the value at the previous gap value, or if the gap corresponds to a part-spherical profile, it is calculated from the radius of this profile. Then the ODE is solved, which allows to calculate the volume of the bubble. The pressure inside the bubble is calculated with Laplace law. Then using the ideal gas law, the number of mole is calculated. It is finally compared to the mole number set point. If the calculated n is different from the set point, a new value for H is calculated using a Newton method

The resolution usually requires only 1 or 2 steps to converge to the solution with a relative tolerance on n of 10^{-5} . However, combined with the resolution of the ODE, the determination of one profile can take up to a few seconds, which is prohibitively long if the model is intended for being implemented in a controller.

One solution to this problem is to calculate in advance the results with a certain parameters resolution, and to place it in a look-up table. Another solution is presented in Sect.5.3.7.

5.3.4 Application of the Model

We will use the model proposed above to describe a real situation. Therefore, we will in this section present the situation and the assumptions we make. The device on which we use the model has been introduced in Sect. 5.2. To run the simulations, we have to define the geometry of the anchoring circles, as they constitute the boundary conditions of the ODE. These are given by s_1 and s_2 , the diameters of the anchoring circles on the platform and on the table.

The method used to simulate the behavior of the compliant table is as follow. First three bubbles are generated. We suppose that each bubble has an initial height h_1 . We suppose the total volume in the gas circuit is known, which is equal to the sum of bubble volume and container volume. With initial bubble height and s_1 , it is possible to find the radius R of the bubble which is assimilated to a portion of a sphere. From this radius, the initial pressure $(P_0 + \Delta P_0)$ in the gas circuit can be found (4.2.4), and together with the total volume of gas, the initial number of mole can be found (4.2.1) by:

$$n = \frac{\left(P_0 + \frac{2\gamma}{R}\right) (V_0 + V)}{R_g T} \quad (5.3.8)$$

This number of mole is assumed to be constant.

Then the table is laid on the bubbles. We suppose that when the contact is made, the bubbles are spherical. Because of the diameter of the anchoring holes in the table, the bubble will penetrate inside the table until a contact is established. We assume that the holes are

deep enough to avoid contact of the top of the bubble with the end of the hole. The portion of the bubble inside the table is at that moment a portion of a sphere. We assume that the contact line at the edge of the holes in the table, which is the triple line of the top solid, may be considered as a sealing joint, preventing liquid passing across it.

In the case of blind holes in the table, the liquid caught between the bubble and the end of table hole is trapped. The amount of liquid trapped in table hole being constant, the shape of the bubble portion in the table hole is therefore also constant, no matter the pressure inside the gas circuit. Indeed, the pressure in the liquid trapped in the table hole ($P_0 + \Delta P - \Delta P_0$) is not necessarily the same as the pressure inside the liquid surrounding the bubble.

In the case of a through hole in the table, the liquid above the bubble is in contact with the surrounding liquid through the hole. In this case, the shape of the portion of the bubble inside the table will change in order to have the same mean curvature as the lateral bubble profile. However, its shape remains a portion of a sphere since it is an axisymmetric surface with a constant mean curvature touching the symmetric axis. This is shown in Fig. 5.3.6.

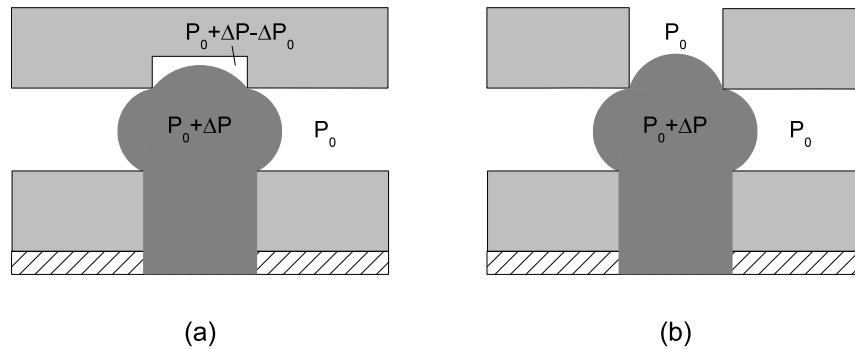


Figure 5.3.6: Pressure repartition. In the case of a table with blind holes (a), the pressure in the liquid in table hole is not equal to pressure outside bubble. In the case of a table with through holes (b), the pressure in the liquid in the table is equal to the pressure outside bubble

To model the force generated by a bubble, we run our model starting from the initial gap and progressively varying the gap distance between the platform and the table.

5.3.5 Limitation of the Model

Some questions arise when considering the presented model.

The first question is to know if a solution to ODE (5.3.4) exists.

In our model, the profile is represented as a function $r(z)$. The numerical resolution of the equation will fail when the derivative of the profile becomes too large, i.e. when the profile becomes parallel to the platform or the table. The question is: is the failure of the resolution due to a bad mathematical formulation, or is there no solution? An element of answer is that there might be no physical solution, for example if the gap becomes too large, the amount of gas in the system may be too small and the gaseous bridge will break up.

On the contrary, when the gap becomes too small, the curvature of the bubble may in some case reach values that induce contact angles in gas phase close to 180° . In this case, as mentioned above, the algorithm generally fails to converge due to a singular Jacobian.

Table 5.3.1: Examples of receding angles (source: [52])

Liquid	Solid	Receding angle	Standard deviation
water	steel	56°	8.3°
water	silicon	33°	4.6°
water	PTFE	98°	3.2°
silicone oil (R47V50)	steel	16°	3.5°
silicone oil (R47V50)	silicon	16°	5.8°
silicone oil (R47V50)	PTFE	47°	3.1°

However, this situation is not physically realistic since the contact angles will generally not exceed a value, which is the receding contact angle of the liquid on the solid. Once the angle reaches this value, the anchoring is not efficient anymore and the bubble will escape the system. The force that a bubble will be able to generate should therefore be limited to corresponding angles below that limit angle. Examples of receding angles are given in Table 5.3.1 [52].

A second question is the uniqueness of the solution. There are two parts to this answer.

First we have to verify if there is only one solution to (5.3.4) for a given H and given boundary conditions. Analytically, the uniqueness of solution for this problem is guaranteed if the solution is a Lipschitz function² [24]. This means that the profile must have a bounded derivative. From a physical point of view, since the contact angles are smaller than 180°, this condition shall be assumed fulfilled.

Second we have to verify that there is one value for H that leads to a solution of the problem under the constraint for constant mole number. Our algorithm is iterative and needs an initial guess. Since we start from a known realistic configuration (a portion of a sphere when the table is posed on the bubbles), we use the shape at the previous gap as initial guess for the current gap. Doing this, we suppose the solution found to be realistic. However this does not guarantee the uniqueness of the found solution. To answer the question, we made a swept for values of H from 50% to 150% of the assumed correct value, instead of searching a correct value by a Newton search which gives only one solution. We found only one solution in this range.

If another solution should exist, its shape would lead to a bubble having a larger revolution surface. This is energetically not favorable, so we consider that the solution found by our algorithm is the only physically realistic solution.

5.3.6 Analysis of the Model

In this section we will analyze the model and deduce some design rules and some interesting properties of bubbles.

Except if otherwise specified, we will always consider the parameters as indicated in Table 5.3.2. The surrounding liquid is supposed to be water.

The weight of a silicon table described in Sect. 5.2 is estimated to be $102 \cdot 10^{-6}$ N. The density of silicon is 2.33. Hence, the total force applied by the table on the three bub-

² $\bar{f} : U \subseteq \mathbb{R}^n \times \mathbb{R}^m \rightarrow \mathbb{R}^p$ is a Lipschitz function at point \bar{y} on U if there is a constant $\Lambda \in \mathbb{R}$ such as $\forall (\bar{x}, \bar{y}), (\bar{x}, \bar{y}^*) \in U : \|\bar{f}(\bar{x}, \bar{y}) - \bar{f}(\bar{x}, \bar{y}^*)\|_p \leq \Lambda \|\bar{y} - \bar{y}^*\|_m$ [24]. This means that Λ is the maximal slope admissible for chords in the planes defined by constant \bar{x}

Table 5.3.2: Recurrent parameters for model analysis

Parameters	Values
P_0 (Pa)	101325
T (K)	293.15
γ (N m^{-1})	$72 \cdot 10^{-3}$
s_1 (m)	10^{-3}
s_2 (m)	$800 \cdot 10^{-6}$
h_1 (m)	$400 \cdot 10^{-6}$

bles is $58.4 \cdot 10^{-6} \text{N}$ if the surrounding liquid is water. If the table is horizontal, the force is equally distributed on all three bubbles. Each bubble must generate a force of approximately $20 \cdot 10^{-6} \text{N}$ to support the table.

Therefore, in the simulation we will focus on two particular points: the first is when the force generated by the bubble is $20 \cdot 10^{-6} \text{N}$ and the second when this force is $40 \cdot 10^{-6} \text{N}$. The first point gives the situation when only the table is posed. The second point supposes an additional force is applied on the table, with an amplitude equal to the effort applied by one table.

For each simulation we will also calculate σ , the dimensionless number found in Chap. 4 to discriminate between stable and unstable bubble growing. This will first indicate if it is possible to grow a bubble of any size, or if there is a limitation on the height of the bubble. Since this number was relevant to see the effects of surface tension and gas compressibility, it is also interesting to see if the output of the model will change according to this number.

We define other parameters. The initial gap u_0 , which is the gap when the table touches the bubbles when laid on the bubbles, i.e. when no force is applied on the bubbles. The initial pressure drop ΔP_0 , which is the pressure drop for the gap u_0 . The stiffness of the bubble is calculate from the partial derivative of the force with respect to the gap: $k = \frac{\partial F}{\partial u}$. The variation of bubble volume (ΔV), which is the variation of the bubble volume without including the volume of gas caught in table hole (V_t). Finally: \bar{V} is the total volume of gas when no table is laid on the bubble, i.e. $\bar{V} = V_0 + V$ in the configuration without table.

We also calculate the contact angles at both end of profile: θ_1 near the platform and θ_2 near the table.

Generalities

The force increases when the gap distance decreases. To explain this evolution, let us have a look at the contribution of surface tension force and pressure force.

When the table comes in contact with the bubble, the shape of the bubble is a portion of a sphere. With this configuration, the surface tension forces exactly counterbalance the pressure force (App. D). When the gap distance decreases, the curvature of the bubble increases. This increases the pressure force. But it also has an effect on the contact angle, which decreases. At the theoretical limit for which the profile becomes tangent to the contact plane ($\theta = 0$), the surface tension force is zero, so the capillary force is equal to the pressure force. This is illustrated in Fig. 5.3.7, for a configuration with $\bar{V} = 10^{-7} \text{m}^3$.

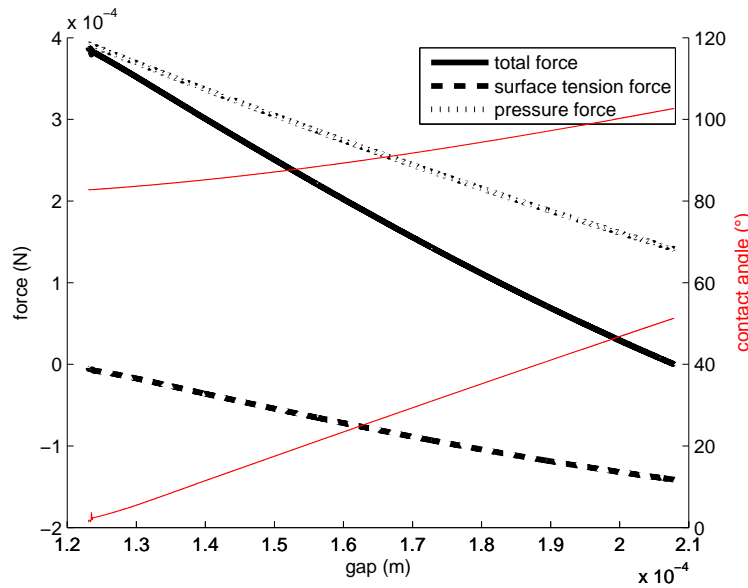


Figure 5.3.7: Evolution of surface tension force and pressure force along symmetry axis (z) with the gap. When the gap decreases, the contact angle on the table decreases and comes close to zero. This means that the surface tension force along symmetry axis decreases, making the total force come close to the pressure force component

Gas Container Size

In this set of simulation, we present results of the model for identical geometries, but for systems having different initial gas volumes.

The different volumes and the main simulation results are summarized in Table. 5.3.3. The plot of the interface shape at one position and the plot of the force with respect to the gap is shown in Fig. 5.3.8. Of course, because each configuration has the same initial geometry (s_1 , s_2 and h_1), the initial gap (u_0) and the initial pressure drop across bubble interface (ΔP_0) are the same for each test. In this table are shown the gap at which the force is effectively generated by the bubble, the stiffness, the variation of bubble volume V (ΔV), the variation of pressure drop and the contact angles.

From these results, it is interesting to notice that the stiffness of a bubble depends on the volume. It is also interesting to notice that bubble volume variation, which conveys the gas compressibility property, is more significant for bubbles generated from large container volume.

The explanation comes from the comparison of the variation of bubble volume with respect to the total volume. If the total volume is small, a decrease of bubble volume will produce a more significant pressure variation than if the total volume is large. Hence if the total volume of gas is small, bubble behavior will be closer to the behavior of a system with constant volume.

When the volume of gas is large, the change in bubble curvature is smaller than when the volume of gas is small. When the force increases on a system with a large volume, the bubble seems to penetrate in the platform channel, while in the case of a small volume, the bubble seems to crush instead of penetrating the channel.

Table 5.3.3: Parameters for the simulations to compare the effect of gas system volume. These tests differ by the volume of gas present initially in the system

Parameters	Test 1	Test 2	Test 3	Test 4
\bar{V} (m ³)	$2.5 \cdot 10^{-9}$	10^{-8}	10^{-7}	10^{-6}
u_0 (m)	$208 \cdot 10^{-6}$	$208 \cdot 10^{-6}$	$208 \cdot 10^{-6}$	$208 \cdot 10^{-6}$
ΔP_0 (Pa)	281	281	281	281
σ (l)	563	141	14.1	1.41
At 20μN				
u (m)	$205 \cdot 10^{-6}$	$202 \cdot 10^{-6}$	$177 \cdot 10^{-6}$	$137 \cdot 10^{-6}$
k (N m ⁻¹)	7.55	3.89	0.673	0.432
ΔV (m ³)	0.49%	1.91%	15.2%	34.7%
θ_1 - θ_2 (°)	100-48	101-48	106-46	115-43
$\Delta(\Delta P)$ (Pa)	28.2	27.8	21.5	5.00
At 40μN				
u (m)	$203 \cdot 10^{-6}$	$197 \cdot 10^{-6}$	$149 \cdot 10^{-6}$	$102 \cdot 10^{-6}$
k (N m ⁻¹)	7.82	3.88	0.774	0.715
ΔV (m ³)	0.97%	3.81%	28.6%	51.7%
θ_1 - θ_2 (°)	98-45	99-45	110-42	125-35
$\Delta(\Delta P)$ (Pa)	55.1	54.8	40.4	7.40

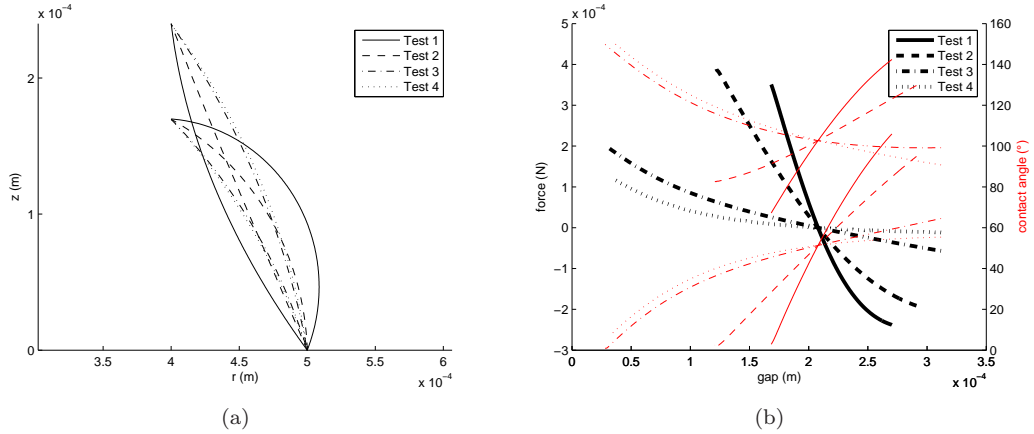


Figure 5.3.8: Illustration of the effect of total gas volume variation on the shape (a) of the interface, and on the force vs. gap plot (b) (thick lines), on which we clearly see the attractive and repulsive behavior. The evolution of the contact angles are also shown on (b) (thin lines), allowing to predict the maximal force before the bubble escapes the anchoring area

Table 5.3.4: Simulation parameters to compare blind holes (B) and through holes (T)

Parameters	Test 1 (B)	Test 5 (T)	Test 2 (B)	Test 6 (T)	Test 3 (B)	Test 7 (T)
\bar{V} (m ³)	$2.5 \cdot 10^{-9}$	$2.5 \cdot 10^{-9}$	10^{-8}	10^{-8}	10^{-7}	10^{-7}
u_0 (m)	$208 \cdot 10^{-6}$					
ΔP_0 (Pa)	281	281	281	281	281	281
σ (1)	563	563	141	141	14.1	14.1
At 20μN						
u (m)	$205 \cdot 10^{-6}$	$192 \cdot 10^{-6}$	$202 \cdot 10^{-6}$	$189 \cdot 10^{-6}$	$177 \cdot 10^{-6}$	$170 \cdot 10^{-6}$
k (N m ⁻¹)	7.55	1.13	3.89	1.01	0.673	0.557
ΔV (m ³)	0.49%	7.53%	1.91%	8.67%	15.2%	18.6%
θ_1 - θ_2 (°)	100-48	103-48	101-48	103-48	106-46	107-46
$\Delta(\Delta P)$ (Pa)	28.2	25.2	27.8	24.7	21.5	19.4
At 40μN						
u (m)	$203 \cdot 10^{-6}$	$171 \cdot 10^{-6}$	$197 \cdot 10^{-6}$	$168 \cdot 10^{-6}$	$149 \cdot 10^{-6}$	$137 \cdot 10^{-6}$
k (N m ⁻¹)	7.82	0.864	3.88	0.829	0.774	0.620
ΔV (m ³)	0.97%	17.3%	3.81%	19.2%	28.6%	34.5%
θ_1 - θ_2 (°)	98-45	105-44	99-45	106-44	110-42	113-41
$\Delta(\Delta P)$ (Pa)	55.1	48.4	54.8	47.3	40.4	34.5

Blind Holes or Through Holes

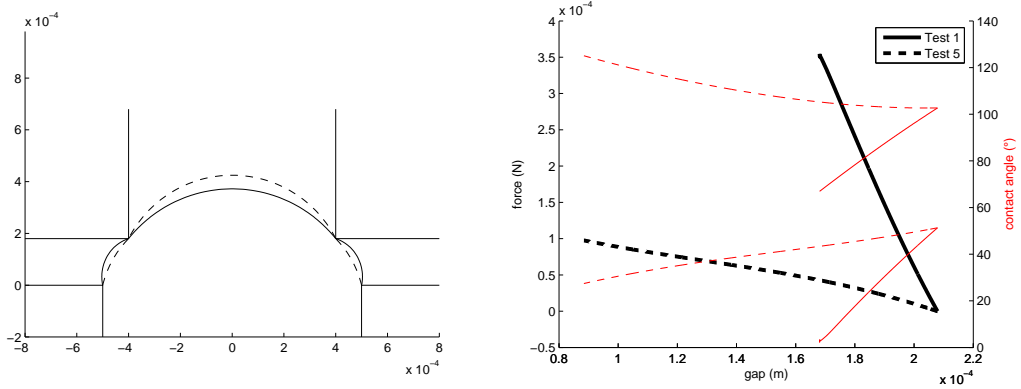
Let us now compare the configuration with a table having blind holes and the configuration with a table having through holes. Parameters for the simulations are shown in Table 5.3.4. They are the same as for test 1 to test 3 in Table 5.3.3.

Figure 5.3.9 represents the profiles of the bubbles for each test, compared to the profiles obtained in the same conditions for a table with blind holes. The plot of force (F) and contact angles (θ_1 and θ_2) with respect to the gap (u) are shown in Fig. 5.3.10.

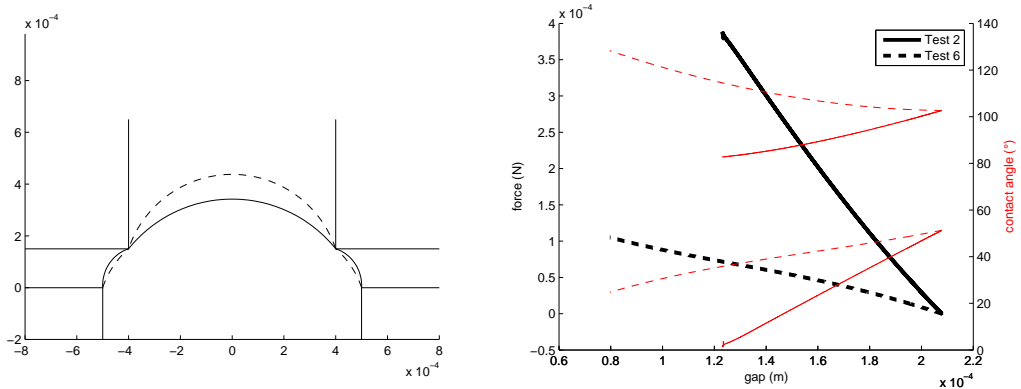
The evolution of the contact angle is more gentle compared to the one obtained with blind holes (Fig. 5.3.8). However, this does not mean the risk of a bubble escaping is reduced. The illustration of the profiles clearly shows that when the gap decreases, due to the pressure rise inside the gas system, the bubble part caught in the table hole grows. Indeed, since the pressure rises, its mean curvature increases. The theoretical limit is reached when the bubble is a half-sphere. But practically, when the contact angle of this profile with the lateral surfaces of the hole reaches the receding angle, the bubble will escape through the hole.

The comparison with the blind hole configuration also shows lower stiffnesses, especially when the gas system volume is small (values of k are larger for test 1 than for test 5). The decrease of the stiffness can be explained by a significantly larger V variation, i.e. volume of the bubble within the lateral profile (excluding the volume caught in the table). Indeed, the volume caught in the table (V_t) increases when the gap u decreases. But since this volume has always the shape of a portion of a sphere, it does not generate any force of the table. So instead of crushing and increasing its curvature, the bubble partially escapes towards the hole in the table.

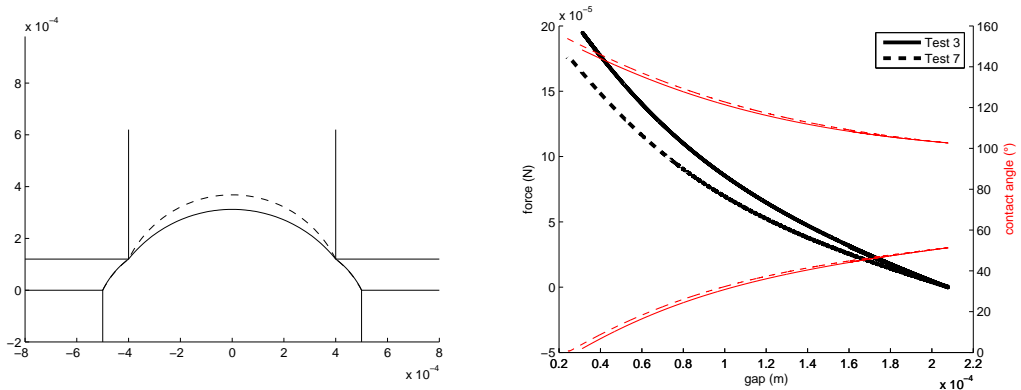
Therefore the pressure rise due to volume variation in the system is lower than in the blind hole configuration, which means that the force generated at a same gap distance u is lower. The effect of total gas volume is less significant for through holes configuration.



(a) Test 1 (—) blind hole and 5 (---) through hole



(b) Test 2 (—) blind hole and 6 (---) through hole



(c) Test 3 (—) blind hole and 7 (---) through hole

Figure 5.3.9: Comparison of bubble profiles obtained with blind holes and through holes. In the case of through holes, the gas contained in the hole of the table changes its geometry and grows when the gap distance decreases

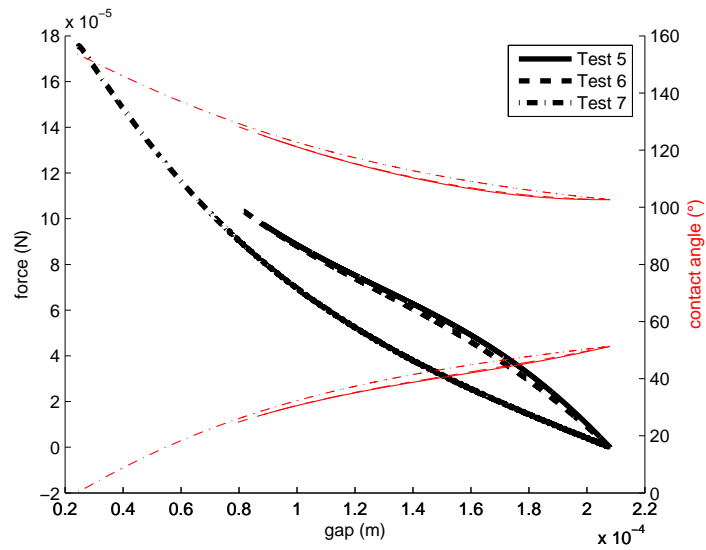


Figure 5.3.10: Evolution of the force (thick lines) and contact angles (thin lines) for different gas volumes when using a table with through holes. The effect of the total volume of gas is less significant than in the blind hole configuration. Tests parameters are given in Table 5.3.4

Table 5.3.5: Parameters for the simulations to evaluate the effect of anchoring diameter s_2 variation. N.S. stands for "No Solution", meaning the algorithm could not converge to a valid solution

Parameters	Test 1	Test 8	Test 2	Test 9	Test 3	Test 10
\bar{V} (m ³)	$2.5 \cdot 10^{-9}$	$2.5 \cdot 10^{-9}$	10^{-8}	10^{-8}	10^{-7}	10^{-7}
s_2 (m)	$800 \cdot 10^{-6}$	$400 \cdot 10^{-6}$	$800 \cdot 10^{-6}$	$400 \cdot 10^{-6}$	$800 \cdot 10^{-6}$	$400 \cdot 10^{-6}$
u_0 (m)	$208 \cdot 10^{-6}$	$359 \cdot 10^{-6}$	$208 \cdot 10^{-6}$	$359 \cdot 10^{-6}$	$208 \cdot 10^{-6}$	$359 \cdot 10^{-6}$
ΔP_0 (Pa)	281	281	281	281	281	281
σ (l)	563	563	141	141	14.1	14.1
At 20μN						
u (m)	$205 \cdot 10^{-6}$	$338 \cdot 10^{-6}$	$202 \cdot 10^{-6}$	$335 \cdot 10^{-6}$	$177 \cdot 10^{-6}$	$303 \cdot 10^{-6}$
k (N m ⁻¹)	7.5	0.96	3.89	0.85	0.67	0.37
ΔV (m ³)	0.49%	0.38%	1.91%	1.52%	15.2%	12.53%
θ_1 - θ_2 (°)	100-48	98-12	101-48	99-12	106-46	104-12
$\Delta(\Delta P)$ (Pa)	28.2	29.4	27.8	29.1	21.5	24.3
At 40μN						
u (m)	$203 \cdot 10^{-6}$	N. S.	$197 \cdot 10^{-6}$	N. S.	$149 \cdot 10^{-6}$	N. S.
k (N m ⁻¹)	7.82	N. S.	3.88	N. S.	0.774	N. S.
ΔV (m ³)	0.97%	N. S.	3.81%	N. S.	28.6%	N. S.
θ_1 - θ_2 (°)	98-45	N. S.	99-45	N. S.	110-42	N. S.
$\Delta(\Delta P)$ (Pa)	55.1	N. S.	54.8	N. S.	40.4	N. S.

Effect of Anchoring Diameter

The anchoring diameter s_2 on the table has been so far chosen smaller than the anchoring diameter s_1 on the platform. The purpose of this was to have a device that could be used with any bubble. Indeed, if $s_2 > s_1$, the bubble must be larger than a half-sphere in order for the anchoring circle on the table to touch the bubble. And we have demonstrated in Sect. 4.2.6 that in some cases, i.e. when $\sigma < 128/(27\pi)$, the growth of a bubble can be unstable beyond certain height.

However we can wonder if decreasing s_2 compared to results of Table 5.3.3 would lead to a more efficient device. Results of this simulation are shown in Table 5.3.5. Of course, the initial gap u_0 is different for both simulations since the anchoring circle touches the bubble at a larger gap for a smaller s_2 .

These results brings to light that with a smaller anchoring circle in the table, the contact angles on the table side θ_2 are smaller (see Fig. 5.2.5 for definition of θ_2). From a numerical point of view, this algorithm will therefore stop to converge to a profile function $r(z)$ for smaller gap variation. From a practical point of view, this means that with such a configuration, bubbles are more likely to escape the anchoring circle since the contact angle will sooner reach the receding angle. The stroke of the table is therefore smaller if s_2 is reduced. Because of that, it was not possible to reach a force value of $40 \cdot 10^{-6}$ N in Table 5.3.5, the algorithm failed to converge before that value.

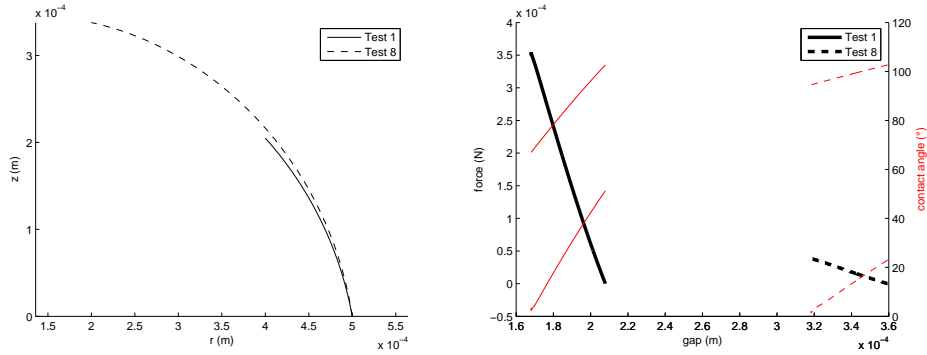
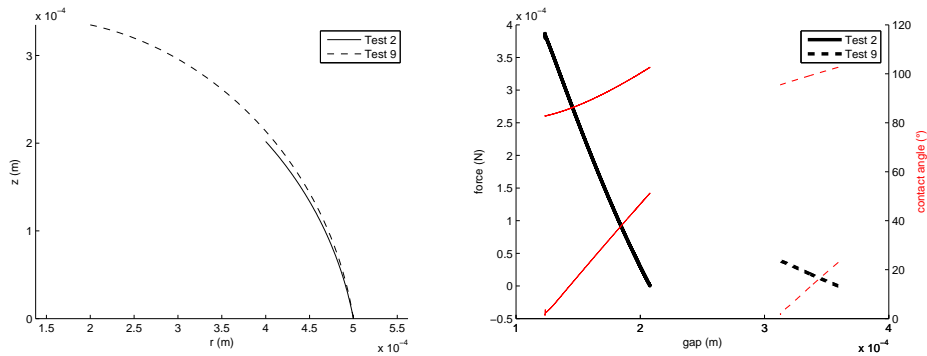
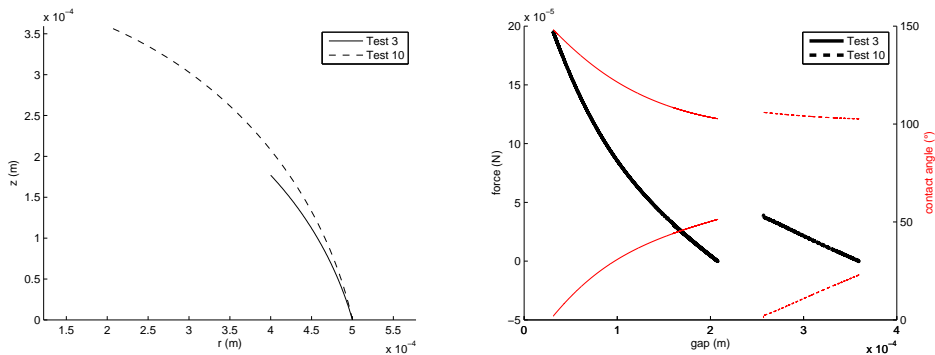
(a) Test 1 (—) large s_2 and 8 (---) small s_2 (b) Test 2 (—) large s_2 and 9 (---) small s_2 (c) Test 3 (—) large s_2 and 10 (---) small s_2

Figure 5.3.11: Comparison of bubble profiles (left) and force (right) obtained for $s_2 = 800 \cdot 10^{-6}$ m and $s_2 = 400 \cdot 10^{-6}$ m. Profiles are plotted for a force of $20 \cdot 10^{-6}$ N. Because the anchoring points on the table are closer to the symmetry axis, the contact angles are smaller. This leads to a shorter stroke for the table before the algorithm does not converge anymore to a solution, which means in real situation that the bubble escapes the anchoring circle. Configurations with smaller anchoring circle are henceforth less stable

Scaling Effect

We have simulated a size reduction of the geometries by a factor of 10: $s_1 = 100 \cdot 10^{-6}$ m, $s_2 = 80 \cdot 10^{-6}$ m and $h_1 = 40 \cdot 10^{-6}$ m. In order to keep constant dimensionless number σ constant, representing combined effects of gas compressibility and surface tension, the initial gas volume \bar{V} has been reduced by a factor 10^4 . Indeed, we suppose that the reduced setup uses the same liquid (so surface tension γ is kept constant) and is operated at the same pressure (so P_0 is kept constant). To strictly verify the conditions for a similarity study, V_0 should be decreased by 10^3 , P_0 should be increased by 10^2 and surface tension γ should be increased by a factor 10. Some distortion will therefore occur since the simulations are done without scaling pressure P_0 neither surface tension γ .

To compare the results with those of Table 5.3.3, we will first examine the results of the model at points where force levels are also reduced by a factor of 10. Then we will also examine the results for a force of 20N. The results are shown in Table 5.3.6.

If we compare the results with those of the 10 times larger device, we see that the position at which the force is 10 times smaller is for a gap which is 10 times smaller. This confirms that capillary forces, which are responsible for the force developed by the bubble, are indeed proportional to the characteristic length of the device, as predicted in Sect. 3.2.3. As expected from dimensional analysis, the stiffness remains approximately constant after downscaling the device.

Another interesting point is that the pressure is inversely proportional to the characteristic length. This is obvious since pressure drop is a function of the mean curvature (3.2.3), which is inversely proportional to the length.

The scaled comparison between reference and scaled tests is illustrated in Fig. 5.3.12.

Table 5.3.6: Parameters for the simulations to evaluate scaling effects on the device

Parameters	Test 1	Test 11	Test 2	Test 12	Test 3	Test 13
\bar{V} (m ³)	$2.5 \cdot 10^{-9}$	$2.5 \cdot 10^{-13}$	10^{-8}	10^{-12}	10^{-7}	10^{-11}
u_0 (m)	$208 \cdot 10^{-6}$	$20.8 \cdot 10^{-6}$	$208 \cdot 10^{-6}$	$20.8 \cdot 10^{-6}$	$208 \cdot 10^{-6}$	$20.8 \cdot 10^{-6}$
ΔP_0 (Pa)	281	2809	281	2809	281	2809
σ (1)	563	563	141	141	14.1	14.1
At	20μN	2μN	20μN	2μN	20μN	2μN
u (m)	$205 \cdot 10^{-6}$	$20.5 \cdot 10^{-6}$	$202 \cdot 10^{-6}$	$20.3 \cdot 10^{-6}$	$177 \cdot 10^{-6}$	$17.7 \cdot 10^{-6}$
k (N m ⁻¹)	7.55	7.63	3.89	3.81	0.673	0.690
ΔV (m ³)	0.49%	0.48%	1.91%	1.89%	15.2%	14.9%
θ_1 - θ_2 (°)	100-48	100-48	101-48	101-48	106-46	106-47
$\Delta(\Delta P)$ (Pa)	28.2	278	27.8	275	21.5	216
At	40μN	4μN	40μN	4μN	40μN	4μN
u (m)	$203 \cdot 10^{-6}$	$20.3 \cdot 10^{-6}$	$197 \cdot 10^{-6}$	$19.7 \cdot 10^{-6}$	$149 \cdot 10^{-6}$	$15.0 \cdot 10^{-6}$
k (N m ⁻¹)	7.82	7.92	3.88	3.97	0.774	0.784
ΔV (m ³)	0.97%	0.95%	3.81%	3.73%	28.6%	28.1%
θ_1 - θ_2 (°)	98-45	98-45	99-45	99-45	110-42	110-42
$\Delta(\Delta P)$ (Pa)	55.1	552	54.8	543	40.4	408
At	20μN	20μN	20μN	20μN	20μN	20μN
u (m)	$205 \cdot 10^{-6}$	$18.5 \cdot 10^{-6}$	$202 \cdot 10^{-6}$	$16.2 \cdot 10^{-6}$	$177 \cdot 10^{-6}$	$3.01 \cdot 10^{-6}$
k (N m ⁻¹)	7.55	9.58	3.89	4.98	0.673	1.94
ΔV (m ³)	0.49%	4.38%	1.91%	8.67%	17.7%	85.2%
θ_1 - θ_2 (°)	100-48	82-23	101-48	89-24	106-46	149-1
$\Delta(\Delta P)$ (Pa)	28.2	2595	27.8	2618	21.5	1244

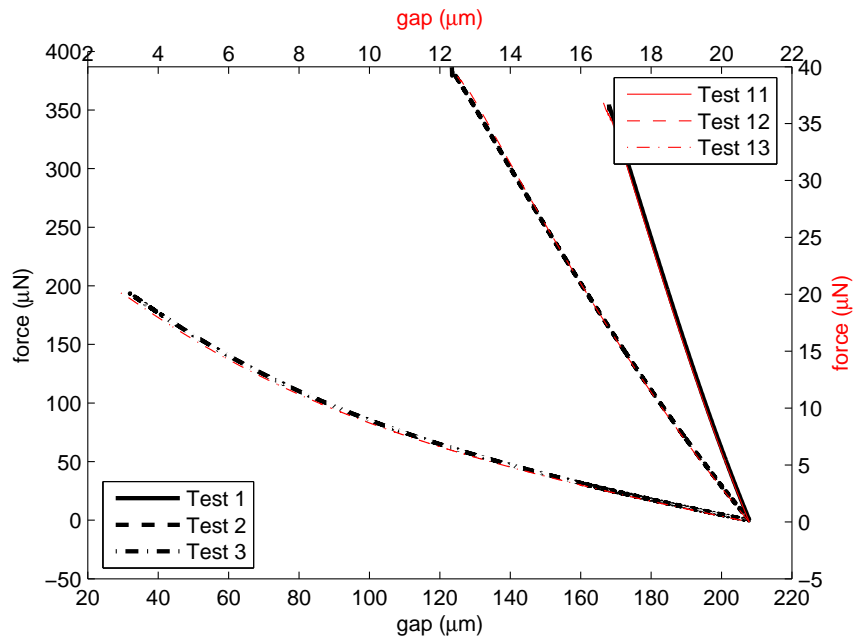


Figure 5.3.12: Comparison of the force with respect to gap distance for a scaled model. Curves for original model are represented by thick lines (bottom-left axes), and curves for downscaled model are represented by thin lines (top-right axes). If the dimensions are reduced by a factor of 10 and the volume is reduced by a factor 10^4 to keep constant dimensionless number σ , representing combined effects of compressibility and surface tension. Some distortion is therefore introduced since pressure P_0 and surface tension γ are not scaled. It is interesting to notice that the force generated by the downscaled model is decreased by the same factor, with curves for both models overlaying nicely, confirming that the capillary force is proportional to the characteristic length of the device, whatever the gas system volume

Pressure Measurement

Table 5.3.3 shows that the pressure drop across bubble interface is initially $\Delta P = 280$ Pa. When a bubble generates a force, its mean curvature changes, and the pressure drop conveys the amplitude of the force. This is interesting since the pressure can be measured anywhere in the gas circuit.

However, the amplitudes of pressure variation are relatively small, so the pressure sensor that should be used must have a high resolution. But as seen in the results of Table 5.3.6, the pressure levels are larger if the device is geometrically downscaled, with the same force level.

In Sect. 4.4.1, we proposed to use bubbles as a pressure sensor. Since it is based on the same physics, it can be adapted to the range of the pressure to measure. However the holes from which the pressure sensing bubbles are generated have to be smaller than the actuating bubbles.

Conclusions on Model Analysis

From the analysis of the model, we can infer some design rules to improve the design efficiency of the compliant table (Fig. 5.3.13).

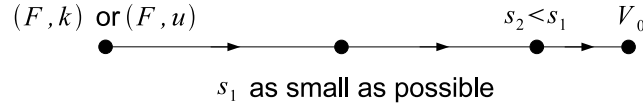


Figure 5.3.13: Design flow chart for compliant table

First the maximal force applied on a bubble must be defined, together with either the maximal stroke or the stiffness.

From the scaling law, we conclude that the dimensions of the device should be as small as possible to fulfill the force and stroke requirement. This allows to increase the pressure inside the bubbles, making possible the use of a pressure sensor to infer the amplitude of the force applied on the table.

The anchoring circle on the table should be slightly smaller than the anchoring circle on the platform, to allow any bubble generated from platform to reach the table. But on the other hand, the anchoring circle on the table must be as large as possible to have the largest contact angles, and prevent bubble escape.

The configuration of a table with through holes should be avoided if possible, because the bubbles tend to escape through the holes. This makes the device more compliant, but the maximal force accepted is then lower than with blind holes.

Finally, an interesting property of bubbles is that the stiffness of the device can be adjusted within some range by varying the total volume of gas in the device. If the application requires different stiffnesses, a special design with different gas volumes that can be connected or disconnected through valves could be used.

5.3.7 Parabolic Approximation

To avoid a long calculation in a time sensitive application, a solution is to approximate the profile by a curve which is not a constant mean curvature curve. We propose to approximate the interface geometry by a second order curve: a parabola.

$$r(z) = a_2 z^2 + a_1 z + a_0 \quad (5.3.9)$$

This formulation allows to consider different values for s_1 and s_2 . The determination of the profile is therefore limited to the calculation of the 3 parameters: a_0 , a_1 and a_2 . The constraints to satisfy are here also the boundary positions, corresponding to the bubble anchoring circles (5.3.5) (Fig. 5.3.14) This gives the first two equations to find the parameters:

$$a_0 = \frac{s_1}{2} \quad (5.3.10)$$

$$a_0 + a_1 u + a_2 u^2 = \frac{s_2}{2} \quad (5.3.11)$$

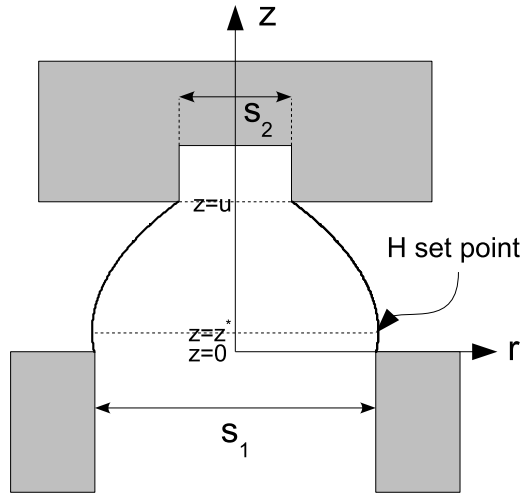


Figure 5.3.14: Illustration of parabolic approximation of bubble profile. Profile boundaries must reach the anchoring points, and the mean curvature is set at the apex of the parabola ($z = z^*$)

Since the mean curvature is not constant, we propose to calculate it at the apex of the parabola, where $dr/dz = 0$ located at $z = z^* = -\frac{a_1}{2a_2}$. The definition of the mean curvature is:

$$2H = \frac{1}{r_1} + \frac{1}{r_2} \quad (5.3.12)$$

with:

$$\begin{aligned}
r_1 &= r \left(1 + \left(\frac{dr}{dz} \Big|_{z=z^*} \right)^2 \right)^{0.5} = a_0 + a_1 z^* + a_2 z^{*2} = a_0 - \frac{a_1^2}{2 a_2} + \frac{a_1^2}{4 a_2} \\
r_2 &= - \frac{\left(1 + \left(\frac{dr}{dz} \Big|_{z=z^*} \right)^2 \right)^{1.5}}{\frac{d^2 r}{dz^2} \Big|_{z=z^*}} = - \frac{1}{2 a_2}
\end{aligned} \tag{5.3.13}$$

Finally:

$$2H = -2 a_2 + \frac{1}{a_0 - \frac{a_1^2}{4 a_2}} \tag{5.3.14}$$

The pressure in the gas circuit is given by:

$$P = P_0 + \Delta P = P_0 + \gamma \left(-2 a_2 + \frac{1}{a_0 - \frac{a_1^2}{4 a_2}} \right) \tag{5.3.15}$$

The volume of the bubble is given by:

$$V = \pi \int_0^u (a_0 + a_1 z + a_2 z^2)^2 dz \tag{5.3.16}$$

$$= \pi \left(a_0^2 u + a_0 a_1 u^2 + (a_1^2 + 2 a_0 a_2) \frac{u^3}{3} + a_1 a_2 \frac{u^4}{2} + a_2^2 \frac{u^5}{5} \right) \tag{5.3.17}$$

The third equation to find the parabola parameters is given by mole number, from ideal gas law (4.2.1):

$$\begin{aligned}
n &= \frac{\left(P_0 + \gamma \left(-2 a_2 + \frac{1}{a_0 - \frac{a_1^2}{4 a_2}} \right) \right)}{R_g T} \\
&\cdot \pi \left(\frac{V_0}{\pi} + a_0^2 u + a_0 a_1 u^2 + (a_1^2 + 2 a_0 a_2) \frac{u^3}{3} + a_1 a_2 \frac{u^4}{2} + a_2^2 \frac{u^5}{5} \right)
\end{aligned} \tag{5.3.18}$$

The combination of (5.3.10), (5.3.11) and (5.3.18) leads to a fifth order polynomial with a_2 as dependent variable:

$$p_5 a_2^5 + p_4 a_2^4 + p_3 a_2^3 + p_2 a_2^2 + p_1 a_2 + p_0 = 0 \tag{5.3.19}$$

If we posit:

$$\begin{aligned}
K &= \frac{s_2 - s_1}{2u} \\
A_0 &= -P_0 K^2 \\
A_1 &= 2P_0 (uK + s_1) + 4\gamma + 2\gamma K^2 \\
A_2 &= -u^2 P_0 - 4\gamma (uK + s_1) \\
A_3 &= 2\gamma u^2 \\
B_0 &= \frac{K^2 u^3}{3} + \frac{s_1 K u^2}{2} + \frac{s_1^2 u}{4} + \frac{V_0}{\pi} \\
B_1 &= -\left(\frac{K u^4}{6} + \frac{s_1 u^3}{6}\right) \\
B_2 &= \frac{u^5}{30}
\end{aligned} \tag{5.3.20}$$

the coefficients of the polynomial are:

$$\begin{aligned}
p_5 &= A_3 B_2 \\
p_4 &= A_2 B_2 + A_3 B_1 \\
p_3 &= A_1 B_2 + A_2 B_1 + A_3 B_0 \\
p_2 &= A_2 B_0 + A_1 B_1 + A_0 B_2 + \frac{u^2 n R_g T}{\pi} \\
p_1 &= \left(A_1 B_0 + A_0 B_1 - \frac{2 n R_g T}{\pi} (uK + s_1) \right) \\
p_0 &= \left(A_0 B_0 + \frac{n R_g T K^2}{\pi} \right)
\end{aligned} \tag{5.3.21}$$

The polynomial can be solved with the `root` method of Matlab. However, it is necessary to find the adequate value among the 5 potential solutions to the polynomial. We first eliminate the complex solutions. In order to discriminate the best among the real solution, we have defined three criteria. First we could select the curve with the minimum length. Second we could select the curve that will produce the smallest revolution surface. But the method giving the best results consists in selecting the curve which has the least variation of H . For this selection, we evaluate H using (5.3.4) at both ends and midpoint of the profile. We then select the curve having the lowest relative standard deviation.

Once the 3 parabola parameters are found, the force can be easily calculated:

$$F = \pi \Delta P \frac{s_1^2}{4} - \pi s_1 \gamma \cos(\theta|_{z=u}) \tag{5.3.22}$$

where ΔP is found from (5.3.14) and the contact angle cosine is:

$$\cos(\theta|_{z=u}) = \frac{1}{\sqrt{1 + \tan^2(\theta)|_{z=u}}} = \frac{1}{\sqrt{1 + (a_1 + 2a_2 u)^2}} \tag{5.3.23}$$

Comparison of Both Methods

We will now compare the results for both calculation methods: the ODE resolution and the parabolic approximation. To do this, we have run both models with the same input parameters and we will compare the shape of the profile, the mean curvature and the calculated force. The objective is to settle the limits of parabolic approximation.

Table 5.3.7: Parameters for the comparison between parabolic approximation and ODE calculation

Parameters	Test 1	Test 2	Test 3
V_r (m ³)	$2.309 \cdot 10^{-9}$	$9.809 \cdot 10^{-9}$	$9.981 \cdot 10^{-8}$
n (mol)	$1.0205 \cdot 10^{-7}$	$4.1472 \cdot 10^{-7}$	$4.1667 \cdot 10^{-6}$

The parameters are shown in Table 5.3.7. For each simulation, we assumed a temperature $T = 293.15$ K, a pressure of $P_0 = 101325$ Pa, and a surface tension of $\gamma = 72 \cdot 10^{-3}$ N m⁻¹. The geometry of the anchoring circles is $s_1 = 10^{-3}$ m and $s_2 = 800 \cdot 10^{-6}$ m. These parameters give a force that should be equal to zero for a gap distance of approximately $208 \cdot 10^{-6}$ m.

Illustration of the profiles obtained by both methods are shown in Fig. 5.3.15. We can see that the H -based selection method seems to be efficient since it keeps the parabolic profile which is closest to the ODE solutions.

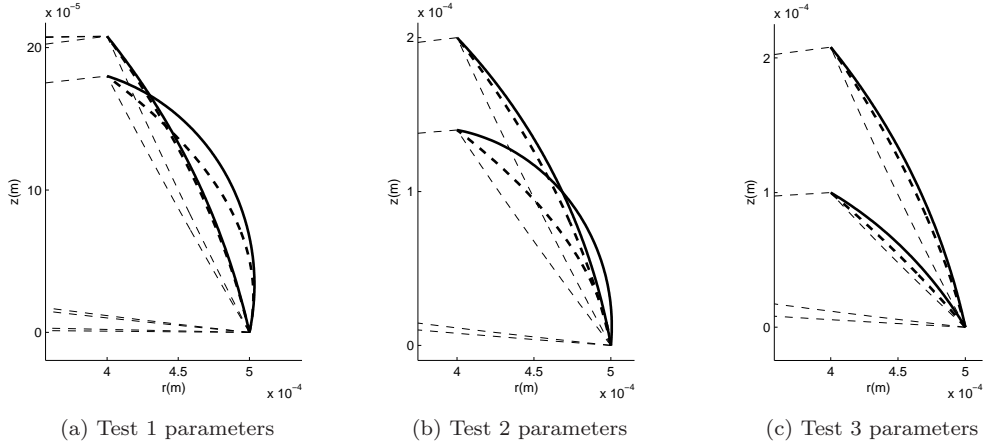
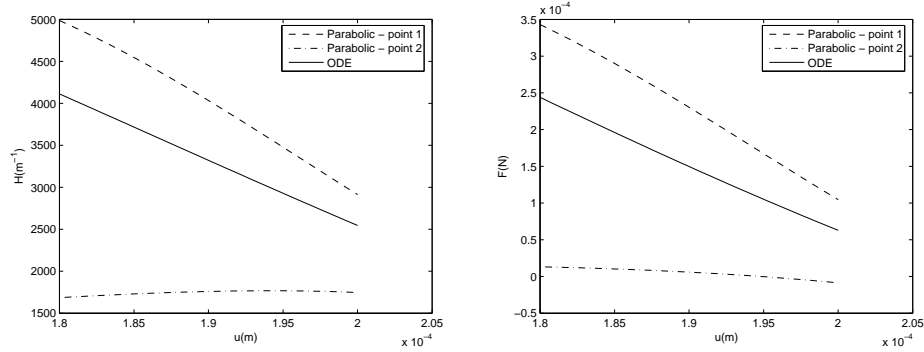


Figure 5.3.15: Illustration of the profiles obtained by ODE calculation (—), and parabolic approximation (---). The bold dashed lines are the selected solutions for parabolic approximation, i.e. the curve for which the mean curvature variation is the smallest. Thin lines are the other solutions of the parabolic approximation. The results are plotted for two different separation distances. We see that the selected solution is indeed the closest to the ODE solution, yet the correspondence is limited

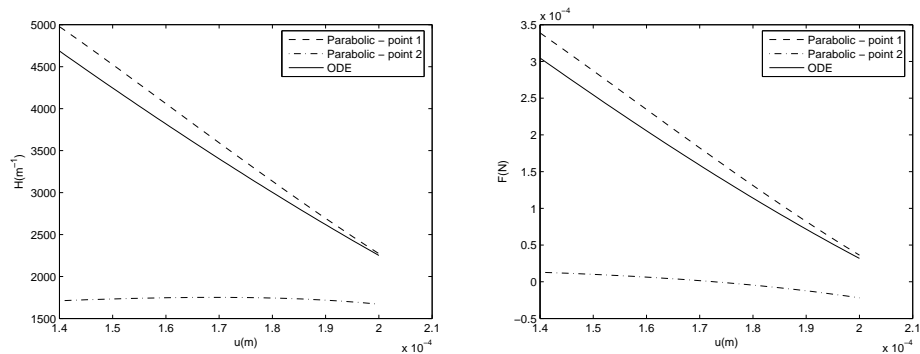
However, the force deduced from the parabolic approximation, illustrated in Fig. 5.3.16, presents rapidly a large deviation compared to ODE results. This can be explained by the deviation of the contact angle and the curvature, which seem to increase when the gap decreases. Nevertheless we notice that the force calculation performed on the side with the larger triple line diameter circle provides better results, as ODE and parabolic profiles have contact angles that are closest at this point.

As a consequence, the parabolic approximation should be used for configurations leading to a small force, i.e. gap values close to zero force configuration. The comparison of H or F at both ends of the profile does not give a clear indication of the exactness of parabolic model, and cannot be used as a criterion to estimate the relevance of this approximation.

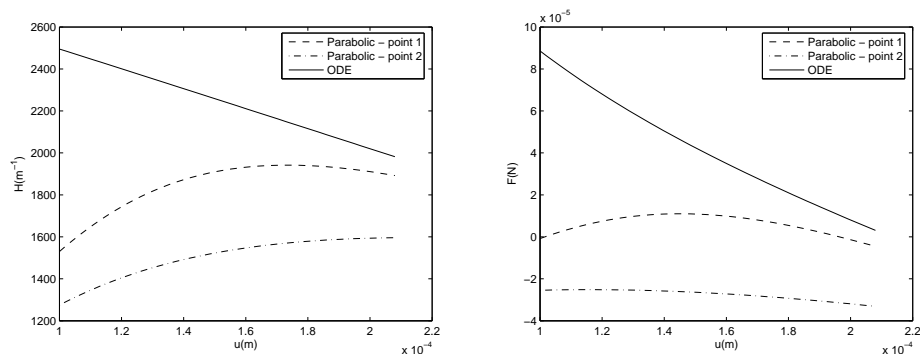
If the bubble is to be used with a large stroke, and the application needs fast resolution,



(a) Test 1 parameters



(b) Test 2 parameters



(c) Test 3 parameters

Figure 5.3.16: Evolution of the mean curvature (left) and force (right) at both ends of the parabolic approximation profile, together with the values obtained with the ODE resolution. The force calculated at first end of the profile, which is the large anchoring circle, is always closer to the force calculated by ODE resolution. Unfortunately, there seems to be no relevant criterion based on the difference of H or F at both ends of the profile to predict the adequacy of the parabolic approximation

we suggest the use of a look-up table for best results.

5.4 Validation of the Model

In this section we present the method used to validate the model developed in Sect. 5.3. We present in Sect. 5.4.1 a first experimental validation, which turned out to be inconclusive but gave interesting qualitative results. Then we present in Sect. 5.4.2 how to address this problem by proposing a different experimental setup and a different mean to measure forces. Then we present the test bed we used (Sect. 5.4.3), the technological issues we encountered (Sect. 5.4.4) and the analysis procedure (Sect. 5.4.5). Finally we present the results (Sect. 5.4.6).

5.4.1 First Experimental Trials

To validate qualitatively the behavior of a gas bubble, we made a test on an atomic force microscope (AFM) based force measurement station (*AMIS* station). The principle of force measurement with an AFM is based on the deflection measurement of an AFM tip, which can be considered as a cantilever beam [11]. The deflection is measured by mean of a laser beam reflecting on the AFM tip and impacting a photodiode. The AFM head is mounted on a moving vertical axis.

The methodology is as follow. First the correspondence between displacement of the tip and position of the beam on the photodiode (measured as a voltage) is measured. To do so, the AFM tip is moved down while it is in contact with a solid. In this case, the deflection of the tip is equal to the displacement of the head. Then we generate a bubble, and the AFM tip is aligned above the bubble. Then an approach and recede sequence is applied on the head of the AFM, and the deflection of the tip is measured. Knowing the stiffness of the tip, it is possible to infer the force applied on it. The stiffness of the tip can be measured either by geometrical and mechanical analysis of the tip, or more accurately by measuring its resonance frequency³. If the resonant frequency is measured, it is important to make the measurement in air, because the viscosity of the liquid will influence the results. This results can then be used to measure a quasi-static force in a liquid.

Since the experiment is performed in water, the laser beam could interfere with the water free surface. To avoid this, a glass prism is placed between the tip and the rest of the AFM system, containing the laser emitter and the photodiode. The AFM device used for this experiment was a commercial AFM (type *SMENA-B* from *NT-MDT*). The prism and its functioning is illustrated in Fig. 5.4.1. The methodology is illustrated in Fig. 5.4.2.

Due to the small space available, the volume controlled bubble generator is not suitable. We have therefore decided to generate the bubble from an electrolysis system (Sect. 4.1.1). This system is limited, because it is not possible to set the size of the bubble nor its exact location. Anyway, there are two cameras in the system, one giving a view from bottom and allowing to position the laser on the tip and to position the bubble beneath the tip, and the second giving a lateral view. From these views, the position and size of the bubble can be measured.

Because the tip is tilted, the configuration is not axisymmetric. To correct that, we have used an AFM tip on which a small 10 μm diameter borosilicate sphere is glued. The stiffness of the tip is 0.330 N/m (measured). However, it is impossible to be sure that the sphere does not penetrate in the bubble, so that the effective contact is between the bubble and the beam. The actual setup is illustrated in Fig. 5.4.3.

Figure 5.4.4 shows some pictures from lateral and bottom view taken during the test. Figure 5.4.5 shows the curve recorded during the approach and receding movement. Since

³resonance frequency of an oscillating mass m function of oscillator stiffness k : $\frac{1}{2\pi} \sqrt{\frac{k}{m}}$

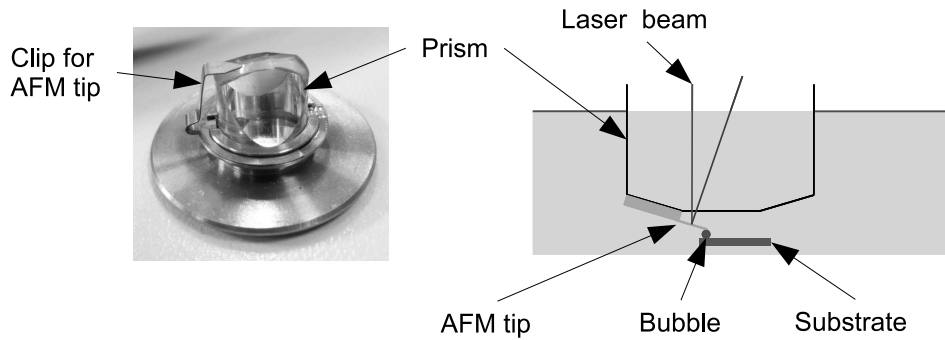


Figure 5.4.1: View of the prism used to perform force measurement in water with an AFM. The prism is placed between the AFM and the tip, at the level of water free surface. It allows to avoid the laser beam crossing the free surface, which could interfere with its path. The AFM tip is placed below the prism

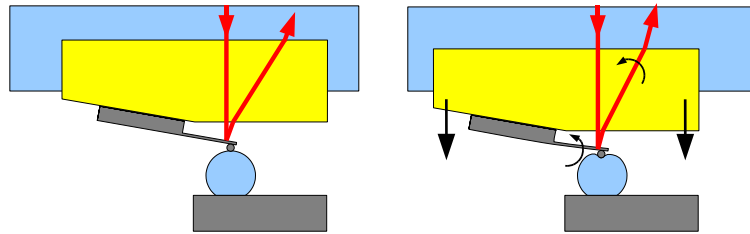


Figure 5.4.2: Methodology of bubble force measurement using an AFM. A ball is glued at the end of the AFM tip to ensure an axisymmetric contact with the bubble. A laser beam is emitted through the prism, and reflected on the tip. The tip, which is fixed to the prism, is moved down to push on the bubble. The resulting force induces the bending of the tip, changing the direction of the reflected laser beam. The correspondence between the bending of the tip and the movement of the laser beam is calibrated. Knowing the stiffness of the tip, it is possible to infer the force generated by the bubble

we have no confidence in the exact contact area between the tip and the bubble, we did not quantify precisely this results (order of magnitude of the peak compression force is 300 nN and of bubble stiffness is 0.1 N/m) . However, the curve has a significant profile, which confirms that the force generated by the bubble is repelling the AFM tip during the approach movement, when the contact has been established between the bubble and the tip. Then, during the receding movement, the force becomes attractive and the bubble pulls on the AFM tip. This is what has been predicted by the model in Sect. 5.3.6.

5.4.2 Validation Strategy

Our purpose is to validate the model giving the force with respect to the gap, the geometry of the table, the initial gap and the number of mole in the gas system.

We first set the volume of gas in the gas tank. Then we generate three bubbles of approximately equal height, which will be measured. Then we lay the table on the bubbles, and we measure the gap and the geometry of the bubble. Next, we pose objects of known mass and density (in our case, other tables), and in turn we measure the new gap and new bubble geometry (i.e. curvature). This is illustrated in Fig. 5.4.6.

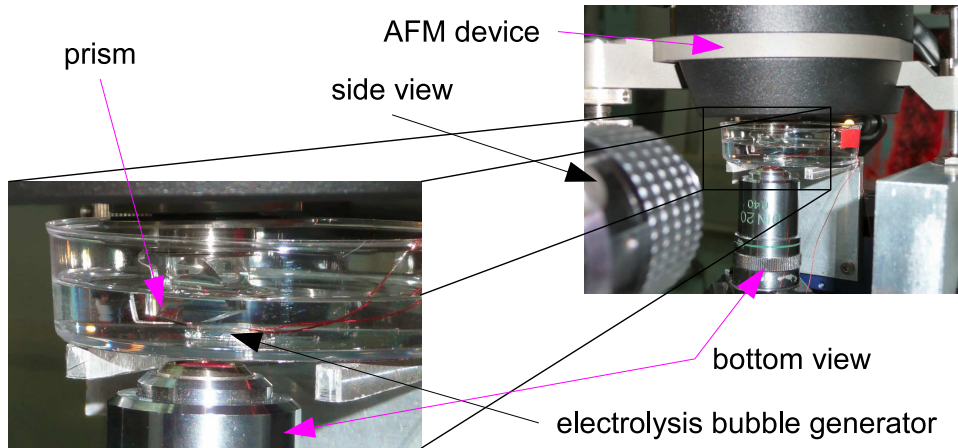


Figure 5.4.3: View of the actual setup for the AFM-based force measurement of a bubble

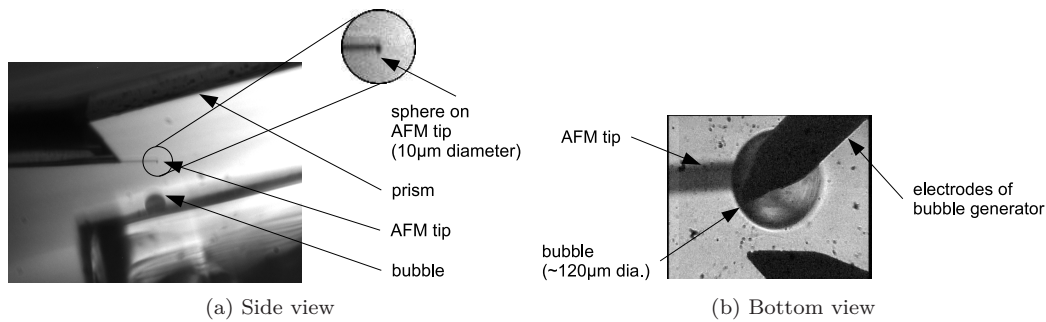


Figure 5.4.4: Views of the bubble and the AFM tip used to measure the force generated by a bubble

This strategy requires a mean to measure the gap and the curvature of the profile. The force applied on the table is deduced from the mass and the density of the object, but could also be deduced from the geometry of bubble profile, thanks to (5.3.3). According to Laplace law, the curvature measurement could be replaced by a pressure measurement but this has not been implemented in this prototype. Since the force applied by the bubbles is deduced from the weight and density of the object, we suppose that the table is parallel to the platform, and that each bubble applies the same force on the table. This is of course an approximation, but since the relative angle between the table and the platform is small (maximum tilt angle 15° , but practically less than 3°), the approximation is acceptable.

All these measurements have been performed using an image analysis process. It was therefore necessary to have an image acquisition system able to take pictures of the bubbles caught between the platform and the table.

5.4.3 Test Bed Design

A schematic view of the test bed is presented in Fig. 5.4.7, which is the same test bench as the one used to validate the controlled volume bubble generator model. A view of the actual test cell is shown in Fig.5.4.8.

The flexible hoses are made of silicone. They have an inner diameter of $500 \cdot 10^{-6}$ m and

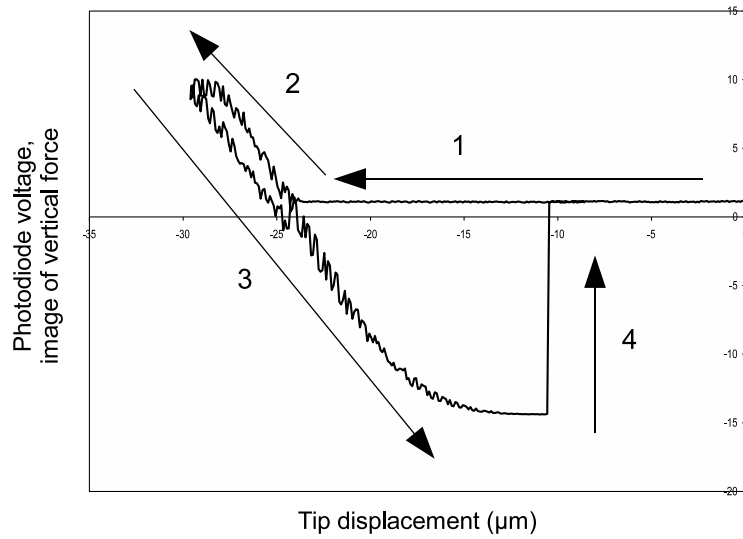


Figure 5.4.5: View of an approach-recede curve to estimate qualitatively the force generated by a bubble, using an AFM tip with a $10\ \mu\text{m}$ borosilicate sphere. First the tip is moving towards the bubble (1), then when the contact is established between the tip and the bubble, the force repulsing the tip increases (2). When the tip is moved backwards, the bubble pulls the tip when the distance is larger than the zero-force position (3). Finally, the bubble and tip separates, and the tip comes back to its normal position (4). Since the exact contact point of the bubble with the tip is not known, we present only a qualitative result, which shows the existence of an attractive and repulsive force depending on the gap, as predicted by the model (order of magnitude of the peak compression force is $300\ \text{nN}$ and of bubble stiffness is $0.1\ \text{N/m}$)

an outer diameter of $2.1 \cdot 10^{-3}\ \text{m}$.

The flexible hose constitutes the gas tank. The first step of the experiment consists in filling these hoses with an incompressible fluid until the desired volume of gas remains in the hose. Then the bubbles are generated from the platform by compressing the hoses where they are filled with liquid.

The optic system is composed of a *Marlin F-131B* camera from *Allied Vision Technologies*, having a resolution of 1280×960 pixels, and a *Navitar* optical system composed of a $3.5\times$ mini-adaptor, an adjustable $12\times$ zoom and a $2\times$ objective.

The flexible hoses are glued beneath the platform. The gas tank is a 1.5L PET bottle, and the flexible hoses have been glued in its cap. This system has the advantage that it can be used like a medical drip system, to avoid gas inclusion in the hoses. This is illustrated in Fig. 5.4.9.

5.4.4 Technological Issues

We present here some of the technological issues we had to face when we performed the experimental validation of the model predicting the force generated by a bubble.

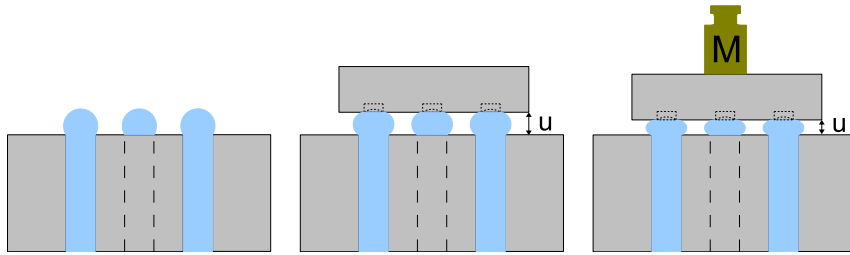


Figure 5.4.6: Procedure of the experimental validation. First, three bubbles are generated. Then the table is put down on the bubbles. The gap u between the platform and the table is measured. Then other objects of known mass and density are put down on the table, and the gap u is again measured

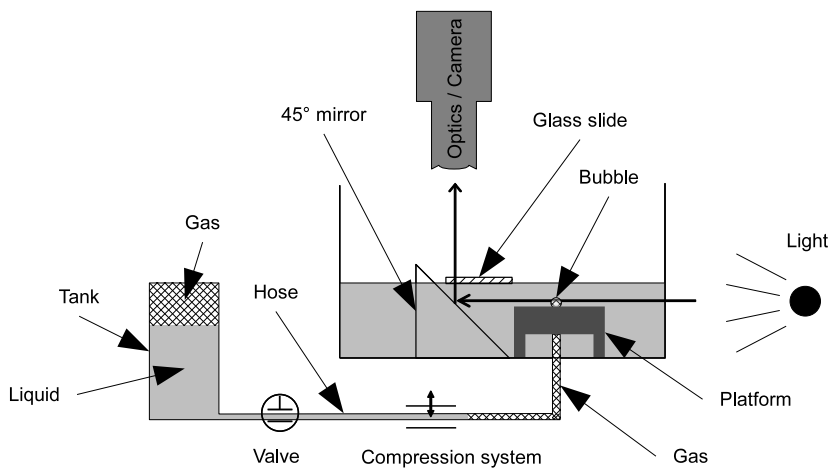


Figure 5.4.7: Schematic view of the second experimental setup used to validate the volume controlled bubble generation model

Vision System and Image Acquisition

The vision system is used to capture images. These images will be used to calculate the gap between the table and the platform, and to measure the mean curvature of a bubble profile.

The objects are immersed in a liquid. We have already mentioned in Sect. 4.3.1 some issues for acquiring images of small parts in a liquid. For example we have mentioned that the object should be as close as possible to the point where the optic path exits the liquid. In this case, we have put the object as close as possible considering the volume of the surrounding equipment.

An additional difficulty is that the bubble is caught between two planes. The parallax effect hides a part of the bubble. When the gap becomes small, it is compulsory to have the optic path as parallel to the platform plane as possible. Otherwise it will not be possible to see the contact points of the profiles and the solids. However, it is possible to demonstrate that the force developed by a bubble is constant all along its height (App. C). Therefore, not seeing the entire profile is not a problem concerning force calculation.

Concerning the gap measurement, the parallax effect could affect the measure (Fig. 5.4.10). To avoid this problem, we have supposed that the line joining both bottom vertices of the

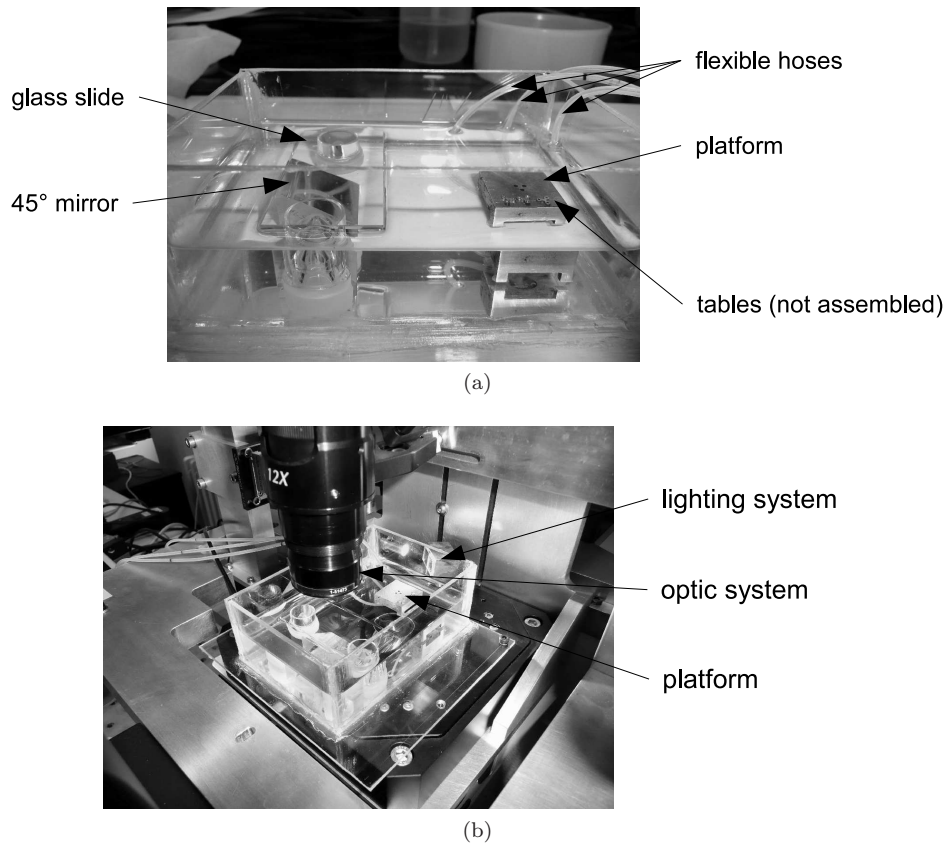


Figure 5.4.8: View of the actual test cell, comprising the platform and the optical system. Some tables are placed on the platform (next to the holes), before bubbles are generated. They will be superposed to increase progressively the force applied on the bubbles

table, visible on the images, crosses the center of the anchoring circle on the table. The line crossing the center of the anchoring circle on the platform was easier to see thanks to an adjustment of camera position and to the mirror shape of the profile reflecting on the platform surface.

Another issue encountered during the test was the superposition of two profiles (Fig. 5.4.11). This made the detection of the profile more difficult.

The calibration between length and image pixel has been done by moving the cell test using *PI M-161* microstages. The conversion ratio is $3.3 \mu\text{m}/\text{pixel}$. However we did this for the first bubble. The depth of view of the system allowed to see clearly the second bubble. But we noticed that the second bubble was in fact slightly on the background, making the calibration incorrect for this bubble. The third bubble was partially masked by the two other bubbles, and the parallax effect was more pronounced since the bubble is at the back of the table (Fig. 5.4.12).

Finally, due to bad image contrast in some cases, image analysis has been made by a mix of automatic profile detection using least square method to approximate the best profile with a constant mean curvature, and manual pointing for example to determine the anchoring points. To estimate the errors made when using manual pointing, we have repeated each image analysis five times, to estimate the dispersion of the pointing. Each repetition are illustrated on the final graphics.

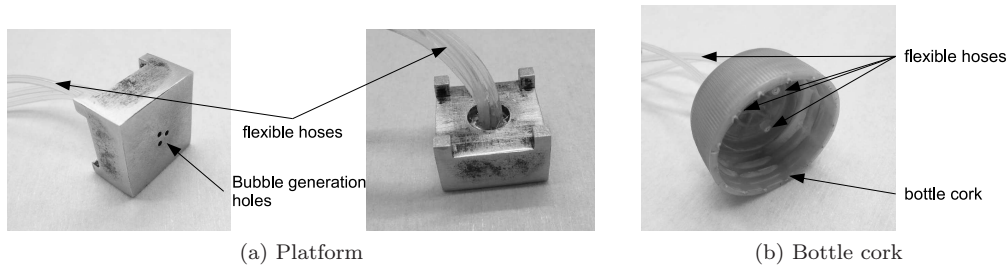


Figure 5.4.9: View of the flexible hoses connections

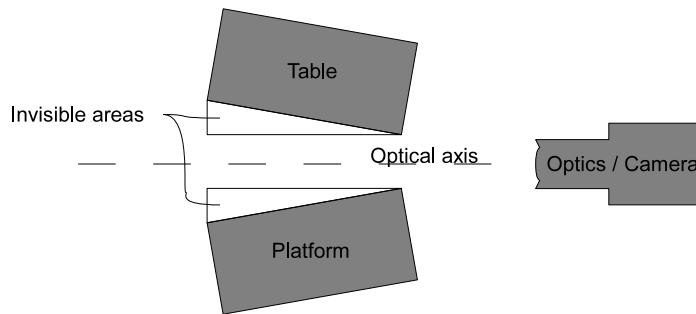


Figure 5.4.10: Illustration of the parallax effect. If the platform plane and the table plane are not parallel to optical axis, some areas are not visible

Gas Leakage

During the tests we have encountered several problems concerning the hypothesis of constant number of mole.

First, direct leaking of the gas at connections. Indeed, we glued the hoses using cyanoacrylate glue, which seems to be weakened after some time spent in the water. To avoid this problem we have covered the cyanoacrylate glued connections by another layer of *acryfix* glue.

Second, we know that air dissolves in water. It is very difficult to estimate this effect since it depends on the saturation level of the water, which is not constant. To avoid this problem, we proposed to use silicone oil instead of water. To minimize at maximum the dissolution of air, we chosen a highly viscous oil *Rhodorsil 47V5000*. But this oil has two major drawbacks that prevented the accomplishment of the experiment. First, silicone flexible hoses have a limited compatibility with silicone oil: they swell and are permeable to the oil which is seeping through them. Second, the chosen oil was so viscous that any movement of a tweezer around the table was able to take the table off the bubbles. It was not possible manually to move slowly enough to avoid that phenomenon. A third issue is the permeability of silicone to gas. We first choose hoses made of silicone for its elastomer behavior, since the volume variation is done by squeezing the hoses. A model of membrane permeability is given by [99]:

$$Pe = \frac{V_g d}{At \Delta P} \quad (5.4.1)$$

where Pe is the permeability of the material, V_g is the volume of gas permeating through the material, A is the area of the hose wall, equal to $\pi D l$ where D is the inner diameter of the flexible and l is the length of the hose filled with gas, t is the time and ΔP is the pressure

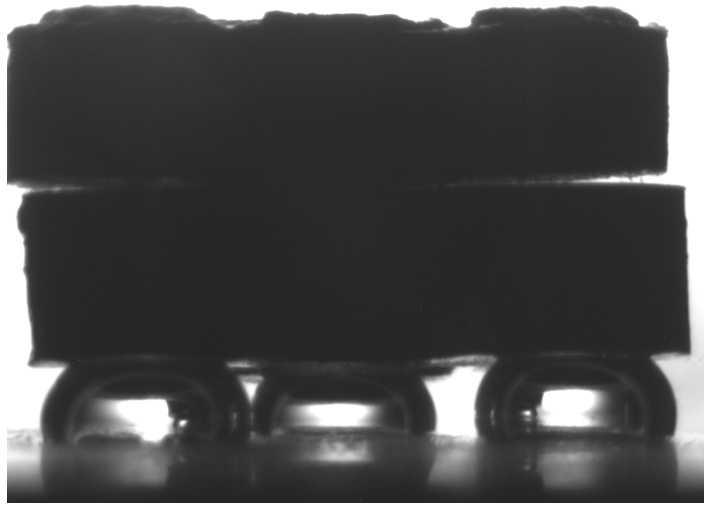


Figure 5.4.11: Example of image capture with two tables load. Bubble 1 (left) and bubble 3 (background) are partially superposed

difference between inner and outer side of the hose. Pe is a function of the material, but also a function of the gas considered. For silicone, $Pe = 65 \cdot 10^{-9} \text{ cm}^2 \text{ s}^{-1} \text{ cmHg}$ for O_2 molecules, and $Pe = 28 \cdot 10^{-9} \text{ cm}^2 \text{ s}^{-1} \text{ cmHg}$ for N_2 molecules. For gas mixes, partial pressures must be used. Silicone is the elastomer with the largest permeability. It would therefore have been necessary to use another material, such as PTFE.

For our application, if we suppose $\Delta P_{\text{O}_2} = 0.2 \Delta P$ and $\Delta P_{\text{N}_2} = 0.8 \Delta P$, we can estimate the number of mole permeating through the hose wall.

To evaluate the decrease of mole number in the gas system, we have recorded a single bubble at the rate of 1 frame per second in water (length of hose filled with air: 0.3 m, pressure drop estimated from first bubble and assumed constant: 186 Pa). We represent some of the frames in Fig. 5.4.13. The same experiment has been realized with silicone oil (length of

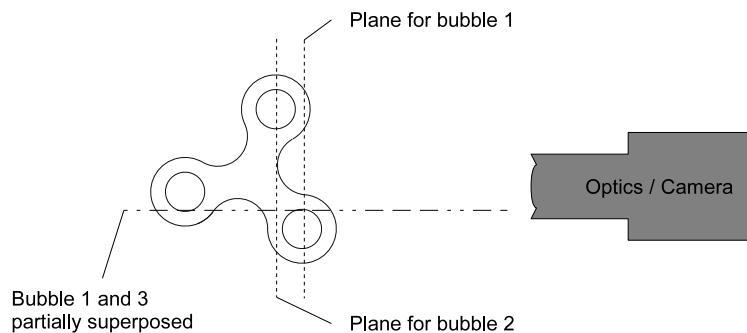


Figure 5.4.12: This schematic explains the calibration error due to the difference of plane position relative to the camera for bubble 1 and 2. The superposition of bubble 1 and bubble 3 is also explained

hose filled with air⁴: 0.7 m, pressure drop estimated from first bubble and assumed constant: 62 Pa). We have plotted in Fig. 5.4.14 the evolution of mole number from experiments with water and oil, and the corresponding results due to the model of permeability. We see that the permeability explains the gas mole number variation in the case of oil, but does account only for a part of the variation in the case of water. With water, we suppose that the difference between model and experiment is due to air dissolution in the water.

This phenomenon is very important because any variation of mole number will have a significant influence on the model results (Sect. 5.4.6).

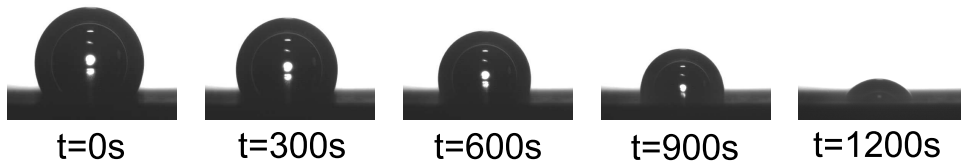


Figure 5.4.13: Experiment to illustrate gas mole decrease over time in an air-water system

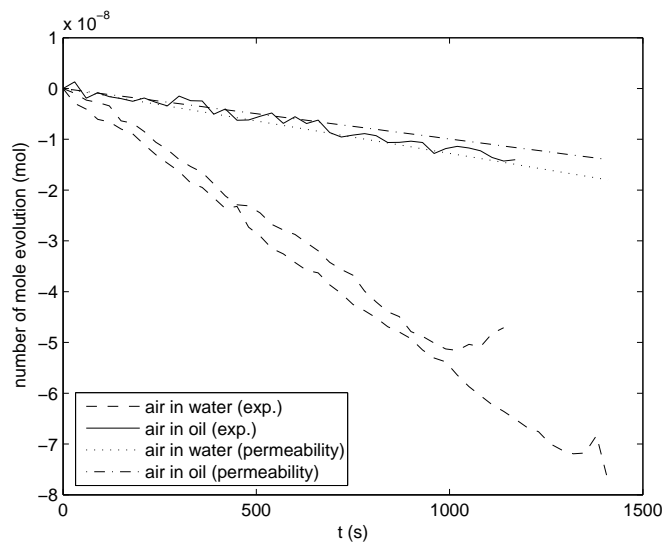


Figure 5.4.14: Comparison of permeability model of gas permeation through flexible hoses with experiments. When the liquid is silicone oil, the permeability of the silicone hoses explains the origin of gas mole decrease in the system. When the liquid is water, only a part of the gas mole decrease is explained by the permeability of the silicone hose, the difference is probably due to gas dissolution in the water

Liquid Inclusion in Hoses

The model we developed accounts for a volume of gas in the container. There is a risk, when using the test bed, that some liquid drops remain in the hose (Fig. 5.4.15). This affects the behavior of the system, since the continuity of the gas in the container is not realized.

⁴the remaining of the hose was filled with water

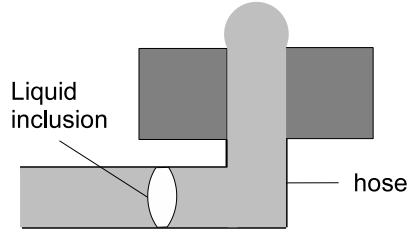


Figure 5.4.15: Illustration of a liquid inclusion in a flexible hose. The behavior of the system is modified because the volume of the gas container is limited to the portion between the bubble and the inclusion

Table 5.4.1: Mass of the tables and the force they apply on each bubble, assuming the load is distributed evenly on three bubbles in water

Table number	Type	Mass (kg)	Force on a bubble (N)
1	Blind holes	$14.4 \cdot 10^{-6}$	$29.6 \cdot 10^{-6}$
2	Through holes	$12.3 \cdot 10^{-6}$	$25.3 \cdot 10^{-6}$
3	Blind holes	$14.8 \cdot 10^{-6}$	$30.5 \cdot 10^{-6}$

It is therefore important to avoid the presence of these drops. Experimentally, we have seen that silicone oil was more likely to form these drops, probably because the liquid penetrates in the platform holes more easily than water, since its surface tension is lower.

5.4.5 Methodology for Results Analysis

We present here the method used to analyze the images captured to validate the model.

First, the different tables were weighted, as they will be the load applied on the bubbles. The weight of the tables is shown in Table 5.4.1. They are all made out of aluminum, material for which we assume the density is $\rho_a = 2700 \text{ kg m}^{-3}$. We have also indicated the force exerted by each table on a single bubble (F_{bubble}), given by:

$$F_{bubble} = m g \left(1 - \frac{\rho_w}{\rho_a} \right) \frac{1}{3} \quad (5.4.2)$$

where m is the mass of the table, $g = 9.81 \text{ m s}^{-2}$ is the gravity constant and $\rho_w = 1000 \text{ kg m}^{-3}$ is the density of water.

For the experiments, we will always use table 1 in contact with the bubbles. Then, to increase the load, we lay table 2 on table 1, and finally we lay table 3 on table 2.

Measurement of the Anchoring Circle Diameter

We have measured by mean of an inverted microscope *DMI3000 M* from *Leica* with a $5\times$ lens the geometry of the table and the platform. The image has been acquired by a *Marlin F-131B* camera from *Allied Vision Technologies*, and the calibration between length and pixel has been made using a 1mm ceramic reference part from *Mitutoyo*.

Measurement of the table has been made by manually clicking several points of the edge

Table 5.4.2: Measurement of the diameter of the anchoring circles (5 measurements)

Hole	Mean diameter (m)	Standard Deviation (m)
Table		
1	$916 \cdot 10^{-6}$	$1.19 \cdot 10^{-6}$
2	$874 \cdot 10^{-6}$	$1.40 \cdot 10^{-6}$
3	$878 \cdot 10^{-6}$	$2.43 \cdot 10^{-6}$
Platform		
1	$1.23 \cdot 10^{-3}$	$1.81 \cdot 10^{-6}$
2	$1.26 \cdot 10^{-3}$	$4.32 \cdot 10^{-6}$
3	$1.25 \cdot 10^{-3}$	$4.06 \cdot 10^{-6}$

(which is the anchoring circle) and searching by a least square method the circle fitting the points. This procedure has been repeated 5 times for each hole.

The same procedure has been used for the platform. The examination of the holes with the microscope showed that the holes have been chamfered. The nominal diameter is supposed to be 1 mm, but due to the chamfers, the effective diameter is larger.

The results of the measurements are shown in Table 5.4.2.

Initial Bubble Height Measurement

The first step of the experimentation is to generate three bubbles. We first measure the height of these bubbles as it will influence the initial gap when the table is laid on the bubbles.

The bubbles have been measured using the same method as for the experimental validation of the volume controlled bubble generator. The measurement has been made five times in order to estimate the manual point clicking errors. Figure 5.4.16 shows an example of such image.

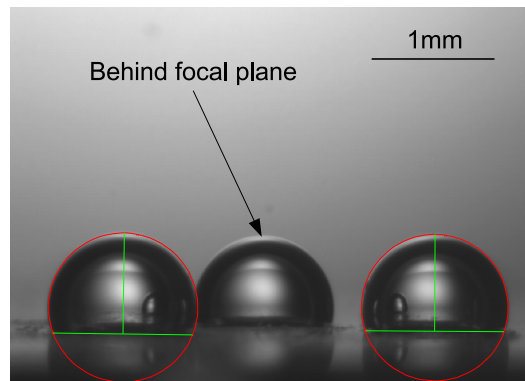


Figure 5.4.16: View of free bubble measurement. This image is acquired before the table is put on the bubbles, and allows to calculate the number of gas mole

Calculation of Number of Mole

The number of gas mole is calculated on the basis of the first image (Fig. 5.4.16 for example), i.e. image of the bubble without table.

Knowing the volume in the gas container (level of gas in the flexible hose V_0 , which have scale marks), and measuring the parameters of the first bubble (volume V and radius R), it is possible to calculate the number of gas mole in the system:

$$n = \left(P_0 + \frac{2\gamma}{R} \right) \frac{V_0 + V}{R_g T} \quad (5.4.3)$$

Profile Measurement

Due to parallax, it is difficult to image the anchoring sites. Nevertheless, the profile of the bubbles is supposed to be axisymmetric and have a constant mean curvature. Therefore, it can theoretically be measured on any portion of the meniscus.

We thus first select a rectangle including a part of the profile with a good contrast. Then a routine finding automatically the edge, i.e. a sudden transition of gray level, is run. This returns a set of points belonging to the profile. This selection is performed on both sides of the bubble.

Then a least square method is run to find the position of bubble symmetry axis and the mean curvature of the profile.

An example of such analysis is shown in Fig. 5.4.17.

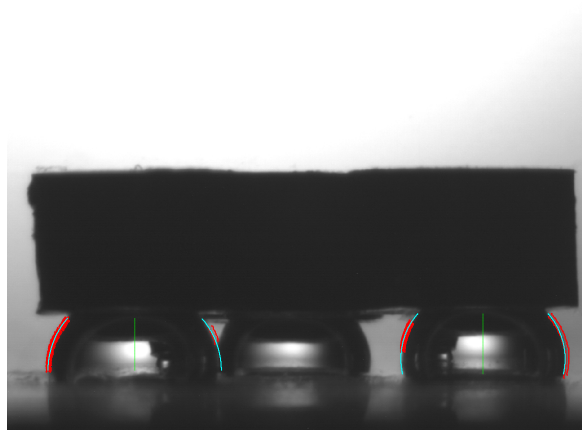


Figure 5.4.17: Example of profile measurement. The crosses (very close to each other, creating a thick line) correspond to edge detection inside the rectangle manually drawn. The lines represent the constant mean curvature curve fitting best these points. The symmetry axis is also represented

Gap Distance Measurement

Because of the parallax problem explained in Sect. 5.4.4, it is difficult to see the contact points of bubble profile with the table and platform.

To measure the gap distance, we have manually detected the left and right bottom vertices of the table, and defined a line between these two points. This line passes through the center of the anchoring circles of the table. We have also detected manually the line passing through the center of the anchoring circles on the platform by manually detecting the points at which the left profile of the left bubble and the right profile of the right bubble start to appear mirrored in the platform.

Using the position of the symmetry axis on the abscissa, calculated during the profile measurement, we calculate the difference of ordinate of both lines. This difference is the measurement of the gap distance between the table and the platform. This is illustrated in Fig. 5.4.18.

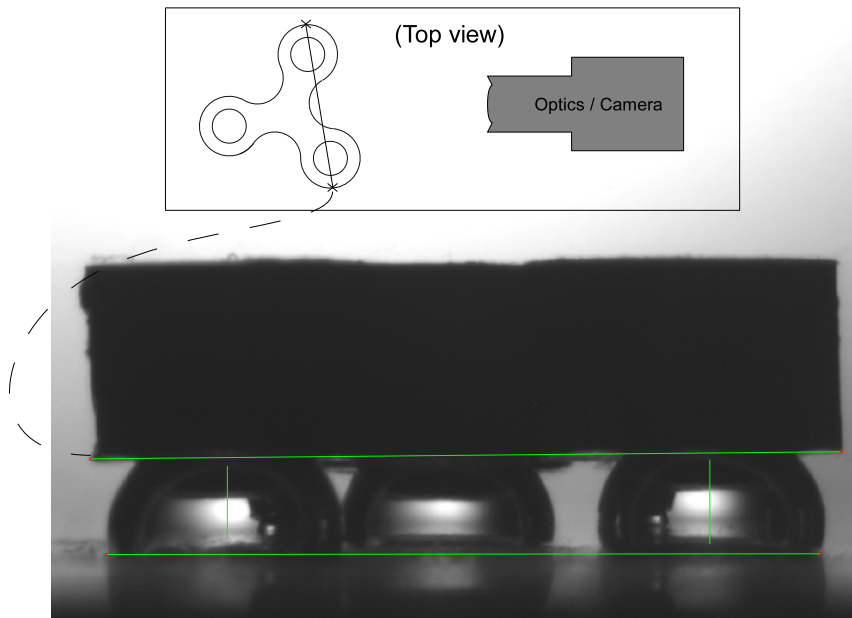


Figure 5.4.18: Illustration of gap measurement. Two lines are drawn, each of these lines is supposed to cross the center of the anchoring circles. The line on the table is drawn between the bottom left and bottom right vertices (see the top view). The line on the platform is drawn using the point where bubble profile starts to reflect in the platform. The gap is the difference of ordinate for both lines, at the abscissa of the bubble symmetry axis

5.4.6 Experimental Results

We made in total four different tests in water, using always table 1 in contact with the bubbles. We varied the volume of gas in the system, and the initial height of the bubbles. These parameters are summarized in Table 5.4.3. Due to technological issues, we could not perform relevant measurements in silicone oil, as this requires significant changes in the experimental setup. We only analyzed bubble from hole 1 (on the left on the images), due to image calibration issue.

Table 5.4.3: Input parameters for the experimental validation of model predicting the force developed by a gas bubble

Test	V_r (m ³)	h_0 (m)	ΔP_0 (Pa)	n (mol)
1	$9.82 \cdot 10^{-8}$	$816 \cdot 10^{-6}$	239	$4.051 \cdot 10^{-6}$
2	$9.82 \cdot 10^{-8}$	$903 \cdot 10^{-6}$	217	$4.059 \cdot 10^{-6}$
3	$5.89 \cdot 10^{-8}$	$848 \cdot 10^{-6}$	229	$2.445 \cdot 10^{-6}$
4	$1.96 \cdot 10^{-8}$	$733 \cdot 10^{-6}$	235	$8.299 \cdot 10^{-7}$

For each test, the model has been run with the same parameters, assuming the number of mole in the gas system is constant. The results are shown in Fig. 5.4.19. For each experiment, the results of the five repetitions of the analysis procedure is shown, in order to estimate the errors from the manual pointing. From these results, we see that the model systematically predicts a force larger than the experimental results for a given gap u .

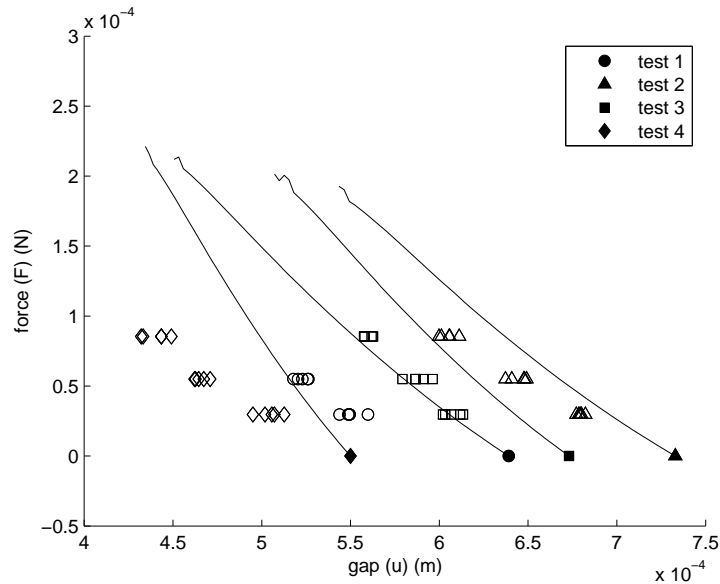


Figure 5.4.19: Comparison between model and experiments. The four tests (parameters in Table 5.4.3) are represented with the open symbols. There are five repetitions of the analysis for each point. Test 1 has been performed with table 1 and 2 only. The model curve corresponding to the input parameters is represented by continuous lines identified by a filled symbol. There is a significant difference between experiment and model, that can be explained by the disagreement about the constant mole number hypothesis

The origin of this error could be an error in the input parameters. All parameters would require a significant change to fit the results, except the number of gas moles which turned out to be a very sensitive parameter.

Indeed, a small variation of the number of mole in the gas system has a very significant influence on the output of the model, assuming the volume in the gas container is constant. We have found that assuming a linear variation of the gas mole number of 0.45% in the worst case, it is possible to make the model fit the experiments (Fig. 5.4.20). In these corrected simulations, we have supposed that the number of moles changes linearly with the gap. The

Table 5.4.4: Maximal variations of n corresponding to the smallest gap (experimental results) for each test and corresponding permeation time

Test	Variation of n at smallest experimental gap (percent of initial value)	Corresponding permeation time through flexible hose (s)
1	0.09%	131
2	0.06%	96
3	0.13%	199
4	0.45%	682

variations are shown in Table 5.4.4, together with the time needed for this amount of gas mole to permeate through the silicone flexible hose (Sect. 5.4.4). This time is an upper bound of the time effectively needed for the gas to leave the system since it accounts only for permeation, and not for dissolution for example. The linear variation of n with u is only approximative, since the real evolution should be taken with respect to time. This may explain for example the deviation still observed for test 1 and test 3.

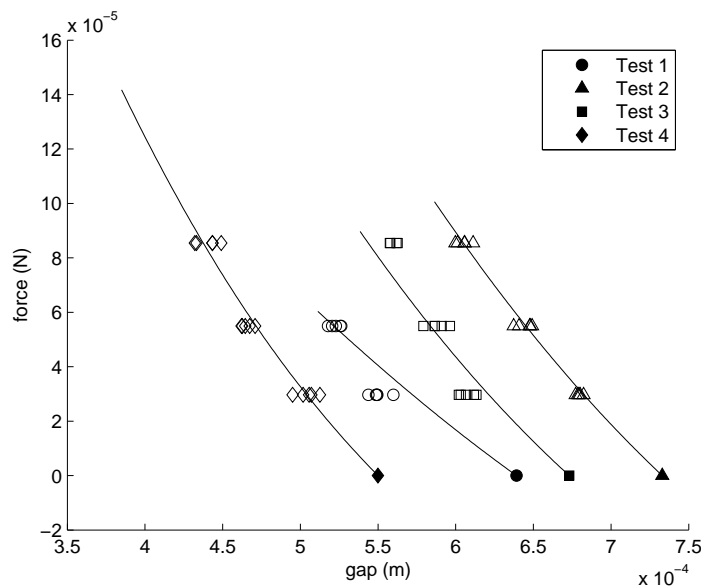


Figure 5.4.20: Comparison between experiments (open symbols) and model (continuous line) with a linear correction of gas mole number. This shows that the model is very sensitive to a variation of gas mole number

5.4.7 Conclusion on the Experimental Results

The experimental validation of the model shows results with a good adequacy after correction of the mole number. Indeed, the model initially assumes that the mole of gas is constant in the system, which is in fact not the case when we use our prototype with silicone flexible

hoses in water. We can explain these mole number variation from the permeation of the gas through the flexible hoses, and from the dissolution of air in water. However these phenomena, especially the dissolution, are not easy to quantify precisely. We have tried to isolate the dissolution phenomenon by using silicone oil instead of water. But it turns out that silicone material of the hoses shows poor properties if used with silicone oil. Indeed, the hoses wall swells up and becomes fragile, with oil seeping through it.

The best solution to refine the experimental validation is to use other connections to the platform, and other actuators. We suggest to use PTFE hoses (PTFE has a permeability 150000 times lower with oxygen than silicone [99]) and syringes as actuation mean. Using syringes would allow to change the volume of the gas container over several orders of magnitude.

To avoid dissolution of the gas in the liquid, we suggest to perform the experiments in silicone oil. This oil should not be too viscous, to ease the manual manipulation of the table. A viscosity of $10 \text{ mm}^2/\text{s}$ (*200 Fluid 10CST* from *Dow Corning* for example) seems to have good properties.

Moreover, the analysis of the experimental results is not easy due to bad image contrast. This could be improved by looking at a single and isolated bubble, to avoid overlaying (Fig. 5.4.21). The two other bubbles could then be adjusted to ensure that the table is parallel to the platform. Finally, to avoid parallax phenomenon, the platform should be as small as possible.

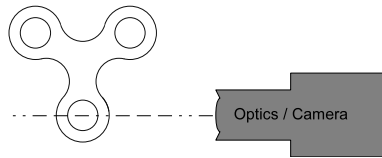


Figure 5.4.21: To avoid the problem of bubble overlaying, we suggest to look at only one bubble. The other bubbles could then be adjusted to ensure the parallel alignment of the table with the platform

Finally, the measurement of the force with respect to gap could also be performed on an AFM based system, as the one used in Sect. 5.4.1. The idea is to use the AFM tip to push directly on the surface of the table. This would be very interesting because it would produce a curve with a much better resolution than what we get by placing discrete components on the table as loads. The actual test bed has been developed in order to be inserted in the AFM device of the BEAMS Department (Fig. 5.4.22).

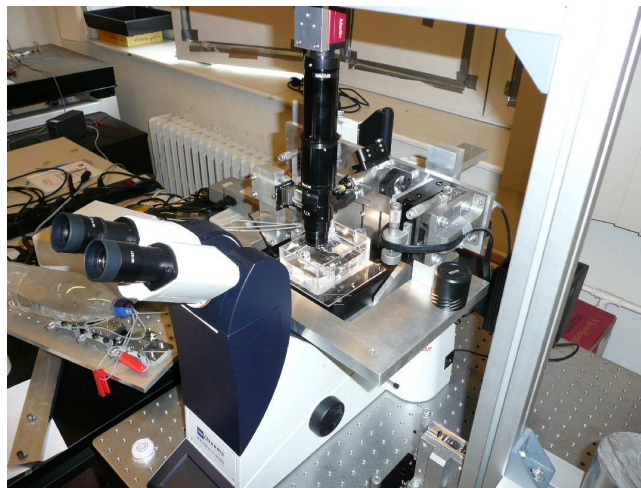


Figure 5.4.22: View of the test bed placed in the AFM device of the BEAMS Department

5.5 Improvement of the Prototype

The prototype presented in Sect. 5.2 and used for the validation of the force model has some drawbacks, as presented through Sect. 5.4. Thanks to these experiments, we are able to suggest improvements to design a better device.

5.5.1 Layout of the device

In the current design, there are three bubbles to support the table. These bubbles should be as far from each other as possible, considering the size of the table. We have also seen that it could be useful to add three other bubbles to measure the pressure (Sect. 4.4.1). Since laser measurement of bubble height needs technological development, we suggest as a first step to place the three sensing bubbles aligned one next to one another, in an area away from the table position, so that their shape can be analyzed easily with an image acquisition system.

The layout we currently consider is shown in Fig. 5.5.1.

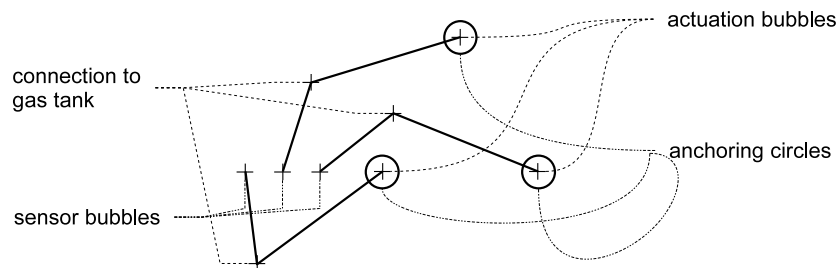


Figure 5.5.1: View of suggested improvement of the device platform layout. The crosses represent holes, and the lines represent grooves in the material, making improved anchoring circles and microchannels

5.5.2 Manufacturing

The manufacturing of the improved device requires another technology to manufacture precisely and without burrs on the grooves and holes. CNC milling showed some limitations in the manufacturing of our prototype.

Another technology investigated is the excimer laser technology [72]. It is a laser ablating method, with a small wavelength (typically 248 nm or 193 nm) allowing to machine polymeric materials (polycarbonate for example), with details of 1 μm . This technology seems to fit our needs, especially in the case of downscaling the device.

Currently some prototypes have been manufactured using the excimer laser (see Table 5.5.1 for laser parameters), but we are still investigating to find the best method to seal the channels and make the connections with the flexible hoses to the gas container. Figure 5.5.2 shows a view of the current layout realization in a 750 μm thick polycarbonate plate using an excimer laser. The dark marks are material residues generated during the ablation process.

Table 5.5.1: Parameters of excimer laser used to manufacture prototypes

gases	Kr F
wavelength	248 nm
pulse energy	0.3 J/burst
attenuator	94%
beam size	10 mm × 30 mm
demagnification	10×
burst number	2100 burst for 750 μm in polycarbonate

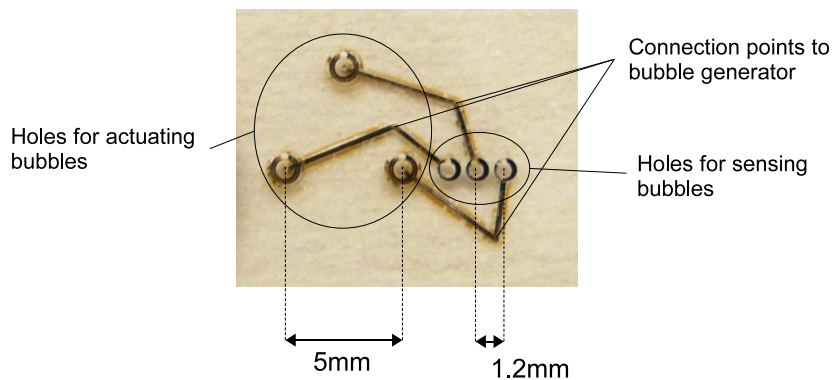


Figure 5.5.2: View of a manufacturing test of a new platform layout using excimer laser on a 750μm thick polycarbonate plate. The dark marks come from material residues generated during the ablation process

5.5.3 Lateral Forces

The prototype proposed in this section is laying on three bubbles. The lateral forces acting on the table are counterbalanced by the forces resulting from the non axisymmetric configuration of the bubbles. Those forces are responsible for the self-assembly of the tables, but they are smaller than the vertical forces.

If the table has to withstand larger lateral forces, it is possible to add lateral bubbles (Fig. 5.5.3), giving the device 6 actuated degrees of freedom. However this would probably make the manufacturing of the platform more difficult, since it becomes a 3-D structure.

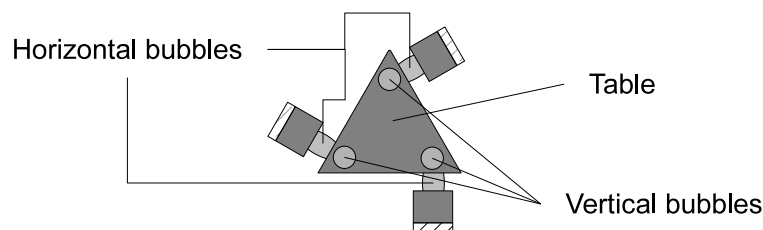


Figure 5.5.3: Design of a device with 6 bubbles, allowing to have 6 actuated degrees of freedom, and therefore able to support larger lateral forces than the design based on 3 bubbles

5.6 Conclusions

We have presented in this chapter a model to predict the force generated by a bubble. This model is based on the coupling between surface tension and gas compressibility. It is valid for a bubble caught between two solids, assuming an axisymmetric configuration. Its resolution requires to solve an ODE, which may be time consuming. To reduce calculation time, we have presented the idea of a parabolic approximation for bubble profile, but this approximation lacks of precision. If the application is time constrained, such as a real time controller, we therefore suggest to tabulate the results. From this model, it is easy to infer the vertical stiffness of a bubble.

We have shown that bubbles have interesting properties, such as self-assembly, adjustable stiffness, compactness, and their ease to be regenerated. We presented a device making use of these properties: a compliant table laying on three bubbles that could be used in microrobotic assembly tasks. This application indeed requires compliance to compensate positioning and manufacturing errors, and the parasitic forces inherent to microworld (electrostatic forces for example). The analysis of the model allowed to give some design rules to improve the performance of the device.

A prototype of this device has been manufactured and used to validate the model. However, we discovered that the pneumatic hoses were permeable to gas, nullifying the hypothesis of constant mole number. Yet the behavior of the prototype agreed with the model prediction.

Finally, based on the analysis of the model, and on the feedback of the technological issues encountered during the manipulation of the device, we suggested improvements for prototype design and for the experimental validation setup.

Next chapter will present some perspective for this work, and the final conclusions.

Chapter 6

Perspectives and Conclusions

So far, we have presented the interest to make use of surface tension forces in immersed microsystems. We have proposed in Chap. 4 a mean to generate single bubbles of predefined geometry, and we have presented a model to predict the force and stiffness of a gas bubble caught between two solids in Chap. 5. We have also presented a prototype of compliant microtable, based on the use of microbubbles as actuated legs.

The model we presented in Chap. 5 was based on quasi-static situations. In this chapter, we will first present some perspectives of further works to be achieved on this model. Then we will conclude this document by summing up the work accomplished during this thesis.

6.1 Prospective Developments

In this section we propose two developments that could be done on the compliant table, based on the models we have developed.

6.1.1 Controlled Microtable

The model of force generated by a bubble, such as presented in Sect. 5.3, takes the number of gas mole n and the gap between both solids u as input parameters, and outputs the force F and the profile mean curvature H (Fig. 6.1.1 (a)).

However, it would be more interesting to invert this model, in order to input n and H , and to output F and u (Fig. 6.1.1 (b)). This new model is more interesting for two major reasons.

First profile mean curvature could be easier to measure. Indeed we have seen that measuring the gap u was uneasy. We used an imaging based method, which was made difficult by parallax and bad contrast issues. Other non contact measurement techniques exist, but they have to be efficient to measure the position of an immersed object. Besides, the measuring device must generally be placed above or below the object, which is not easy in our configuration.

Pressure measurement, on the other hand, can be made anywhere in the gas circuit. We know that the pressure gauge in the gas circuit with relation to the pressure in the surrounding liquid is an image of the profile mean curvature (3.2.3). The knowledge of H is

therefore easier to get than the knowledge of u .

The knowledge of n can be measured initially, when no table is placed on the bubbles. Or, it could be determined by a calibration if the force applied on the bubbles is known (Fig. 6.1.1 (c)).

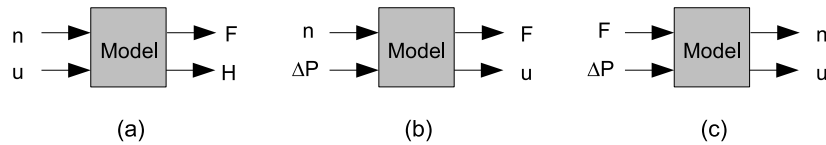


Figure 6.1.1: View of different variants of the force model. The model proposed in Sect. 5.3 (a) needs u as an input, which is not easy to measure. It is therefore more interesting to have a model with H as input, which is equivalent thanks to Laplace Law to have ΔP as input (b), because pressure is easier to measure. Finally, (c) presents the variation that could be used to calibrate the device with a predefined force in order to determine n

The second reason of this second model is the possibility to insert it in a control loop allowing to set the position of the table. Figure 6.1.2 shows how such control loop could be implemented, and where the model we developed should be used.

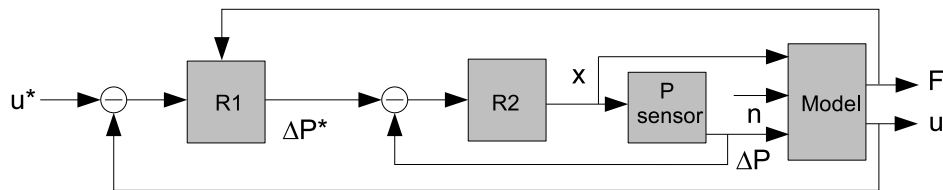


Figure 6.1.2: Proposition of a feedback loop to control the position of the table. This structure allows also to know the force applied on the table

In this schematic, u^* is the table position set point. The first controller $R1$ takes position error and force applied on the table as input, and outputs the pressure drop required. This value is compared to the actual pressure which is measured in the system. In the design presented, it is not possible to act directly on the pressure. But it is possible to use the actuation of the bubble generator to change the pressure. So the error between actual pressure gauge and set pressure gauge is entered in $R2$ controller, which outputs the bubble generator set point x . This modifies the pressure in the gas system, which is measured by a pressure sensor. Finally, the pressure and the number of mole in the system is entered in the model, which outputs the force applied on the table and its position. The volume of the gas container should also be included in the model, since it is modified to adjust the pressure. This is why we add the parameter x to the inputs of the model.

Such kind of control principle has already been investigated in the field of fluidic flexible actuators [34]. This implementation could greatly improve the compliant table prototype, since it would allow to have a reading of the force exerted by the assembly system on the table, for example to control the insertion force.

6.1.2 Dynamics of the Table

Chapter 5 gives a model for the force and for the stiffness of a bubble in a quasi-static situation. For microrobotic applications, it is also interesting to know the dynamic response of the system. This is interesting for example to determine the resonance frequency of the

device, or to estimate the time needed for the table to change its position, and if it will oscillate.

We propose to model the dynamic of the table as a mass-spring-dashpot system. The general equations for the study of table dynamics along the actuated DOF are:

$$m \ddot{u} + b_t \dot{u} + k_t u = R_z \quad (6.1.1)$$

$$I_{x,y} \alpha_{x,y}'' + b_r \alpha_{x,y}' + k_r \alpha_{x,y} = \Gamma_{x,y} \quad (6.1.2)$$

where m is the mass of the table, u is the gap between the platform and the table, b_t is the viscous friction coefficient, k_t is the stiffness coefficient, R_z is the force resultant component along the axis orthogonal to the platform (z axis), $I_{x,y}$ is the moment of inertia along x and y axes, $\alpha_{x,y}$ is the rotation angle in the direction x and y , b_r is the viscous coefficient for rotation movement, k_r is the rotation stiffness coefficient, and $\Gamma_{x,y}$ is the torque resultant along x and y direction.

The stiffness k_t can be inferred from the stiffness of a bubble, considering three bubbles as parallel springs:

$$k_t = 3k \quad (6.1.3)$$

The objective is to find the three other parameters. We will in the next paragraphs give some estimations for b_t and k_r .

Vertical Damping

The vertical damping of the device will probably be essentially governed by the damping of the table due to the viscosity of the surrounding liquid. Due to the proximity of the table and the platform, a squeeze film configuration occurs.

Guyon [36] gives the value of the force exerted by the liquid on a table as a function of the table velocity:

$$F = -\frac{3\pi\eta R^4}{2u^3} \dot{u} \quad (6.1.4)$$

where v is table velocity along z axis, η is liquid dynamic viscosity, R is platform radius (assumed circular) and u is the distance between the table and the platform. The damping coefficient can be deduced from this equation.

In the case of a 1 mm radius table in liquid, with a gap distance of 500 μm , the damping coefficient is $b_t = 3.8e - 5 \text{ N s m}^{-1}$

Rotational Stiffness

Kaneda [46] studied the dynamic of a liquid bridge for a tilt movement. The order of magnitude for the rotational stiffness of a single water liquid bridge having a 2 mm diameter anchoring circle is $\simeq 2 \cdot 10^{-9} \text{ N m}$.

This is much lower than the effect due to the distribution of the three bubbles under the table. For example, if 2 bubbles having a vertical translation stiffness of 1 N m^{-1} are at a distance of 2 mm from each other, this produces an equivalent rotational stiffness of $4 \cdot 10^{-6} \text{ N m}$.

It is therefore acceptable to assume that the rotational stiffness will be determined by the geometry of the table and the vertical stiffness of a bubble.

Rotational Damping

Rotation damping of a single bubble has also been studied by Kaneda [46]. But it is likely that the predominant phenomenon here will also be the damping of the hole table and not the damping of isolated bubbles. However, this point must still be more deeply investigated.

Conclusion

The dynamic approach must still be investigated, and experimentally validated. To perform the experimental validation, our idea is to perform an actuation step, or to apply a force step to the table and to record the dynamic response of the system, with a high speed camera or with a displacement sensor. From the frequency and damping of the response, it should be possible to infer the value of the parameters.

6.1.3 Non Axisymmetric Bubbles

Another possible improvement of this work would be the modeling of non axisymmetric bubbles.

This would allow to predict the lateral forces that the table with three bubbles can withstand, and the corresponding stiffness. Such work can be done using numerical softwares like *Surface Evolver*, which is based on surface energy minimization to find the profile of the bubble. From there, it is once again possible to infer the force generated by a bubble.

This problem is currently investigated with liquid drops instead of gas bubble. A test bench, based on two parallel long cantilever beams of small thickness has been developed. It allows to move two solids in a direction parallel to their mating surfaces. The bottom solid is moved, and the liquid bridge pulls the top solid, which is attached to the cantilever beams. The stiffness of the cantilever beams opposes a resistance to the movement of the top solid, and the lateral force can be deduced from the relative movement between both solids and the stiffness of the beams.

6.2 Conclusions

This work started by the study of fluid-solid interaction in microsystems, with the purpose of determining the most relevant forces acting on micro objects in liquid environment. This approach would allow to find new design rules for the miniaturization of mechanical components, such as pumps, valves, gripper,...

The interest of liquid environment was on one hand the design of fluidic systems, and on another hand the micromanipulation in immersed environment, such as proposed in *Pronomia* project. Manipulation in liquid was seen as a solution to avoid parasitic and unpredictable forces that hinder the automation of manipulation and assembly tasks. These forces are essentially electrostatic forces and surface tension forces.

During our investigations, we have found out that other forces exist in liquid media, and that it is important to consider them when designing a microsystem. Electrostatic forces still

exist, in the form of electrophoresis or dielectrophoresis. The viscosity of the liquid induces hydrodynamic forces. And surface tension forces appear as soon as an interface exists in the liquid, which happens when bubbles are present in the liquid phase.

Considering these forces not as parasitic forces, but as potential actuation means, allows to create innovative designs. Indeed, simply downscaling macroscopic designs of mechanical devices is generally not a good idea, because the relative effects of the different forces change when the sizes are reduced. On the contrary, making use of the specificities of microworld opens the way to new implementations of mechanical functions.

With that in mind, we have decided to investigate the surface tension forces, more precisely the force a microbubble is able to produce. This force is indeed very promising, because scaling laws are favorable to surface tension effects, and because the study of these force depends mainly on mechanical quantities.

By modeling these forces, we have discovered phenomena going against our common "macroscopic" senses. For example, our first idea to generate bubbles was to use a simple syringe, and to push the required volume of gas to grow a bubble. But we have seen that it is not always possible to grow a bubble continuously from a syringe, because of the surface tension and the compressibility of the gas. In some cases, the bubble will suddenly explode, making the generation of a whole range of bubble sizes impossible. We have successfully modeled this phenomenon, and the model helped us to understand the relevant parameters and their relative importance.

The model of the force generated by a bubble between two solids brought also interesting properties. We have for example demonstrated that a bubble could be seen as a non linear spring, with a stiffness depending on the volume of the total gas system. We have also verified the scaling effects, which agreed that small bubbles have more effects than large bubbles.

Among different possible bubble based prototypes, such as a gripper or a force sensor, we have decided to make use of these interesting properties to design a novel kind of actuated compliant micro-assembly table. We have manufactured a prototype of this table, and we have been able to demonstrate the predicted properties.

Nevertheless, some improvements still have to be done. This first prototype allowed us to discover technological issues. The major problem is currently the disappearance of the gas molecules, through dissolution or permeation process. Since the volumes of gas are small, these phenomena are not negligible and hinder the behavior of the device. From the experience acquired with this first prototype, we have been able to suggest improvements of the design, such as changing liquid and materials, or improving the geometry.

Other properties, such as the lateral stiffness or the dynamic behavior, must still be investigated. The opportunity to control the position of the table must also be studied. We have presented basic ideas to initiate such development in this last Chapter.

Appendix A

Demonstration of Jurin's Law

Jurin's law describes the spontaneous rise of a liquid in a tube having a small diameter. It is based on the equilibrium of gravity force and surface tension force.

Suppose a liquid having a density ρ . A tube of diameter d , opened on both ends, is introduced in the free surface of the liquid. The liquid shows a surface tension γ and has a contact angle θ with the material of the tube. If θ is smaller than 90° , the liquid will spontaneously rise in the tube until the difference of its level with free surface is h . The schematic view of the system is shown in Fig. A.0.1.

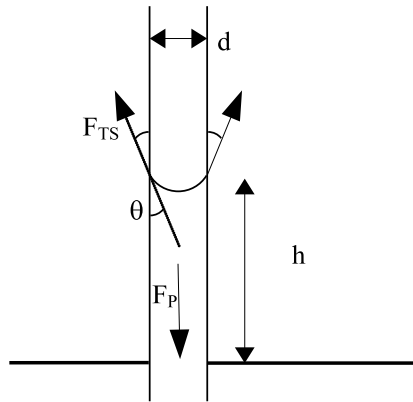


Figure A.0.1: Schematic view of equilibrium in Jurin's law. Surface tension force F_{TS} compensates the weight of the liquid comprised in the tube F_P

Jurin's law is given by the equilibrium between surface tension force F_{TS} and the weight of the risen liquid F_P :

$$F_{TS} = F_P \quad (\text{A.0.1})$$

$$\pi d \gamma \cos(\theta) = \pi \frac{d^2}{4} h \rho g \quad (\text{A.0.2})$$

where g is the gravitational constant. From this relation, we deduce that the capillary rise is larger if the tube has a small diameter. The capillary rise is therefore:

$$h = \frac{4\gamma \cos(\theta)}{\rho g d} \quad (\text{A.0.3})$$

The relation can also be demonstrated considering the pressures and Laplace law (3.2.3). Suppose the atmospheric pressure is P_0 . In Fig. A.0.2 are indicated the different pressures in the liquid. Since the top of the liquid is higher than the free surface on the represented situation, the pressure in the liquid at the interface is $P_0 - \rho g h$. If we assume that the mean curvature near the triple line is $1/r$, we deduce from Laplace law:

$$\frac{2\gamma}{r} = \rho g h \quad (\text{A.0.4})$$

and the relation with contact angle θ :

$$2r \cos(\theta) = d \quad (\text{A.0.5})$$

which leads to the same relation as above.

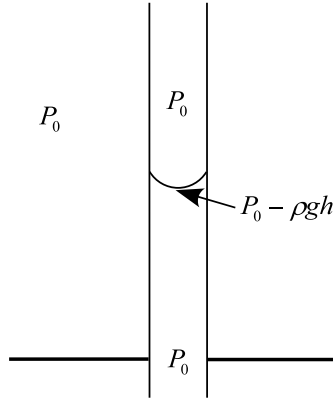


Figure A.0.2: Schematic view of pressure distribution in Jurin's law. The pressure on the top of the liquid is smaller than atmospheric pressure

If the tube is closed on the opposite side to the one inserted in the free surface of the liquid, the equilibrium must take account of the pressure rise in the gas comprised between the liquid and the end of the tube when the liquid rises. If we assume that the pressure in the sealed tube is equal to atmospheric pressure P_0 when $h = 0$, the pressure force F_{Pr} due to gas compression is:

$$F_{Pr} = \pi \frac{d^2}{4} \Delta P = \pi \frac{d^2}{4} P_0 \left(\frac{V_0}{V_0 - \pi d^2 h} - 1 \right) \quad (\text{A.0.6})$$

where V_0 is the volume of the sealed tube.

The equilibrium is in this case:

$$\pi d \gamma \cos(\theta) = \pi \frac{d^2}{4} h \rho g + \pi \frac{d^2}{4} P_0 \left(\frac{V_0}{V_0 - \pi d^2 h} - 1 \right) \quad (\text{A.0.7})$$

The relation allows to calculate the height of the capillary rise in the case of a sealed tube.

Appendix B

Construction of Fifth Order Polynomial Modeling Volume Controlled Bubble Generator

This appendix presents the detailed calculation of (4.2.8).

We first combine (4.2.4) and (4.2.7) in (4.2.5).

$$\left(\frac{2\gamma}{R} + P_0\right) \left(\frac{\pi h}{6} \left(\frac{3s^2}{4} + h^2\right) + V_0 - \Delta V\right) = n R_g T \quad (\text{B.0.1})$$

We develop this expression:

$$\frac{2\gamma}{R} \frac{\pi h}{6} \left(\frac{3s^2}{4} + h^2\right) + (V_0 - \Delta V) \frac{2\gamma}{R} + \frac{P_0 \pi h}{6} \left(\frac{3s^2}{4} + h^2\right) + (V_0 - \Delta V) P_0 = n R_g T \quad (\text{B.0.2})$$

Since R is different from 0, we have:

$$\frac{\gamma \pi h s^2}{4} + \frac{\gamma \pi h^3}{3} + 2\gamma(V_0 - \Delta V) + \frac{R P_0 \pi h s^2}{8} + \frac{R P_0 \pi h^3}{6} + R P_0 (V_0 - \Delta V) = n R R_g T \quad (\text{B.0.3})$$

The spherical cap is defined by R , s and h . But (4.2.6) shows that only two parameters are independent. It is of course necessary to keep h as it is the output of our model. As second variable, it is preferably to keep s as it is measurable on the device and is constant, no matter the value of h . Hence we eliminate R from the equation:

$$\begin{aligned} \frac{\gamma \pi h s^2}{4} + \frac{\gamma \pi h^3}{3} + 2\gamma(V_0 - \Delta V) + \left(\frac{s^2}{8h} + \frac{h}{2}\right) \frac{P_0 \pi h s^2}{8} + \\ \left(\frac{s^2}{8h} + \frac{h}{2}\right) \frac{P_0 \pi h^3}{6} + \left(\frac{s^2}{8h} + \frac{h}{2}\right) P_0 (V_0 - \Delta V) = n \left(\frac{s^2}{8h} + \frac{h}{2}\right) R_g T \end{aligned} \quad (\text{B.0.4})$$

We now have to simplify this expression. We assume h is different from 0, but we will verify that in the final expression, $\Delta V = 0$ means $h = 0$. We multiply the equation by h :

$$\begin{aligned} & \frac{\gamma \pi h^2 s^2}{4} + \frac{\gamma \pi h^4}{3} + 2\gamma h (V_0 - \Delta V) + \left(\frac{s^2}{8} + \frac{h^2}{2} \right) \frac{P_0 \pi h s^2}{8} + \\ & \left(\frac{s^2}{8} + \frac{h^2}{2} \right) \frac{P_0 \pi h^3}{6} + \left(\frac{s^2}{8} + \frac{h^2}{2} \right) P_0 (V_0 - \Delta V) = n \left(\frac{s^2}{8} + \frac{h^2}{2} \right) R_g T \end{aligned} \quad (\text{B.0.5})$$

Finally, we regroup the terms to form a polynomial with h as dependent variable:

$$\begin{aligned} & \frac{\pi}{12} P_0 h^5 + \frac{\pi}{3} \gamma h^4 + \frac{\pi}{12} P_0 s^2 h^3 \\ & + \left(-\frac{1}{2} n R_g T + \frac{1}{2} P_0 (V_0 - \Delta V) + \frac{\pi}{4} \gamma s^2 \right) h^2 \\ & + \left(\frac{\pi}{64} P_0 s^4 + 2\gamma (V_0 - \Delta V) \right) h \\ & + \frac{1}{8} P_0 s^2 (V_0 - \Delta V) - \frac{1}{8} n R_g T s^2 = 0 \end{aligned} \quad (\text{B.0.6})$$

Appendix C

Demonstration for Equality of Forces Along Bubble Profile

To be at equilibrium, the sum of forces acting on any slice of the meniscus must be equal to zero. Indeed, let us consider the meniscus depicted in figure C.0.1.

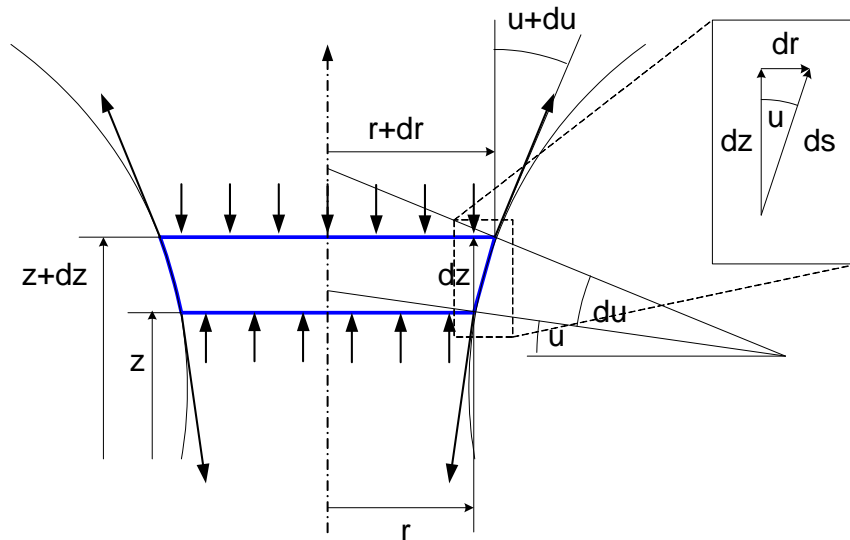


Figure C.0.1: Equilibrium of a meniscus slice comprised between z and $z + dz$. It can be shown that the capillary force computed at height z exactly balance the the capillary force computed at height $z + dz$.

The force exerted on the bottom face of the slice is equal to:

$$\bar{F}(z) = (\pi r^2 \Delta p - 2\pi r \gamma \cos u) \bar{1}_z \quad (\text{C.0.1})$$

while the force acting on the top face of the slice is given by:

$$\begin{aligned}\bar{F}(z + dz) &= (-\pi(r + dr)^2 \Delta p + 2\pi(r + dr)\gamma \cos(u + du)) \bar{1}_z \\ &= \left[-\pi r^2 \Delta p + 2\pi r \gamma \cos u + 2\pi \underbrace{(-r dr \Delta p + r \gamma \sin u du + \gamma \cos u dr)}_I + O^2 \right] \bar{1}_z\end{aligned}\tag{C.0.2}$$

The underbraced expression I can be shown to be equal to zero by expressing the Laplace law:

$$\begin{aligned}\Delta p &= 2H\gamma \\ &= \left(-\frac{r''}{(1+r'^2)^{3/2}} + \frac{1}{r(1+r'^2)^{1/2}} \right) \gamma\end{aligned}\tag{C.0.3}$$

$$= \left(\frac{du}{ds} + \frac{\cos u}{r} \right) \gamma\tag{C.0.4}$$

$$= \left(\frac{du}{dr} \sin u + \frac{\cos u}{r} \right) \gamma\tag{C.0.5}$$

leading to:

$$I = -r du \sin u \gamma - dr \cos u \gamma + r \gamma \sin u du + \gamma \cos u dr = 0\tag{C.0.6}$$

Consequently, the forces $\bar{F}(z) + \bar{F}(z + dz)$ balance, and the capillary force given by $F(z)$ can be computed at any value of z . This means that in the case of a bubble between two solids, the force can be computed anywhere along bubble axis.

In the case of the force calculation by image analysis, it is therefore not necessary to have a clear view of the anchoring circle to calculate the force applied by the bubble on the table, since the force can be evaluated on any portion of the bubble which is clearly visible.

Appendix D

Demonstration for Nullity of Force for Part-Spherical Profiles

In this appendix, we demonstrate that the capillary force exerted by a bubble having the shape of a portion of a sphere is zero.

Suppose the configuration represented in Fig. D.0.1. The bubble is portion of a sphere having a radius R . Its base disk has a radius r . Surface tension force along z axis (unitary vector $\bar{1}_z$) is given by (3.2.7):

$$\bar{F}_{TS} \cdot \bar{1}_z = -2\pi r \gamma \cos(\theta) \quad (\text{D.0.1})$$

where

$$r = R \cos(\theta) \quad (\text{D.0.2})$$

Pressure force along z axis is given by:

$$\bar{F}_P \cdot \bar{1}_z = \pi r^2 \Delta P \quad (\text{D.0.3})$$

where ΔP is given by Laplace law (3.2.3):

$$\Delta P = \frac{2\gamma}{R} \quad (\text{D.0.4})$$

Therefore we have:

$$F_{TS} \cdot \bar{1}_z + F_P \cdot \bar{1}_z = -2\pi r \gamma \frac{r}{R} + \pi r^2 \frac{2\gamma}{R} = 0 \quad (\text{D.0.5})$$

which demonstrates that the capillary force exerted by a bubble having the shape of a portion of a sphere is zero.

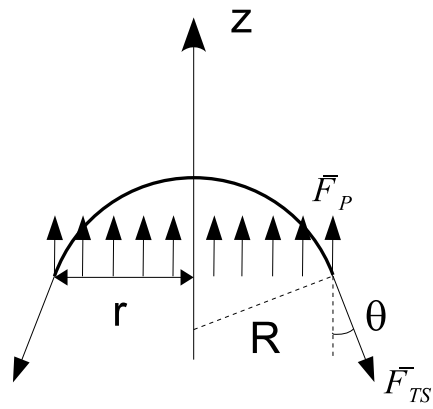


Figure D.0.1: Schematic of force balance in the case of a bubble having a part spherical shape

Appendix E

Complements About Forces Acting on Immersed Microcomponents

E.1 Electrophoresis

ζ -potential can be expressed as follow [30]:

$$\zeta = \frac{\sigma_0 K^{-1}}{\epsilon} \quad (\text{E.1.1})$$

where σ_0 is the equivalent surface charge density on the solid surface, ϵ is the permittivity of the liquid and K^{-1} is the distance between the shear plane and the solid (K is called Debye-Hückel parameter). This distance is a function of the ionic force of the solution (between 3nm and 96nm in water at 25°C):

$$K = \sqrt{\frac{2000 F a^2}{\epsilon_f R T}} \sqrt{\mu} \quad (\text{E.1.2})$$

where μ is the ionic strength of the liquid:

$$\mu = 0.5 \sum c_i z_i^2 \quad (\text{E.1.3})$$

where the sum is extended to all ions in the solution, c_i is the concentration and z_i is the charge of the ion.

ζ -potential is measured with a zeta-meter, usually with respect to the pH of the solution. Zeta-meter is a device with a cell containing the fluid and the particles, two electrodes to apply an electric field, and an optical system to measure the velocity of the particles. From the equilibrium between viscous forces and electrophoresis, the zeta potential can be inferred. An interesting result is the pH corresponding to $\zeta = 0$.

E.2 Dielectrophoresis

Approximations of the dielectric force can be found in the literature, for example in the case of a sphere [84, 15]:

$$F_{DEP} = 2\pi\epsilon_f r^3 \text{Re}(\text{CM}(\omega)) \nabla E_{rms}^2 \quad (\text{E.2.1})$$

where ϵ_f is the permittivity of the surrounding medium, r is the radius of the sphere, E_{rms} is the root mean square value for the electric field and CM is called Clausius-Mossotti factor, taking into account the complex permittivity of the particle ϵ_p^* and the medium ϵ_m^* and the frequency of the electric field:

$$\text{CM} = \frac{\epsilon_p^* - \epsilon_m^*}{\epsilon_p^* + 2\epsilon_m^*} \quad (\text{E.2.2})$$

and

$$\epsilon^* = \epsilon - \frac{i\sigma}{\omega} \quad (\text{E.2.3})$$

where σ is the conductivity and ω is the frequency of the electric field.

The sign of the real part of Clausius-Mossotti factor will determine if DEP force will induce a repulsive or an attractive behavior.

E.3 Hydrodynamic Forces

Another approach to calculate hydrodynamic force, compared to (2.2.2) is to use the drag coefficient C_D to express the force [43]:

$$F_{HD} = 0.5 C_D \rho U_\infty^2 \pi a^2 \quad (\text{E.3.1})$$

where ρ is the fluid density.

Drag coefficient is a function of Reynolds number (Re). For $Re \leq 1$, comparing (2.2.2) and (E.3.1), we can show the dependency of C_D with Re :

$$C_D = \frac{12}{Re} \quad (\text{E.3.2})$$

which is in these conditions inversely proportional to Re . We have tested this theory with a simulation using *Comsol Multiphysic* FEM software. This simulation solves Navier-Stokes equation in axisymmetric configuration (cylindrical coordinates (r, z)), with a no-slip condition at the surface of the sphere. Fluid velocity (u_r, u_z) is set on the outer boundaries of the box defining the calculated area. Some captions of the velocity field are shown in Fig. E.3.1. The force is postprocessed from the velocity and pressure field:

$$F = \int_S 2\pi r P n_z ds - \int_S 2\pi r (n_r \tau_{rz} + n_z \sigma_z) ds \quad (\text{E.3.3})$$

where (n_r, n_z) are the components of the inward normal to the surface, and:

$$\tau_{rz} = \mu \left(\frac{\partial u_r}{\partial z} + \frac{\partial u_z}{\partial r} \right) \sigma z = 2 \mu \frac{\partial u_z}{\partial z} \quad (\text{E.3.4})$$

the integration is made along the profile of the sphere.

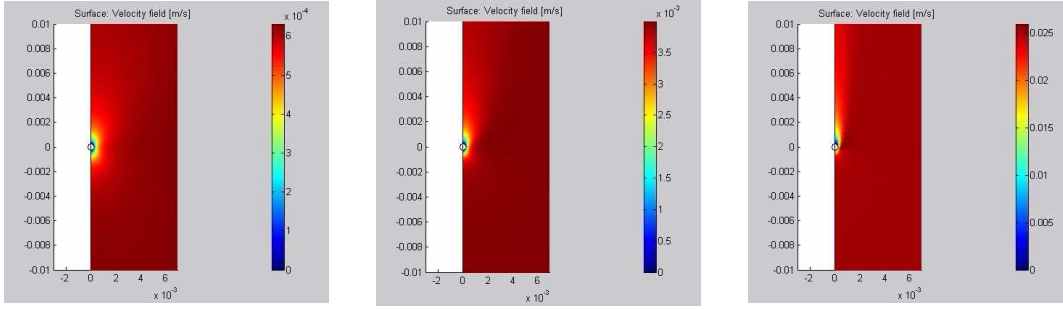


Figure E.3.1: View of simulation results. The velocity field around the sphere is shown for different velocity of approach U_∞

The force calculated on a $500\mu\text{m}$ sphere in water with respect to approach velocity is shown in Fig. E.3.2.

Simulation results have been compared to the drag coefficient with respect to Reynolds number curve found in [43]. This comparison is illustrated in Fig. E.3.3.

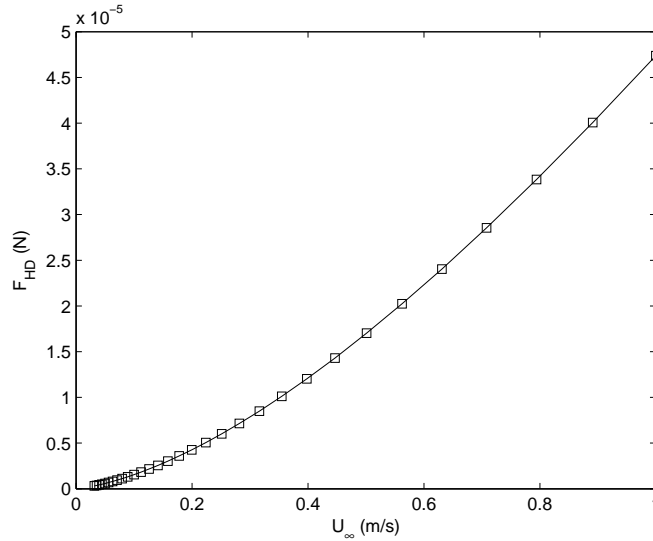


Figure E.3.2: Hydrodynamic force calculated from simulation on a $500\mu\text{m}$ sphere in water

Simulation results have also been compared to the sedimentation time of small spheres drop in a liquid. This experimental validation consists in dropping the particles in the liquid, and to measure the time needed for the particles to travel a predefined distance [25]. We suppose there that the steady state speed is reached instantaneously. This steady state speed corresponds to the balance of hydrodynamic force and gravity force (minus the buoyancy

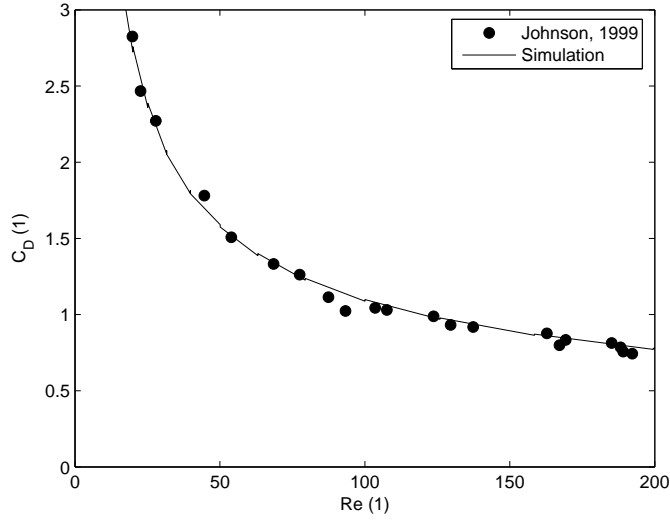


Figure E.3.3: Comparison of drag coefficient from simulations and from literature [43]

Table E.3.1: Sedimentation velocity of a particle dropped in a liquid: comparison between simulation (own results) and experiments [25]

Configuration	Simulation (m/s)	Experiment (m/s)	Re (Exp. Value)
500 μ m ruby sphere in water	0.116	0.121	60.5
500 μ m stainless steel sphere in water	0.207	0.214	107
500 μ m ruby sphere in oil	0.0085	0.0074	0.074
500 μ m stainless steel sphere in oil	0.0193	0.0177	0.177
300 μ m ruby sphere in oil	0.0031	0.0027	0.0162

force). The comparison between the simulations and the experiments is shown in table E.3.1, showing good agreement.

We have applied fluidic simulation tools to the design of a micro-object feeder inside a liquid [61]. As we have already mentioned, parasitic forces can prevent the gripping of an object because the object is moving away when the gripper is approaching, or make several components stick together (Sect. 1.2). The objective of a feeder is to place components that are in bulk at predefined locations, and separated from each other.

The design proposed is based on the use of hydrodynamic forces to guide components to housings, by creating streamlines heading towards these housings. When a component reaches a housing, it is supposed to block the streamline, making the remaining components heading towards the free housings (Fig. E.3.4). However, this design had a major flaw: some space is managed between the object and the housing wall to ease its extraction by the gripper. Because of this space, the streamline is not cut, and components are attracted above a filled housing. This prototype has been developed in an applicative context of clock assembly but show the proof of concept of feeder in submerged environment.

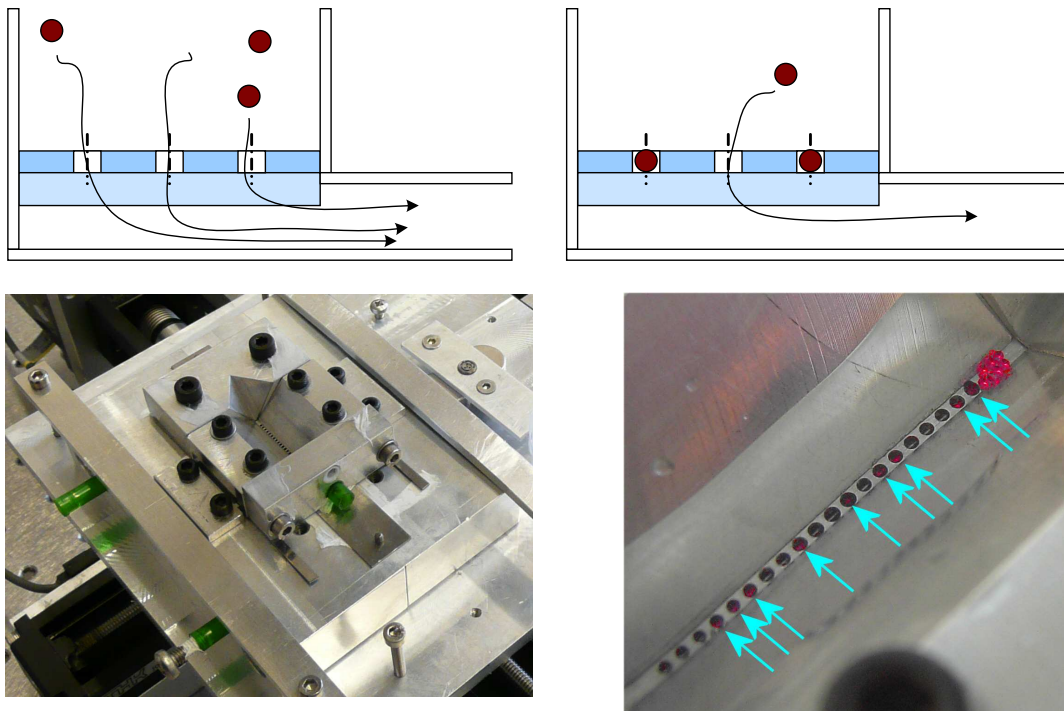


Figure E.3.4: Schematic view of a component feeder based on the use of hydrodynamic forces. The components are guided by the streamlines, heading towards the housings for the components. When a housing is filled with a component, the streamline is cut, guiding the remaining components to the free housings. The bottom views show a prototype of the device, used with $500\mu\text{m}$ ruby spheres. Arrows indicate the housings filled with a sphere

Appendix F

List of Publication

Journal

- Marie Blondeau, Aline De Greef, Pierre-Alexis Douchamps, Benjamin Genêt, Marc Haelterman, Cyrille Lenders, Erwan Leroy, Pascal Nardone, Vincent Raman, Aliénor Richard, and Frédéric Robert. Apprentissage par projet : Réalisation d'une éolienne urbaine en matériaux de récupération. *J3EA*, 8, 2009

Conference Proceedings

- Cyrille Lenders, Michaël Gauthier, and Pierre Lambert. Microbubble generation using a syringe pump. In *Proceedings of the 2009 IEEE International Conference on Intelligent Robots and Systems*, Saint-Louis (Missouri), October 11-15 2009
- Cyrille Lenders, Jean-Baptiste Valsamis, Maxime Desaedeleer, Alain Delchambre, and Pierre Lambert. Assembly of a micro ball-bearing using a capillary gripper and a microcomponent feeder. In *Micro-Assembly Technologies and Applications*. International Precision Assembly Seminar (IPAS), Springer, 2008
- Patricia Van Dale, Aline De Greef, Cyrille Lenders, and Nadine Warzée. Biomedical engineer and phlebologist: a midship frame. In *International Angiology - Proceedings of the XVI World Congress of the Union Internationale de Phlebologie (31 August - 4 September 2009)*, volume 28, page 138, 2009
- Marie Blondeau, Aline De Greef, Pierre-Alexis Douchamps, Benjamin Genêt, Marc Haelterman, Cyrille Lenders, Erwan Leroy, Pasquale Nardone, Vincent Raman, Aliénor Richard, and Frédéric Robert. Apprentissage par projet : Réalisation d'une éolienne urbaine en matériaux de récupération. In *Proceedings of the "7ème Colloque sur l'Enseignement des Technologies et des Sciences de l'Information et des Systèmes - CETISIS 08" (27-29 octobre 2008, Brussels, Belgium)*, October 2008

Others

- Cyrille Lenders: Study of valves used in microfluidics. *DEA*, Université libre de Bruxelles, Brussels, Belgium, 2006

A patent request has also been submitted in October 2009 and is currently under approval process. This patent is entitled "Meniscus-Supported Compliant Table". It is about the use of microbubbles as compliant actuators, such as described in Sect. 5.2.

In Preparation

- Cyrille Lenders, Pierre Lambert, and Michaël Gauthier. Three DOF microrobotic platform based on capillary actuation. To be submitted to *IEEE Transactions on Robotics*

List of Symbols

Table F.0.1: List of Symbols

Symbols	SI Units	Meaning
γ	N m^{-1}	surface tension at the interface of two fluids
γ_{s1}	N m^{-1}	surface tension at the interface of a solid and fluid 1
γ_{s2}	N m^{-1}	surface tension at the interface of a solid and fluid 2
T	K	absolute temperature of the (gas) system
T_c	K	temperature at critical point in a phase diagram
d	m	thickness of a geometry
h	m	height of a geometry
l	m	characteristic length of a component
R	m	radius of a sphere, or of a spherical cap
r_1	m	radius of triple line in case of an axisymmetric configuration. Index 1 means the lower triple line in case two exists
r_2	m	radius of triple line in case of an axisymmetric configuration. Index 2 means the upper triple line in case two exists
s	m	diameter of a circular hole
δ	m	displacement of the piston
H	m^{-1}	mean curvature of an interface
S	m^2	section of the piston
V_0	m^3	initial volume in the syringe or gas container
V	m^3	volume of gas in the spherical cap
ΔV	m^3	variation of container (positive if volume decreases)
g	m s^{-2}	gravitational constant (value: 9.81)
F_a	C mol^{-1}	Faraday constant (value: 96485)
R_g	$\text{Pa m}^3 \text{ mol}^{-1} \text{ K}^{-1}$	ideal gas constant (value: 8.314)
θ	$^\circ$	contact angle in liquid phase. Index 1 means the contact with bottom solid, index 2 means the contact with top solid
F_{cap}	N	capillary force
F_P	N	component of capillary force due to pressure drop
F_{TS}	N	component of capillary force due to surface tension along the triple line
n	mol	amount of gas mole
P	Pa	pressure inside the gas system
P_0	Pa	pressure outside the system, generally the sum of atmospheric pressure and hydrodynamic pressure
ΔP	Pa	pressure drop across interface between two fluids
ρ_l	kg m^{-3}	liquid density
U	V	voltage
Bo	1	Bond number
σ	1	dimensionless number used to predict the existence of an instability during bubble growth
C	C	electric charge
k	N m^{-1}	mechanical stiffness
E	Pa	Young modulus

Bibliography

- [1] Antonio Affanni and Giovanni Chiorboli. Development of an enhanced mhd micromixer based on axial flow modulation. *Sensors and Actuators B*, 147:748–754, 2010.
- [2] Joël Agnus, David Hériban, Michaël Gauthier, and Valérie Pétrini. Silicon end-effectors for microgripping tasks. *Precis. Eng.*, 33:542–548, 2009.
- [3] Daniel A. Ateya, Ashish A. Shah, and Susan Z. Hua. Impedance-based response of an electrolytic gas bubble to pressure in microfluidic channels. *Sensors and Actuators A*, 122:235–241, 2005.
- [4] Peter Atkins and Loretta Jones. *Chimie: molécules, matière, métamorphoses*. De Boeck, 1998. Translated from English by A. Pousse.
- [5] Ahmet Fatih Ayhan. Design of a piezoelectrically actuated microvalve for flow control in fuel cells. Master’s thesis, Middle East Technical University, 2002.
- [6] Charles N. Baroud and Hervé Willaime. Multiphase flows in microfluidics. *C.R. Physique*, 5:547–555, may 2004.
- [7] B. Berge. Electrocapillarité et mouillage de films isolants par l’eau. *Académie des sciences*, 317, série II:157, 1993.
- [8] B. Berge and J. Peseux. Variable focal lens controlled by an external voltage: An application of electrowetting. *Eur. Phys. J. E*, 3:159–163, 2000.
- [9] H. Bouazaze, S. Cattarin, F. Huet, M. Musiani, and R.P. Nogueira. Electrochemical noise study of the effect of electrode surface wetting on the evolution of electrolytic hydrogen bubbles. *J. Electroanalytical Chemistry*, 597:60–68, 2006.
- [10] S.E. Burns, S. Yiacoumi, and C. Tsouris. Microbubble generation for environmental and industrial separations. *Sep. Purif. Technol.*, 11:221–232, 1997.
- [11] Hans-Jürgen Butt, Brunero Cappella, and Michael Kappl. Force measurements with atomic force microscope: Technique, interpretation and applications. *Surf. Sci. Rep.*, 59:1–152, 2005.
- [12] Mathilde Callies, Yong Chen, Frédéric Marty, Anne Pépin, and David Quéré. Micro-fabricated textured surfaces for super-hydrophobicity investigations. *Microe. Eng.*, 78-79:100–105, 2005.
- [13] Moon-Hwan Chang, Dosi Dosev, and Ian M. Kennedy. Zeta-potential analyses using micro-electrical field flow fractionation with fluorescent nanoparticles. *Sensors and Actuators B*, 124:172–178, 2007.

- [14] Alexandre Chau. *Theoretical and experimental study of capillary condensation and of its possible use in micro-assembly - Etude théorique et expérimentale des forces dues à la condensation capillaire*. PhD thesis, Université libre de Bruxelles, 2007.
- [15] D.F. Chen, H. Du, and W.H. Li. Bioparticle separation and manipulation using dielectrophoresis. *Sensors and Actuators A*, 133:329–334, 2007.
- [16] Cédric Clévy, Arnaud Hubert, and Nicolas Chaillet. Flexible micro-assembly system equipped with an automated tool changer. *J. Micro-Nano Mech.*, 4(1-2):59–72, 2008.
- [17] J. R. Cooper. Iapws release on surface tension of ordinary water substance. Issued by the International Association for the Properties of Water and Steam, 1994.
- [18] Stephen Richard Coulson, Ian Burnett, and John Sambell. Coating of a polymer layer using low powder pulsed plasma in a plasma chamber of a large volume, 2005. Patent: WO2005089961A1.
- [19] Ron Darby and M. S. Haque. The dynamics of electrolytic hydrogen bubble evolution. *Chem. Eng. Sci.*, 28:1129–1138, 1973.
- [20] Pierre-Gilles de Gennes, Françoise Brochart-Wyart, and David Quéré. *Gouttes, bulles, perles et ondes*. Belin, 2002.
- [21] Nikolai Dechev, William L. Cleghorn, and James K. Mills. Microassembly of 3-d microstructures using a compliant, passive microgripper. *J. Microelectromechanical Syst.*, 13(2):176–189, 2004.
- [22] Jerome Dejeu, Patrick Rougeot, Michael Gauthier, and Wilfrid Boireau. Reduction of micro-object's adhesion using chemical fonctionnalisation. *Micro Nano Lett.*, 4(2):74–79, 2009.
- [23] Jérôme Dejeu, Patrick Rougeot, Michaël Gauthier, and Wilfrid Boireau. Robotic submerged microhandling controlled by ph switching. In *Proceedings of the 2009 IEEE International Conference on Intelligent Robots and Systems*, Saint-Louis (Missouri), October 11-15 2009.
- [24] Anne Delandtsheer. *Analyse - chapitre 18*. Université libre de Bruxelles, 2000.
- [25] Maxime Desaedeleer. Etude et réalisation d'un dispositif d'alimentation en composants microtechniques. Master's thesis, Université Libre de Bruxelles, 2007.
- [26] Timothy Eastman and Da-Ming Zhu. Adhesion forces between surface-modified AFM tips and a mica surface. *Langmuir*, 12(11):2859–62, 1996.
- [27] Stéphane Colin et al. *Microfluidique*. Hermes, 2004.
- [28] N. Eustathopoulos, E. Ricci, and B. Drevet. Tension superficielle. *Techniques de l'ingénieur*, M(67), 1999.
- [29] Y. Feng, Z. Zhou, X. Ye, and J. Xiong. Passive valves based on hydrophobic microfluidics. *Sensors and Actuators A*, 108:138–143, 2003.
- [30] Frantisek Foret, Ludmila Krivankova, and Petr Bocek. *Capillary Zone Electrophoresis*. VCH, 1993.
- [31] Yusuke Furuta, Hiroyuki Nishikawa, Takahiro Satoh, Yasuyuki Ishii, Tomihiro Kamiya, Ryota Nakao, and Satoshi Uchida. Fabrication and evaluation of 3d-electric micro filters using proton beam writing. *Microe. Eng.*, 86:1396–1400, 2009.

- [32] Michaël Gauthier, D. Heriban, D. Gendreau, S. Regnier, N. Chaillet, and P. Lutz. Microfactory for submerged assembly : Interests and architectures. In *Proc. of the 5th International Workshop on Microfactories*, pages 1–6, Besançon, France, October 2006.
- [33] Walter H. Graf. *Hydrodynamique, Une Introduction*. Presses polytechniques et universitaires romandes, 1995.
- [34] Aline De Greef, Pierre Lambert, Thomas Delwiche, Cyrille Lenders, and Alain Delchambre. Flexible fluidic actuators: Determining force and position without force or position sensors. In *Proceedings of the IEEE ISAM2009 conference (17-20 November 2009, Suwon, Korea)*, page 6, 2009.
- [35] M. Götzinger and W. Peukert. Dispersive forces of particle-surface interactions: direct AFM measurements and modelling. *Powder Technol.*, pages 102–109, 2003.
- [36] Etienne Guyon, Jean-Pierre Hulin, and Luc Petit. *Hydrodynamique Physique*. CNRS Editions, 2001.
- [37] Chien-Chong Hong, Po-Hsiang Chang, Chih-Chung Lin, and Chian-Lang Hong. A disposable microfluidic biochip with on-chip molecularly imprinted biosensors for optical detection of anesthetic propofol. *Biosensors and Bioelectronics*, 25:2058–2064, 2010.
- [38] L. L. Howell. *Compliant Mechanisms*. Interscience, July 2001.
- [39] Fangrong Hu, Jun Yao, Chuankai Qiu, and Hao Ren. A mems micromirror driven by electrostatic force. *J. Electrostat.*, 68:237–242, 2010.
- [40] Kaixuan Hu, Jung H. Kim, James Schmiedeler, and Chia-Hsiang Menq. Design, implementation, and control of a six-axis compliant stage. *Rev. Sci. Instrum.*, 79:025105, 2008.
- [41] T. P. Hunt and R. M. Westervelt. Dielectrophoresis tweezers for single cell manipulation. *BIOMED MICRODEVICES*, 8:227–230, 2006.
- [42] S. Jeffery, A. Oral, and J.B. Pethica. Quantitative electrostatic force measurement in afm. *Appl. Surf. Sci.*, 157:280–284, 2000.
- [43] T. A. Johnson and V. C. Patel. Flow past a sphere up to a reynolds number of 300. *J. Fluid Mech.*, 378:19–70, 1999.
- [44] Robert Jones, Hubert M. Pollock, Jamie A. S. Cleaver, and Christopher S. Hodges. Adhesion forces between glass and silicon surfaces in air studied by afm: Effects of relative humidity, particle size, roughness and surface treatment. *Langmuir*, 18:8045–55, 2002.
- [45] Thomas B. Jones. An electromechanical interpretation of electrowetting. *J. Micromech. Microeng.*, 15(21):1184–7, 2005.
- [46] M. Kaneda, M. Yamamoto, K. Nakaso, T. Yamamoto, and J. Fukai. Oscillation of a tilted circular pad on a droplet for the self-alignment process. *Precis. Eng.*, 31:177–184, 2007.
- [47] Mohamed Kharboutly, Michaël Gauthier, and Nicolas Chaillet. Modeling the trajectory of a microparticle in a dielectrophoresis device. *J. Appl. Phys.*, 106:114312, 2009.
- [48] Dongshin Kim and David J. Beebe. A bi-polymer micro one-way valve. *Sensors and Actuators A*, 136:426–433, 2007.

- [49] Hyonse Kim, Chihyun In, Gilho Yoon, and Jongwon Kim. A slim type microvalve driven by pzt films. *Sensors and Actuators A*, 121:162–171, 2005.
- [50] M. Koch, A.G.R. Evans, and A. Brunnschweiler. Simulation and fabrication of micro-machined cantilever valves. *Sensors and Actuators A*, 62:756–759, 1997.
- [51] Pierre Lambert. *A Contribution to Microassembly: a Study of Capillary Forces as a gripping Principle*. PhD thesis, Université libre de Bruxelles, Belgium, 2004.
- [52] Pierre Lambert. *Capillary Forces in Microassembly: Modeling, Simulation, Experiments, and Case Study*. Microtechnology and MEMS. Springer, October 2007.
- [53] Pierre Lambert, Frank Seigneur, Sandra Koelemeijer, and Jacques Jacot. A case study of surface tension gripping: the watch bearing. *J. Micromech. Microeng.*, 16(7):1267–1276, 2006.
- [54] Dmitri Lapotko and Ekaterina Lukianova. Laser-induced micro-bubbles in cells. *International Journal of Heat and Mass Transfer*, 48:227–234, 2005.
- [55] Bernard Le Neindre. Tensions superficielles des composés inorganiques et mélanges. *Techniques de l'ingénieur*, K(476), 1993.
- [56] Bernard Le Neindre. Tensions superficielles et interfaciales. *Techniques de l'ingénieur*, K(475), 1993.
- [57] S. Lee and W. Sigmund. AFM study of repulsive van der Waals forces between teflon AF thin film and silica or alumina. *Colloids Surf. A*, 204(1-3):43–50, 2001.
- [58] S. Lee, W. Sutomo, C. Liu, and E. Loth. Micro-fabricated electrolytic micro-bubblers. *International Journal of Multiphase Flow*, 31:706–722, 2005.
- [59] Woo Ho Lee, Byoung Hun Kang, Young Seok Oh, Harry Stephanou, Arthur C. Sanderson, George Skidmore, and Matthew Ellis. Micropeg manipulation with a compliant microgripper. In *Proceedings of the 2003 IEEE International Conference on Robotics and Automation*, pages 3213–3218, Taipei, Taiwan, September 2003.
- [60] Cyrille Lenders. DEA: Study of valves used in microfluidics. Master's thesis, Université libre de Bruxelles, Brussels, Belgium, 2006.
- [61] Cyrille Lenders, Jean-Baptiste Valsamis, Maxime Desaedeleer, Alain Delchambre, and Pierre Lambert. Assembly of a micro ball-bearing using a capillary gripper and a microcomponent feeder. In *Micro-Assembly Technologies and Applications*. International Precision Assembly Seminar (IPAS), Springer, 2008.
- [62] Gabriel Lippmann. Relations entre les phénomènes électriques et capillaires. *Ann. Chim. Phys.*, 5(5):494–549, 1875.
- [63] Xianming Liu, John L. Spencer, Alan B. Kaiser, and W. Mike Arnold. Selective purification of multiwalled carbon nanotubes by dielectrophoresis within a large array. *Curr. Appl. Phys.*, (6):427–431, 2006.
- [64] B. Lopez-Walle, M. Gauthier, and N. Chaillet. Principle of a submerged freeze gripper for micro-assembly. *IEEE transactions on robotics*, 24(4):897–902, august 2008.
- [65] Steven Lubetkin. The motion of electrolytic gas bubbles near electrodes. *Electrochimica Acta*, 48:357–375, 2002.

- [66] A. Luque, J.M. Quero, and C C. Hibert. Integrable silicon microfluidic valve with pneumatic actuation. *Sensors and Actuators A*, 118(1):144–151, 2005.
- [67] Hsiao-Kang Ma, Bo-Ren Hou, Cheng-Yao Lin, and Jhong-Jhih Gao. The improved performance of one-side actuating diaphragm micropump for a liquid cooling system. *International Communications in Heat and Mass Transfer*, 35:957–966, 2008.
- [68] M. Mastrangeli, S. Abbasi, C. Varel, C. Van Hoof, J.-P. Celis, and K.F. Bohringer. Self-assembly from milli- to nanoscales: methods and applications. *Journal of Micromechanics and Microengineering*, 19, 2009.
- [69] Massimo Mastrangeli. *Enabling Capillary Self-Assembly for Microsystem Integration*. PhD thesis, Katholieke Universiteit Leuven, 2010.
- [70] Jessica Melin, Niclas Roxhed, Guillem Gimenez, and Patrick Griss. A liquid-triggered liquid microvalve for on-chip flow control. *Sensors and Actuators B*, 100:463–468, 2004.
- [71] F. Mugele and J.C. Baret. Electrowetting: from basics to applications. *J. Phys.: Condens. Matter*, 17:R705–75, 2005.
- [72] K. Naessens. *Excimer laser ablation of microstructures in polymers for photonic applications*. PhD thesis, Universiteit Gent, 2004.
- [73] Henry K. Nahra and Y. Kamotani. Prediction of bubble diameter at detachment from a wall orifice in liquid cross-flow under reduced and normal gravity conditions. *Chem. Eng. Sci.*, 58:55–69, 2003.
- [74] Kwang W Oh and Chong H Ahn. A review of microvalves. *J. Micromech. Microeng.*, 16(5):R13–R39, 2006.
- [75] Takahiro Ohori, Shuichi Shoji, Keisuke Miura, and Akira Yotsumoto. Partly disposable three-way microvalve for a medical micro total analysis system (microtas). *Sensors and Actuators A*, 64:57–62, 1998.
- [76] J. F. Padday and D.R. Russel. The measurement of the surface tension of pure liquids and solutions. *J. Colloid Sci.*, 15:503–511, 1960.
- [77] Alexandros Papavasiliou, Albert Pisano, Dorian Liepmann, and John Evans. Controlling physical motion with electrolytically formed bubbles, 2001. Patent: WO0194823.
- [78] Ronald Plak, Roger Görtzen, and Erik Puik. Impact forces reduction for high-speed micro-assembly. In *Micro-Assembly Technologies and Applications*, volume 260, pages 325–332. International Precision Assembly Seminar (IPAS), Springer, 2008.
- [79] Dan O. Popa and Harry E. Stephanou. Micro and meso scale robotic assembly. In *WTEC Workshop: Review of U.S. Research in Robotics*. WTEC, 2004.
- [80] I. Rivollet, D. Chatain, and N. Eustathopoulos. Simultaneous measurement of contact angles and work of adhesion in metal-ceramic systems by the immersion-emersion technique. *Journal of materials science*, 25:3179–3185, 1990.
- [81] Jason H. Sakamoto, Anne L. van de Ven, Biana Godin, Elvin Blanco, Rita E. Serda, Alessandro Grattoni, Arturas Ziemys, Ali Bouamrani, Tony Hu, Shivakumar I. Ranganathan, Enrica De Rosa, Jonathan O. Martinez, Christine A. Smid, Rachel M. Buchanan, Sei-Young Lee, Srimeenakshi Srinivasan, Matthew Landry, Anne Meyn, Ennio Tasciotti, Xuewu Liu, Paolo Decuzzi, and Mauro Ferrari. Enabling individualized therapy through nanotechnology. *Pharmacol. Res.*, 62(2):57–89, 2010.

- [82] P. Selvaganapathy, E. T. Carlen, and C. H. Mastrangelo. Electrothermally actuated inline microfluidic valve. *Sensors and Actuators A*, 104:275–282, 2003.
- [83] M. Sobocinski, J. Juuti, H. Jantunen, and L. Golonka. Piezoelectric unimorph valve assembled on an Itcc substrate. *Sensors and Actuators A*, 149:315–319, 2009.
- [84] Cheng Xiang Song, Guirong Liu, Guirong Liu, and Xu Han. Simulation of an extruded quadrupolar dielectrophoretic trap using meshfree approach. *Engineering Analysis with Boundary Elements*, 30:994–1005, 2006.
- [85] Hiroaki Suzuki and Rei Yoneyama. Integrated microfluidics system with electrochemically actuated on-chip pumps and valves. *Sensors and Actuators B*, 96:38–45, 2003.
- [86] Yusuke Suzuki, Masumi Yamada, and Minoru Seki. Sol-gel based fabrication of hybrid microfluidic devices composed of pdms and thermoplastic substrates. *Sensors and Actuators B*, xxx:xxx–xxx, 2010. doi:10.1016/j.snb.2010.04.018.
- [87] T. Szirtes. *Applied Dimensional Analysis and Modeling*. MacGraw-Hill, New York, 1997.
- [88] Hidekuni Takao, Kazuhiro Miyamura, Hiroyuki Ebi, Mitsuaki Ashiki, Kazuaki Sawada, and Makoto Ishida. A mems microvalve with pdms diaphragm and two-chamber configuration of thermo-pneumatic actuator for integrated blood test system on silicon. *Sensors and Actuators A*, 119:468–475, 2004.
- [89] R. B. H. Tan, W. B. Chen, and K. H. Tan. A non-spherical model for bubble formation with liquid cross-flow. *Chem. Eng. Sci.*, 55:6259–6267, 2000.
- [90] Francis E.H. Tay, Liming Yu, Ah Ju Pang, and Ciprian Iliescu. Electrical and thermal characterization of a dielectrophoretic chip with 3d electrodes for cells manipulation. *Electrochimica Acta*, 52:2862–2868, 2007.
- [91] Vincent Vandaele. *Contactless handling for micro-assembly: acoustic levitation*. PhD thesis, Université libre de Bruxelles, Brussels, Belgium, 2008.
- [92] A. Volanschi, W. Olthuis, and P. Bergveld. Gas bubbles electrolytically generated at microcavity electrodes used for the measurement of the dynamic surface tension in liquids. *Sensors and Actuators A*, 52:18–22, 1996.
- [93] Z.J. Wei, W.L. Liu, D. Tian, C.L. Xiao, and X.Q. Wang. Preparation of lotus-like superhydrophobic fluoropolymer films. *Appl. Surf. Sci.*, 256:3972–3976, 2010.
- [94] R.P. Welle, B.S. Hardy, and M.J. O’Brien. Peltier-actuated microvalves: performance characterization. In *P SOC PHOTO-OPT INS 5591*, pages 158–166, 2004.
- [95] Zongyuan Xiao and Reginald B.H. Tan. An improved model for bubble formation using the boundary-integral method. *Chem. Eng. Sci.*, 60:179–186, 2005.
- [96] Wei Xu, Liang L. Wu, Yang Zhang, Hong Xue, Guann-Pyng Li, and Mark Bachman. A vapor based microfluidic flow regulator. *Sensors and Actuators B*, 142:355–361, 2009.
- [97] Z.L. Yang, T.N. Dinh, R.R. Nourgaliev, and B.R. Sehgal. Numerical investigation of bubble growth and detachment by the lattice-boltzmann method. *International Journal of Heat and Mass Transfer*, 44:195–206, 2001.
- [98] Kazushi Yoshida, Shuji Tanaka, Yosuke Hagihara, Shigeaki Tomonari, and Masayoshi Esashi. Normally closed electrostatic microvalve with pressure balance mechanism for portable fuel cell application. part i: Design and simulation. *Sensors and Actuators A*, 157:299–306, 2010.

-
- [99] Haibing Zhang and Andy Cloud. The permeability characteristics of silicone rubber. In *Proceedings of the 2006 SAMPE Fall Technical Conference "Global Advances in Materials and Process Engineering", Coatings and Sealants Section*, Dallas, TX, November 2006. Society for the Advancement of Material and Process Engineering.